THE UNIVERSITY OF QUEENSLAND

AUSTRALIA

Mechanical, hydraulic, and dielectric characterisation of fine-grained soils during densification

Moritz Schwing

Dipl.-Ing.

A thesis submitted for the degree of Doctor of Philosophy at

The University of Queensland in 2015

School of Civil Engineering

Geotechnical Engineering Centre

Abstract

Soil characterisation is of primary interest for several disciplines, including geotechnical and geo-environmental engineering, soil science, and agriculture. An upcoming and promising method for soil characterisation relies on the high-frequency electromagnetic measurement technique which provides the potential to explore and investigate soils. However, successful application of this technique requires a profound understanding of the multi-physical processes arising from interactions between soil as a porous medium and the propagation of electromagnetic waves. This thesis focuses on a coupled experimental investigation of the mechanical, hydraulic, and dielectric characterisation of fine-grained soil during densification. In the framework of this thesis, the following steps have been completed and novel findings have been made:

1. Probe designs have been developed, modified and improved to measure the dielectric soil properties in a frequency range from 1 MHz to 3 GHz during shrinkage and compaction. A low-cost in-house-manufactured probe was introduced, which was specifically designed for standardised geotechnical soil shrinkage test. During preliminary investigations, the calibration procedure and performance of these sensors were experimentally and numerically tested. The results showed agreement in the targeted frequency window.

2. Compaction and shrinkage tests on fine-grained soils were conducted in combination with dielectric and soil suction measurements. The shrinkage curve and soil water characteristic curve (SWCC) was established and successfully parameterised with physical based models. The complex permittivity was determined in a frequency range from 1 MHz to 3 GHz. The dielectric properties measured during the shrinkage test showed a sudden drop of complex permittivity which could be located in the residual shrinkage zone.

3. A theoretical electromagnetic mixture approach was used to model the measured frequency dependent dielectric properties of soils during shrinkage and compaction based on the parameterised shrinkage curve and SWCC. The theoretical results were compared to the dielectric measurements on different fine-grained soils. The comparison

showed that the real part of permittivity could be well predicted whereas the imaginary part suffered inaccuracies.

4. A sensitivity analysis was performed with the theoretical electromagnetic mixture approach in consideration of the shrinkage behaviour and SWCC in order to investigate the influence of soil suction and dry density on the frequency dependent permittivity. The sensitivity analysis showed that the real part of the permittivity near 1 GHz was insensitive to changes in the soil suction and dry density. In the MHz range, the real part of the permittivity was more sensitive to changes in soil suction than it was to dry density. The imaginary part of the permittivity was generally observed to be more sensitive to soil suction over the entire frequency range.

5. The dielectric relaxation spectra obtained during compaction or shrinkage were decomposed based on a multimodal Cole-Cole model with a global optimisation algorithm by means of Markov Chain Monte Carlo algorithm. It was found that the dielectric spectrum of compacted soil could be modelled with three Cole-Cole type relaxation processes in the studied frequency range from 1 MHz to 3 GHz. The dielectric spectrum of shrinking soil was decomposed into two relaxation processes due to the reduced investigated frequency range of 50 MHz to 3 GHz.

Declaration of author

This thesis is composed of my original work, and contains no material previously published or written by another person except where due reference has been made in the text. I have clearly stated the contribution by others to jointly-authored works that I have included in my thesis.

I have clearly stated the contribution of others to my thesis as a whole, including statistical assistance, survey design, data analysis, significant technical procedures, professional editorial advice, and any other original research work used or reported in my thesis. The content of my thesis is the result of work I have carried out since the commencement of my research higher degree candidature and does not include a substantial part of work that has been submitted to qualify for the award of any other degree or diploma in any university or other tertiary institution. I have clearly stated which parts of my thesis, if any, have been submitted to qualify for another award.

I acknowledge that an electronic copy of my thesis must be lodged with the University Library and, subject to the policy and procedures of The University of Queensland, the thesis be made available for research and study in accordance with the Copyright Act 1968 unless a period of embargo has been approved by the Dean of the Graduate School.

I acknowledge that copyright of all material contained in my thesis resides with the copyright holder(s) of that material. Where appropriate I have obtained copyright permission from the copyright holder to reproduce material in this thesis.

Publications during candidature

Journal publication:

N. Wagner, M.Schwing, and A. Scheuermann. Numerical 3-D FEM and experimental analysis of the open-ended coaxial line technique for microwave dielectric spectroscopy on soil. *IEEE Transactions on Geoscience and Remote Sensing*, 52(2):880-893, 2014.

Z. Chen, M. Schwing, J. Karlovsek, N. Wagner, and A. Scheuermann. Broadband dielectric measurement methods for soft geomaterials: Coaxial transmission line cell and open-ended coaxial probe. *International Journal of Engineering and Technology*, 6(5):373-380, 2014.

Conference publication:

M. Schwing, Z. Chen, N. Wagner, A. Scheuermann, and D. Williams. Experimental study on the relationship of mechanic and hydraulic state variables, and the dielectric properties of clays. In *6^{th} International Conference on Unsaturated Soils (UNSAT), 2014, Sydney, Australia*, pages 247-253.

M. Schwing, Z. Chen, A. Scheuermann, and N. Wagner. Non-destructive coaxial transmission line measurements for dielectric characterization on soils. In *Sensors Applications Symposium (SAS) IEEE 2014, Queenstown, New Zealand*, pages 248-252.

N. Wagner, F. Daschner, A. Scheuermann, and Moritz Schwing. Estimation of the soil water characteristics from dielectric relaxation spectra. In *Sensors Applications Symposium (SAS) IEEE 2014, Queenstown, New Zealand*, pages 242-247.

M. Schwing, A. Scheuermann, and N. Wagner. Dielectric properties of a clay soil determined in the frequency range from 1 MHz to 40 GHz. In *10^{th} International Conference on Electromagnetic Wave Interaction with Water and Moist Substances (ISEMA), 2013, Weimar, Germany*, pages 242-250.

N. Wagner, F. Daschner, M. Schwing, and A. Scheuermann. Analysis of coupled hydraulic and dielectric material properties of soils: A multivariate approach. In *International Workshop on Impedance Spectroscopy (IWIS), 2012, Chemnitz, Germany*, pages 38-39.

Publications included in this thesis

No publications included

Contributions by others to the thesis

No contributions by others

Statement of parts of the thesis submitted to qualify for the award of another degree

None

Acknowledgements

The work presented in this thesis could not have been completed without the support, guidance, and involvement of many people. I would like to take the chance to acknowledge those people who contributed to this project.

First, I would like to thank A. Scheuermann and N. Wagner for their great supervision of my journey throughout my studies. They not only gave me the opportunity to undertake this research, but also allowed me to develop my own research interests with freedom and assisted me with valuable feedback and suggestions. Thank you for being there whenever I needed your help and assistance. I also want to acknowledge D.J. Williams and Z. Chen for supporting my research. Moreover, I want to acknowledge Elite Editing for editing the thesis according to Standards D and E of the Australian Standards for Editing Practice.

An enormous part of the project involved experimental investigations which were mostly conducted in the geotechnical laboratories in the Advanced Engineering Building at The University of Queensland. This experimental work could have not been done without the help of many people. I would like to thank all those people in the technical staff team. I would also like to thank J. Speer for helping me run my experiments successfully.

Plenty of people crossed my path since I arrived at The University of Queensland almost four years ago. I have had many coffees and lunch breaks with interesting conversations with them. Many of these people enriched my time not only at university but also outside the university life in Brisbane. They have become more than colleagues to me. Special thanks go to my friends Max Kumm, Patrick Schmidt, Jurij Karlovsek, Hassan Karampour, Julia Busse, Robin Dawson, Luc Turner, Florent Birrien, Thierry Bore, William Hawker, Theo Garcia Rolim de Moura, Scott Lines, Tilman Bittner and Thomas Riviere.

Last, but not least, I would like to say thank you from the bottom of my heart to my family for their endless love. You have made me what I am today. I want to thank Eva Maria, Maximilian, and Erwin for being my siblings. A big and lovely thank you to my girlfriend Yodit. There are no words to express what you have done for me. I will never forget it. Finally, I would like to dedicate my thesis to my parents, and thank them for their unlimited belief in me, restless support and love that I have received from them in my life.

Keywords

fine-grained soil, permittivity, shrinkage curve, soil suction, soil water characteristic curve, vector network analyser

Australian and New Zealand Standard Research Classifications (ANZSRC)

ANZSRC code: 090501, Civil Geotechnical Engineering, 100%.

Fields of Research (FoR) Classification

FoR code: 0905, Civil Engineering, 100%.

Contents

List of Figures

List of Tables

Abbreviations

3-D	Three-Dimensional
AS	**A**lluvial **S**oil
BJ	Modified Nicolson-Ross-Weir algorithm
BIJ	Iterative method
CRIM	**C**omplex **R**efractive **I**ndex **M**odel
CT	**C**oaxial **T**ransmission Line
DDL	**D**iffuse **D**ouble **L**ayer
DLVO	**D**erjaguin-**L**andau-**V**erwey-**O**verbeek
EM	**E**lectro **M**agnetic
GPR	**G**round **P**enetrating **R**adar
HF	**H**igh **F**requency
HFSS	**H**igh **F**requency **S**tructure **S**imulator
IDC	**I**nitial **D**rying **C**urve
KA	**Ka**olin
kHz	Kilohertz
IWC	**I**nitial **W**etting **C**urve
MCMC	**M**arkov **C**hain **M**onte **C**arlo
MHz	Megahertz
MUT	**M**aterial **U**nder **T**esting
NRW	**N**icolson **R**oss **W**eir Method
OE	**O**pen **E**nded Coaxial Line
OWL	**O**pen **W**ater **L**iquid
OWS	**O**pen **W**ater **S**hort
PDC	**P**rimary **D**rainage **C**urve
PI	**P**lasticity **I**ndex

PL	**P**lastic **L**imit
PM	**P**ropagation **M**atrix Method
PWC	**P**rimary **W**etting **C**urve
RMSE	**R**oot **M**ean **S**quare **E**rror
RW-MWG	**R**andom **W**alk **M**etropolis-**W**ithin-**G**ibbs
SL	**S**hrinkage **L**imit
SWCC	**S**oil **W**ater **C**haracteristic **C**urve
TDR	**T**ime **D**omain **R**eflectometry
VNA	**V**ector **N**etwork **A**nalyser

Physical Constants

Speed of light	c_0	$=$	$2.997\ 924\ 58 \times 10^{8}\ \mathsf{ms}^{-1}$
Acceleration of standard gravity	g	$=$	$9.806\ 66\ \mathsf{m} \cdot \mathsf{s}^{-2}$
Permittivity of free space	ε_0	$=$	$8.854\ 1878\ 176 \times 10^{-12}\mathsf{F/m}$
Boltzmann constant	k_B	$=$	$1.380\ 66 \times 10^{-23}\mathsf{J} \cdot \mathsf{K}^{-1}$
Universal gas constant	R_{Gas}	$=$	$8.314\ 462\ 1\ \mathsf{J} \cdot (\mathsf{mol} \cdot \mathsf{K})^{-1}$

Symbols

a_{ch}	shrinkage curve parameter related to the minimum internal dimension of the last isolated air-filled pore (Equation 2.28) [-]
a_{fx}	Fredlund and Xing SWCC fitting parameter (Equation 2.13) [-]
a_{p}	Peng shrinkage curve fitting parameter (Equation 2.17) [-]
a_{soil}	soil specific calibration constant (Equation 4.21) [-]
a_{vG}	van Genuchten SWCC fitting parameter (Equation 2.12) [1/cm]
a_x	constant defined by Low [7] (Equation 4.27) [ÅK]
b_{soil}	soil specific calibration constant (Equation 4.21) [-]
c_i	probe calibration constant (Equation 5.7) [-]
c_x	dynamic viscosity of interfacial water (Equation 4.27) [Pa·s]
d_{BW}	thickness of the bound water phase (for example, Equation 4.27) [μm]
e	void ratio of soil [-]
e_I	initial void ratio of soil [-]
e_N	void ratio at end of proportional shrinkage [-]
e_R	void ratio at end of structural shrinkage [-]
e_Z	void ratio at shrinkage limit [-]
f	frequency [Hz]
$f^\star$	cut-off frequency (Equation 4.27 [Hz]
f_c	relaxation frequency [Hz]
h	soil sample height [mm]
k	number of mineralogical soil components [-]
l	length [mm]
m_{fx}	Fredlund and Xing SWCC fitting parameter (Equation 2.13) [-]
m_{p}	Peng shrinkage curve fitting parameter (Equation 2.17) [-]
m_{vG}	van Genuchten SWCC fitting parameter (Equation 2.12) [-]

n	porosity of soil [-]
n_{fx}	Fredlund and Xing SWCC fitting parameter (Equation 2.13) [-]
n_p	Peng shrinkage curve fitting parameter (Equation 2.17) [-]
n_{vG}	van Genuchten SWCC fitting parameter (Equation 2.12) [-]
p	partial pressure of pore water vapour (Equation 2.8) [kPa]
p_0	saturation pressure of water vapour (Equation 2.8) [kPa]
q	electric charge density (Equation 4.1c) [C/m^3]
r	pore size radius [μm]
r_i	internal pore dimension (Equation 2.20) [μm]
r_m	maximum external pore dimension (Equation 2.20) [μm]
r_{mol}	radius of water molecule (Equation 4.27) [Å]
$r_{m,M}$	maximum external pore dimension at maximum water content [μm]
r_0	minimum external pore dimension [μm]
$r_{0,M}$	minimum external pore dimension at maximum water content [μm]
$r_{0,Z}$	minimum external pore dimension at shrinkage limit [μm]
u_w	pore water pressure [kPa]
u_a	pore air pressure [kPa]
w	gravimetric water content [-]
w_I	initial gravimetric water content [-]
w_{Pr}	optimum water content [-]
x	distance to particle surface [Å]
A_1 and A_1	incident VNA signal from port 1 and 2
A_{CH}	connection factor in Chertkov model (Equation 2.18) [-]
A_s	total specific particle surface of the soil [m^2/g]
$\bar{B}$	magnetic flux density (Equation 4.1d) [(V·s)/m^2]
B_1 and B_2	reflected and transmitted VNA signal from port 1 and 2
C_0	capacitance dependent on the fringing fields effects outside between the probe tip and sample (Equation 5.5) [F]
C_f	capacitance dependent on the fringing fields effect inside the probe (Equation 5.5) [F]
$C(\lvert\Psi_t\rvert)$	correction factor proposed by Fredlund and Xing [8] [-]
$\bar{D}$	electric flux density (Equation 4.1c) [(A·s)/m^2]

$\bar{E}$	electric field vector (Equation 4.1a [V/m]
F	characteristic fraction of pore volume occupied by water (Equation 2.20) [-]
F_Z	characteristic fraction of pore volume occupied by water at shrinkage limit (Equation 2.28) [-]
$\Delta G_w^{\ddagger}$	free enthalpy of activation of water (Equation 2.6) [kJ/mol]
$\Delta G_w^{\ddagger\circ}$	free enthalpy of activation of water at reference state (Equation 4.36) [kJ/mol]
$\Delta H_w^{\ddagger}$	activation enthalpy (Equation 2.6) [kJ/mol]
$\bar{H}$	magnetic field vector (Equation 4.1b) [A/m]
H_c	height of capillary rise of water [cm]
$\bar{J}$	electric current density vector (Equation 4.1b) [A/m^2]
$\bar{J}_D$	displacement current density (Equation 4.3) [A/m^2]
$\bar{J}_{\text{eff}}$	effective current density (Equation 4.3) [A/m^2]
LL	water content at liquid limit [-]
M	bulk soil mass [g]
M_{I}	bulk soil mass at shrinkage test beginning [g]
M_{U}	weight of paraffin-coated soil sample in water [g]
M_{W}	mass of water [g]
M_{wax}	mass of soil sample coated with paraffin [g]
M_{S}	mass of solid particles [g]
PI	plasticity index of soil [-]
PL	water content at plastic limit [-]
S	saturation degree of soil [-]
$\Delta S_w^{\ddagger}$	activation entropy (Equation 2.6) [kJ/(mol·K)]
S_{ij}	scattering parameters (Equation 5.1) [-]
S_{11}^{O}	reflection coefficient of open measurement [-]
S_{11}^{S}	reflection coefficient of short circuited measurement [-]
S_{11}^{W}	reflection coefficient of deionised water measurement [-]
S_{e}	dimensionless effective saturation of soil [-]
$S_{\text{dep,i}}$	depolarisation factor (Equation 4.28) [-]
SL	water content at shrinkage limit [-]
T	temperature [°C or K]
T_P	period time of EM field [s]
V	volume fraction of soil [cm^3]

V_A	volume of air [cm^3]
V_W	pore water volume [cm^3]
V_P	pore volume [cm^3]
V_S	volume of solid phase [cm^3]
V_{mol}	molecular mass of water [mol]
W_i	weighting factors [-]
Z_0	characteristic impedance of the probe (Equation 5.2) [Ω]
$Z_S^\star$	characteristic impedance of the sample (Equation 5.2) [Ω]
α	structure parameter (Equation 4.23) [-]
β_{CC}	stretching exponent of Cole Cole model (Equation 4.8) [-]
$\gamma_S^\star$	propagation factor (Equation 5.14) [-]
δ	loss tangent (Equation 4.5) [°]
δ_w	contact angle (Equation 2.9) [°]
$\varepsilon^\star$	absolute complex permittivity [F/m]
ε'	real part of absolute complex permittivity [F/m]
ε''	imaginary part of absolute complex permittivity [F/m]
$\varepsilon^\star_{r,eff}$	complex relative effective permittivity [-]
$\varepsilon'_{r,eff}$	real part of complex relative effective permittivity [-]
$\varepsilon''_{r,eff}$	imaginary part of relative permittivity [-]
$\varepsilon''_{r,d}$	imaginary part of relative permittivity due to dielectric losses (Equation 4.4) [-]
$\varepsilon_{r,G}$	relative permittivity of soil mineral [-]
$\varepsilon^\star_{r,L}$	relative permittivity of liquid calibration measurement [-]
$\varepsilon_{r,O}$	permittivity of open calibration measurement [-]
$\varepsilon^\star_{r,W}$	relative permittivity of deionised water calibration measurement [-]
ε_A	permittivity of air [-]
$\varepsilon^\star_{BW}$	permittivity of bound water [-]
ε'_{BW}	real part of permittivity of bound water [-]
ε''_{BW}	imaginary part of permittivity of bound water [-]
ε_S	static permittivity [-]
$\varepsilon_{S,W}$	static permittivity of free water (Equation 4.13) [-]
$\varepsilon_{S,G}$	static permittivity at the particle surface (Equation 4.37) [-]
$\varepsilon^\star_W$	complex permittivity of water [-]

ε_W	maximum permittivity of water [-]
$\varepsilon_{W,min}$	minimum permittivity of water [-]
$\Delta\varepsilon$	relaxation magnitude (Equation 4.6) [-]
ε_∞	high-frequency (HF) limit of permittivity (Equation 4.6) [-]
$\varepsilon_{\infty,FW}$	high-frequency limit (HF) of permittivity of free water [-]
ζ	relative water content [-]
ζ_N	relative water content at end of proportional shrinkage [-]
ζ_Z	relative water content at shrinkage limit [-]
θ	volumetric water content [-]
θ_{BW}	volumetric water content of bound water [-]
θ_{FW}	volumetric water content of free water [-]
θ_R	residual volumetric water content [-]
θ_S	saturation volumetric water content [-]
θ_U	unsaturated maximum volumetric water content due to entrapped air [-]
ϑ	moisture ratio of soil [-]
ϑ_I	initial moisture ratio (e.g. beginning of shrinkage test) [-]
ϑ_N	moisture ratio at end of proportional shrinkage [-]
ϑ_R	moisture ratio at end of structural shrinkage [-]
ϑ_Z	moisture ratio at shrinkage limit [-]
λ	particle surface parameter (Equation 4.16) [1/cm]
λ_{BC}	SWCC shape parameter (Equation 2.11) [-]
λ_P	wavelength of EM fields [m]
$\mu^\star$	absolute magnetic permeability [(V·s)/(A·m)]
μ_0	magnetic permeability of free space [(V·s)/(A·m)]
$\mu_r^\star$	relative magnetic permeability [-]
μ_W	absolute chemical potential of pure water (Equation 2.4) [kJ/kg]
μ_W°	chemical potential of pure water at reference state [kJ/kg]
$\Delta\mu_W$	difference of chemical potential [kJ/kg]
$\Delta\mu_{W,V}$	difference of chemical potential due to van der Waals forces [kJ/kg]
$\Delta\mu_{W,E}$	difference of chemical potential due to Coulomb electrostatic forces [kJ/kg]
$\Delta\mu_{W,O}$	difference of chemical potential due to osmotic forces [kJ/kg]
$\Delta\mu_{W,C}$	difference of chemical potential due to capillary forces [kJ/kg]
ν	relative volume of soil [-]

v_N	relative volume at end of proportional shrinkage [-]
v_S	relative volume of solid phase [-]
v_Z	relative volume at shrinkage limit [-]
ρ_D	dry density [g/cm^3]
$\rho_{D,Pr}$	optimum dry density [g/cm^3]
ρ_G	solid density [g/cm^3]
ρ_W	water density [g/cm^3]
ρ_{wax}	density of paraffin [g/cm^3]
ρ_X	X-ray density [g/cm^3]
σ	total stress [kPa]
σ'	effective stress [kPa]
$\sigma_{w,S}$	electrical conductivity at saturation (Equation 4.38) [S/m]
$\sigma_{w,U}$	empirical coupling parameter for electrical conductivity at unsaturated soil conditions (Equation 4.38) [S/m]
σ_{wa}	surface tension (Equation 2.9) [kN/m^2]
σ_{DC}	direct current conductivity [S/m]
$\sigma_E^\star$	electrical conductivity [S/m]
τ	relaxation time [s]
τ_{FW}	relaxation time of free water [s]
χ	soil parameter in unsaturated stress conditions (Equation 2.16) [-]
Ψ_t	total soil suction [kPa or MPa]
Ψ'_t	normalised total suction [-]
Ψ_{AEV}	soil suction at air entry value [kPa or MPa]
Ψ_G	gravitational soil suction [kPa or MPa]
Ψ_M	matric soil suction [kPa or MPa]
Ψ_O	osmotic soil suction [kPa or MPa]
Ψ_R	soil suction at residual water content [kPa or MPa]
ω	angular frequency [1/s]
Γ	ideal reflection coefficient [-]
Δ	average thickness of plate-like clay particles [μm]
Δ_M	average thickness of plate-like clay particles at maximum water content [μm]
Δ_Z	average thickness of plate-like clay particles at shrinkage limit [μm]

Υ	ideal transmission coefficient [-]
$\Omega^{\star}$	water bonding state [-]
$\bar{\nabla}\times$	curl operator
$\bar{\nabla}\cdot$	divergence operator
j	imaginary unit

Chapter 1

Preface

1.1 Background

Constitutive soil properties play an important role in the design of civil engineering structures because soil is involved in almost every construction project, as part of building foundations, tunnels, dams and many other aspects. As part of civil engineering, it is the task of geotechnical engineers to determine the soil properties of interest and contribute these properties to other civil engineering disciplines. In order to provide successful and sustainable design for any construction that involves geotechnical expertise, it is necessary to deliver an accurate prediction of soil properties. In general, the soil properties in traditional geotechnical engineering can be summarised as either mechanical or hydraulic soil properties which may be determined either in field or laboratory investigations. However, the existing traditional experimental techniques used to determine soil properties entail potential disadvantages:

- Sampling may disturb the soil structure.
- Numerous experiments are frequently required to enable complete characterisation of the mechanical and hydraulic soil behaviour.
- Laboratory and field investigations are highly time consuming and result in increased costs.

These disadvantages support the need to determine other innovative methods to enable soil characterisation. Promising techniques include geophysical radio to microwave electromagnetic (high-frequency electromagnetic - [HF-EM]) methods, which are increasingly used in geotechnical and geo-environmental engineering to explore and investigate soil properties

[9]. The application of methods such as ground penetrating radar (GPR) or time domain reflectometry (TDR) is becoming more attractive, and these are frequently used due to being non-invasive or less invasive, and because they have the potential to retrieve physical and structural material parameters in an accurate and time-saving manner [10, 11, 12]. However, successful application of these methods requires a profound understanding of the measurement techniques, equipment used, and data processing, as well as the constitutive material properties [13, 14]. These constitutive properties have material-specific parameters that may be used to derive traditional soil state parameters. Herein, the dielectric property is of interest and is used to characterise the soil as a porous material.

Early studies mainly focused on TDR, with a particular interest on the relationship between soil water content and apparent permittivity via material-specific calibration equations [15, 16, 17]. However, soils generally respond dielectrically in a broad frequency range. These responses not only originate from pore water but also from the soil composition, structure, and mineralogy, as well as many other important soil characteristics [18, 19]. With continuing research, the dielectric soil property at around 1 GHz is found to be not only a function of water content, but also of porosity and saturation [20, 21, 22]. Recent studies have focused on the broadband electromagnetic behaviour of soil as a porous multiple-phase material. Hence, the focus is particularly on the relationship between soil hydraulic – especially soil suction – and mechanical and constitutive HF-EM properties [19, 23, 24].

However, interpreting the relationship between the dielectric properties and mechanical and hydraulic properties of porous materials is highly complex, particularly for fine-grained soils, due to the multi-physical and chemical processes involved. In this context Hilhorst et al. [25] stated:

'Probably the most important drawback to using the dielectric properties of soils is the complexity of the dielectric theory, which involves a number of physical processes that are not well understood.'

1.2 Scope and objectives

The scope of this study is to perform mechanical, hydraulic, and dielectric tests to reveal the characteristics of fine-grained soils during densification. Since the coupled characterisation involves multi-physical processes with enormous complexity, numerical investigations are generally not accessible. Hence, this systematic investigation and analysis of the coupled soil properties is based entirely on experimental work. As this kind of investigation is novel, the experimental work is focused on laboratory tests with well-defined boundary conditions

to minimise environmental influences such as temperature changes due to extreme weather conditions. Many state parameters and variables characterise the mechanical and hydraulic properties of fine-grained soils. In this study, the primarily investigated soil state parameters are water content, density, and soil suction because these parameters mainly describe the densification and consistency of fine-grained soils. In addition, the dielectric properties are measured in the experiments in a range from 1 megahertz (MHz) to 3 gigahertz (GHz), and the dielectric results are subsequently related to the obtained soil state parameters.

The study aims to improve understanding of the coupled mechanical, hydraulic and dielectric properties of fine-grained soils during densification which is the basis for enhanced successful application of HF-EM methods. The objectives of this study can be summarised as follows:

- developing an experimental methodology and procedure to characterise the coupled properties of soils based on novel and innovative laboratory setups.
- developing two innovative probes specifically designed for prevailing test requirements, where the objective is to verify the suitability and applicability of these probes for the use in standard geotechnical laboratory tests.
- employing standard geotechnical tests to simulate different densification scenarios in fine-grained soils, with the tests modified to allow characterisation of the coupled properties of fine-grained soils.
- establishing an analysis procedure to interpret the measured frequency-dependent dielectric spectrum.
- establishing an enhanced theoretical mixture approach on the basis of parameterised soil mechanical and hydraulic characterisation.
- undertaking sensitivity analysis to quantify the influence of mechanic and hydraulic soil parameters on dielectric characteristics.

1.3 Strategy

The strategy of this thesis can be divided into following steps:

1. Identifying practical standard geotechnical testing methods to investigate the densification of soils. Fine-grained soils are always subject to volume changes, whether due to external or internal stress situations. Two different standard geotechnical tests – compaction test and shrinkage test – are chosen to simulate the densification of fine-grained

soils. It is intended to measure the targeted soil state parameters throughout the tests. Volume measurement techniques are introduced to record density changes during the test, particularly for the shrinkage test. Since these standard geotechnical tests are not designed to determine hydraulic properties during testing, appropriate measurement techniques are sighted based on the literature review, and are introduced to measure the soil suction in parallel to the densification. Physical and empirical fitting models are selected to quantitatively describe density changes and soil suction changes as a function of the water content.

2. Commercial probes fulfilling the requirements of standard geotechnical tests rarely exist. In order to measure the dielectric properties in a frequency range from 1 MHz to 3 GHz, appropriate probes to conduct dielectric measurements need to be developed. Therefore, this study introduces and extensively describes two different innovative probes. The applicability of both probes in standard geotechnical tests is verified. One of these probes is a low-cost in-house-manufactured probe, specifically designed to measure the dielectric behaviour of fine-grained soils under shrinkage. During the first step, numerical simulations of the in-house-made probe are conducted to numerically determine the performance and propagation characteristics of HF-EM waves in different standard materials in order to assess the sensitive volume of the probe. The success of the dielectric measurements using these probes strongly depends on the calibration procedure and data processing. In this study, a calibration procedure for both probes is proposed and experimentally evaluated with standard calibration materials. Data processing techniques are compared experimentally and numerically to existing techniques that are required to deduct the broadband dielectric soil properties by determining the complex permittivity from 1-port and 2-port reflection and transmission measurements. Further, the dielectric measurements of these two probes are compared to commercially available high performance probes to evaluate their performance.

3. To compare the dielectric results with existing solutions, first, the measured dielectric spectrum of soil during densification is compared and verified with existing empirical material-specific calibration equation and theoretical mixture approaches. Second, it is aimed to couple the different soil properties. A theoretical mixture approach in combination with phenomenological relaxation models is further developed and coupled with parameterised shrinkage curves and soil water characteristic curves (SWCCs) to model the frequency-dependent dielectric properties based on mechanical and hydraulic soil characterisation. This coupled model is compared to the measured dielectric spectrum in a frequency from 1 MHz to 3 GHz. A sensitivity analysis is performed to verify the

coupled model and give a quantitative description of the influence of soil state parameters on the dielectric spectrum in a frequency from 1 MHz to 3 GHz.

4. The dielectric spectrum is analysed with an existing relaxation model to quantify the dielectric dispersion over the measured frequency range. An optimisation procedure based on the Markov Chain Monte Carlo algorithm is established to fit the multi-termed relaxation models and detect the underlining fundamental relaxation mechanism.

1.4 Thesis outline

The remainder of this thesis is structured as follows. Chapter 2 introduces the physics for characterising fine-grained soils that are relevant in the context of this thesis. It begins by discussing clay mineralogy which characterises fine-grained soil and general soil composition. Subsequently, it explains soil-water interaction, and introduces the potential concept. It then reviews the available models that enable researchers to quantitatively parameterise the soil-water interaction. Further, it describes soil volume changes due to shrinkage and discusses the available empirical and physical models.

Chapter 3 focuses on the existing test methods that are available for mechanical and hydraulic soil characterisation. It presents a literature review of the existing methods to measure soil suction and discusses the advantages and disadvantages of existing methods. Further, this review is complemented by a literature review of the methods available to determine soil volume changes. It highlights the advantages and disadvantages of the available methods. In addition, it introduces and details the methods used in this study.

Chapter 4 reviews the electromagnetic characterisation of fine-grained soils by explaining the electromagnetic theory and constitutive equations. It then details the fundamental mechanisms causing dielectric dispersion over a broad frequency range, and introduces models for quantification. Moreover, it defines the electromagnetic properties of individual soil components, and reviews different dielectric models.

Chapter 5 focuses on the electromagnetic measurement technique used in this study. It details the design and working principle, including calibration procedure of the two probes used in this study. In addition, it presents the preliminary investigation results, including the numerical simulation on both probes. Further, it presents the preliminary experimental results, which evaluate the calibration procedure of the in-house-manufactured probe using standard calibration materials. At the end of this chapter is an experimental comparison of the used and commercial probes presented.

Chapter 6 explains the experimental investigations that were conducted in the frame of this study. Initially, it introduces the soils tested and classifies them based on the soil parameters gained in the standardised geotechnical testing methods. It then details the combined mechanical, hydraulic, and dielectric soil characterisation during the compaction test and shrinkage test, including soil preparation, test setup, methodology and experimental procedure.

Chapter 7 focuses on the analysis of the experimental data of the compaction test and shrinkage test. This chapter is divided into two sections that have a similar structure: compaction test and shrinkage test. Both sections extensively describe and discuss the establishment and parameterisation of the shrinkage curve and SWCC. Subsequently, the sections determine the dielectric properties of the compacted and shrunk fine-grained soil, and compare these to material-specific empirical calibration equations and theoretical mixture approaches. These sections also present a spectrum analysis of the frequency dependent dielectric soil property for the compaction test and shrinkage test.

Chapter 8 concludes the thesis by providing a summary of the study's outcomes, and presenting an outlook for future studies.

Chapter 2

Characterisation of fine-grained soils

2.1 Introduction

Soil is a porous medium that is composed of different phases. The proportions of these phases, involved in the soil body, greatly influence the mechanical and hydraulic soil properties. In the case of fine-grained soil such as clay, the interaction between phases also plays an important role in influencing the mechanical and hydraulic soil behaviour. To give an overview and understand the complexity of soil as a porous medium, this thesis begins with a presentation of the literature review that examines the characterisation of fine-grained soils.

To begin, the structural composition of soil is explained in general to define the terminology of the variables used in the thesis. After explaining the soil structure, the composition of clay is introduced to provide an understanding of the crystalline structure composition of clay particles at the micro-scale. Understanding of the clay mineralogy is required for the subsequent explanation of the soil phase interaction. The potential concept used to define the soil-water interaction is discussed, and models are introduced to enable the quantification of the water potential in fine-grained soils. The final sections of this chapter focus on reasons for the densification of fine-grained soils in the presence of external and internal stress conditions, which is followed by a detailed explanation of the shrinkage behaviour of soils.

2.2 Structural composition of soil

Soil is generally a porous medium that can be described as a three-phase medium, consisting of a solid, fluid and gaseous phase. The solid phase is built by solid particles, such as clay

minerals, silt, and sand. The porous space, V_P, between the solid particles is filled by the fluid phase (water) and/or gaseous phase (air). The following graph presents an idealised illustration of a soil body, showing the relationships between those three phases in terms of volume, V, and mass, M [26]. In this idealised illustration, the solid phase is assumed

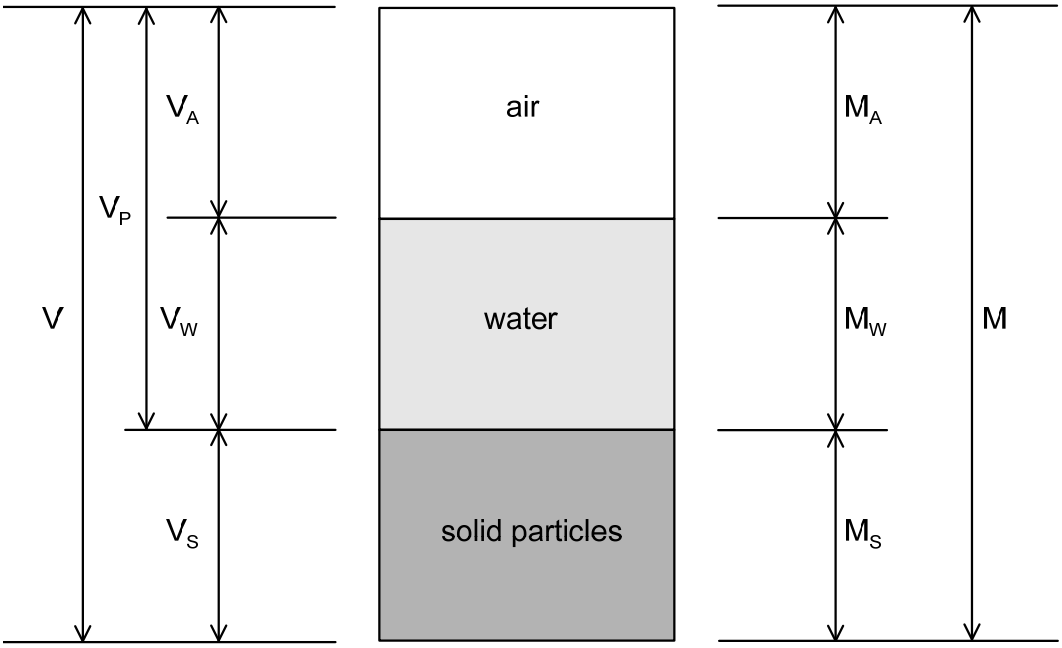

Figure 2.1: Phase diagram for a unsaturated soil, adapted from [26].

to be void free. Under this assumption, the density of the solid phase is given by the solid density, $\rho_G = M_S/V_S$, which is a physical soil property. ρ_G is taken as a constant value and is not influenced by any environmental factors. In contrast, there are state parameters that describe the actual state of a soil in situ. These state parameters are not seen as constant values and are subject to environmental influences as well as internal and external stress conditions. The following explains some relevant state parameters for this thesis.

The amount of water in the soil matrix is normally described by the gravimetric water content which is defined as:

$$w = \frac{M_W}{M_S}, \tag{2.1}$$

where, M_W is the pore water mass, and M_S is the mass of solid particles. The density state of soil can be expressed by the dry density, ρ_D, which is per definition $\rho_D \leq \rho_G$:

$$\rho_D = \frac{M_S}{V}, \tag{2.2}$$

where, $V = V_S + V_W + V_A$ is the total volume of the soil body, which consists of the pore volume ,$V_P = V_A + V_W$, and volume of solid particles, V_S. The pore volume might be filled by air and/or water. A measure of the amount of pore volume filled by water is given by the

saturation degree, S, according to:

$$S = \frac{w \cdot \rho_D \cdot \rho_G}{\rho_W \cdot (\rho_G - \rho_D)}. \tag{2.3}$$

where, ρ_W is the density of water. However, various other definitions exist – such as void ratio, volumetric water content and so forth – and can be calculated based on the aforementioned physical and state parameters [27].

2.3 Clay mineralogy

Fine-grained soils are composed of a high content of clay minerals, which belong to the group of crystalline materials [28]. These crystalline materials can be further distinguished into kaolinite, montmorillonite and illite [29]. As shown in Figure 2.2, kaolinite, illite and mont-

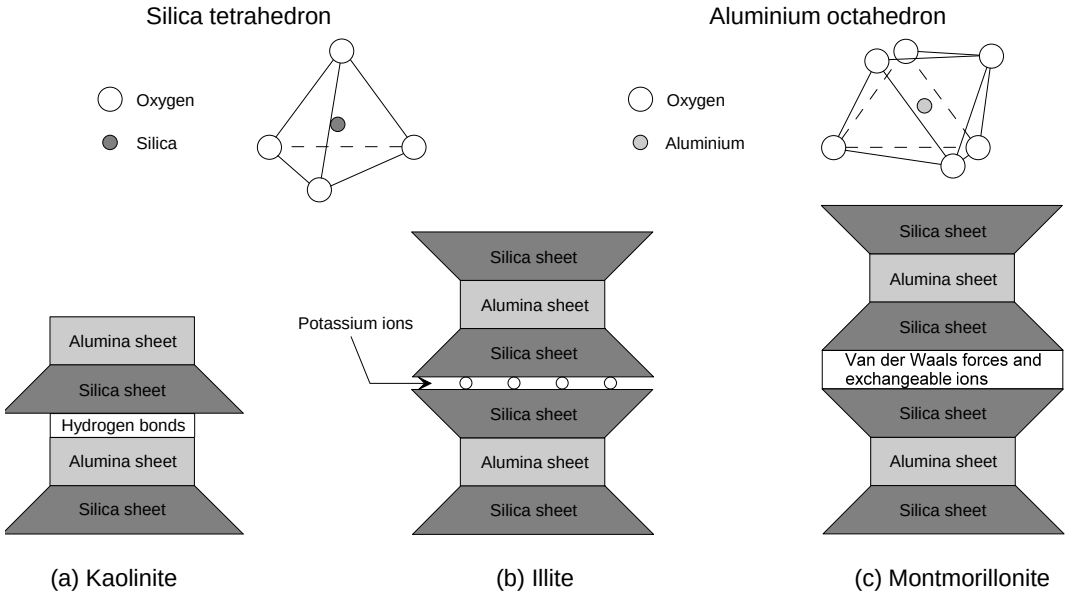

Figure 2.2: Structural composition of different naturally occuring clay minerals, adapted and modified from [30].

morillonite are commonly composed of silica sheets and alumina sheets. A silica sheet is formed by silica tetrahedrons which consist of one central silica cation and four surrounding oxygen anions. In contrast, an alumina sheet is built by aluminium octahedrons where an aluminium cation is surrounded by six oxygen anions. The crystalline materials are formed by a stack of several layers of these silica and alumina sheets. The structure of kaolinite shows a stack of layers that are held together by hydrogen bonds, in between two neighbouring layers. Each of these layers is built by a pair of one silica and alumina sheet which is coupled by common oxygen anions. In the case of illite and montmorillonite, the structure

of one layer differs to that of kaolinite. A layer contains one aluminium sheet embedded between two silica sheets, which are tied up with shared oxygens. For illite, a stack of several layers is bonded by enclosed potassium ions, whereas layers of montmorillonite are bonded together by van der Waals forces acting on ions and water molecules of interlayered water.

2.4 Soil - water interaction

2.4.1 Interaction between solid particle surface and water phase

The particle surface area of clay is negatively charged due to the isomorphous substitution of cations occurring in the silica sheets and alumina sheets, which leads to a charge deficit of the mineral surface [31, 32]. This negative charge of the mineral surface creates an electrical field with an electrostatic force – also called 'surface force'. In contrast, a water molecule is composed of one oxygen atom and two hydrogen atoms, which are bound under an angle of 104.45 degrees. Due to the fact that the centre of the positive and negative charges is not aligned under an angle of 180 degrees, a water molecule behaves as a dipole, having a positively and negatively charged molecule side. The natural dipole character enables water molecules to produce hydrogen bonds among each other. The electrostatic force of the mineral surface of particles attracts ions and polarised water molecules from the ambient pore water solution to neutralise its negatively charged particle surface [33]. However, it has been observed that the bond between silica sheets and alumina sheets is disturbed at the edges [33]. Dependent on the chemistry and pH-value, the disturbed bond can lead to a positively charged edge of the clay particle surface [33, 34].

This attraction and interaction between the particle surface and pore water phase becomes much more dominant in fine-grained soils due to the high particle surface area of clay minerals [31]. As shown in Figure 2.3c, the electrical potential reaches its maximum on the particle surface and decreases successively with the distance to the particle surface. As a result, the electrostatic force attracting cations is also strongest at the particle surface (see Figure 2.3b), which produces an enhanced cation concentration around the particle. In contrast, anions are repelled by the negatively charged particle surface. With increasing distance to the particle surface, the electrostatic force reduces which leads to lower cation attraction and anion repulsion. Hence, the concentration of cations decreases and anion concentration increases with distance to the particle. The negatively charged particle surface, together with ion concentration distribution of the pore water, is defined as the diffuse double layer (DDL) [33, 35]. In this layer, cations and anions are permanently diffusing and changing their placement. The DDL is characterised by the Stern-Gouy double layer theory [33, 34, 35, 36],

which considers the surface charge density, adsorbed cation type, and pore solution salinity upon ion distribution dependent on the particle surface distance [37].

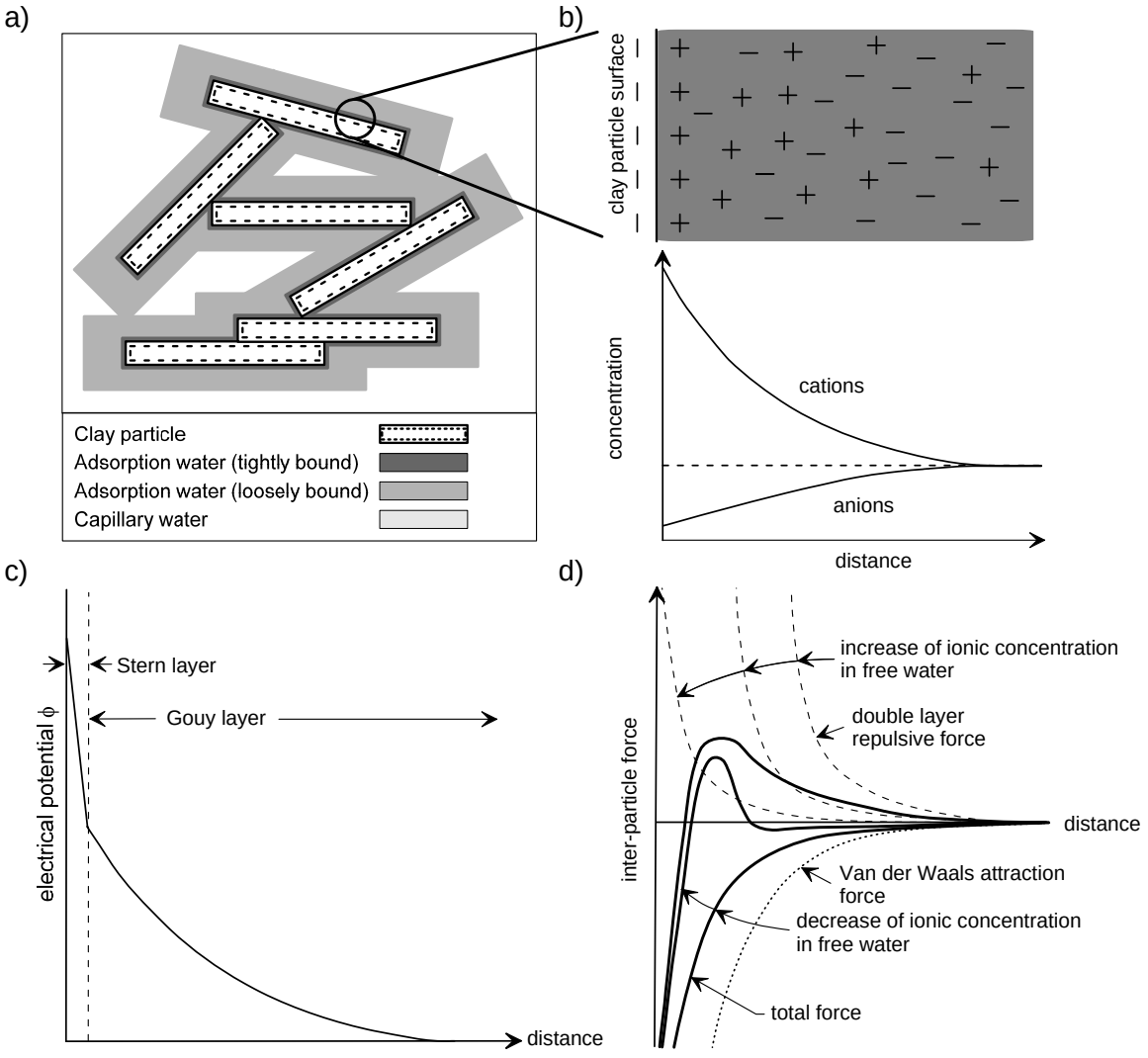

Figure 2.3: Qualitative illustration of (a) water types existing in fine-grained soil, (b) ionic concentration dependent on particle distance, (c) electrical potential dependent on particle distance, and (d) inter-particle force dependent on the particle distance and ionic concentration, adopted from [35, 37, 38].

The chemistry and cation and anion concentration of the pore water solution are important factors that have an enormous influence on inter-particle forces [33, 39]. The inter-particle force between fine-grained soil particles can be distinguished into three categories [34]:

1. Coulomb electrostatic force
2. van der Waals attraction force
3. double layer repulsive force

The Coulomb electrostatic force is caused by the attraction of negatively charged particle surfaces and positively charged edges of the particle surface. The quantitative description of the summation of the van der Waals attraction forces and double layer repulsive forces is given in the well-known Derjaguin-Landau-Verwey-Overbeek (DLVO) theory [39]. Derjaguin et al. [40] pointed out that the double layer repulsive force acts in a long range, with a distance from particle surface $x > 500$Å, whereas the van der Waals forces are found in a short distance, from particle surface $x < 100$Å [41]. Figure 2.3d qualitatively presents the effects of changing ion concentration on the inter-particle forces. With high ionic concentration in free water, inter-particle attraction mainly exists due to the van der Waals forces, whereas the double layer repulsive force between particle surfaces occurs with decreasing ionic concentration. The total inter-particle force, which is the sum of either force, is an attractive force for extremely short distances of particles. Depending on ionic concentration, the attractive total force can turn into a repulsive force with increasing inter-particle distance. The direction and extent of the inter-particle forces, as well as electrostatic forces of the surface, depend on the specific particle surface, pore fluid chemistry and mineral type [29, 31, 33, 35].

In the case of fine-grained soils, water appears in different bonding states that are dependent on the distance to the particle surface. Figure 2.3a presents schematic illustration of the water types that can exist particularly in fine-grained soils. The water types can be classified as follows:

- The adsorbed water to the particle surface is called **adsorption water**. It can be further divided into loosely and tightly bound adsorption water [42]. Tightly bound water forms a monomolecular layer enclosing the mineral surface [42]. This water layer is also known as DDL [27]. With further distance to the particle surface, the adsorbed water builds successively water layers that are loosely bound.
- The surface force acting on water molecules mitigates with increasing distance from the particle surface. **Capillary water** is associated with water molecules that are yet to be attracted by particle surface forces, but are not as tightly bound as adsorption water to the particle surface [42, 43].
- The water molecules that are not held against gravitational forces are termed **free water**. As soon as the distance from the particle grows too large, the surface force is too weak to hold the water in the soil fabric, which means that the free water will leak out of the soil.

2.4.2 Soil water potential

The particle surface forces acting on the water phase are called 'soil suctions' which describe how strongly water is bound in the soil matrix. A general thermodynamic characterisation of the soil suction is given by the chemical potential of the pore water, which is also known as 'water activity' [41, 44, 45, 46, 47]. The absolute chemical potential, μ_{W}, of pure water is related to a reference state by:

$$\Delta\mu_{\mathrm{W}} = \mu_{\mathrm{W}} - \mu_{\mathrm{W}}^{\circ}, \tag{2.4}$$

where, μ_{W}° is the chemical potential of pure water at a reference state (e.g. μ_{W}° at 100 kPa and 20 °C [23]) and $\Delta\mu_{\mathrm{W}}$ is the difference between the absolute chemical potential and chemical potential at reference state. In order to consider the chemical potentials due to interfacial processes in the DDL, as well as capillary forces, Equation 2.4 can be rewritten as:

$$\Delta\mu_{\mathrm{W}} = \sum_{k=1}^{N} \mu_{\mathrm{W,k}} - \mu_{\mathrm{W,k}}^{\circ} = \sum_{k=1}^{N} \Delta\mu_{\mathrm{W,k}} \tag{2.5}$$

where, $\Delta\mu_{\mathrm{W}}$ is the result of the superposition, N, of the appropriate potentials, $\Delta\mu_{\mathrm{W,k}}$, due to van der Waals forces, $\Delta\mu_{\mathrm{W,V}}$; Coulombian electrostatic forces, $\Delta\mu_{\mathrm{W,E}}$; osmotic forces, $\Delta\mu_{\mathrm{W,O}}$ due to the presence of charges in clay interlayers; and capillary forces, $\Delta\mu_{\mathrm{W,C}}$ [39]. If the molecular volume of pore water is known, the energy status of interface pore water can be determined by the free enthalpy or Gibbs free energy, which is defined as [23, 48]:

$$\Delta G_w^{\ddagger}(T,\Psi_t) = \Delta H_w^{\ddagger}(T,\Psi_t) - T\Delta S_w^{\ddagger}(T,\Psi_t), \tag{2.6}$$

where, $\Delta H_w^{\ddagger}(T,\Psi_t)$ is the activation enthalpy, $\Delta S_w^{\ddagger}(T,\Psi_t)$ is the activation entropy, and T is the temperature. Basically, the Gibbs energy describes the water potential existing between the reference state (such as pure water) and bonding state [19, 23, 48]. In the case of thermodynamic equilibrium condition, the water potential defines the amount of work required to lift a unit quantity of water from a pure water pool at reference elevation to a specific elevation under investigation [47, 48]. If the unit quantity of water is considered a unit mass, the water potential equals the chemical potential, $\Delta\mu_{\mathrm{W}}$, which is defined as the energy per unit mass (e.g., in J/kg) [47]. Under a constant water density, ρ_{W}, the water potential is often referred to as energy per volume, which leads to [23, 47]:

$$\Psi_t = \Delta\mu_{\mathrm{W}} \cdot \rho_{\mathrm{W}}, \tag{2.7}$$

where, Ψ_t is the total water potential (also known as soil suction) in a pressure unit (e.g. in Pa). The total water potential represents all forces that hold pore water in the soil matrix.

In soil science, the potential concept is used to define quantitatively the soil suction inherent in a soil. In general, the potential is categorised in different components, which give in summation the total potential, Ψ_t [47, 49, 50]:

- gravitational potential Ψ_G
- osmotic potential Ψ_O
- matric potential Ψ_M

This study focuses mainly on the osmotic potential, Ψ_O, and matric potential, Ψ_M, because these potentials play a more significant role in fine-grained soils at unsaturated conditions [26, 47, 51]. The **osmotic potential** defines the amount of work required to extract a unit quantity of water at a certain elevation point through a selectively permeable membrane or diffusion barrier [26]. Osmotic potential usually occurs in soils at air-water interfaces that have a high amount of solutes in the pore water (e.g. high salinity content). The **matric potential** is a result of capillary forces and adsorption forces in the soil matrix [41, 47]. Capillarity is caused by the rise of water in finer pores in the soil matric [52, 53]. At water table level, the pore water pressure is assumed to be zero. Below the water table with ongoing depth, the soil is usually saturated and the pore water pressure increases positively due to the hydrostatic water pressure [47]. Above the water table, the soil is assumed to be unsaturated. In unsaturated soil conditions, the energy state of the pore water held in the soil matrix is lower than the energy state of the free water (e.g. due to the capillary rise of pore water) [50]. Thus, pore water pressure is noted as a negative quantity.

Soil suction is commonly termed as the ratio of the partial pressure of pore water vapour to the free energy state of the soil water [26, 49]. In the case of dominating adsorption forces on the water phase, this relationship is given by Kelvin's equation [41, 54]. By re-arranging Kelvin's equation, the total soil suction, Ψ_t, can be expressed as follows [26]:

$$\Psi_t = -\frac{R_{Gas} \cdot T}{\frac{V_{\text{mol}}}{\rho_W}} \cdot \ln \frac{p}{p_0}, \tag{2.8}$$

where, T is the temperature, R_{Gas} is the universal gas constant, V_{mol} is the molecular mass of water, ρ_W is the water density, p is the partial pressure of pore water vapour and p_0 is the saturation pressure of water vapour above a flat surface of pure water. The ratio of $\frac{p}{p_0}$ gives the relative humidity. It should be noted that this equation is only valid if the partial pressure of the pore water vapour and saturation pressure of the water vapour above the flat surface of pure water are in equilibrium.

The force that drives the capillary rise of pore water is the surface tension, σ_{wa}, which occurs at the interface of the water phase and air phase, and the contact angle, δ_W (see Figure 2.4, [26, 55]). The interface of the air and water phase is created by adsorption forces between the soil particles and water molecules, and by cohesion forces between the water molecules. The interface, where the surface tension occurs, builds a meniscus that is curved under a contact angle, δ_W. The height of the capillary rise, H_c, of pore water can be calculated by the equilibrium of the forces in the vertical direction, which leads to following equation [38, 56]:

$$H_c = -\frac{2 \cdot \sigma_{wa} \cdot cos\delta_W}{r \cdot \rho_W \cdot g}, \tag{2.9}$$

where, δ_W is the contact angle, σ_{wa} is the water surface tension at the interface between the water phase and air phase, r is the radius of the pore size, g is the acceleration of gravity, and ρ_W is the density of water. As Equation 2.9 shows, the capillary rise, H_c, increases with decreasing radius of the pore sizes.

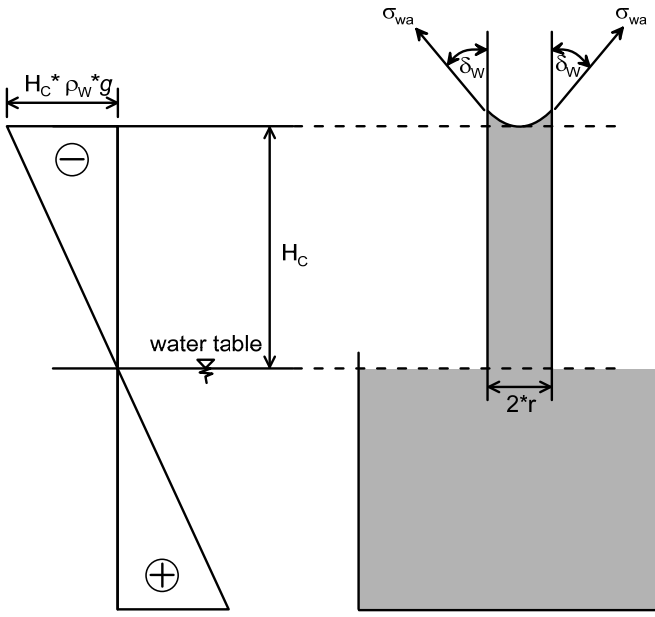

Figure 2.4: Simplified illustration of the capillary rise of pore water in a soil pore, adapted and modified from [38].

2.4.3 SWCC

The relationship between soil suction and the water content of a soil is defined by the SWCC [8, 57]. In soil science, soil suction is commonly related to the 'volumetric water content', θ:

$$\theta = \frac{w \cdot \rho_D}{\rho_W}, \tag{2.10}$$

where, w is the gravimetric water content, ρ_W is the water density, and ρ_D is the dry density of the soil. Figure 2.5a qualitatively shows SWCCs that typically have a S-shape and exhibit a hysteretic nature [58, 59]. The initial drying curve (IDC) and initial wetting curve (IWC) constrain the area for the primary drying curve (PDC) and primary wetting curve (PWC). The IDC and IWC represent the two extreme situations, with either saturated or completely dry conditions. The IDC describes the soil suction development, starting at saturated condition. At the saturation condition, the soil suction is relatively low and the entire pore space is occupied by water, leading to a saturated volumetric water content, θ_S [60]. With minimally decreasing water content (e.g. water loss due to soil desiccation), the soil suction increases while the soil condition remains saturated. With continuously decreasing water content, the soil suction is insufficient to hold water in the soil, which results in a significant drop of the volumetric water content. If the soil suction equals Ψ_{AEV}, the air phase enters the pore space, leading the soil from saturated to unsaturated conditions [38]. Beyond this air entry into the pore space, the soil suction is steadily increasing, with reducing volumetric water content. In the case of extremely high soil suction, the volumetric water content approaches a residual water content, θ_R, at which water is not further drained out and is held in the soil matrix by adsorptive forces to the particle surface [61]. In contrast to the IDC, the IWC starts at dry condition, with water content close to zero. The IWC describes the soil suction development with increasing water content. As can be seen in Figure 2.5a, the IWC converges to a volumetric water content, θ_U, at low soil suction range [58]. θ_U shows a saturation degree less than 100% due to entrapped air, which prevents the soil from reaching θ_S. Within the domain of the IDC and IWC, the PDC and PWC are found, which are restricted to the water content range reaching from θ_R to θ_U.

This study focuses on the IDC of soils. To avoid confusion, it should be noted that the expression 'SWCC' is used instead of 'IDC' in the following sections of the thesis.

Figure 2.5b shows a qualitative comparison of SWCCs for different soil types, presenting the difference in the curve trends. The volumetric water content at a given soil suction is much higher for fine-grained soils than for coarse-grained soils. This effect can be attributed to two reasons. First, a fine-grained soil, such as clay, includes finer pores than does sandy soil [27, 52]. Referring to Equation 2.9, it is obvious that the smaller the pore size radius, r, the higher the capillary rise in the pore. This leads to enhanced soil suction, holding water in the soil matrix. Second, the total particle surface area per unit volume of clay, for example, is typically larger than that of sand [62]. As a result, the amount of superficial adsorptive forces in fine-grained soils is greater, which causes a higher attraction of water molecules to the particle surface, and subsequently an increase in soil suction [41, 46, 63].

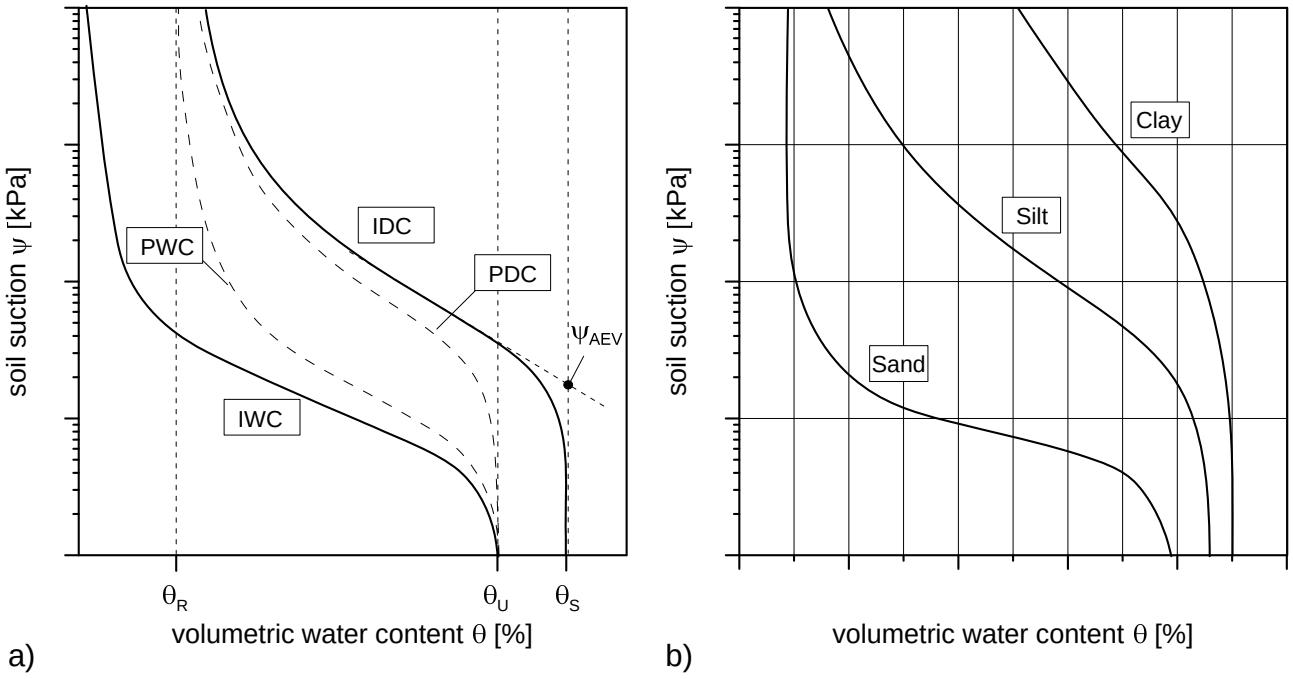

Figure 2.5: (a) Schematic illustration of SWCC for initial drying curve (IDC), initial wetting curve (IWC), primary drying curve (PDC), and primary wetting curve (PWC), and (b) qualitative comparison of SWCC for IDCs in the case of sand, silt, and clay. Adapted and modified from [38].

In the past, several equations have been proposed to model and parameterise the typical shape of SWCCs [8]. Most SWCC equations are limited in their application to different soil types [8, 60]. A thorough review of common existing equations to describe the SWCC is provided in Leong and Rahardjo [60]. Most SWCC equations can be derived from a single generic equation. Nevertheless, a general equation describing the $\Psi_t - \theta$ relationship has not yet been delivered; thus, some existing and well-established equations are frequently used. One of the most cited and well-known equations is proposed by Brooks and Corey [64], who developed the equation based on an empirical statistical approach:

$$S_e = \frac{\theta - \theta_R}{\theta_S - \theta_R} = \left(\frac{|\Psi_{AEV}|}{\Psi_t} \right)^{\lambda_{BC}} \qquad |\Psi_t| > |\Psi_{AEV}| \tag{2.11a}$$

$$S_e = 1 \qquad |\Psi_t| \leq |\Psi_{AEV}| \tag{2.11b}$$

where, Ψ_t is the total suction, Ψ_{AEV} is the soil suction at air entry into the soil matrix, λ_{BC} is a dimensionless pore size distribution index that shapes the curve slope, and S_e is the dimensionless effective saturation that depends on the residual water content θ_R, saturated volumetric water content θ_S, and actual volumetric water content θ [65]. The θ_R, Ψ_{AEV}, and λ_{BC} are fitting parameters to optimise the curve shape. It should be noted that Equation 2.11 is not a single equation over the entire soil suction range, as the SWCC is split at Ψ_{AEV}. In the case of $|\Psi_t| \leq |\Psi_{AEV}|$, the soil suction becomes independent from θ, which means that soil

suction is continuously increasing with the constant volumetric water content, $\theta = \theta_S$. Another empirical relationship applicable over the entire SWCC is suggested by van Genuchten [66]:

$$S_e = \frac{\theta - \theta_R}{\theta_S - \theta_R} = \left[\frac{1}{1 + (a_{vG} \cdot |\Psi_t|)^{n_{vG}}}\right]^{m_{vG}} \tag{2.12}$$

where, a_{vG}, n_{vG}, and m_{vG} are constant optimisation parameters that need to be fitted. The reciprocal value, a_{vG}, is closely related to the Ψ_{AEV} because it defines the location of the curve pivot point [65], where a_{vG} increases with decreasing Ψ_{AEV}.

In contrast to the empirical Equation 2.11 and 2.12, Fredlund and Xing [8] developed a general equation for determining SWCC, assuming the SWCC shape is related to the pore size distribution. The proposed equation represents a modified version of Equation 2.12 according to:

$$\begin{aligned} S_e = \frac{\theta - \theta_R}{\theta_S - \theta_R} &= C(|\Psi_t|) \cdot \left\{\frac{1}{ln\left[e + \left(\frac{|\Psi_t|}{a_{fx}}\right)^{m_{fx}}\right]}\right\}^{n_{fx}} \\ \text{with} \quad C(|\Psi_t|) &= 1 - \frac{ln\left(1 + \frac{|\Psi_t|}{|\Psi_R|}\right)}{ln\left(1 + \frac{1{,}000{,}000}{|\Psi_R|}\right)} \end{aligned} \tag{2.13}$$

where, a_{fx}, m_{fx}, and n_{fx} are parameters for optimising the curve fit, e is the void ratio, $C(|\Psi_t|)$ is a correction factor, and Ψ_R is the soil suction when the residual water content, θ_R, is reached. Fredlund and Xing [8] defined an correction factor $C(|\Psi_t|)$, to achieve a better approach for SWCC at extremely high soil suction. Based on experimental investigations, a soil suction of 1,000,000 kPa was defined, at which the volumetric water content was $\theta \to 0$. As a result, the correction factor in Equation 2.13 forces the SWCC to approach a residual water content of $\theta_R = 0$ for high soil suction.

A modified description of Equation 2.12, proposed by van Genuchten [66], is presented in Durner [67]. In soils with a heterogeneous pore size system, the SWCC shows a curvilinear and multimodal curve shape [67, 68, 69]. In order to consider the curvilinear shape of SWCCs, a multimodal function is introduced, based on a linear superposition of subsystems [67, 68]:

$$S_e = \frac{\theta - \theta_R}{\theta_S - \theta_R} = \sum_{i=1}^{N} W_i \left[\frac{1}{1 + (a_{vG,i} \cdot |\Psi_t|)^{n_{vG,i}}}\right]^{m_{vG,i}} \tag{2.14}$$

where, i counts for the number of appropriate N subsystems with the weighting factors $0 \leq W_i \leq 1$, and van Genuchten parameters $a_{vG,i}$, $n_{vG,i}$, and $m_{vG,i}$.

The disadvantage of most of these models is their inability to consider volumetric changes in the SWCC [70]. Most models have been established without accounting for volumetric

changes of soils. For instance, Equation 2.13 suggested by Fredlund and Xing [8] assumes that the SWCC shape is related to the single pore size distribution. However, in fact, the pore size distribution alters with suction-induced volume changes, particularly in fine grained soils. A SWCC model considering pore size distribution changes was developed by Hu et al. [71]. In this model, a pore size distribution function was introduced into van Genuchten's equation 2.12 to account for the volume changes of deformable soils. Similarly to Hu et al. [71], Gallipoli et al. [72] modelled the volume changes of deformable soils based on van Genuchten's equation 2.12. Based on experimental evidence, it was found that the van Genuchten parameter, a_{vG}, can be expressed as a function of the soil volume [72, 73]. This re-definition of a_{vG} in Equation 2.12 enables consideration of suction-induced volume changes.

2.5 Densification of fine-grained soils

2.5.1 External stress and internal stress

Soil is subject to stress and changing environmental conditions that cause soil to deform. This volume deformation causes variations in soil's mechanical, hydraulic and chemical properties [74]. Considering only a two phase soil system consisting of water and solid particles, the effective stress of porous medium is described by Terzaghi's effective stress theory [75, 76, 77, 78]:

$$\sigma' = \sigma - u_{\mathrm{w}}, \tag{2.15}$$

where σ' is the effective stress between solid particles contacts, σ is the total stress, and u_{w} is the pore water pressure. In unsaturated conditions, the air phase enters the soil matrix, which leads to soil suction. This soil suction – also often referred to negative pore pressure – affects the mechanical behaviour and stress conditions of unsaturated soils [47, 76, 79]. Bishop [76] considered the effective stress of a three-phase porous medium as follows:

$$\sigma' = (\sigma - u_{\mathrm{a}}) + \chi \cdot (u_{\mathrm{a}} - u_{\mathrm{w}}) \tag{2.16}$$

where, u_{a} is the pore air pressure, and $0 \leq \chi \leq 1$ is a coefficient accounting for the saturation degree of the soil. At dry conditions with $\chi = 0$, the effective stress equals the total stress, with $\sigma' = \sigma$. In the case of saturated conditions, with $\chi = 1$, Equation 2.16 reduces to Equation 2.15.

Soil stress situations can be distinguished into three categories [77]:

1. external stress

2. internal stress

3. combination of external and internal stress

External stress is caused by mechanical stress, such as when a soil is exposed to a mechanical load, and the volume changes occur due to exceeding shear resistance between the solid particles on microscale [77]. Internal stress – also known as 'hydraulic stress' – is applied to the water phase in the soil matrix. At soil-water phase state equilibrium, hydraulic stress is described by negative pore water pressure [77, 80]. For instance, volume reduction occurs under soil desiccation due to the suction-induced capillary forces [26, 51, 61, 81]. The capillary rise of water during desiccation implies a contractile force exerted by the curved meniscus at the interface of the air and water phase [82]. This contractile force pulls soil particles together which leads to soil volume reduction. Volume reduction continues as long as the contractile force of the meniscus is higher than the counteracting shear resistance between the solid particles [80]. In geoscience, the volume reduction due to desiccation is widely known as 'soil shrinkage'. However, external and internal stress may also occur in combination.

2.5.2 Soil shrinkage

As explained in the previous section, shrinkage is caused by soil volume changes due to an internal stress situation. In engineering science, the extent of soil shrinkage behaviour can be described by the shrinkage curve which gives the relationship between soil volume change and water content [83]. Different definitions of the shrinkage curve can be found in the literature; however, the most commonly used are as follows:

- $w - \rho_D$ or $w - 1/\rho_D$ - relationship [84, 85]
- $\vartheta - e$ - relationship [6, 86]
- $\zeta - \nu$ - relationship [87]

where, $\vartheta = w \cdot \rho_G / \rho_W$ is the moisture ratio, e is the void ratio, $\zeta = w/w_M$ is the relative water content given by the ratio of current water content to the maximum water content w_M (e.g. liquid limit), and $\nu = V/V_M = \rho_{D,M}/\rho_D$ is the relative volume defined as the ratio of the clay volume, V, at a water content to the clay volume, V_M, at maximum water content.

Figure 2.6 qualitatively shows a schematic illustration of typical shapes of observed reference shrinkage curves with $\vartheta - e$ - relationship.

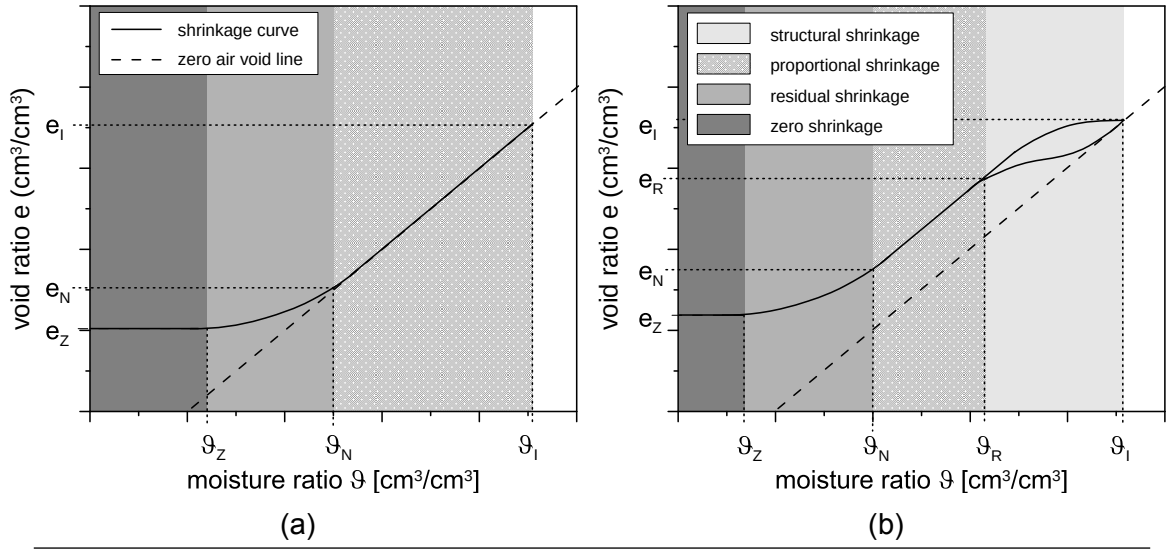

Figure 2.6: Qualitative and schematic illustration of typical shapes of the shrinkage curve, with indication of different shrinkage zones: (A) shrinkage curve of pure clay and (B) shrinkage curve of mixed soil minerals. Modified based on [88].

Two aspects need to be highlighted and explained prior to further description of soil shrinkage behaviour:

1. In most cases, the shrinkage starts at a relatively high water content that is close to or even slightly higher than the **liquid limit** [3]. Considering deformable fine-grained soils, the liquid limit is generally interpreted as the water content at which soil reveals a liquid consistency with low shear strength [3, 89]. Hence, in geotechnical engineering, the maximum water content of interest on the shrinkage curve is usually defined at the liquid limit [3].

2. The term **reference shrinkage curve** defines the shrinkage curves without any soil cracks [88, 90]. The idea behind this concept is that any further measured shrinkage curve which might include soil cracks, shows the same or greater void ratio at identical water content. Any shrinkage curve with soil cracks would be shifted relative to the reference shrinkage curve, without qualitative changes in the curve shape [88]. The difference between the reference shrinkage curve and any measured shrinkage curve gives the crack volume contribution [88, 90, 91]. The experimental determination of the reference shrinkage curve is only achieved at slow soil shrinkage, with a small sample size. Cracks might still develop on the microscopic scale, but the crack volume is negligibly lower than the sample volume [88, 90]. This study focuses on the reference shrinkage curve without taking cracks into account. Hence, the term 'shrinkage curve' is used instead of 'reference shrinkage curve' in the coming sections of the thesis. To avoid any confusion, it should be stated that the following explanations will be valid

for the reference shrinkage curve, but only partly for any shrinkage curve with crack development.

A soil mixture is usually composed of clay, silt, and sand particles and eventually organic matter. If the content of the organic matter is zero or negligibly low, then soil shrinkage is only induced due to the presence of clay particles [88]. However, the shrinkage curve of pure clay and the shrinkage curve of a soil mixture, composed of broad range of minerals and clay particles, differ essentially in their shape. Figure 2.6a shows a qualitative shrinkage curve for pure clay, while Figure 2.6b) shows a qualitative shrinkage curve for a soil mixture containing partly clay particles.

Comparing Figure 2.6a and b, it is obvious that the curve shapes differ. Different zones during the shrinkage process are observed, including [92, 93, 94]:

- structural shrinkage
- proportional shrinkage
- residual shrinkage
- zero shrinkage

The proportional, residual and zero shrinkage zones are observed in the shrinkage curves of both the pure clay and the soil containing a proportion of clay. In contrast, structural shrinkage only occurs in soils containing clay particles. Figure 2.7 shows a schematic illustration of a soil structure consisting of grain particles and clay particles.

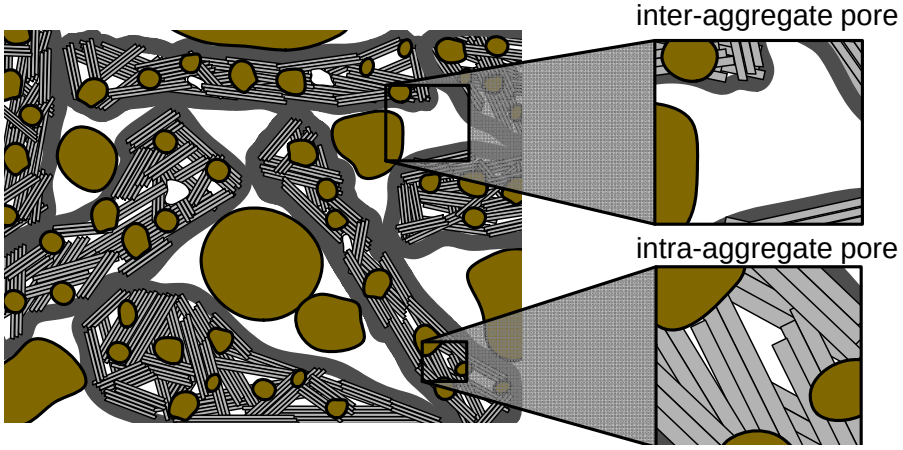

Figure 2.7: Schematic illustration of soil structure, showing inter-aggregate and intra-aggregate pores, adapted and modified from [19].

Clay particles build aggregates by accumulation of stacked clay mineral layers in which coarser grained particles might be embedded. In these aggregates, the pore space between these clay particles is termed 'intra-aggregate pores' [88, 95]. In addition to intra-aggregate pores, structural pore space is created between these aggregates, which is associated with inter-aggregated pores [88, 91, 95]. Both inter-aggregate and intra-aggregate pores are normally found in structured well-aggregated soils [93, 96], such as a soil mixture with considerably high clay content. Pure clay is associated with structureless soil because it consists mostly of intra-aggregate pores [88, 96]. In the beginning of soil shrinkage at high water content – such as at ϑ_I (see Figure 2.6) – pore water loss appears first in the largest pore space. In structured, well-aggregated soils (soil mixture containing clay particles), this water loss only occurs in the largest inter-aggregated pores [96]. At the same time, the volume of water loss is not completely compensated by the volume reduction of pore space, which leads to air entry into the soil matrix [90, 96]. This phenomenon causes a water saturation reduction in the inter-aggregate pores; thus, the shrinkage curve leaves the zero air void line. The area where the shrinkage curve deviates from the zero air void line is called **structural shrinkage** (see Figure 2.6b). In the case of structureless pure clay, the intra-aggregate pores persist saturated at the beginning of shrinkage because this pore space is relatively smaller than the inter-aggregate pore space and compensates water volume loss by pore volume reduction [96]. At this stage, structural shrinkage is not present for pure clay and, as a result, the shrinkage curve follows the zero air void line.

The stage at which the shrinkage curve follows the zero air void line is termed **proportional shrinkage**. Here, the loss of pore water – both in the intra-aggregate and inter-aggregate pore space – is compensated by pore volume reduction with ongoing soil shrinkage [96], which maintains the degree of saturation. In pure clays, the pore space is completely saturated and the shrinkage curve is identical to the zero air void line, having a slope equal to 1 [3, 97]. For a soil mixture containing clay particles, the curve leads from structural shrinkage into proportional shrinkage at the transition water content, ϑ_R, where the curve slope is then equal to 1, and follows parallel to the zero air void line [3, 87, 96]. In this context, it should be mentioned that the curve slope is not necessarily equal to 1. The slope of a shrinkage curve at proportional shrinkage is equal to 1 only for soils with sufficiently large clay content and small sample size [88]. Otherwise, soils with low clay content contain intra-aggregate clay with large 'lacunar' pores that grow with shrinkage [88]. Similarly, soil layers or large soil samples can contain inter-aggregate (structural) pores and cracks that also grow with shrinkage [88, 98]. In such conditions, the slope of a shrinkage curve at proportional shrinkage is also constant, but less than unity [91, 99]. However, this study focuses on soils with sufficiently high clay content; thus, the curve slope of proportional shrinkage can be considered equal to 1.

With further shrinkage, the decrease of pore water results in air-entry into the intra-aggregate pore space, and **residual shrinkage** is reached at the transition water content, ϑ_N [87, 92]. At this stage, pore water fills only partly intra-aggregate pores, and the decrease of water volume exceeds the pore volume reduction [96]. The soil shrinkage and void ratio, e, becomes a non-linear function of water content, and the curve subsequently deviates from the zero air void line and runs non-proportional to it.

Finally, the **zero shrinkage** mode for water content, $\vartheta \leq \vartheta_Z$, is reached, at which the soil volume is unaltered and the void ratio remains constant with a value of e_Z because the resistance against deformations due to solid particle friction is too high. The soil shows its densest configuration [96, 100] and the water volume loss during shrinkage is equal to the air volume entering the pore space, which leads to a continuous air-phase in the soil matrix [87].

2.5.3 Shrinkage curve equations

A number of approaches and models have been proposed in previous research to predict soil shrinkage behaviour and describe the obtained experimental shrinkage curves [3, 83, 84, 86, 87, 96, 101, 102, 103]. Apart from the model of Chertkov [3, 87], the currently available approaches are empirical fitting models that are based on approximation of the experimental shrinkage data. However, these models vary in their approach. Some models describe the experimental shrinkage curve via different geometrisation using a number of straight lines or exponential or polynomial description of curvilinear parts [84, 102, 104, 105]. Other models use mathematical parametric expressions to represent the shrinkage curve [6, 86, 96, 103, 106]. The mathematical expressions used in most of the models, fit the experimental data with a number of independent parameters (the number of the parameters varies depending on the models). The common feature of these approaches is that the fitting models and their parameters are not derived from theoretical and physical considerations of the soil structure, such as the inter- and intra-aggregate pore space, pore water distribution, and pore size distribution [91, 95, 107, 108]. The only available theoretical model was proposed by Chertkov [3, 87], which couples the shrinkage curve of a pure clay with its microstructure and pore-size distribution.

In the following, two selected models are further explained. The first model was suggested by Peng and Horn [6], which is a mathematical parametric expression. This model was essentially chosen in this study for two reasons:

1. the model represents an rearranged type of van Genuchten [66] equation (see Equation 2.12)

2. instead of visual determination, the model enables the mathematical determination of the different shrinkage zones, as explained in Section 2.5.2

Under the assumption that the shrinkage curve of a soil is the inverse of its SWCC, Peng and Horn [6] rearranged Equation 2.12 in order to express the shrinkage curve as follows:

$$e(\vartheta) = \begin{cases} e_Z & \text{if } \vartheta = 0 \quad (2.17a) \\ e_Z + \dfrac{e_I - e_Z}{\left[1 + \left(\frac{a_p \cdot \vartheta}{e_I - \vartheta}\right)^{-n_p}\right]^{m_p}} & \text{if } 0 < \vartheta < \vartheta_I \quad (2.17b) \\ e_I & \text{if } \vartheta = \vartheta_I \quad (2.17c) \end{cases}$$

where, e_I is the void ratio at the beginning of the shrinkage curve at the initial moisture ratio, ϑ_I, e_Z is the void ratio at the moisture ratio $\vartheta = 0$, and a_p, m_p, and n_p are the fitting parameters that control the shrinkage curve shape.

Equation 2.17 allows the mathematical determination of the shrinkage zones [6]. As can be seen in Figure 2.8, the shrinkage curve reveals one inflection point at the moisture ratio, ϑ_2 and, void ratio, e_2. This inflection can be found either by the extreme of the first derivative,

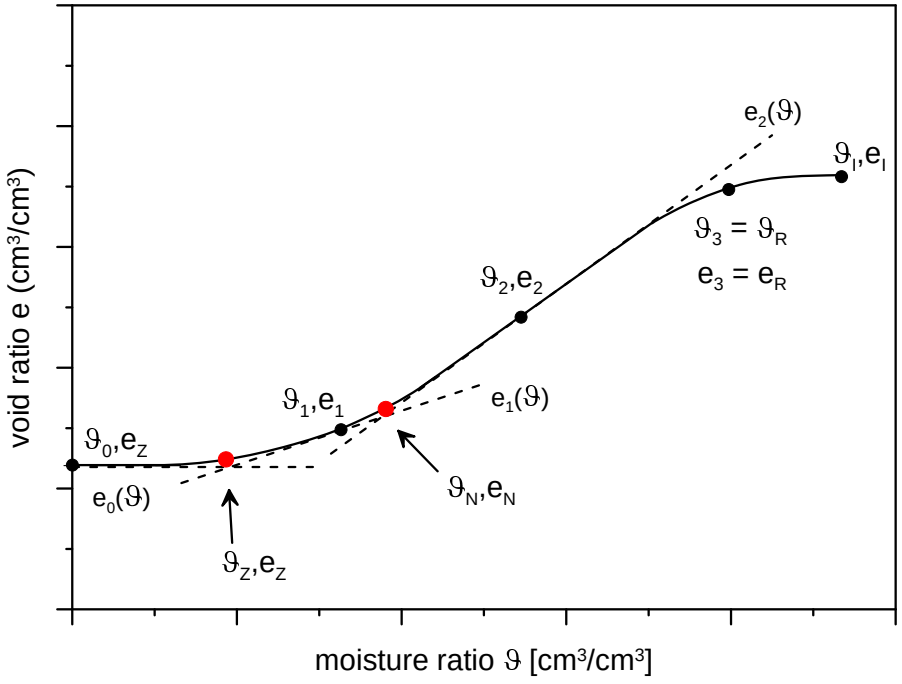

Figure 2.8: Schematic illustration of the determination of different shrinkage zones as suggested by [6].

$e'(\vartheta)$, of Equation 2.17b, or by finding the root of its second derivative, $e''(\vartheta)$. Further, the shape of the shrinkage curve shows two maximum curvatures, where one is found on the wet side of the shrinkage curve (ϑ_3,e_3) and the other on the dry side (ϑ_1,e_1). The location

of these maximum curvatures is obtained by the extremes of $e''(\vartheta)$. The endpoint of the structural shrinkage zone (ϑ_R,e_R) is suggested to be at the maximum curvature on the wet side, according to $\vartheta_R = \vartheta_3$ and $e_R = e_3$ [6, 86]. The endpoint (ϑ_N, e_N) of the proportional shrinkage zone and transition to the residual shrinkage zone is found by the intersection between the tangent $e_2(\vartheta)$ through the inflection point (ϑ_2,e_2), and the tangent $e_1(\vartheta)$ through the moisture ratio (ϑ_1,e_1) at maximum curvature on the dry side. Finally, the transition (ϑ_Z,e_Z) from residual shrinkage to zero shrinkage zone is defined as the intersection of the tangent $e_1(\vartheta)$ and the horizontal line $e_0(\vartheta)$ through the point (ϑ_0,e_Z). In the case of soil shrinkage without a distinctive structural shrinkage zone, such as pure clay, the maximum curvature on the wet side is not found on the shrinkage curve. In this case, the proportional shrinkage zone starts from the initial shrinkage conditions (ϑ_I, e_I).

The second model used in this study, is the theoretical model for the shrinkage curve of pure clays developed by Chertkov [3, 87]. In this model, the macro-parameters that characterise the shrinkage behaviour of clay are linked with its micro-parameters. In the following, the $\zeta - \nu$ - relationship is used to explain the macro-parameters of an observed shrinkage curve, with $0 \leq \zeta \leq 1$ and $0 \leq \nu \leq 1$, respectively [87]. Figure 2.9 shows a qualitative illustration of a shrinkage curve in the $\zeta - \nu$ - relationship compared to one in the $\vartheta - e$ - relationship. In

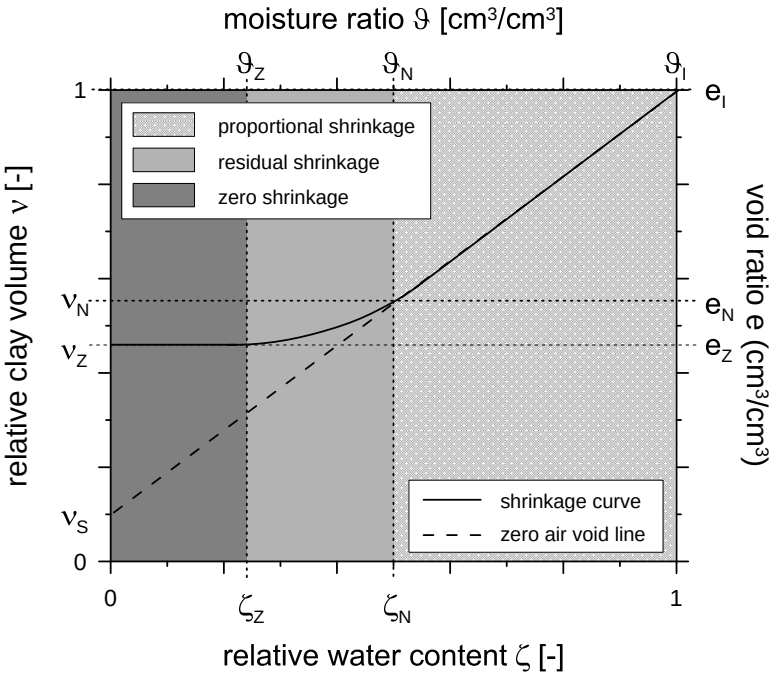

Figure 2.9: Schematic illustration of macro-parameters observed in the shrinkage curve in the $\zeta - \nu$ and $\vartheta - e$ - relationship, including shrinkage zones in case of pure clay, adapted and modified from [3].

this $\zeta - \nu$ - relationship, the transition points from proportional to residual shrinkage (ζ_N,ν_N)

and from residual to zero shrinkage (ζ_Z,v_Z) correspond to the points (ϑ_N,e_N) and (ϑ_Z,e_Z) in the $\vartheta - e$ - relationship.

On one hand, Chertkov [3] stated that the three essential macro-parameters expressing the shrinkage curve are v_S, ζ_Z, and v_Z. On the macroscopic scale, the v_S value is given by the volume ratio of the solid phase volume, V_S, to the volume at maximum water content, V_M, according to $v_S = V_S/V_M = \rho_{D,M}/\rho_G$. The relative water content, ζ_Z, defines the transition from residual to zero shrinkage. The minimum relative volume, v_Z, for $0 \leq \zeta \leq \zeta_Z$ is defined as $v_Z = V_Z/V_M = \rho_{D,M}/\rho_{D,Z}$, with clay volume, V_Z, at zero shrinkage and clay volume, V_M, at maximum water content. The relative water content, ζ_N, at the transition from proportional to residual shrinkage is then determined by v_S, ζ_Z, and v_Z.

On the other hand, the microstructure of a clay matrix is determined through the following factors, according to Chertkov [3]:

1. the average thickness, Δ, of deformable clay particles which build up the pore space
2. mininum external pore dimension, r_0
3. maximum external pore dimension, r_m
4. pore dimension distribution, $f(r/r_m)$.

Based on these factors, the macro-parameter, v_S, is expressed on the microstructure scale as follows [3]:

$$\begin{aligned} v_S &= \frac{\Delta_M}{r_{m,M}} \cdot A_{CH} \\ \text{with} \quad A_{CH} &= 3\int_0^1 \frac{1}{x}\frac{df(x)}{dx}dx \end{aligned} \tag{2.18}$$

where, x is the ratio of $x = r/r_m$, Δ_M is the average thickness of clay particles at maximum water content and $r_{m,M}$ is the maximum pore dimension at maximum at water content. The v_Z value is related to the microstructure by the following expression [3].

$$v_Z = \frac{r_{0,Z}}{\Delta_Z}\frac{\Delta_M}{r_{0,M}} \tag{2.19}$$

where, $r_{0,Z}$ is the minimum pore dimension at v_Z, $r_{0,M}$ is the minimum pore dimension at the maximum water content ($\zeta = 1$), and Δ_Z is the average thickness of the clay particles at v_Z.

Based on these microstructural parameters, the characteristic fraction of pore volume occupied by pore water, equivalent to the saturation, is defined as a function $0 \leq F \leq 1$ [3], dependent on:

$$F(\zeta) = f\left(\frac{r_i(\zeta)}{r_m(\zeta) - \Delta(\zeta)}\right) \tag{2.20}$$

where, r_i is the internal pore dimension with $r_0(\zeta) - \Delta(\zeta) \leq r_i \leq r_m(\zeta) - \Delta(\zeta)$.

At the same time, the characteristic fraction of pore volume occupied by pore water, $F(\zeta)$, can be expressed by the macro-parameters v_S and v_Z, which are related to the microstructure according to Equation 2.18 and 2.19, respectively. $F(\zeta)$ is written in a general form by [3]:

$$F(\zeta) = \frac{V_W(\zeta)}{V_P(\zeta)} \tag{2.21}$$

where, V_W is the pore water volume and V_P is the pore volume. The pore water volume in the clay at maximum relative content ($\zeta = 1$) is identical to the pore volume, V_P, at $v = 1$. Therefore, the pore water volume, V_W, at any given relative water content, $0 \leq \zeta \leq 1$, can be expressed:

$$V_W(\zeta) = \zeta \cdot n(\zeta = 1) \cdot V_M \tag{2.22}$$

where, V_M is the clay volume at maximum water content, and $n(\zeta = 1)$ is the porosity at maximum water content with its general form according to:

$$n = \frac{V - V_S}{V} = 1 - \frac{V_S}{V_M}\frac{V_M}{V} = 1 - \frac{v_S}{v} \tag{2.23}$$

where, V is the total clay volume, and V_S is the volume of clay particles. Further, the pore volume at any given ζ can be written by means of Equation 2.23 as:

$$V_P = n \cdot V \tag{2.24}$$

Using Equation 2.23 and 2.24, Equation 2.21 can be rewritten to:

$$\begin{aligned} F(\zeta) = \frac{V_W(\zeta)}{V_P(\zeta)} &= \frac{\zeta \cdot n(\zeta = 1) \cdot V_M}{n \cdot V} \\ &= \frac{1 - v_S}{v(\zeta) - v_S} \cdot \zeta \end{aligned} \tag{2.25}$$

Thus, the relative water content, ζ_Z, can be expressed by:

$$\zeta_Z = \frac{v_Z - v_S}{1 - v_S} \cdot F_Z \tag{2.26}$$

Finally, the three essential macro-parameters in the shrinkage curve (ζ_Z, v_Z, and v_S) are expressed by microstructural parameters with Equation 2.18, 2.19, and 2.26. Based on these equations, the entire shrinkage curve can be formulated by the following set of equations:

$$v(\zeta) = \begin{cases} v_S + (1 - v_S) \cdot \zeta & \text{if } \zeta_N < \zeta \leq 1 \quad \text{(2.27a)} \\ v_Z + a_{ch} \cdot (\zeta - \zeta_Z)^2 & \text{if } \zeta_Z < \zeta \leq \zeta_N \quad \text{(2.27b)} \\ v_Z & \text{if } 0 \leq \zeta \leq \zeta_Z \quad \text{(2.27c)} \end{cases}$$

where, a_{ch} is defined as:

$$a_{ch} = \frac{(1 - v_S)^2}{4 \cdot (v_Z - v_S)(1 - F_Z)} \tag{2.28}$$

where, F_Z is the pore volume fraction occupied by pore water at transition from residual to zero shrinkage ($\zeta = \zeta_Z$). The coefficient a_{ch} is related to the minimum internal pore dimension at $\zeta = \zeta_Z$, at which the air-phase is continuous and the last isolated air pore vanishes.

As explained in Section 2.5.2 and shown in Figure 2.9, the shrinkage curve follows the zero air void line in the proportional shrinkage zone ($\zeta_N \leq \zeta \leq 1$). Hence, the pore volume fraction occupied by pore water is $F = 1$ for $\zeta_N \leq \zeta \leq 1$. Substituting $F = 1$ in Equation 2.25, the shrinkage curve of pure clay as a function of $v(\zeta)$ in the proportional shrinkage zone can be expressed according to Equation 2.27a. In the residual shrinkage zone, air enters the pore space, which results in a pore volume fraction occupied by pore water, $F \neq 1$. Then, the shrinkage curve $v(\zeta)$ in the residual shrinkage zone is described by Equation 2.27b as an expansion to the second power of $(\zeta - \zeta_Z)$ in consideration of v_Z [87]. In the zero shrinkage zone, the shrinkage curve reaches a constant value according to Equation 2.27c. In the case of an experimental shrinkage curve with known macro-parameters (ζ_Z, v_Z, v_S), it is possible to describe the shrinkage curve by means of this theoretical shrinkage model.

2.6 Conclusion

The introduction of fundamentals has demonstrated the complexity of the characterisation of volume changes in fine-grained soils. This review showed that there is strong interaction of the soil phases existing in fine-grained soils. This is due to the nature of the negatively charged clay particle surface, and the dipole character of pore water molecules. The literature review further showed that the SWCC is commonly used in geoscience to define the soil phase interaction on the basis of the potential concept. Several models exist to quantitatively describe the SWCC, in which soil suction is expressed as a function of the water content.

Moreover, soil as a porous medium is subject to densification due to volume changes. This may be caused either by internal or external stress conditions, or a combination of both. Soil shrinkage induced by internal stress causes remarkable volume changes due to pore water evaporation. During the shrinkage process, soil undergoes different shrinkage modes, which is linked to the aggregate structure of fine-grained soils. Several fitting approaches and a theoretical model are presented in the literature to describe the shrinkage curve and determine the different shrinkage zones.

The following chapter focuses on reviewing the existing test methods to measure soil suction and volume changes. These measurements are needed to establish the SWCC and shrinkage curve to enable a quantitative description of soil's mechanical and hydraulic properties. The chapter introduces different methods and discusses measurement principles. It also highlights the limitations of the introduced techniques. Based on the review, the preferred methods, used in this study, are justified and explained in detail.

Chapter 3

Test methods for hydraulic and mechanical soil characterisation

3.1 Introduction

The previous chapter theoretically explained the characterisation of fine-grained soils. It showed that the behaviour of fine-grained soils, as a porous medium, depends strongly on the interaction of the phases of air, pore water and solid particles [50]. This chapter introduced structural and mineralogical aspects, as well as soil state parameters, which represent the interaction of the phases. The important state parameters, among others, that govern the mechanical and hydraulic behaviour of saturated and unsaturated fine-grained soils, are [47]:

- water content
- compaction state (such as density and void ratio)
- soil suction.

An exact determination of these parameters provides the basis for successful interpretation of the mechanical and hydraulic behaviour of soils. Hence, the focus in this chapter is on test methods for the experimental determination of these soil state parameters. A literature review of existing methods is given for measuring the soil suction, which is required to establish the SWCC. The principles of the methods are explained, and the measurable soil suction range is highlighted. The advantages and disadvantages of these methods are addressed and discussed. In addition, the available soil volume measurement methods are introduced, which are used to determine the compaction and density state of soils, such as

during shrinkage. The test methods are discussed and evaluated in respect to the applicability of the experimental objectives of this thesis. Subsequently, the soil volume measurement methods preferably used in this study are pointed out and justified by their advantageous applicability. The experimental procedure and measurement methodology of the used test methods are then introduced in detail.

3.2 Soil suction measurement methods

There are several methods available to investigate the soil suction to establish the SWCC, which are partly summarised and standardised in ASTM D6836-02 [109], ASTM D5298-10 [110], and ASTM D3152-72 [111]. These methods differ in their measurement approach, test design, performance and soil suction range under investigation. The use of an appropriate test method mainly depends on the considered soil suction range. For instance, if nearly saturated soil conditions are given, the soil suction range is expected to be lower than in the case of low saturated soil conditions. Therefore, the selected test method should be suitable to measure precisely at the low suction range. In contrast, for low saturated soil conditions, the test method should measure at high soil suction range as accurate as possible. Table 3.1 provides an overview of the most common test methods used in geotechnical engineering and soil science, together with a description of the test principles and possible suction measurement range.

Basically, the different test methods can be divided into the following categories depending on their measurement principles and the soil suction that is measured [38, 114]:

- static methods
- equilibrium of vapour pressure
- equilibrium of moisture condition between the soil sample and porous medium
- equilibrium of moisture condition between the soil sample and porous medium but measured at different physical properties

The **static method** comprises tests such as the axis translation technique and hanging column test. In the case of static methods, soil samples are exposed to an air-overpressure or negative pressure of the pore water phase, which induces drainage of the pore water out of the soil matrix. At equilibrium, when pore water drainage stops, the difference between the atmospheric pressure and applied pressure on the soil equals the soil suction. It should

Table 3.1: Summary of methods available for the establishing the SWCC

Test method	Test principle	Range	Potential	Literature
Centrifuge	Application of centrifugal velocity on soil sample	0-120 kPa	Ψ_M	[112]
Non-contact filter paper method	Vapour equilibrium between air phase and pore water phase	3-100 MPa	Ψ_t	[113, 114, 115]
Contact filter paper method	Suction induction on soil water phase by filter paper	0.01-100 MPa	Ψ_M	[115, 116]
Axis translation technique	Application of air-overpressure on soil matrix	0-1500 kPa	Ψ_M	[117, 118, 119]
Tensiometer	Infiltration applied on soil matrix	0-100 kPa	Ψ_M	[119, 120, 121]
Psychrometer	Vapour equilibrium between air phase and pore water phase	0.1-8 MPa	Ψ_t	[113, 114, 116, 117, 122]
Hanging column	Equilibrium measurement of negative pressure applied on pore water	0-80 kPa	Ψ_M	
Thermal conductivity sensors	Indirect measurement of thermal properties at moisture equilibrium condition	1-1500 kPa	Ψ_M	[114, 123, 124]
Chilled mirror hygrometer	Water vapour equilibirium between soil surrounding air-phase and pore water phase	0.5-100 MPa	Ψ_t	[113, 114, 118, 119, 125, 126, 127]
Sorption method	Water vapour equilibrium between aqueous solution and pore water	0-700 MPa	Ψ_t	[113, 122]

be pointed out that the static method measures soil suction as the matric potential, Ψ_M (see Section 2.4.2). The water content, corresponding to the applied pressure difference, is determined by balancing the initial water content with the water drainage. This procedure is repeated for several pressure steps in order to obtain multiple points of the SWCC. As Table 3.1 shows, the axis translation technique and hanging column test also differ in their applicable suction range. The application of negative pressure to the pore water phase with a hanging water column is more practical for the very low suction range. As a result, the hanging column test is recommended for use in a low suction range from 0 to 80 kPa, which is suitable for less cohesive soils (coarse-grained soil) or fine-grained soils at high water content where low suctions are expected [38]. In contrast, the axis translation technique based on the application of air-overpressure is able to measure up to a suction of 1500 kPa, which covers a broad suction range for fine-grained soils.

Another measurement principle is based on an indirect measurement principle, which measures the **vapour pressure at moisture equilibrium condition** [114] between the air phase and pore water phase of the soil sample. This vapour pressure is subsequently related to the soil suction based on Kelvin's Equation 2.8. The SWCC is established pointwise by measuring several moisture equilibrium conditions and determining each soil water content. In contrast to the static method, this method measures the soil suction as total potential, Ψ_t. Test methods based on this measurement principle are the non-contact filter paper method, psychrometer, chilled mirror hygrometer, and sorption methods. As shown in Table 3.1, the test methods cover the extremely high suction range ($>$100 MPa). Therefore, these methods are best suited to suction measurement on fine-grained soils with low water content, at which high suction is assumed due to the exclusive presence of adsorbed water.

A further indirect measurement principle measures the **equilibrium of the moisture condition between the soil sample and porous medium**. A test based on this principle is the contact filter paper method, in which soil is placed directly on filter paper. At constant environmental conditions, there is moisture exchange initiated between the soil and filter paper, which reaches equilibrium after a while. At equilibrium conditions, the water content of the filter paper is determined and the suction is obtained based on the filter paper calibration curve. The contact filter paper method measures the soil suction as matric potential, Ψ_M. The use of the contact filter paper method is proposed in a suction range from 0.01 to 100 MPa.

Another basic principle measures the **different physical properties at moisture equilibrium condition between the soil sample and porous medium**. An example is the thermal conductivity sensor, which consists of a porous block with a heater and temperature sensor in the centre. If the sensor is embedded in a soil sample, moisture exchange will occur due to a suction gradient. The water content variation in the porous block is determined indirectly by measuring the heat dissipation in the block [124] because the magnitude of the head dissipation is governed by water as a thermal conductor. The heat that does not dissipate through the porous block leads to a temperature rise in the block. Since the relationship between the water content and suction of the porous block is known, the temperature rise determined by the sensor can be calibrated to measure the soil suction. A thermal conductivity sensor measures the soil suction as matric potential, Ψ_M, in range from 1 to 1500 kPa.

A special case of a measurement principle is given by the test method using a centrifuge. In this method, drainage of the pore water of a soil sample is initiated by applying an increased gravity due to centrifugal velocity [128]. At equilibrium between the soil sample and increased gravity, the soil suction can be related to the angular velocity of the centrifuge [109]. The SWCC is then constructed by increasing step-wise the centrifugal velocity, and recording

the corresponding water content. This method is recommended to measure soil suction as matric potential, Ψ_M, in range from 0 to 120 kPa.

As Table 3.1 and the current literature show, numerous test methods are available to determine the SWCC of fine-grained soils. However, the use of some techniques entails disadvantages, which are further discussed in the following section:

1. Given that most techniques determine the soil suction at equilibrium conditions, a long measurement time may be expected.

2. Since fine-grained soils cover a broad suction range, there is currently no experimental technique available that allows determination of the entire SWCC by means of a single experiment. The construction of the SWCC of fine-grained soils is normally obtained by a combination of several measurement techniques, which is even more time consuming and tedious. Further, the combined use of several techniques may be accompanied by another drawback. As Table 3.1 lists, diverse techniques may measure different soil water potential – namely Ψ_t and Ψ_M. Hence, the application and combination of multiple techniques to obtain the SWCC may cause discontinuities in the curve.

3. As explained in detail in Section 2, the fundamentals of SWCC and soil shrinkage are closely related. Volume changes in fine-grained soils can be caused by internal stress due to soil suction. Even though volume changes play an important role and are necessary to calculate the volumetric water content (see Equation 2.10), most techniques do not allow the observation and quantification of volume changes during testing. The assumption that volume changes are negligibly low is reasonable and satisfying in the case of coarse-grained and less deformable soils. For fine-grained soils with water content below the shrinkage limit and a high suction range, the assumption may still be appropriate. However, this assumption is not correct with water content higher than the shrinkage limit because remarkable volume changes are expected in the suction range. Therefore, there is an obvious need for the possibility to record volume changes in order to ensure successful determination of the entire SWCC, ranging from high water content at the liquid limit to $w = 0\%$.

3.3 Soil volume measurement methods

3.3.1 Review of available methods

The soil volume is an important parameter for determining the porosity of a soil, which can be described by its density (see Equation 2.2). Further, volume changes play a significant role in the shrinkage behaviour of fine-grained soils. Therefore, there is a need for techniques to enable the accurate determination of soil volume and volume changes.

Numerous authors have proposed the indirect determination of the total soil volume via the **fluid displacement method** based on Archimedes' principle [96]. Saturated soil samples are submerged into a fluid (such as kerosene or toluene – for details, see [96]), and displacement of the fluid by mass or volume is measured and used for the subsequent calculation of the soil volume. A similar technique is based on the same principle, but uses water as the fluid in which the sample is submerged. Prior to submerging the soil sample into water, the sample is coated with paraffin or resin in order to prevent dissolution of the soil in water [1, 2, 83, 92]. Another technique uses the rubber balloon method proposed by Tariq and Durnford [129], which is also based on Archimedes' principle. A soil sample is packed into a rubber balloon and submerged in water. Based on the water displacement, the volume of the soil sample is determined. The disadvantage of this rubber balloon method is that the soil sample is usually disturbed when packed into the rubber balloon [130], which influences the accuracy of the volume determination. Further, the general disadvantage of all techniques based on Archimedes' principle is that the sample is not reusable after applying this method. Each volume determination requires a new single specimen. This implies that numerous specimens are needed to determine, for example, the entire shrinkage curve [130]. In addition, it is nearly impossible to prepare several soil samples with exactly the same initial test conditions in terms of water content, density and so forth. Hence, these techniques require an enormous and tedious laboratory effort that does not even ensure successful determination of the shrinkage curve.

Other techniques found in the literature are based on direct determination of the soil volume by measuring the sample dimensions in height and diameter [131, 132, 133, 134, 135]. Berndt and Coughlan [131] measured the dimension of soil cores during shrinkage by measuring the sample height using a dial gauge and the diameter using a flexible ruler. Similar to [131], Schafer and Singer [132] measured the length of a rod-shaped soil sample under shrinkage using a calliper. The major disadvantage of measuring the soil sample dimension is that axis-symmetric volume changes are typically assumed [130]; hence, the volume determination of the irregular sample shapes is complicated.

A more sophisticated measurement technique was proposed by Braudeau and Boivin [133] and Braudeau et al. [134], which allows continuous measurement of the dimension of irregular soil sample shapes by means of a retractometer. Using the retractometer, the dimensions in height and diameter of a soil sample are measured during shrinkage with several laser sensors. A new technique called the 'clodometer method' was suggested only recently by Stewart et al. [130]. This method determines the dimension of a soil sample based on images taken with a standard digital camera. Here, a soil clod is placed on a rotating image stand that includes a reference object with a known volume. Both the soil clod and reference object are imaged from $360°$. Based on open-source software, three-dimensional (3-D) surface meshes of both the soil and object are created, and the reference object is subsequently used as a calibration to determine the soil volume [130]. Both the retractometer and clodometer method have the disadvantage that the soil sample needs to be visually detectable. However, in the case of a shrinkage test, a soil sample at slurry conditions typically needs to be installed into a mould or sample ring. The mould or sample ring then covers the soil sample, and it is nearly impossible for a laser or imaging technique to measure the soil dimensions. As a consequence, these techniques seem to be more suitable to measure soil clods and stiff soil samples.

3.3.2 Methods used in this study

Two different measurement methods were used to measure soil volume changes in this study:

1. direct determination of the sample geometry
2. the water displacement method

Direct determination of the sample geometry based on height and diameter measurements was the preferred method for recording the volume changes during the shrinkage process of the soil sample. As stated in the Section 3.3.1, the major disadvantage of this method is found in the general assumption of axis-symmetric volume changes. Moreover, this method requires an enormous amount of work and time to determine the sample geometry and its volume. Despite these disadvantages, a couple of benefits need to be considered, which strongly encourage and support the use of this method.

- This study used shrinkage rings with cylindrical geometry to obtain a regular sample shape at the beginning of the shrinkage test. Given that axis-symmetric volume

changes are expected at the beginning of the shrinkage test in the case of a cylindrically shaped homogeneous soil sample, it is believed that this assumption is plausible and applicable.

- This study measured the sample dimensions in diameter and height in four different directions, with a rotating pattern of 45°. Hence, it was possible to detect and determine soil shrinkage with occurring irregular and axis-dissymmetric volume changes.
- This method is considered ideal for measuring shrinkage at soft conditions close to the liquid limit, at which a sample ring is required to keep the soil mass in a regular sample shape.
- This method requires limited and low-cost equipment to perform the volume measurements.

The shrinkage tests for the slurry and compacted soil samples conducted in this study were not notably different in their procedures. The shrinkage rings used were identical in geometry and dimensions. Figure 3.1A represents the shrinkage rings with dimensions in diameter and height. Shrinkage rings made of stainless steel were manufactured to be 70 mm in diameter and 14 mm in height. One side of the shrinkage rings was sharpened to allow coring and retrieving of undisturbed samples from the compacted soil specimen. Further, the same experimental procedure was applied for shrinkage tests on the slurry and compacted soil samples. Shrinkage tests on the slurry and compacted soil sample only differed in terms of their soil preparation. The following section describes the general procedures to continuously measure mass and volume changes during soil shrinkage, without explaining the soil and sample preparation prior to the actual shrinkage tests. The soil and sample preparation will be explicitly described later in the section for each particular test.

Prior to the shrinkage tests, the bulk soil mass, M, and initial water content, w_1, of the sample were determined both for the slurry and compacted soil samples. The initial dry density was calculated based on the known ring volume and measured bulk soil mass and initial water content. As soon as the shrinkage test began, the mass and volume changes were continuously recorded every two hours. For each record, the soil sample was weighed by a balance with 0.01 g precision, and the diameter and height of the sample were measured. A high-precision calliper was used to determine the height and diameter changes in 0.01 mm increments. As Figure 3.1C shows, the diameter changes were measured in four different directions, d_i (with $i = 4$), indicated by red lines, with a rotating pattern of 45°. The height changes were measured for each diameter direction at five predefined points. Figure 3.1B shows the location of the points for the height measurements with their distance to the sample centre. One height measurement was exactly taken at the sample centre, h_3. Two further

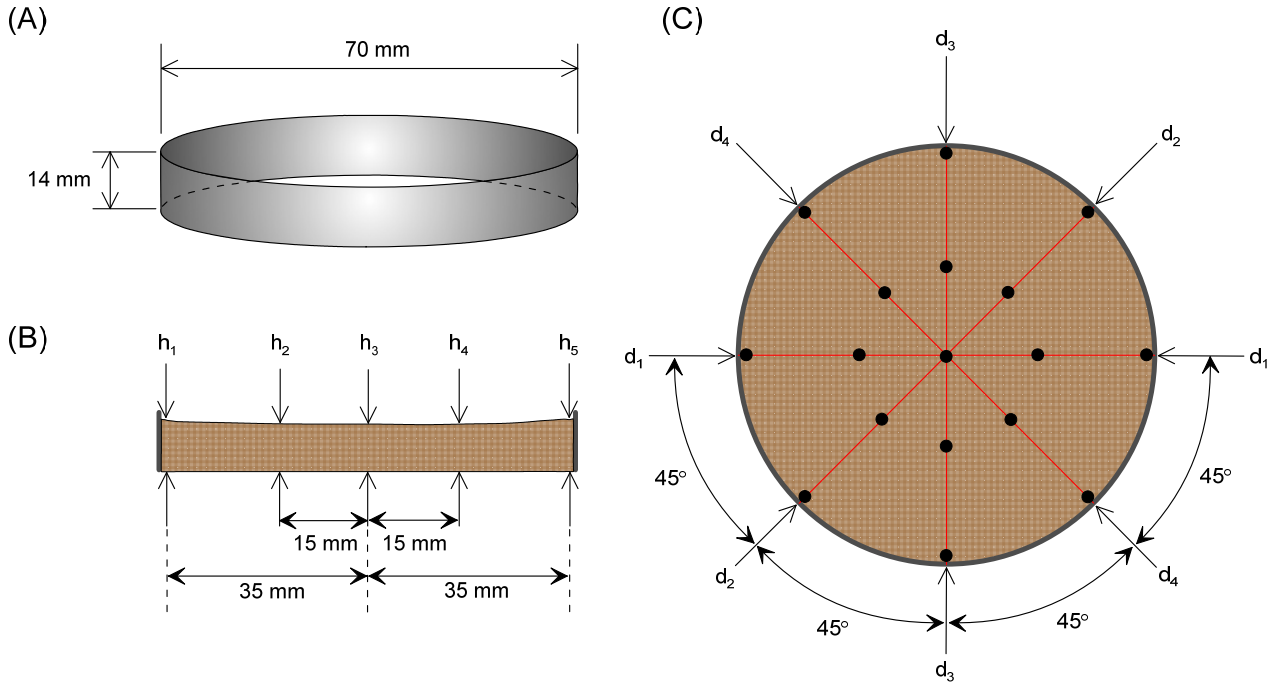

Figure 3.1: (A) Geometry and dimension of the shrinkage ring used in this study; (B) sample cross-section showing the five measurement points, with distance to the sample centre, used to measure the changes in sample height, h_i, for one measurement direction; (C) sample top view indicating four directions (d_i) in a 45° rotating pattern for measuring changes in diameter. Additionally, the points for height measurement are indicated by black dots.

sample heights, h_2 and h_4, were measured at 15 mm distance to the sample centre. The heights of h_1 and h_5 were taken at the shrinkage ring corner at a distance of 35 mm from the sample centre.

The soil volume, V, for each two-hour reading was calculated by the averaged volumes of the measured directions, with their determined diameters and average heights, according to the following equation:

$$V = \frac{1}{4} \cdot \sum_{i=1}^{4} V_i = \frac{1}{4} \cdot \sum_{i=1}^{4} \pi \cdot \left(\frac{d_i}{2}\right)^2 \cdot \left(\frac{h_{i,1} + h_{i,2} + h_{i,3} + h_{i,4} + h_{i,5}}{5}\right) \tag{3.1}$$

where, d_i with $i = (1,4)$ is the diameter measured in each direction, i, and $h_{i,j}$ with $i = (1,4)$ & $j = (1,5)$ is the sample height in direction, i, and point, j. Since the dry soil mass, M_S, is a constant value throughout the shrinkage test, it can be calculated by the initial water content, w_I, and bulk soil mass, M_I, at the shrinkage test beginning. By substituting w_I and M_I into Equation 2.2, the dry density for each reading can be expressed with following equation:

$$\rho_{D,k} = \frac{M_I}{(1 + w_I) \cdot V_k} \tag{3.2}$$

where, V_k is the measured and calculated soil volume at the k-te reading. By using Equation 2.1, the water content, w_k, corresponding to the measured dry density, $\rho_{D,k}$, is calculated by:

$$w_k = \frac{M_{\mathrm{k}} \cdot (1 + w_{\mathrm{I}})}{M_{\mathrm{I}}} - 1 \tag{3.3}$$

where, M_{k} is the weighed bulk soil mass at the k-te reading, w_{I} is the initial water content, and M_{I} is the bulk soil mass at the beginning of the shrinkage test.

The shrinkage tests with continuous readings were run beyond the shrinkage limit, until no significant mass changes were observed. Once the shrinkage test was finished, the entire set of readings was analysed and the shrinkage curve of the investigated soil was constructed based on the relationships explained in Section 2.5.2.

The second method employed in this study was the **water displacement method** based on Archimedes' principle. The water displacement method is a standardised procedure that is commonly used to measure, for example, the soil sample volume at the shrinkage limit [1, 2]. In this study, the water displacement method was used whenever only a single-volume determination of a soil sample was required. For example, when a specific shrinkage test was finished, the water displacement method was employed to determine the final dry density. The water displacement method was performed as an additional test to compare, check and confirm the final result of the direct measurement of the sample geometry.

(a) (b)

Figure 3.2: Preparation steps for water displacement method according to ASTM D4943-08 [1], ASTM D7263-09 [2]: (A) melting process of a paraffin block in a pot on a hot plate, (B) prepared soil sample with a wax coating

Prior to the test, the soil sample needed to be coated with paraffin to prevent dissolving of the soil mass when submerged in the water. Commercially available and purchased paraffin with known density, ρ_{wax}, was first heated in a pot on a hot plate (see Figure 3.2A). As soon as the entire paraffin block was melted, the heating temperature of the paraffin was lowered and kept constant at 75°C. The soil sample was then pre-treated and prepared. The soil sample

was trimmed to remove any irregular shape and visual large air voids, which might cause later air gaps between the soil and paraffin coating. After pre-treatment and preparation, the soil sample was weighed to determine the bulk soil mass, M. In order to minimise water evaporation and any loss of water content during the test, the experimental work was undertaken under controlled environmental conditions. In the next step, the prepared and weighed soil sample was submerged into the melted paraffin to coat the entire soil body. While coating with paraffin, visual inspection of the soil sample was undertaken with special care to avoid any large air enclosure and air gaps underneath the wax coat, which might cause additional buoyancy of the soil sample under water. The soil sample was submerged multiple times into the melted paraffin, as long as the entire sample body was covered by paraffin and the sample was completely air-sealed and water proof. Next, the weight, M_{wax}, in the air of the soil sample – including the paraffin coat – was determined. Then, the paraffin-coated soil sample was placed on a wire basket, which was hooked onto the balance as shown in Figure 3.3. Before submerging the soil sample into the water container, the temperature, T, of the water

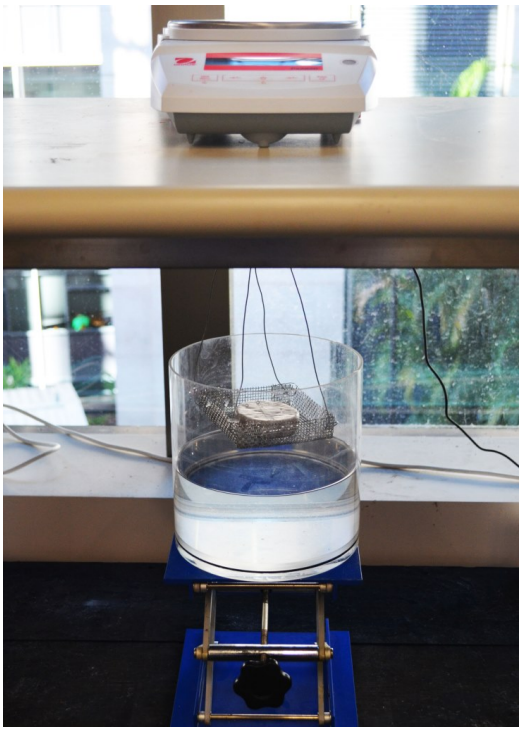

Figure 3.3: Measurement setup for water displacement method; paraffin coated soil sample placed in a wire basket that is hooked onto the balance.

was measured and recorded in order to determine the exact water density. Subsequently, the soil sample was slowly submerged into water by elevating the water filled container with a small lifting ramp. The soil sample mass, M_{U}, under water buoyancy was determined when a constant value was indicated by the balance. Then, the volume, V, of the soil sample was

calculated based on the following relationship:

$$V = \frac{M_{\text{wax}} - M_{\text{U}}}{\rho_{\text{W}}(T)} - \frac{M_{\text{wax}} - M}{\rho_{\text{wax}}} \tag{3.4}$$

where, M_{wax} is the weight in air of the paraffin-coated soil sample, M_{U} is the weight in water of the paraffin-coated soil sample, M is the bulk soil mass without paraffin coating, ρ_{wax} is the density of the paraffin, and $\rho_{\text{W}}(T)$ is the water density at the measured temperature, T. After conducting the water displacement method, the paraffin coating was peeled off and completely removed from the soil sample. The retrieved soil sample was taken to determine the water content, w, according to ASTM D2216-10 [136]. Finally, the dry density could be calculated based on Equation 3.2.

3.4 Conclusion

This chapter has presented a literature review of the available methods (see Table 3.1) to measure soil suction and establish the SWCC. It introduced the different test methods and categorised them into measurement principles. It also highlighted the application limits in terms of the measurable soil suction for each individual method. In addition, it highlighted and discussed the disadvantages of the methods, relevant to the presented study. The major disadvantages found in the literature review can be summarised as follows:

- A combination of methods is required to measure soil suction over a range that is as broad as possible.
- Different methods measure different water potential – namely Ψ_t and Ψ_{M} – which may result in a mismatch while establishing the SWCC.
- There is a lack of possibility to measure the volume change of soil.

These highlighted disadvantages are relevant to this study, and will be further investigated later in the thesis.

In addition, this chapter reviewed the soil volume measurement methods, and their applicability to the experimental investigations in this study. On the basis of the literature review and the experimental objectives, two soil volume measurement methods were selected for this study:

- direct determination of the soil sample geometry

- the water displacement method

Subsequently, the experimental procedure of the selected methods was extensively explained.

The following chapter introduces the electromagnetic properties of fine-grained soils in order to understand the correlation between the mechanical, hydraulic, and dielectric aspects of soils.

Chapter 4

Electromagnetic (EM) characterisation of fine-grained soils

4.1 Introduction

Due to their less or non-invasive nature, geophysical electromagnetic (EM) methods are increasingly used to explore and investigate soils [9]. Generally, these methods have the potential to retrieve physical and structural state parameters in both laboratory and field investigations [12]. However, a profound knowledge of both EM theory and EM soil properties is required to achieve successful application of these methods [13].

This chapter begins with a general description of the EM theory in order to provide a general understanding of EM wave propagation and the constitutive equations that describe the material response under the EM field exposure. The phenomenological aspects – namely polarisation and relaxation effects – that influence the material-specific constitutive parameters are discussed over a broad frequency range. Since soil is considered a porous medium, the EM properties of the individual phases in fine-grained soils are introduced. Approaches to determine the EM properties of the individual soil phases are provided. Finally, a literature review of the dielectric models relevant to this study is provided to predict the EM properties of fine-grained soils.

4.2 EM theory

4.2.1 EM wave propagation

In general, the propagation of a plane EM wave can be described by a space and time harmonic field, as shown schematically in Figure 4.1, in which the electric $\bar{E}$ and magnetic $\bar{H}$ wave are transversely oscillating. The $\bar{E}$ and $\bar{H}$ are propagating in time and space with period, T_P, and wavelength, λ_P. The period time, T_P, describes the time distance between the two repeating waves. The relationship and interactions of the EM fields are expressed by four Maxwell equations [137]:

$$\bar{\nabla} \times \bar{E} = -\frac{\partial \bar{B}}{\partial t} \tag{4.1a}$$

$$\bar{\nabla} \times \bar{H} = \bar{J} + \frac{\partial \bar{D}}{\partial t} \tag{4.1b}$$

$$\bar{\nabla} \cdot \bar{D} = q \tag{4.1c}$$

$$\bar{\nabla} \cdot \bar{B} = 0 \tag{4.1d}$$

where:

$\bar{E}$ is the electric field vector,

$\bar{H}$ is the magnetic field vector,

$\bar{D}$ is the electric flux density,

$\bar{B}$ is the magnetic flux density,

$\bar{J}$ is the electric current density,

q is the electric charge density,

$\bar{\nabla}\times$ is the curl operator,

$\bar{\nabla}\cdot$ is the divergence operator.

Equation 4.1a states that a rotation of an electric field is equal to the negative temporal change of a magnetic field. A temporal change of a magnetic field induces an electric field. Similar to Equation 4.1a is Equation 4.1b, where a rotation of the magnetic field is equal to the sum of the temporal change of the electric field and electric current density. Equation 4.1c states how the electric field of an electric charge changes with increasing distance to it. In contrast to Equation 4.1c, the divergence of the magnetic fields is equal to zero, as stated in equation 4.1d.

4.2.2 Constitutive equations

As Maxwell's Equation 4.1 describes in mathematical terms the relationship between electricity and magnetism [138], the following constitutive Equations 4.2 describe the macroscopic response of a material when it is exposed to harmonic EM fields [139]:

$$\bar{J}_C(\omega) = \sigma_E^\star \bar{E}(\omega) \tag{4.2a}$$

$$\bar{D}(\omega) = \varepsilon^\star \bar{E}(\omega) \tag{4.2b}$$

$$\bar{B}(\omega) = \mu^\star \bar{H}(\omega) \tag{4.2c}$$

where, $\sigma_E^\star$ is the electrical conductivity; $\varepsilon^\star = \varepsilon_0 \varepsilon_r^\star$ is the complex absolute permittivity with permittivity of free space ,ε_0, and relative complex permittivity, $\varepsilon_r^\star$; and $\mu^\star = \mu_0 \mu_r^\star$ is the complex absolute magnetic permeability with magnetic permeability of free space, μ_0, and relative complex magnetic permeability, $\mu_r^\star$. The parameters $\varepsilon_r^\star$, $\mu_r^\star$, and $\sigma_E^\star$ are generally a second-order tensor with nine independent material parameters [140]. However, quasi-isotropy is assumed at the sample scale [141]. Hence, $\varepsilon^\star$, $\mu^\star$, and $\sigma_E^\star$ are assumed to be material-specific parameters with scalar quantities, which is a valid assumption especially in the case of soils. It should be noted here that the material-specific constitutive parameters depend on the frequency, f, temperature, T, and pressure, p. The importance of each of these material-specific parameters is dependent on the purpose of the investigation. The parameters investigated in this research study are the dielectric permittivity and electric conductivity.

Commonly, the electrical conductivity, $\sigma_E^\star$, characterises the movement of free charges in a material if an external electric field is applied [138]. In the case of a 'perfect' conductor, $\sigma_E^\star$ appproaches an infinite value because all charges are able to move freely in the medium. In

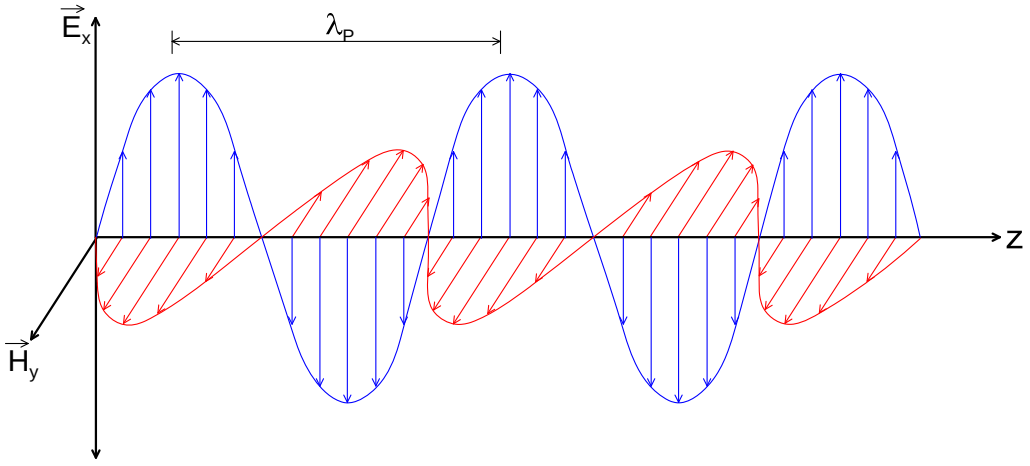

Figure 4.1: One-dimensional propagation of an EM signal as a transverse oscillating wave of coupled electric (blue) and magnetic (red) fields, dependent on time.

contrast, a medium is called a 'perfect' dielectric if $\sigma_{\mathrm{E}}^{\star}$ is zero, which means that the bonding forces between electrons and atoms are too tight, and free charge movements do not occur [138]. Therefore, the electrical conductivity is commonly associated with high conductive materials (such as metal) and is expressed by Equation 4.2a.

However, it should be noted that different mechanisms of conductivity exist. Low conductive materials, such as insulators and dielectrics, also exhibit conductivity due to the displacement of charges in the presence of an external alternating electric field [29, 142, 143]. A third mechanism is observed in terms of electrolyte conductivity. When an electric field is applied to a material with a high ionic concentration, ions in the material move towards the opposite charge and cause electrolyte conductivity [142]. In the presence of an electric field with alternating potential, the electric current density, $\bar{J}_C$, as in Equation 4.2a, is replaced by the effective current density, $\bar{J}_{\mathrm{eff}}$, in order to consider the displacement current density [143]:

$$\bar{J}_{\mathrm{eff}} = \bar{J}_C + \bar{J}_D = \sigma_{\mathrm{E}}^{\star}\bar{E} + \varepsilon^{\star}\frac{\partial \bar{E}}{\partial t} = j\omega\varepsilon_0\left(\varepsilon_r^{\star} - \frac{j\sigma_{\mathrm{E}}^{\star}}{\omega\varepsilon_0}\right)\bar{E} = j\omega\varepsilon_0\varepsilon_{r,\mathrm{eff}}^{\star}\bar{E} \tag{4.3}$$

where, j is the imaginary unit; $\bar{J}_D$ is the displacement current density, which is a function of $\varepsilon^{\star}$ and $\bar{E}$; ω is the angular frequency; and $\varepsilon_{r,\mathrm{eff}}^{\star}$ is the relative effective complex permittivity. The relative effective complex permittivity is generally dependent on the frequency, temperature, and pressure. The real part, $\varepsilon_{r,\mathrm{eff}}'$ of $\varepsilon_{r,\mathrm{eff}}^{\star}$, characterises the storage ability of EM energy in a medium when an EM field is applied [144]. The imaginary part, $\varepsilon_{r,\mathrm{eff}}''$ of $\varepsilon_{r,\mathrm{eff}}^{\star}$, represents the electrical losses and dielectric losses of materials that occur due to polarisation effects [145]. At low frequencies, the direct current conductivity, σ_{DC}, can be separated from the imaginary part, $\varepsilon_{r,\mathrm{eff}}''$ of the $\varepsilon_{r,\mathrm{eff}}^{\star}$, of low conductive soils [29, 146, 147, 148], which leads to an additional term accounting for σ_{DC}. Thus, the relative effective complex permittivity, $\varepsilon_{r,\mathrm{eff}}^{\star}$, can be expressed as follows:

$$\varepsilon_{r,\mathrm{eff}}^{\star}(\omega,T,p) = \varepsilon_{r,\mathrm{eff}}'(\omega,T,p) - j\cdot\varepsilon_{r,\mathrm{eff}}''(\omega,T,p) = \varepsilon_{r,\mathrm{eff}}'(\omega,T,p) - j\left(\varepsilon_{r,\mathrm{d}}'' + \frac{\sigma_{\mathrm{DC}}}{\omega\varepsilon_0}\right) \tag{4.4}$$

where, $\omega = 2\pi f$ is the angular frequency , T is the temperature , p is the pressure, $\varepsilon_{r,\mathrm{eff}}'$ is the real part and $\varepsilon_{r,\mathrm{eff}}''$ is imaginary part of the complex relative effective permittivity, $\varepsilon_{r,\mathrm{eff}}^{\star}$, σ_{DC} is the direct current conductivity describing electrical losses, and $\varepsilon_{r,\mathrm{d}}''$ is the imaginary part standing for dielectric losses. A measure for the strength of losses is given by the loss tangent δ [42, 149], which is defined as:

$$\tan\delta(\omega) = \frac{\varepsilon_{r,\mathrm{eff}}'}{\varepsilon_{r,\mathrm{eff}}''} \tag{4.5}$$

4.3 Polarisation and relaxation effects

4.3.1 Background

In simple terms, the permittivity is a dielectric material property that measures the storage ability and release of electrical energy when an external field is applied [144]. In the absence of an electric field, charges in a material are randomly orientated and non-polarised. As soon as an electric field is applied, charges in a dielectric become displaced relative to each other [29, 144] in order to compensate for the applied electric field. This phenomenon of charge displacements and reorientations is termed 'polarisation'. The real part, $\varepsilon'_{r,\text{eff}}$ of $\varepsilon^{\star}_{r,\text{eff}}$, measures the material polarisability when an external electric field is applied, and is often referred to as the ability of materials to store electrical energy [23, 145, 150, 151]. The imaginary part, $\varepsilon''_{r,\text{eff}}$, represents the electrical losses and dielectric losses of materials that occur due to polarisation effects [18, 25, 145].

4.3.2 Polarisation effects

There are several polarisation mechanisms active at the specific frequency range under investigation. Figure 4.2 shows a simplified schematic illustration in which different polarisation mechanisms are shown in a frequency range from ~ 1 Hz to $\sim 10^{15}$ Hz. In the frequency range $f > 10^{10}$Hz, only single component polarisation – that is, dipolar, atomic, and electronic – is observed on pure homogeneous materials [142, 154]. At extremely high frequency (HF) in the terahertz (THz) range, only electronic polarisation can operate. With decreasing frequency, progressively more polarisation effects occur, such as atomic and dipolar polarisation, which contributes to the dielectric property of a material and results in an increasing $\varepsilon^{\star}_{r,\text{eff}}$. At frequency lower than $f < 10^{10}$Hz, additional polarisation mechanisms occur in heterogeneous materials with multiple phases such as soils [153, 154, 155], which include interfacial and counterion polarisation [23, 152, 156].

In the presence of an EM field at HF $f >\sim 10$GHz, only atomic and electronic polarisation effects occur in a material [29, 141, 142]. An atom consists of an atomic nucleus that is positively charged and surrounded by a negatively charged electron cloud. In the presence of an externally applied EM field, the electron cloud becomes displaced relative to the atomic nucleus in the direction of the EM field [142]. This displacement of the electron leads to an induced dipole moment, which causes **electronic polarisation** [142]. In the case of **atomic polarisation**, an EM field disturbs the equilibrium between different atoms in a molecule,

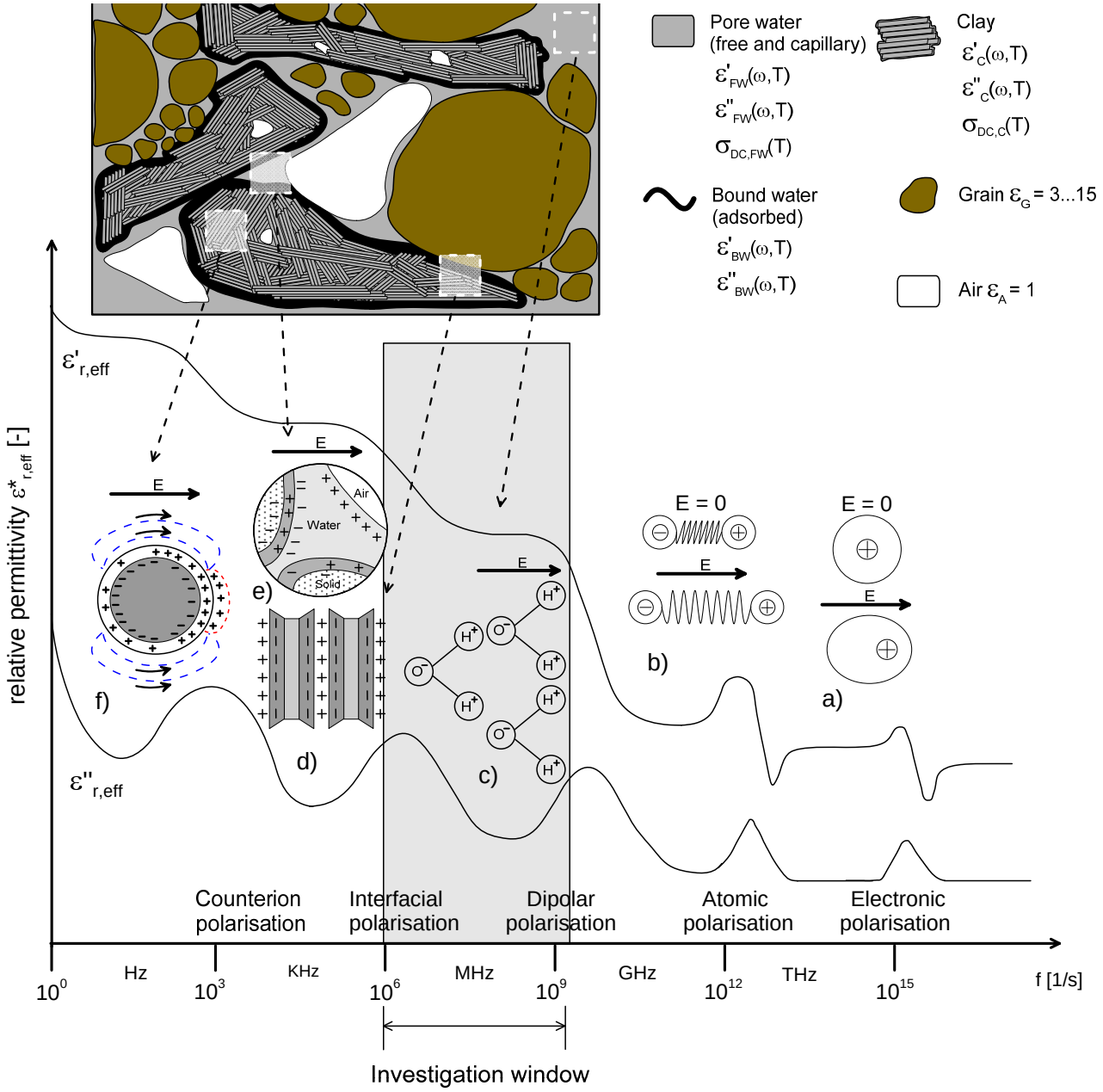

Figure 4.2: Schematic illustration of diverse polarisation mechanisms occurring over a broad frequency range, adapted and modified from [19, 29, 152, 153]. Shown are (a) electronic, (b) atomic, (c) dipolar, (d) double layer, (e) Maxwell- Wagner, and (f) counterion polarisation. An additional graph is given relating the soil phases and their individual dielectric properties to the polarisation effects

which results in atom displacements. Due to this displacement of atoms to each other, another additional dipole moment is induced [142].

At frequency $f < 10$ GHz, **dipolar polarisation** is present. A water molecule is composed of one oxygen atom and two hydrogen atoms which are bound under an angle of $104.45°$. Due to the fact, that the centre of the positive and negative charges is aligned under an angle of $180°$, a water molecule behaves naturally as a dipole with a positively and negatively charged

molecule side. Water molecules in soils that are not bound to the solid particle surface are randomly orientated in the absence of an external EM field [29]. As soon as an EM field is applied, water molecules become polarised as the dipoles begins aligning in the direction of the EM field [29]. If an alternating EM field far below the relaxation frequency is applied, water molecules reorientate in phase with the direction of the EM field [25].

Bound water and interfacial polarisation arises at frequencies lower than $f < 1$ GHz in the MHz and kilohertz (KHz) range [43, 157]. Interfacial polarisation mostly appears at the interface between the two phases, due to their different EM properties [153, 157]. Interfacial polarisation is based on two polarisation mechanisms [19, 144, 145, 157, 158]: the Maxwell-Wagner effect, and electrical double layer polarisation, as shown in Figure 4.2. Bound water polarisation similarly follows the principles of the dipolar polarisation mechanism. In contrast to free water and capillary water, bound water is subject to enormous binding forces that are caused by the attraction of water molecules at the interface to the solid particle surface [159]. Due to this binding force of water molecules to the particle surface, bound water dipoles are restricted in their mobility and ability to rotate under the influence of an alternating EM field [23, 43, 159]. As a result, bound water polarisation occurs at lower frequencies than in the case of the dipolar polarisation of free water and capillary water [43]. Double layer polarisation is caused by charge displacements, where the positively charged ionic cloud is displaced in relation to the negatively charged solid particle [160]. Maxwell-Wagner polarisation occurs in heterogeneous materials in which spatially separated phases with different EM properties and charges with different mobilities are connected by common interfaces. Under the effect of an EM field, the normal component of the EM field must be equalised [161, 162]. This leads to an enhanced charge accumulation at interfaces perpendicular to the direction of the EM field [152, 153, 157, 162]. **Counterion polarisation** emerges in the frequency range of kHz, as well as relaxation effects referred to as the adsorption/desorption rates of counterions in clay interlayers with relaxation times in the range of 2 to 8 ns [163]. Here, the tangential movements and normal diffusion of ions along the solid particle surface are observed, as well as perpendicular movements through the water-filled pores, eventually resulting in an induced dipole moment [155, 164, 165, 166, 167].

4.3.3 Relaxation models

As explained in Section 4.3.2, polarisation describes the storage ability of EM energy in a material due to the charge displacements under the impact of an EM field. Thus, the complex permittivity as a function of frequency is determined by the material polarisability and the dielectric losses. However, when the EM field is removed, the stored energy in the material starts to dissipate with time [18]. The charges return to equilibrium due to the absence of the

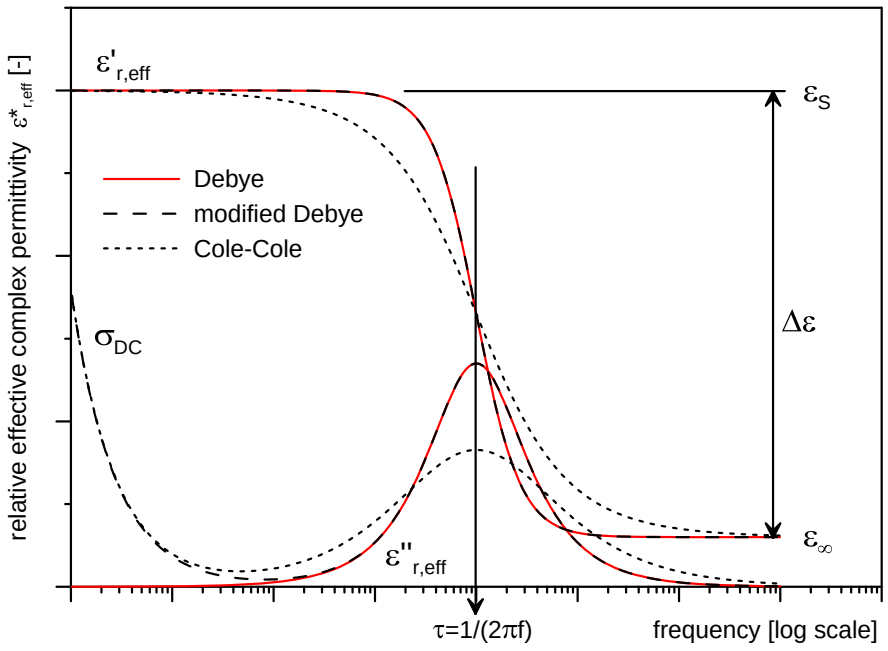

Figure 4.3: Qualitative illustration of the dielectric spectrum under the effect of a relaxation process, with static permittivity, ε_S, HF limit of permittivity, ε_∞, and relaxation magnitude, $\Delta\varepsilon$. Shown is the relaxation process according to the Debye Equation 4.6, modified Debye Equation 4.7 (including direct current conductivity contribution σ_{DC}) and Cole-Cole Equation 4.8, representing relaxation time distribution and direct current conductivity contribution.

EM field which is termed 'relaxation' [29, 142, 156]. A typical frequency and temperature-dependent response for single type relaxation behaviour is described by the Debye equation [23, 168]:

$$\varepsilon^{\star}_{r;\mathrm{eff}}(\omega,T) = \varepsilon_\infty(T) + \frac{\Delta\varepsilon(T)}{1+j\omega\tau(T)} \tag{4.6}$$

where, ε_∞ is the HF limit of permittivity, $\Delta\varepsilon$ is the relaxation magnitude, and τ is the relaxation time. Figure 4.3 shows a schematic illustration of relaxation behaviour according to the Debye equation 4.6, which is the simplest form of the dielectric spectrum and is typically observed in the case of single-phase homogeneous materials, such as pure water [149, 169]. According to the Debye-equation, the real part of complex permittivity shows two asymptotes, where the static permittivity, ε_S, is found at low frequency ($f \to 0$), and the HF limit of permittivity, ε_∞, is found at HF ($f \to \infty$). The characteristic difference between ε_S and ε_∞ gives the relaxation magnitude $\Delta\varepsilon = \varepsilon_S - \varepsilon_\infty$. The imaginary part of complex permittivity ideally shows a log-normal distribution of the dielectric spectrum, in which the peak value is located at the inflection point of the relaxation magnitude, with $\tan(\delta) = 1$, which indicates a single relaxation time, τ. As indicated in Equation 4.4 and Figure 4.3, the imaginary part of complex permittivity is affected by the electrical conductivity. In order to take the conductivity contribution into account, the Debye Equation 4.6 has been modified by an additional term

for the direct current conductivity, σ_{DC} [143, 170]:

$$\varepsilon^{\star}_{r,\text{eff}}(\omega,T) = \varepsilon_{\infty}(T) + \frac{\Delta\varepsilon(T)}{1+j\omega\tau(T)} - j\frac{\sigma_{DC}}{\omega\varepsilon_0} \tag{4.7}$$

As a heterogeneous porous material composed of multiple phases with different EM properties, soil may reveal not only a relaxation behaviour with a single relaxation time, but also a distribution of relaxation times. This phenomenon of a relaxation time distribution results from the complexity of soil structure, including its texture, composition and binding forces on the water phase [29, 146, 149, 158]. In respect to the range of a distribution of relaxation times, the Cole-Cole model is introduced, and qualitatively illustrated in Figure 4.3 [19, 165, 169, 171, 172, 173, 174]:

$$\varepsilon^{\star}_{r,\text{eff}}(\omega,T) = \varepsilon_{\infty}(T) + \frac{\Delta\varepsilon(T)}{1+(j\omega\tau(T))^{\beta_{CC}}} - j\frac{\sigma_{DC}}{\omega\varepsilon_0} \tag{4.8}$$

where, β_{CC} is the stretching exponent or Cole-Cole parameter, which varies between $0 \leq \beta_{CC} \leq 1$ and refers to the relaxation time distribution. In the special case of $\beta_{CC} = 1$, Equation 4.8 equals Equation 4.7.

4.4 EM properties of individual soil phases

As explained in Section 2.2, as a porous material, soil is generally composed of three different phases. Figure 4.2 shows a simplified illustration of these phases and their EM properties. It should be noted that, in this study, the water phase is distinguished between pore water and bound water. Here, pore water is associated with free water and capillary water, whereas bound water only accounts for the type of water that is adsorbed to the surface of solid particles.

Each of these phases exhibits individual EM properties in terms of $\varepsilon^{\star} = \varepsilon_0 \cdot \varepsilon^{\star}_{r,\text{eff}}$ and $\sigma^{\star}_{E}$. The EM properties of the solid particles are generally a second-order tensor with nine independent material parameters. However, mono-crystalline mineral phases are not expected in a natural porous material; thus, quasi-isotropy at the sample scale is assumed [141]. Hence, the material parameters are assumed as scalar qualities, which is a valid assumption, especially in the case of most heterogeneous mixtures. Moreover, in the present study, the relative magnetic permeability of the soils is assumed to be one; hence, μ is equal to the permeability of free space, $\mu = \mu_0$ [19]. As a result, the effective EM soil properties are influenced by the EM properties of the individual phases, the interaction between these phases and the soil structure [19, 143].

4.4.1 Solid phase

The relative permittivity of the solid phase in the case of mineral grains is considered not frequency or temperature dependent in the investigated T, f-range [140]. Thus, the relative permittivity of the solid phase is considered a constant real number, and found to be in the value range between 3 to 15 [19, 175]. Diverse empirical equations were suggested to give the relationship between relative effective real permittivity $\varepsilon_{r,G}$ and solid density ρ_G. An empirical equation for dry soils is suggested by Dobson et al. [37] and Hallikainen et al. [176]:

$$\varepsilon_{r,G} = (1.01 + 0.44 \cdot \rho_G)^2 - 0.062, \tag{4.9}$$

Another relationship between $\varepsilon_{r,G}$ and ρ_G is proposed with the following empirical equation [177, 178]:

$$\varepsilon_{r,G} = A^{\rho_G}, \tag{4.10}$$

where, A is an empirical fitting parameter and is suggested to be $A = 1.93 \pm 0.17$ [177] or $A = 1.96$ [178].

Moreover, the $\varepsilon_{r,G}$ of the solid phase can be estimated based on the mass fraction of the soil mineralogy [141, 175, 179]:

$$\varepsilon_{r,G} = \left(\sum_{k=1}^{N} M_{\mathrm{S},k} \frac{\rho_G}{\rho_{X,k}} \sqrt{\varepsilon_{r,G,k}} \right)^2, \tag{4.11}$$

where, k describes the number of different mineralogical components, $\varepsilon_{r,G,k}$ is the relative effective permittivity of the kth mineralogical soil component and $\rho_{X,k}$ is its X-ray density, ρ_G is the solid density, and $M_{\mathrm{S},k}$ describes the mass fractions of the kth mineralogical soil component.

4.4.2 Free water phase

The dielectric properties of water are strongly frequency and temperature dependent. For example, for a temperature of $T = 20°$, the real part of the complex permittivity around 1 GHz of pure water is $\varepsilon'_{r,\mathrm{eff}} = 80.17 \pm 0.12$ [172]. In contrast, in the case of ice at $T = -20°$, $\varepsilon'_{r,\mathrm{eff}}$ is found to be ~ 3.18 [180, 181, 182]. Further, the dielectric properties of water vary with frequency in the GHz-range. Figure 4.4 shows a dielectric measurement taken on deionised water over a frequency range from 100 MHz to 40 GHz. The equipment used to measure the dielectric spectrum, includes a vector network analyser (VNA; Agilent PNA E8363B) in combination with a commercial open-ended coaxial line probe (Agilent probe performance). For frequency

at the MHz range, the real part, $\varepsilon'_{r,\text{eff}}$, of permittivity reaches a constant value and no dielectric losses are observed, giving an imaginary part of $\varepsilon''_{r,\text{eff}} \approx 0$. With increasing frequency into the GHz range, $\varepsilon'_{r,\text{eff}}$ decreases continuously, whereas $\varepsilon''_{r,\text{eff}}$ shows a parabolic curve shape with a peak located at the inflection point of the $\varepsilon'_{r,\text{eff}}$ - curve. Since water molecules own a natural dipole moment, this dielectric behaviour of pure water is influenced by dipolar relaxation effects in the GHz-range, and can be characterised by the simple Debye Equation 4.6.

Extensive studies on the dielectric behaviour of pure water have been undertaken [172, 183, 184, 185]. As Equation 4.6 shows, the complex permittivity, $\varepsilon^{\star}_{r,\text{eff}}$, is also a function of temperature, T, with $\varepsilon_{\infty}(T)$, $\varepsilon_{\text{S}}(T)$, and $\tau(T)$. In the literature, the HF limit of the pure water permittivity is often given to $\varepsilon_{\infty,\text{FW}} = 5.5$ [186] or $\varepsilon_{\infty,\text{FW}} = 4.22$ [187]. Kaatze [184] proposed an empirical equation for the temperature dependence of the permittivity, $\varepsilon_{\infty,\text{FW}}$, of pure water based on a simple Debye-model, including HF extrapolation:

$$\varepsilon_{\infty,\text{FW}}(T) = 5.77 - 2.74 \cdot 10^{-2}(T - 273.15). \tag{4.12}$$

where, temperature T is in kelvins.

The static permittivity, ε_{S}, reflects the constant permittivity value, which is achieved at low-frequency range. An empirical equation is suggested to model the static permittivity of pure water in the temperature range $0° \leq T(\text{in }°\text{C}) \leq 60°$, as follows [172, 188]:

$$\varepsilon_{\text{S,W}}(T) = 78.35 exp(-4.55 \cdot 10^{-3}(T - 298.15)). \tag{4.13}$$

where, temperature T is in kelvins. Alternatively to Equation 4.13, $\varepsilon_{\text{S,W}}(T)$ can be calculated in a temperature range $0°C \leq T \leq 100°C$ using [189, 190]:

$$\varepsilon_{\text{S,W}}(T) = 87.9144 - 0.404399 \cdot T + 9.58726 \cdot 10^{-4} \cdot T^2 - 1.32892 \cdot 10^{-6} \cdot T^3. \tag{4.14}$$

where, temperature T is in celsius. The relaxation time, $\tau_{\text{FW}}(T)$, of pure water dependent on the temperature, T, can be approached by the following expression [191]:

$$\tau_{\text{FW}}(T) = 1.1109 \cdot 10^{-10} - 3.824 \cdot 10^{-12} \cdot T + 6.938 \cdot 10^{-14} \cdot T^2 - 5.096 \cdot 10^{-16} \cdot T^3 \tag{4.15}$$

where, temperature T is in celsius. Using Equation 4.12, 4.14, and 4.15 in combination with the Debye Equation 4.6, the complex permittivity of pure water can be calculated dependent on the temperature. Figure 4.4 shows a comparison of the calculated and measured dielectric spectrum for deionised water at a temperature of $T = 22°$C, which are identical, and proves the accuracy and quality of the dielectric measurement.

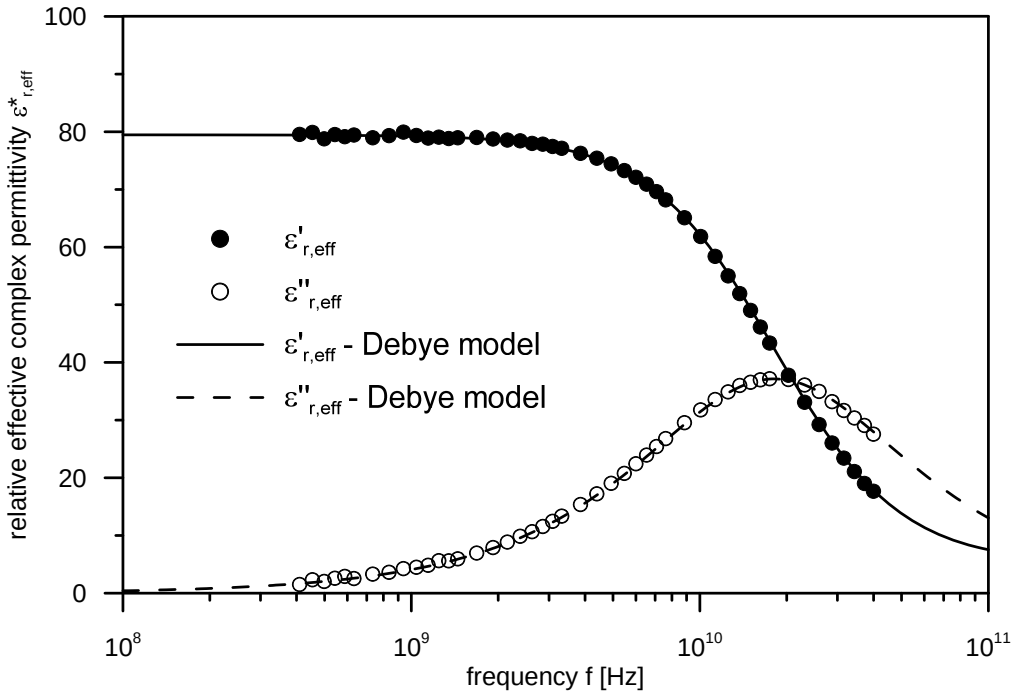

Figure 4.4: Measured dielectric spectrum of deionised water measured over a frequency range from 100 MHz to 30 GHz under defined environmental conditions ($T = 22°C$) and modelled dielectric spectrum based on the Debye Equation 4.6.

Free water in fine-grained soils is not subject to binding forces to the particle surface, and the water phase is seen as an aqueous solution with a certain ion concentration that not only causes dielectric losses, but also contributes to the direct current conductivity [140]. Thus, the frequency and temperature dependent complex permittivity of free water can be described by the modified Debye model, according to equation 4.7 [140, 173, 189].

4.4.3 Bound water phase

The dielectric properties of the **bound water** phase in the high MHz range can be determined by an extreme value consideration. It is known that the complex permittivity of bound water at the GHz range is generally lower than the permittivity for free water due to the restricted mobility of water molecules under the influence of an EM field [186]. As stated at the beginning of this section, the permittivity around 1 GHz of pure water is $\varepsilon'_{r,\text{eff}} = 80.17 \pm 0.12$ with $T = 20°$, whereas the permittivity of ice is $\varepsilon'_{r,\text{eff}}(T = -20°) \sim 3.18$. Therefore, Dirksen and Dasberg [182] assumed only one monomolecular bound water layer surrounding the solid particles with a permittivity of bound water, $\varepsilon'_{\text{BW}} = 3.2$. However, the permittivity of bound water is higher than the permittivity of ice [186]. Looking at these extrema, it can be summarised that the permittivity of bound water must be between $3.2 < \varepsilon'_{\text{BW}} < 87.85 \pm 0.12$. Based on this observation, Friedman [186] suggested the complex permittivity of bound water as an

exponential function dependent on the distance, x, to the particle surface:

$$\varepsilon^{\star}_{\mathrm{BW}}(x) = \varepsilon_{\mathrm{W,min}} + (\varepsilon_{\mathrm{W}} - \varepsilon_{\mathrm{W,min}}) \cdot (1 - e^{-\lambda x}), \tag{4.16}$$

where, $\varepsilon_{\mathrm{W,min}} = 5.5$ is the minimum permittivity, ε_{W} is the maximum permittivity of free water at a given temperature, and $\lambda = 10^8 \mathrm{cm}^{-1}$ is a parameter describing the slope of Equation 4.16 and accounting for binding forces caused by the particle surface [192]. With increasing distance ($x \to \infty$) to the particle surface, $\varepsilon^{\star}_{\mathrm{BW}}$ in Equation 4.16 approaches the permittivity of free water ε_{W}. With decreasing distance ($x \to 0$), the permittivity of bound water comes to $\varepsilon^{\star}_{\mathrm{BW}}(0) = \varepsilon_{\mathrm{W,min}}$.

An exponential description of bound water permittivity as function of distance from the particle surface was proposed by Robinson et al. [193]:

$$\varepsilon^{\star}_{\mathrm{BW}}(x) = \varepsilon_{\mathrm{W}} \cdot (1 - e^{-\frac{1}{d_{\mathrm{BW}}} \cdot x}), \tag{4.17}$$

where, d_{BW} is the thickness of the bound water phase (in $\mathring{A}$). In contrast to Equation 4.16, Equation 4.17 approaches a different permittivity value for decreasing distance to the particle surface. For $x \to 0$, the permittivity of bound water is $\varepsilon^{\star}_{\mathrm{BW}}(0) = 0$.

Previous studies present the average values of the bound water permittivity, which may be used for a first approach, and are suggested to be $\varepsilon^{\star}_{\mathrm{BW}} = 35 - j \cdot 15$ [37]. However, depending on the soil investigated, the amount of bound water and binding forces to the particle surface can vary significantly due to the specific particle surface area. Thus, an average permittivity of the bound water phase is debatable and should not be assumed to be a constant parameter. Boyarskii et al. [12] showed that the complex permittivity of bound water changes with increasing distance from the particle surface. For almost dry conditions, the permittivity of fine-grained soils is determined by one monomolecular layer of bound water having a complex permittivity close to that of ice. With increasing wetness of the soil, more and more monomolecular water layers surround the solid particles differing in their permittivity with distance Boyarskii et al. [12]. The study showed that at 10 monomolecular water layers, the water molecules are distant enough from the particle surface and can be treated as free water Boyarskii et al. [12]. The water molecules are no longer influenced by surface binding forces. As a consequence, the permittivity is close to that of free water. While increasing the wetness of the soil, all additional water is assumed to be free water. Further, Boyarskii et al. [12] indicated that the complex permittivity of bound water depends strongly on the frequencies. For high frequencies in the GHz-range, bound water is not polarised, which leads to a lower permittivity of bound water.

4.5 Dielectric mixture approaches

In the past, dielectric mixture approaches have been developed in order to relate the dielectric soil properties to mechanical and hydraulic state parameters. Here, the relationship between soil water content and relative permittivity at around 1 GHz has been of particular interest. Extensive research was undertaken in early studies focusing on empirical determination of material-specific calibration equations [15, 194, 195, 196]. With advancing studies on dielectric soil properties, it has been found that relative permittivity is not a function of soil water content, but is also influenced by the porous structure of a soil [20, 21, 22, 197, 198, 199]. In order to consider this, semi-empirical material-specific calibration equations have been developed to consider the dry density of soils. Since material-specific calibration equations generally disregard the composition of soil as multiple-phase material, theoretical mixture approaches have been introduced to describe the bulk dielectric property of soils as a function of the volume fraction and relative permittivity of each individual phase [12, 25, 37, 182, 187, 200, 201, 202]. Recently, researchers have investigated the relationship between hydraulic properties and dielectric soil properties, in which the focus is the influence of soil suction on relative permittivity. Here, theoretical mixture approaches are combined with phenomenological relaxation models which are used to describe the soil suction effect on the dielectric soil property [19, 140, 152, 153, 156, 158, 203, 204, 205].

4.5.1 Material-specific empirical calibration equations

Material-specific equations are generally determined empirically in the laboratory, thereby ensuring defined and controlled environmental conditions. In order to determine an empirical calibration equation, several soils need to be tested with varying water content to fit the relationship between water content and relative permittivity Topp et al. [15]. Only the real part of relative permittivity is used to determine the calibration equation, while the imaginary part is neglected. The most popular mathematical equation to fit the experimental data and express the θ-$\varepsilon'_{r,\mathrm{eff}}$-relationship is the third degree polynomial Topp et al. [15]:

$$\theta = A + B \cdot \varepsilon'_{r,\mathrm{eff}} + C \cdot (\varepsilon'_{r,\mathrm{eff}})^2 + D \cdot (\varepsilon'_{r,\mathrm{eff}})^3, \tag{4.18}$$

Numerous empirical calibration equations are available which differ in their applicability for different soil types. Table 4.1 compiles parameter sets for selected calibration equations.

Table 4.1: Parameters of empirically determined material-specific calibration equations using a third degree polynomial according to Equation 4.18

	A	B	C	D
Dasberg [17]	-751.0	424.0	-18.5	0.38
Jacobsen [195]	-701.0	347.0	-11.6	0.180
Roth [194]	-728.0	448.0	-19.5	0.361
Topp [15]	-530.0	293.0	-5.5	0.043

One of the most frequently applied and cited calibration equations is given by Topp et al. [15], where the equation is fitted based on a set of test data of four non-organic soils using TDR. This equation is supposed to be universal and applicable regardless of the soil type. However, it is found that this calibration equation is limited in its use and not applicable for fine-grained soils and soils containing organic matter [17, 182]. Further calibration equations based on extensive experimental investigations on mineral soils are proposed by [17, 194, 195]. All material-specific calibration equations compiled in Table 4.1 are frequency independent and commonly refer to a frequency $\sim$ 1 GHz. In this frequency range, the dielectric behaviour of the free water phase is dominant in soils with low clay content, but may change in soils with higher clay content. Wensink [196] considered the frequency dependence of the relative permittivity and investigated the relationship of water content and relative permittivity at different frequencies. Three calibration equations for frequencies at 5 MHz, 50 MHz and 1 GHz were empirically determined based on measurements taken with 11 different soils:

$$\varepsilon'_{r,\mathrm{eff}}(5\ \mathrm{MHz}) = 279.8 - 272.2 \cdot \theta \tag{4.19a}$$

$$\varepsilon'_{r,\mathrm{eff}}(50\ \mathrm{MHz}) = 1.4 + 87.6 \cdot \theta - 18.7 \cdot \theta^2 \tag{4.19b}$$

$$\varepsilon'_{r,\mathrm{eff}}(1\ \mathrm{GHz}) = 3.2 + 41.4 \cdot \theta - 16.0 \cdot \theta^2. \tag{4.19c}$$

It should be noted that the calibration equation at 1 GHz in Equation 4.19c differs from the polynomial in Equation 4.18. It is evident that Wensink [196] calibrated the relationship at 1 GHz frequency using a second-degree polynomial instead of the third-degree polynomial that was commonly used in other studies.

An advanced calibration equation was proposed by Malicki et al. [20] that also considers the influence of dry density on the dielectric soil behaviour. The following equation was suggested to describe the relationship between relative permittivity, $\varepsilon'_{r,\mathrm{eff}}$, volumetric water content, θ, and dry density, ρ_D:

$$\theta = \frac{\sqrt{\varepsilon'_{r,\mathrm{eff}}} - 0.819 - 0.168 \cdot \rho_D - 0.159 \cdot \theta_D^2}{7.17 + 1.18 \cdot \rho_D} \tag{4.20}$$

A similar equation that considers the dry density, ρ_D, relates the gravimetric water content, w, to the relative permittivity, and was suggested by [199, 206, 207]:

$$\sqrt{\varepsilon'_{r,\mathrm{eff}}} \cdot \frac{\rho_\mathrm{W}}{\rho_D} = a_{soil} + b_{soil} \cdot w \tag{4.21}$$

where, a_{soil} and b_{soil} are soil-specific calibration constants that need to be determined in laboratory investigations. Equation 4.21 can be rewritten in terms of the volumetric water content, θ, using the relationship defined in Equation 2.10, which leads to [22]:

$$\theta = \frac{1}{a_{soil}} \sqrt{\varepsilon'_{r,\mathrm{eff}}} - \frac{a_{soil}}{b_{soil}} \cdot \frac{\rho_D}{\rho_\mathrm{W}} \tag{4.22}$$

Comparing Equation 4.21 and 4.22, it should be noted that the former is supposed to be used as a universal equation, whereas the latter contains specific calibration constants that must be determined for each individual soil. A standard procedure was developed to determine θ and ρ_D based on Equation 4.22 and regulated in ASTM D6780 / D6780M-12 [208].

Generally, it should be noted that the accuracy of empirically determined calibration equations depends on the quality of the fitted experimental data and root mean square deviation (RMSE), which has been achieved by its derivation. The major disadvantage of material-specific calibration equations arises from questions about the influence of temperature and frequency dependence on the dielectric soil properties, which are completely neglected in the derivation. Almost all calibration equations were determined under controlled environmental conditions in the laboratory, where temperature changes do not exist. Controversially, these calibration equations are also promoted to be used in field investigations to determine the dielectric soil behaviour in situ, where temperature changes do exist and definitely reduce the success of applications. Therefore, successful application and practical use of the calibration equations requires not only a profound understanding of the soil investigated, but also a good knowledge of EM theory and the techniques used to measure the dielectric soil behaviour.

4.5.2 Theoretical mixture approaches

Theoretical mixture approaches consider the soil as a porous medium that is composed of different phases [200]. The relative permittivity of the soil is the result of the sum of the dielectric properties of each individual phase, multiplied by its volume fraction. This structure-sensitive relationship can be written in a general form as follows [200]:

$$\varepsilon^\star_{r,\mathrm{eff}} = \left(\sum_\mathrm{i} \varepsilon^\alpha_{r,\mathrm{eff,i}} \cdot V_\mathrm{i}\right)^{\frac{1}{\alpha}} \tag{4.23}$$

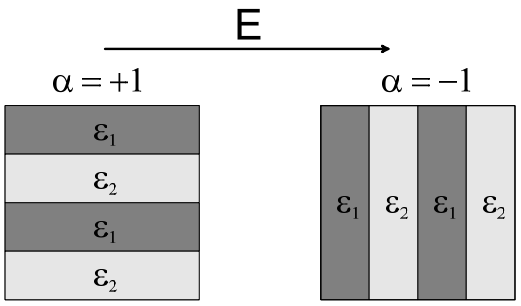

Figure 4.5: Simplified illustration describing the value range of the structure parameter, α, by parallel and perpendicular alignment of soil components to the direction of the EM field.

where, i is the number of phases, α is a parameter dependent on the soil structure, V is the volume fraction of the individual phase, and $\varepsilon_{r,\text{eff,i}}$ is the permittivity of the i-te soil phase.

The value range of the structure parameter, α, can be explained from a simplified observation. Dependent on the alignment of the soil components to the applied EM field, two extrema are observed, as shown in Figure 4.5. If layers of soil components are aligned in the direction of the EM field, a parallel circuit of dielectric is assumed [187]. In this case, the permittivity reaches a maximum value, giving structure parameter of $\alpha = +1$. Looking at the other extrema, gives a series circuit of dielectrics, where the soil components are layered perpendicular to the direction of the applied EM field. In this situation, the permittivity of dielectric gives a minimum value leading to $\alpha = -1$ [187]. It is unlikely that the components of the soil are exactly arranged in a parallel or series circuit. Therefore, the structure parameter usually takes a value between $-1 < \alpha < +1$. Some studies have been undertaken on the determination of the structure parameter. The complex refractive index model by Birchak et al. [201] proposed a structure parameter of $\alpha = 0.5$ for an isotropic soil [209]. However, Hilhorst [48] stated that the assumption of a constant $\alpha = 0.5$ can only be seen as an approximation for polar substances because the physical meaning of the dielectric soil properties in terms of the composition and microstructure is not considered. In another study, the structure parameter was investigated for a broad range of soil types, from sandy loam to silty clays [37]. Herein, the structure parameter was fitted by regression from dielectric measurement data in a frequency range of 1.4 to 18 GHz, and determined to $\alpha = 0.65$. However, experiments on moist mineral soils show that the structure parameter is a non-constant parameter and can change between $0.4 \leq \alpha \leq 0.8$ [210]. Zakri et al. [200] indicated that the structure parameter is dependent on the prevailing soil density, where α reduces with increasing soil porosity. However, recent studies suggest that the structure parameter is not constant and remains a fitting parameter [197, 207].

In its simplest form, soil is seen as a material composed of three phases: solid, air and water phases [16, 209]. The distinction of the water phase in regard to its binding states

is neglected, and the complete pore fluid is considered free water. In the **3-phase model**, Equation 4.23 can be expressed using the porosity, n, and volumetric water content, θ, according to:

$$\varepsilon^{\star}_{r,\text{eff}}(\omega,T) = ((1-n)\cdot\varepsilon^{\alpha}_{r,G} + \theta\cdot\varepsilon^{\alpha}_{\text{W}}(\omega,T) + (n-\theta)\cdot\varepsilon^{\alpha}_{A})^{\frac{1}{\alpha}}. \tag{4.24}$$

where, the permittivity of air is $\varepsilon_A = 1$; the permittivity of solids, $\varepsilon_{r,G}$, can be determined using one of the Equations 4.9 to 4.11 presented in Section 4.4.1; and the permittivity of the free water phase is given by Equation 4.7. As only the contribution of the relative permittivity of free water is considered, the 3-phase model is reasonable to use for cohesion-less soils, such as sand.

In the case of cohesive soils, such as fine-grained soils, the water phase consists of free water and bound water that is attracted to the particle surface by adsorption forces. Due to the particle surface forces, the bound water phase is restricted in its mobility. As a result of this restricted mobility, the permittivity of bound water is lower than the one of free water [211], which subsequently reduces the permittivity of the soil. In order to consider the effects of bound water on the dielectric soil behaviour, the 3-phase model is extended by an additional term to a **4-phase model** [12, 37, 182, 187, 202]:

$$\varepsilon^{\star}_{r,\text{eff}}(\omega,T) = ((1-n)\cdot\varepsilon^{\alpha}_{r,G} + \theta_{\text{FW}}\cdot\varepsilon^{\alpha}_{\text{W}}(\omega,T) + \theta_{\text{BW}}\cdot\varepsilon^{\alpha}_{\text{BW}}(\omega,T) + (n-\theta)\cdot\varepsilon^{\alpha}_{A})^{\frac{1}{\alpha}}. \tag{4.25}$$

where, θ_{BW} is the volumetric water content of the bound water, θ_{FW} is the volumetric water content of the free water, and $\theta = \theta_{\text{FW}} + \theta_{\text{BW}}$.

The volumetric water content, θ_{BW}, of the bound water phase, which is dependent on the temperature, T, can be estimated in a simplified form according to [43, 205]:

$$\theta_{\text{BW}}(T) = d_{\text{BW}}(T)\cdot A_s\cdot\rho_D \tag{4.26}$$

where, A_s is the total specific area of the solid particle surface, ρ_D is the dry density and d_{BW} is the thickness of the bound water phase, which is a function of temperature, T. Or and Wraith [205] predicted the thickness of the bound water phase and suggested the following equation:

$$d_{\text{BW}}(T) = \frac{a_x}{-d + T\cdot ln(\frac{k_B}{8\cdot\pi^2\cdot r^3\cdot c_x\cdot f^{\star}}\cdot T)} \tag{4.27}$$

where:

$a_x = 1621$ in ÅK is a constant adjusted by Low [7],

$c_x = 9.5\cdot 10^{-7}$ Pa·s = dynamic viscosity of interfacial water,

$d = 2047$K,

$f^{\star} \sim 0.8 - 1.0$GHz = cut-off frequency

$r \sim 1.8 - 2.5$ Å = radius of water molecule

$k_B = 1.38066 \cdot 10^{-23} \frac{\mathrm{J}}{\mathrm{K}}$ = Boltzmann constant

T = temperature in kelvins degree

In contrast to the material-specific calibration equations (see Section 4.5.1), theoretical mixture approaches are based on physical models. The dielectric behaviour of each component of a soil mixture can be described depending on temperature and frequency. Hence, the theoretical mixture approaches are more flexible and adaptable in order to consider aspects such as environmental changes. However, the major disadvantage in using theoretical mixture approaches is the simplification of the soil structure, such as in the case of the structure parameter, α, which is commonly assumed to be a constant value. Under this assumption, the microstructural and compositional physical effects on the dielectric soil behaviour are completely neglected. Further, there is still a knowledge deficit regarding soil phases interaction and influence on dielectric soil properties [143]. As a result, theoretical mixture approaches are preferably used for cohesive-less soils or for cohesive soils in a frequency range where soil phases interactions are negligibly low.

4.5.3 Theoretical mixture approaches combined with phenomenological relaxation models

Theoretical mixture approaches are combined with phenomenological relaxation models in order to consider the soil phases interactions and effects on the macroscopic EM properties of the soil. Current research focuses on the systematic analysis and inclusion of EM waves interactions in soils in consideration of structural, mineralogical, and compositional aspects, as well as soil phase interactions [14, 19, 23, 25, 140, 152, 153, 204, 212]. Subsequently, two innovative theoretical approaches are introduced that couple the hydraulic and EM properties of soils in consideration of the relaxation behaviour of free water and bound water [19, 23, 25, 48, 140]. One of these approaches is the theoretical mixture equation proposed by Hilhorst [48], which is based on depolarisation factors:

$$\varepsilon^{\star}_{r,\mathrm{eff}}(\omega, T, \theta) = \sum_{i=1}^{n} \varepsilon^{\star}_{r,\mathrm{eff}}(\omega, T, \theta) \cdot S_{\mathrm{dep,i}}(t, \theta) \cdot V_i \tag{4.28}$$

where, i is the number of soil phases, V is the volume fraction of the individual soil phase, and $S_{\mathrm{dep,i}}$ is the depolarisation factor of each soil phase. Based on the experimental investigations measuring the dielectric properties on glass beads, it was found that the depolarisation

factors of air ($S_{\text{dep,A}}$) and solid particles ($S_{\text{dep,r,G}}$) are negligibly low, and are assumed to be $S_{\text{dep,A}} = S_{\text{dep,r,G}} = 1$ [48]. Further, it was pointed out that an acceptable approach for the depolarisation factor of water, $S_{\text{dep,W}}$, is given by:

$$S_{\text{dep,W}}(\theta) = \frac{1}{3(2n-\theta)} \tag{4.29}$$

Subsequently, Equation 4.28 can be rewritten to [48]:

$$\varepsilon^{\star}_{r,\text{eff}}(\omega,T,\theta) = \frac{\Omega^{\star}_{1}(\omega,T,\theta)}{3(2n-\theta)} + (1-n)\cdot\varepsilon_{r,G}(T) + (n-\theta)\cdot\varepsilon_{A}, \tag{4.30}$$

where, $\Omega^{\star}_{1}(\omega,T,\theta)$ gives the complex permittivity of water in consideration of binding forces on the water phase, which is dependent on the frequency, $\omega = 2\pi f$, temperature, T, and volumetric water content, θ. $\Omega^{\star}_{1}(\omega,T,\theta)$ is defined as [48]:

$$\begin{aligned}\Omega^{\star}_{1}(\omega,T,\theta) = &\int_{\Psi_t(0)}^{\Psi_t(\theta)} \left(\frac{\Delta\varepsilon(T,\theta)}{1 + j\frac{\omega\cdot h}{k_B\cdot T}\exp^{(\Delta G^{\ddagger}_{w} + |\Psi_t(\theta)\cdot|V_{\text{mol}})/(R_{Gas}\cdot T)}} \cdot \frac{\mathrm{d}\theta\Psi_t}{\mathrm{d}\Psi_t}\cdot \mathrm{d}\Psi_t \right) \\ &+ \theta\cdot\left[\varepsilon_{\infty} - j\frac{\sigma_{\text{DC}}(T)}{3\omega\varepsilon_0(2n-\theta)}\right]\end{aligned} \tag{4.31}$$

where, V_{mol} is the molecular mass of water, R_{Gas} is the gas constant, h is Planck's constant, k_B is Boltzmann's constant, $\kappa \approx 1$ is the transmission coefficient, $\Delta G^{\ddagger}_{w}(T,\Psi_t)$ is the free enthalpy of activation or Gibbs energy, and Ψ_t is the total soil suction.

It can be seen in the model proposed by Hilhorst [48] that the complex permittivity of water $\Omega^{\star}_{1}$ is expressed as a function of soil suction, Ψ_t, which is dependent on the volumetric water content, θ.

The other approach is an extended equation based on the complex refractive index model (CRIM) [140, 201]:

$$\varepsilon^{\star 0.5}_{r,\text{eff}}(\omega,T,\theta) = \Omega^{\star}_{0.5}(\omega,T,\theta) + (1-n)\cdot\varepsilon^{0.5}_{r,G}(T) + (n-\theta)\cdot\varepsilon_{A}, \tag{4.32}$$

where, $\Omega^{\star}_{0.5}(\omega,T,\theta)$ describes the complex permittivity for free and bound water. $\Omega^{\star}_{0.5}(\omega,\theta,T)$ at a specific volumetric water content, θ, is calculated by the following general equation [19]:

$$\Omega^{\star}_{0.5}(\omega,T,\theta) = \int_{\Psi_t(0)}^{\Psi_t(\theta)} \varepsilon^{\star 0.5}_{\text{W}}(\omega,T,\Psi_t)\frac{d\theta(\Psi_t)}{d\Psi_t}d\Psi_t, \tag{4.33}$$

where, Ψ_t is the total suction and $\varepsilon^{\star 0.5}_{\text{W}}(\omega,T,\Psi_t)$ is the complex relative effective permittivity of interfacial water, which depends on frequency, ω, temperature, T and total suction, Ψ_t. The

frequency dependence of $\varepsilon^{\star}_{\mathrm{W}}(\omega, T, \Psi_t)$ as a function of the distance from the particle surface is modelled based on a modified Debye type relaxation function [172, 173, 189]:

$$\varepsilon^{\star}_{\mathrm{W}}(\omega, T, \Psi_t) - \varepsilon_{\infty}(T) = \frac{\Delta\varepsilon(T, \Psi_t)}{1 + j\omega\tau_w(T, \Psi_t)} - j\frac{\sigma_{\mathrm{DC}}(T, \Psi_t)}{\varepsilon_0\omega}, \tag{4.34}$$

where, the direct current conductivity, σ_{DC}, of pore water, relaxation strength, $\Delta\varepsilon$, and dielectric relaxation time of water, τ_w, are considered to be dependent on the total suction, Ψ_t. The temperature-pressure dependent dielectric relaxation time of water, τ_w, is calculated by Eyring's equation [173, 191, 213]:

$$\tau_w(T, \Psi_t) = \frac{h}{k_B T}\kappa \exp\left(\frac{\Delta G^{\ddagger}_w(T, \Psi_t)}{R_{Gas}T}\right), \tag{4.35}$$

where, R_{Gas} is the gas constant, h is Planck's constant, k_B is Boltzmann's constant, $\kappa \approx 1$ is the transmission coefficient, and $\Delta G^{\ddagger}_w(T, \Psi_t)$ is the free enthalpy or Gibbs energy [19, 140, 173, 191, 213], according to Equation 2.6. In addition to Equation (2.6), the explicit coupling of the soil suction, Ψ_t, and Gibbs energy, $\Delta G^{\ddagger}_w(T, \Psi_t)$, of dielectric relaxation, proposed by Hilhorst et al. [23], is used and extended by Wagner and Scheuermann [19] based on:

$$\Delta G^{\ddagger}_w(T, \Psi_t) = \Delta G^{\ddagger\circ}_w(T) - \Psi_t(T) \cdot V_{\mathrm{mol}}. \tag{4.36}$$

where, V_{mol} is the molar volume of water and $\Delta G^{\ddagger\circ}_w(T)$ is Gibbs energy of water at a reference state (10.4 kJ/mol at atmospheric conditions and T=293.15 K). To consider the dependence of the dielectric relaxation strength as a function of Ψ_t, the following relationship is used, according to [214] (see Wagner and Scheuermann [19] for details):

$$\Delta\varepsilon = \varepsilon_{\mathrm{S,W}}\left[1 + \left(\frac{\varepsilon_{\mathrm{S,W}}}{\varepsilon_{\mathrm{S,G}}} - 1\right)\exp\left(-\frac{2\theta}{A_s\rho_D\lambda}\right)\right]^{-1} - \varepsilon_{\infty} \tag{4.37}$$

where, $\varepsilon_{\mathrm{S,W}}$ is static free water permittivity, $\varepsilon_{\mathrm{S,G}}$ is static permittivity at the particle surface, θ is the volumetric water content, A_s is the total specific surface area, ρ_D is the dry density, and $\lambda = 10$ nm is chosen as the correlation length between pure water with 15 nm and a 10^{-3} M NaCl solution with 6.9 nm. The direct current conductivity, σ_{DC}, in the modified Debye model (Equation 4.7) is estimated by an empirical relationship, according to Wagner et al. [140]:

$$\sigma_{\mathrm{DC}} = \sigma_{w,U} \cdot \Psi'^{B}_t + \sigma_{w,S}, \tag{4.38}$$

where, $\sigma_{w,S}$ is the electrical conductivity at saturation, $\Psi'_t = \Psi_t/\Psi_t^{1MPa}$ is the normalised total suction, $\log(\sigma_{w,U}[S/m])$ is an empirical coupling parameter for electrical conductivity at unsaturated soil conditions, and B is a coupling exponent.

4.6 Conclusion

This chapter has demonstrated the principles of the EM characteristics of fine-grained soils starting from the EM theory over the constitutive equations which describe the material response when exposed to EM fields. The focus of this study is on one specific dielectric parameter, which is the relative effective complex permittivity, $\varepsilon^{\star}_{r,\mathrm{eff}}$, including the direct current conductivity contributions, σ_{DC}. This chapter has discussed the frequency dependence of $\varepsilon^{\star}_{r,\mathrm{eff}}$ and highlighted the relevant polarisation mechanisms in the frequency window under investigation. It has introduced different empirical relaxation models to approach $\varepsilon^{\star}_{r,\mathrm{eff}}$ as a function of frequency and illustrated the differences in these models.

This chapter has studied the dielectric parameters of the individual soil phases, and presented the available approaches to determine them. It has reviewed dielectric models to calculate the dielectric parameters of soils. It has extensively explained two theoretical mixture approaches in combination with phenomenological relaxation models that can potentially be used to consider the mechanical and hydraulic aspects of soils.

Since this chapter has focused on the EM characterisation of fine-grained soils, the following chapter targets the necessary instrumentation to enable dielectric measurements. EM methods are introduced, which are used in this study to measure the dielectric parameters of soils as a function of frequency f.

Chapter 5

EM measurement Techniques

5.1 Introduction

The choice of an appropriate instrumentation setup is essential for accurate measurement of dielectric soil parameters. Moreover, calibration of the instrumentation and an understanding of data processing are required to enable successful application of EM methods.

This chapter begins with a summary of measurement techniques relevant to the frequency window under investigation in the experimental study. Following this, this chapter introduces in detail the measurement technique preferred in this thesis – the broadband EM technique. It then explains the principle of a VNA and calibration of the network system. Further, it proposes two probes that differ in their measurement principle. The probes were selected based on the objectives of the experimental investigations. As the broadband EM technique is not a standard technique in geotechnical laboratory investigations, commercial probes specifically designed for standard tests, rarely exist. Hence, this chapter presents a novel low-cost in-house-manufactured probe, which is designed to be used in shrinkage tests.

This chapter evaluates the in-house-manufactured probe using numerical simulations to investigate the propagation characteristics of EM waves and the sensitive volume of the probe performance in order to define minimum sample height. The calibration procedure and data processing for both probes are determined and tested on different calibration materials. Finally, the used probes are compared against commercially available probes to test and evaluate the probe performance.

5.2 Measurement techniques

The literature presents a number of non-invasive geophysical EM methods that are able to measure the EM soil parameters and generally provide the potential to explore soils and retrieve physical and structural soil parameters [14, 215]. The relevant methods found in the literature [185, 216, 217, 218] and considered in this thesis are summarised graphically in Figure 5.1, where the grey shaded area indicates the frequency range covered in this study to investigate the dielectric soil properties.

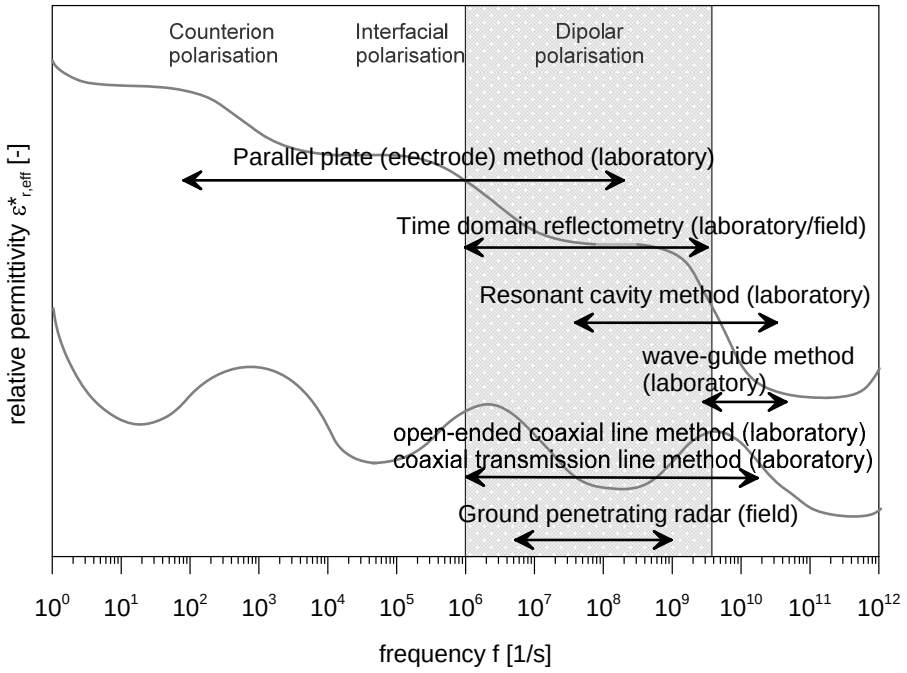

Figure 5.1: Schematic illustration of measurement techniques dependent on the applicable frequency. Grey shaded area indicates the aimed frequency window under investigation

The methods illustrated in Figure 5.1 differ in their test design, measurement approach and applicable frequency range. As can be seen, four methods actually cover the indicated frequency window under investigation: (i) ground penetration radar (GPR), (ii) TDR, (iii) open-ended coaxial line method and (iv) coaxial transmission line method. These four methods again differ in their measurement approach. In general, the EM material response can be measured as a function either of time (time domain) or frequency (frequency domain). Methods such as TDR or GPR are based on time domain measurements. The dielectric soil properties are normally determined based on the reflection travel time of a reflected wave due to a step voltage pulse or incident wave [216, 219]. The TDR measurement results can be analysed in the frequency domain using Fourier series transformation [216, 220]. For several practical reasons, time domain measurement methods are widely applied to investigate soils.

For example, GPR is already used in field applications to image and characterise ground subsurface [13, 144, 219, 221]. TDR is found in frequent applications in geo-environmental and geotechnical engineering for measuring soil water content and monitoring earth structures [21, 222, 223, 224]. In contrast to TDR and GPR, the open-ended coaxial line method and coaxial transmission line method measure the EM material response directly in the frequency domain via a VNA [216]. Thus, a Fourier series transformation into the frequency domain is not required. Further, the use of a VNA allows fast repetition measurements over a broad frequency range in order to average data and reduce easurement error [185, 216]. In this study, the open-ended coaxial line method and coaxial transmission line method, as broadband EM techniques, were selected for the experimental investigation. In the following sections, these methods are further explained, including the principle setup of the VNA and the introduction of two different probe types.

5.3 Broadband EM technique

5.3.1 HF network analyser

VNAs can generally be used to measure the dielectric response of materials, using appropriate measurement cells. Figure 5.2 shows a simplified schematic of a VNA with two ports and a material filled in a measurement cell (material under test – MUT). A VNA consists of a signal source, receiver and signal processor unit [225]. The VNA is connected via coaxial cables to probes that are used to probe the MUT. Under testing conditions, the signal source generates a mono-frequency EM wave, A_1, at Port 1. This incident wave, A_1, travels through a coaxial cable to the MUT. One part of the incident wave A_1 is reflected as signal B_1, and another part of the wave is transmitted as signal B_2 through the material. The receiver is tuned to the applied frequency of the wave, and measures the reflected signal, B_1, at Port 1 and transmitted signal, B_2, at Port 2 of the incident signal, A_1, from Port 1. The same equivalent scheme can be applied if the incident mono-frequency EM wave, at the same frequency with amplitude, A_2, is applied from Port 2. The incident wave A_2 entering the opposite end of the MUT, is partly reflected as signal B_2 at Port 2 and transmitted as signal B_1 to Port 1. Same again, the receiver measures the reflected signal B_2 and transmitted signal B_1. Once the measurement is finished, the source launches again waves from both ports, but stepping in another frequency, and the entire measurement procedure is repeated. The data measured by the receiver are analysed with the signal processor unit so that the appropriate frequency dependent complex scattering parameters $S_{i,j}$ can be exported for a further analysis. Hence, the frequency dependent EM response of the MUT in terms of the reflection and transmission

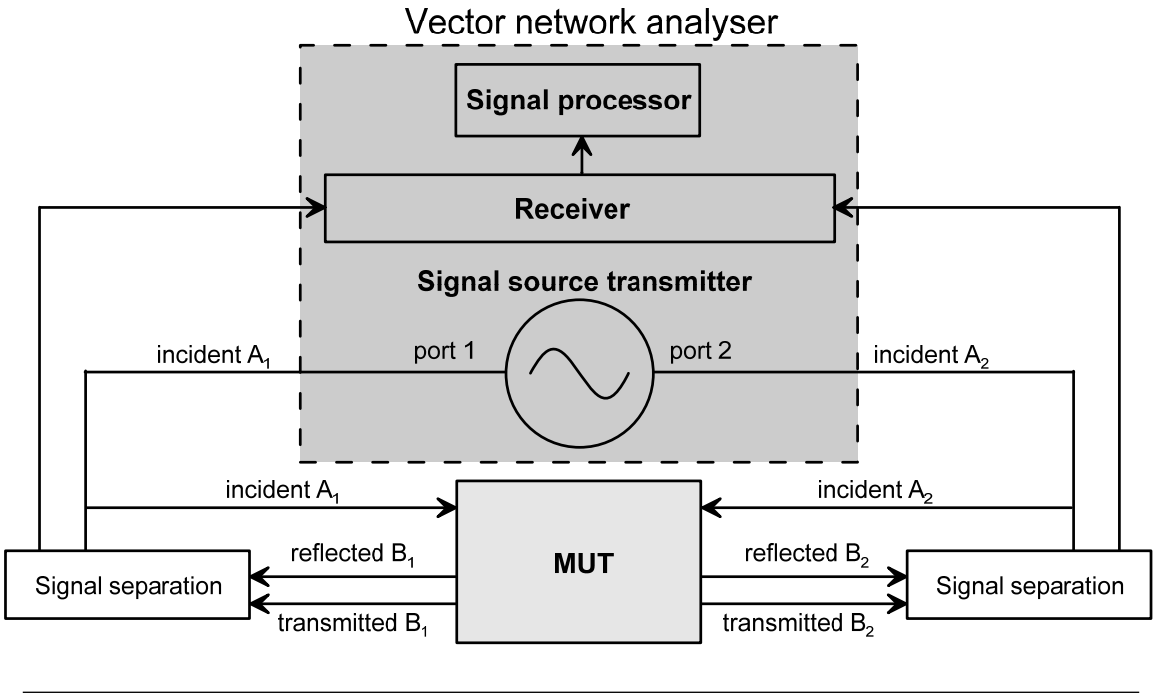

Figure 5.2: Schematic illustration of VNA, showing signal flow chart from measurement ports to MUT, adopted and modified from [225].

of the waves A_1 and A_2 can be written as a function of the frequency according to:

$$\begin{pmatrix} B_1(\omega) \\ B_2(\omega) \end{pmatrix} = \begin{pmatrix} S_{11}(\omega) & S_{12}(\omega) \\ S_{21}(\omega) & S_{22}(\omega) \end{pmatrix} \begin{pmatrix} A_1(\omega) \\ A_2(\omega) \end{pmatrix} \tag{5.1}$$

where, A_i is the signal source, B_i is the signal response, and $S_{\mathrm{i,j}}$ are the scattering S- parameters that give the ratio of the signal source to signal response. Herein, the subscripts i and j describe the port of the signal response and port of the signal source, respectively. For example, S_{12} gives the ratio of incident signal A_2 from Port 2 to the transmitted signal B_1 that was measured at Port 1. The S-parameters are complex numbers and describe the magnitude and phase shift of the EM response.

As the term 'network' indicates, several electronic components in the VNA build a network that finally enables the completion of EM measurements. All these electronic components must be attuned in a manner to minimise the systematic errors that are caused by imperfections in the single components forming the VNA. Systematic errors in the VNA falsify measurements and cause noise of the signal, unexpected signal reflections and signal leakage. However, the design of a VNA without any imperfections and systematic errors, is time consuming and leads to unjustifiably high costs [225]. As a result, a full 2-port calibration procedure is suggested and performed in order to eliminate the systematic errors inherent in the VNA.

Depending on the measurement type – whether 1 or 2 port are used – two different calibration

procedures are available that follow nearly the same principle. In the case of 1-port measurements, the VNA must be calibrated by three defined standard measurements – called one port calibration – with different properties:

1. **open**-standard measurement simulates an open-ended coaxial line that reflects the signal completely without any phase shift ($\delta = 0$)
2. **short**-standard measurement gives a total reflection of the signal, but the response has a phase shift ($\delta = 180°$) against the incident signal
3. **load**-standard measurement ends the coaxial line with defined impedance. The defined impedance is usually set to the system impedance which is 50Ω in most cases. A load standard measurement shows no signal reflections.

For a 2-port measurement, the calibration procedure also includes the above mentioned calibration standard measurements. However, because the open, short, and load standard calibrations are all reflection measurements, a full 2-port calibration requires an additional calibration measurement that simulates the transmission of a signal from one to the other port. Hence, an additional standard measurement is required:

4. **through** connects either port with a defined impedance and accounts for the transmission of a signal.

Once the calibration standards are measured, the VNA uses the measurement results to obtain the deviation from the theoretical definition of the standards that are implemented in the VNA software. This deviation is used to create an error model in order to eliminate these systematic errors for future measurements.

In order to measure the EM soil parameters, different types of probes or cells are available. These probes vary in their design, application purpose, performance and applicable frequency. For HF-EM measurement, the probe type and measurement technique can be categorised into the open-ended coaxial line (OE) technique (1-port), coaxial transmission line (CT) technique (2-port), as well as rod based transmission line technique (2-port) [226].

5.3.2 OE measurement technique

In this study, an in-house-made probe was manufactured based on the OE technique. The in-house-manufactured probe was based on a conventional coaxial line and modified N-type

connector, as shown in Figure 5.3. On top of the connector tip, a copper plate and sealed sample holder were assembled to allow the investigation of liquids and soft materials. As shown in Figure 5.3, the diameter of the copper plate (which served as the outer conductor of the coaxial line) was 70 mm. The diameters of the probe inner connector and dielectric were 3 mm and 5 mm, respectively. The most significant benefits of the in-house-made probe were the cost-effectiveness compared to commercial probes and the individual design with the sample holder, which enabled the investigation of liquids and soft materials. The

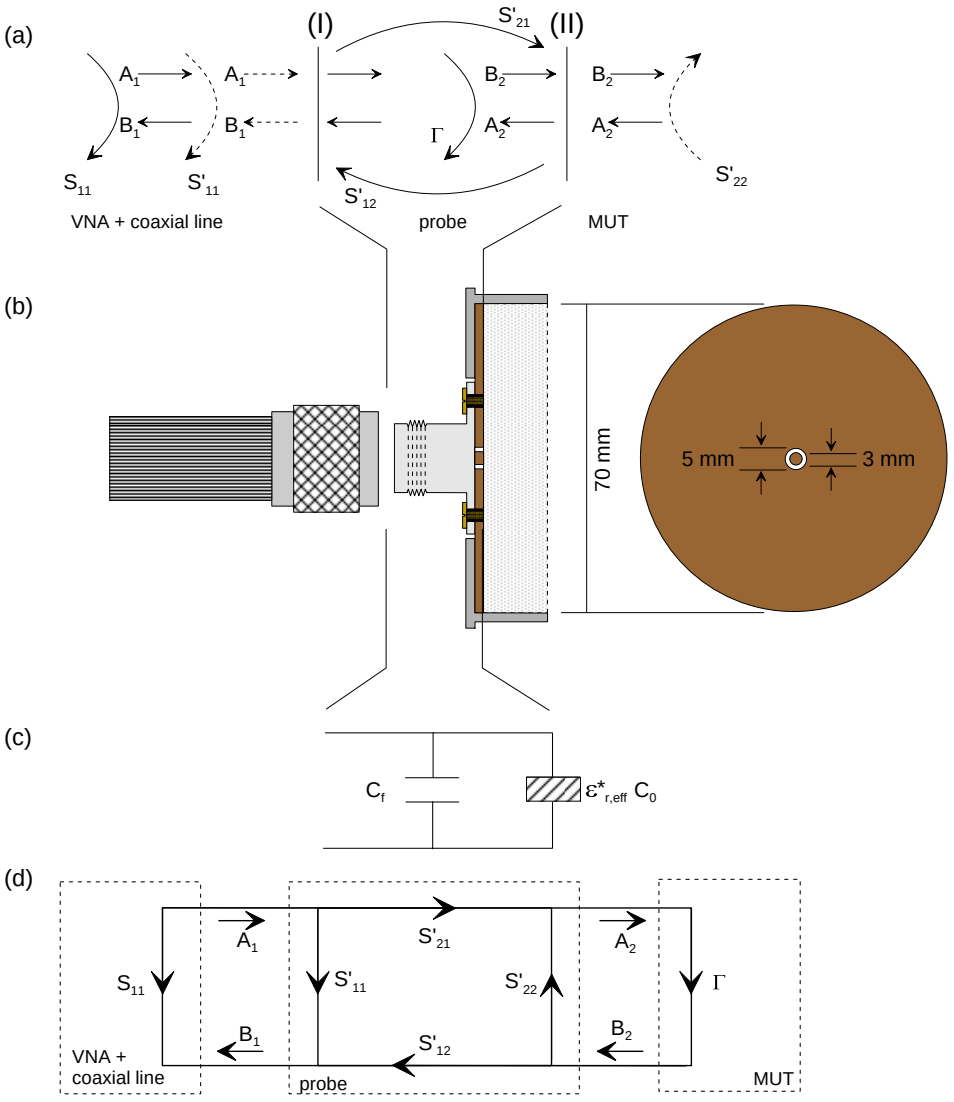

Figure 5.3: Schematic illustration of (a) measurement planes of an OE probe, (b) design of the in-house-made probe based on a modified N-type connector, (c) the probe's lumped-element equivalent circuit presentation, and (d) graph of signal flow, adopted and modified from [227].

relative effective complex permittivity, $\varepsilon^{\star}_{r,\mathrm{eff}}$, was calculated using vector network analysis in combination with a 1-port reflection, S_{11}, measurement based on the OE technique. The complex impedance of the sample at the interface between the OE probe and the sample

was theoretically determined based on the complex reflection coefficient [227]:

$$\Gamma = \frac{Z_0 - Z_S^\star}{Z_0 + Z_S^\star}. \tag{5.2}$$

where, Γ is the reflection coefficient, Z_0 is the real characteristic impedance of the probe ($Z_0 = 50\,\Omega$) and $Z_S^\star$ is the complex impedance of the sample under investigation.

However, the actual reflection coefficient, S_{11}, measured by the VNA was not identical to the reflection coefficient, Γ. As shown in Figure 5.3a and 5.3c, S_{11} was measured at the interface between the coaxial cable and OE probe. Therefore, S_{11} not only contained information about the MUT, but also about the probe itself. In addition, the characteristic impedance, Z_0, was mostly unknown. Thus, a two-step calibration procedure was required [11, 227] to eliminate imperfections and systematic errors in the network system [228]. By doing so, the measurement reference plane (I) was shifted from the end of the coaxial cable to the interface between the probe and MUT (II) in order to obtain the pure reflection coefficient, Γ, of the sample. In the first step, a mechanical calibration kit (Agilent 85032F) was used to remove errors from the VNA and coaxial cable. In the second step, an additional probe calibration was performed to remove errors from the probe. According to the signal flow graph in Figure 5.3, the scattering parameters of the OE probe can be written to:

$$\begin{pmatrix} B_1 \\ B_2 \end{pmatrix} = \begin{pmatrix} S'_{11} & S'_{12} \\ S'_{21} & S'_{22} \end{pmatrix} \begin{pmatrix} A_1 \\ A_2 \end{pmatrix} \tag{5.3}$$

By substituting $S_{11} = \frac{B_1}{A_1}$ and $\Gamma = \frac{A_2}{B_2}$ in Equation 5.3, the complex reflection coefficient, Γ, can be formulated as follows [227]:

$$\Gamma = \frac{S_{11} - S'_{11}}{S'_{22} S_{11} - \det \mathbf{S}'} \tag{5.4}$$

Further, Figure 5.3(c) presents the appropriate lumped-element equivalent circuit of an OE probe, which can be approximated by two parallel capacitors [172, 227, 229, 230]. Hence, the impedance of the interface between probe aperture and MUT can be modelled according to:

$$Z^\star = (j\omega \cdot C_f + j\omega \cdot \varepsilon^\star_{r,\text{eff}} \cdot C_0)^{-1} \tag{5.5}$$

where, ω is the angular frequency, $j = \sqrt{1}$ is the imaginary unit, C_f is the capacitance dependent on the fringing fields effect inside the probe, C_0 is the capacitance dependent on the fringing fields effects outside between the probe tip and sample, and $\varepsilon^\star_{r,\text{eff}}$ is the relative effective complex permittivity of the MUT. Based on Equations 5.2, 5.4 and 5.5, a bilinear relationship between S_{11}, measured by the VNA, and $\varepsilon^\star_{r,\text{eff}}$ of the MUT was derived by Marsland

and Evans [231] and Bao et al. [232]:

$$\varepsilon^{\star}_{r,\text{eff}} = \frac{c_1 \cdot S_{11} - c_2}{c_3 - S_{11}}. \tag{5.6}$$

where, S_{11} is the measured reflection coefficient with the VNA, and c_i are complex calibration constants according to:

$$c_1 = \frac{1 - S'_{22}}{j\omega Z_0 C_0 (1 + S'_{22})} + \frac{C_f}{C_0}, \tag{5.7a}$$

$$c_2 = \frac{S'_{11} - S'_{11}S'_{22} + S'_{12}S'_{21}}{j\omega Z_0 C_0 (1 + S'_{22})} + \frac{C_f (S'_{11} + S'_{11}S'_{22} - S'_{12}S'_{21})}{C_0 (1 + S'_{22})}, \tag{5.7b}$$

$$c_3 = \frac{S'_{11} + S'_{11}S'_{22} - S'_{12}S'_{21}}{1 + S'_{22}}. \tag{5.7c}$$

where, ω is the angular frequency, $j = \sqrt{1}$ is the imaginary unit, C_0 is the capacitance dependent on the fringing fields effects outside between the probe tip and sample, C_f is the capacitance dependent on the fringing fields effect inside the probe, and S'_{ij} are scattering parameters according to the signal flow graph presented in Figure 5.3(a).

As a consequence, the calibration procedure was based on the bilinear relationship in Equation 5.6, which was used to calculate the $\varepsilon^{\star}_{r,\text{eff}}$ of the MUT based on the measured S_{11}-parameter and different calibration measurements [173, 227, 232, 233, 234]. The complex calibration constants, c_i, must be determined by at least three calibration measurements with known $\varepsilon^{\star}_{r,\text{eff}}(\omega)$.

The **open-water-short (OWS)** calibration uses an air, short circuited, and deionised water measurement. For the short measurement, $\Gamma = -1$ and $S_{11} = S^S_{11}$ can be substituted into Equation 5.7c to give [227, 232]:

$$c_3 = S^S_{11} \tag{5.8}$$

By replacing $\varepsilon_{r,O} = 1$ and $S_{11} = S^O_{11}$ for the open measurement and $\varepsilon^{\star}_{r,\text{eff}} = \varepsilon^{\star}_{r,W}$ and $S_{11} = S^W_{11}$ for the deionised water measurement in Equation 5.6, the following two expressions can be derived [227, 232]:

$$S^O_{11} c_1 - c_2 - c_3 = -S^O_{11} \tag{5.9}$$

$$S^W_{11} c_1 - c_2 - \varepsilon^{\star}_{r,W} c_3 = -\varepsilon^{\star}_{r,W} S^W_{11} \tag{5.10}$$

By solving Equations 5.8, 5.9 and 5.10 and obtaining the c_1, c_2 and c_3 parameters, the unknown $\varepsilon^{\star}_{r,\text{eff}}$ in Equation 5.6 can be found from its measured S_{11}-parameter at each frequency. However, the OWS is found to have limitations for the frequency range higher than 500 MHz [227]. These limitations are caused by the inaccuracy of the short measurement at HF, which shows an unstable signal response. To overcome this HF limitation of the OWS calibration,

the **open-water-liquid (OWL)** calibration is proposed [227], which uses an additional electrical lossless liquid calibration instead of the short calibration. Substituting $\varepsilon^{\star}_{r,L}$ and S^{L}_{11} for this additional liquid calibration in Equation 5.6 leads to:

$$S^{L}_{11}c_1 - c_2 - \varepsilon^{\star}_{r,L}c_3 = -\varepsilon^{\star}_{r,L}S^{L}_{11} \tag{5.11}$$

Then, the OWL calibration with the obtained Equations 5.9, 5.10 and 5.11 can be formulated in matrix form, as follows:

$$\mathbf{M}\cdot\mathbf{c} = \mathbf{e}. \tag{5.12}$$

where, the complex calibration constants $\mathbf{c} = \mathbf{M}^{-1}\cdot\mathbf{e}$ are found numerically. Once the complex calibration constants are determined, the $\varepsilon^{\star}_{r,\text{eff}}$ of the MUT is calculated from the measured complex reflection coefficient, S_{11}, using Equation 5.6. In general, the OWL calibration performs more accurate results in the HF range due to the more stable and accurate dielectric response of the additional calibration liquid. Despite better calibration performance at HF, the OWL normally fails for electrical lossy materials at low-frequency measurements ($<$50 MHz) because only lossless calibration standards are applied. In order to obtain stable measurement results over the entire frequency range, a combined OWS and OWL calibration procedure is suggested, at which OWS covers the low-frequency range ($<$500 MHz) and OWL the HF range ($>$500 MHz) [227].

5.3.3 CT measurement techniques

The CT measurement technique is based on 2-port coaxial reflection and transmission measurement giving the full set of S_{ij}-parameters. Figure 5.4 shows a schematic illustration of the CT measurement setup used in this study.

A CT cell consists of an inner and outer conductor, which are made of highly conducting material. As shown in Figure 5.4A, both conductors of the CT cell have a length of 50 mm. The MUT is placed between the inner and outer conductor. The inner diameter of the outer conductor is 38.8 mm, and the outer diameter of the inner conductor is 16.9 mm, which results in a sensitive investigation volume of $47.6\,\text{cm}^3$. One side of the inner and outer conductor is edged to create a sharp end that allows the cell to be cut into soil. With this designed feature, the major advantage of the CT cell is its possibility to core a soil sample in situ or in laboratory experiments [235]. Figure 5.4B schematically presents how the CT cell is assembled between two flange connectors, which are defined adapter units connecting the CT cell via coaxial cable to the VNA. After calibration of the VNA and coaxial cable, the measurement reference plane is set on Position 1 between the end of the coaxial cables

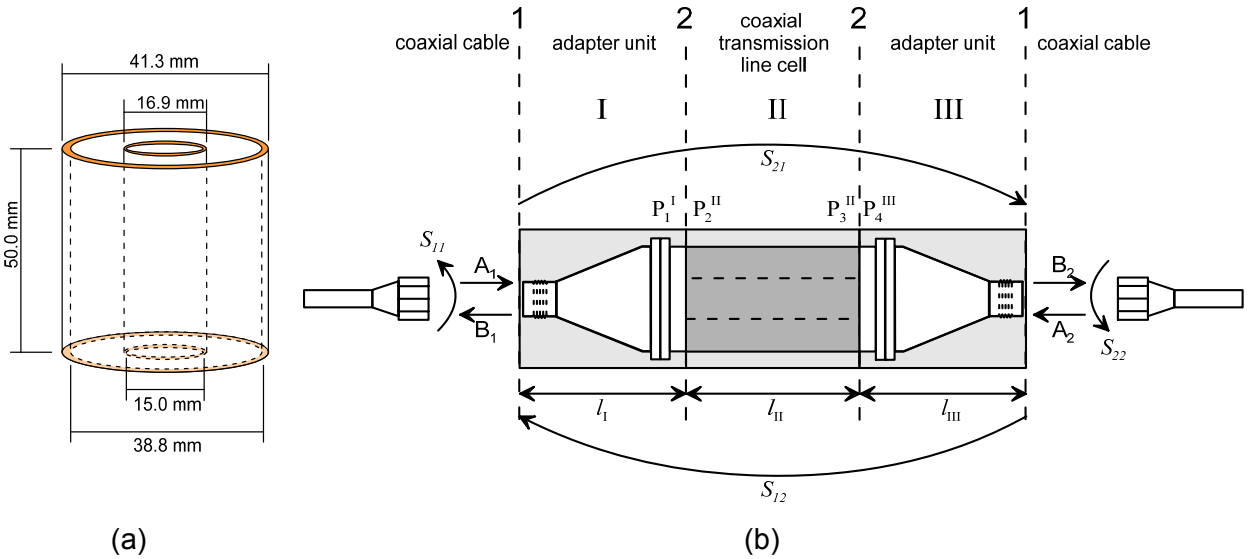

Figure 5.4: (A) Dimension of the CT cell and (B) schematic illustration of a CT setup, including the signal flow of S_{ij} and incident A_i and reflected B_i from either ports ($i = 1,2$). A, B, and C represent the propagation matrices with length l_A, l_B, and l_C and calibration reference plane 1 and 2.

and flange connectors. Hence, the measurement setup can be divided into three sections, where Sections A and C are the flange connectors, and Section B is the CT cell with the MUT. Further, Figure 5.4B shows the signal flow of the scattering parameters, S_{ij}. It can be seen that the signal reflection of the incident waves (A_1 and A_2) occurs at the reference Plane 1, with S_{11} and S_{22}, whereas the transmitted signal crosses the entire three sections from A to C.

Generally, in the case of transverse EM mode propagation in non-magnetic materials, the $\varepsilon^\star_{r,\text{eff}}$ can be described by the following set of equations [140, 215, 226, 236, 237]:

$$\varepsilon^\star_{r,\text{eff}} = \left(\frac{Z_0}{Z^\star_S}\right)^2, \tag{5.13}$$

$$\varepsilon^\star_{r,\text{eff}} = \left(\frac{c_0 \gamma^\star_S}{j\omega}\right)^2, \tag{5.14}$$

$$\varepsilon^\star_{r,\text{eff}} = \frac{c_0 Z_0}{j\omega}\left(\frac{\gamma^\star_S}{Z^\star_S}\right). \tag{5.15}$$

where, $c_0 = (\varepsilon_0 \mu^\star_0)^{-0.5}$ is the light velocity, Z_0 is the characteristic impedance of the empty CT cell, $Z^\star_S$ is the complex impedance of the sample, and $\gamma^\star_S$ is the complex propagation factor. In order to calculate $Z^\star_S$ and $\gamma^\star_S$ based on the measured values of S_{ij}, quasi-analytical approaches and an iterative technique are applicable [215], which are:

- the Nicolson-Ross-Weir (NRW) algorithm [237, 238]

- the modified NRW algorithm (BJ) [239, 240]
- the propagation matrix (PM) method [236, 241, 242]
- the iterative method (BJI) [180, 243].

In the **NRW** algorithm, the scattering parameters are expressed according to the following set of equations:

$$s_{1,j}^{NR} = \left(S_{ij}e^{(l_A+l_C)} + S_{jj}e^{2l_j}\right)e^{\frac{j\omega}{c_0}}, \tag{5.16}$$

$$s_{2,j}^{NR} = \left(S_{ij}e^{(l_A+l_C)} - S_{jj}e^{2l_j}\right)e^{\frac{j\omega}{c_0}}, \tag{5.17}$$

$$g_j = \frac{1 - s_{1,j}^{NR}s_{2,j}^{NR}}{s_{1,j}^{NR} - s_{2,j}^{NR}}. \tag{5.18}$$

where, $i \neq j$ and $i, j = \{1,2\}$. The reflection coefficient, Γ_j, and the transmission coefficient, Υ_j, are subsequently determined as follows:

$$\Gamma_j = g_j \pm \sqrt{g_j^2 - 1}, \tag{5.19}$$

$$\Upsilon_j = \frac{s_{1,j}^{NR} - \Gamma_j}{1 - s_{1,j}^{NR}\Gamma_j}. \tag{5.20}$$

The NRW algorithm was modified by Baker-Jarvis [240], and the modified algorithm **BJ** was subsequently proposed, which is based on the following description of scattering parameters:

$$s_1^{BJ} = (S_{21}S_{12} - S_{11}S_{22})e^{\left[2\frac{j\omega}{c_0}(l-l_B)\right]}, \tag{5.21}$$

$$s_2^{BJ} = \frac{S_{21} + S_{12}}{2}e^{\left[\frac{j\omega}{c_0}(l-l_B)\right]}. \tag{5.22}$$

where, l is the total length between the reference calibration Planes 1 and 2 of the two measurement ports, with $l = l_A + l_B + l_C$, as shown in Figure 5.4B. In this algorithm, Γ and Υ are given as follows:

$$\Gamma = \pm\sqrt{\frac{s_1^{BJ} - \Upsilon^2}{s_1^{BJ}\Upsilon^2 - 1}}, \tag{5.23}$$

$$\Upsilon = \frac{s_1^{BJ} + 1}{2s_2^{BJ}} \pm \sqrt{\left(\frac{s_1^{BJ} + 1}{2s_2^{BJ}}\right)^2 - 1}. \tag{5.24}$$

In order to solve one of the appropriate Equations 5.13, 5.14 and 5.15, the complex impedance $Z_S^\star$ and complex propagation factor $\gamma_S^\star$ of the MUT are calculated, both in the NRW and BJ algorithm, by the following relationships:

$$\gamma_S^\star = -\frac{\ln(\Upsilon)}{l}, \tag{5.25}$$

$$Z_S^\star = Z_0 \left(\frac{\Gamma + 1}{1 - \Gamma} \right). \tag{5.26}$$

A further quasi-analytical approach is the PM method, which is based on the propagation matrix $\mathbf{A}$, $\mathbf{B}$ and $\mathbf{C}$. As shown in Figure 5.4B, $\mathbf{A}$ and $\mathbf{C}$ (with $\hat{\mathbf{A}} = \mathbf{C}$, $\hat{\mathbf{C}} = \mathbf{A}$; [236, 244]) refer to the sections between reference Planes 1 and 2, which include the adapter units. The matrix $\mathbf{B}$ ($\hat{\mathbf{B}} = \mathbf{B}$, [236, 244]) describes the section with the MUT between reference Planes 2-2. The appropriate formulation of the propagation matrices is given by two equations:

$$\begin{bmatrix} 1 \\ S_{11} \end{bmatrix} = \mathbf{ABC} \begin{bmatrix} S_{21} \\ 0 \end{bmatrix}, \tag{5.27}$$

$$\begin{bmatrix} 1 \\ S_{22} \end{bmatrix} = \hat{\mathbf{A}}\hat{\mathbf{B}}\hat{\mathbf{C}} \begin{bmatrix} S_{12} \\ 0 \end{bmatrix}. \tag{5.28}$$

where, $\mathbf{A}$ and $\mathbf{C}$ own identical propagation properties in the numerically implemented structure. In the case of $\mathbf{B}$, the MUT is assumed to be isotropic and homogeneous. The PM algorithm determines the $Z_S^\star$ and $\gamma_S^\star$ of the MUT from measured $S_{i,j}$-parameters, which are subsequently shown in the case of S_{11} and S_{21}. The propagation matrices are developed as follows:

$$\mathbf{A} = (\mathbf{P}_1^A)^{-1} \left[\prod_{k=2}^{k=p-1} \mathbf{P}_k^C (\mathbf{P}_k^A)^{-1} \right], \tag{5.29}$$

$$\mathbf{B} = \mathbf{P}_B^C (\mathbf{P}_B^A)^{-1}, \tag{5.30}$$

$$\mathbf{C} = \left[\prod_{k=p+1}^{k=N-1} (\mathbf{P}_k^A)^{-1} \mathbf{P}_k^C \right] \mathbf{P}_N^C. \tag{5.31}$$

with the section interface from k to $k+1$ and the matrices $\mathbf{P}_k^A$ and $\mathbf{P}_k^C$ (see Figure 5.4B) according to:

$$\mathbf{P}_k^A = \begin{bmatrix} \exp(-\gamma_k^\star l_k) & 1 \\ \frac{1}{Z_k} \exp(-\gamma_k^\star l_k) & -\frac{1}{Z_k^\star} \end{bmatrix}, \mathbf{P}_k^C = \begin{bmatrix} 1 & \exp(-\gamma_k^\star l_k) \\ \frac{1}{Z_k^\star} & -\frac{1}{Z_k^\star} \exp(-\gamma_k^\star l_k) \end{bmatrix}. \tag{5.32}$$

where, $\gamma_k^\star$ is the complex propagation factor and $Z_k^\star$ is the complex impedance of the k-th section. The dielectric spectrum of the material is found in matrix $\mathbf{B}$, which can be rewritten using Equations 5.30 and 5.32 to:

$$\mathbf{B} = \frac{1}{2} \begin{bmatrix} e^{\gamma_p^\star l_p} + e^{-\gamma_p^\star l_p} & Z_p^\star \left[e^{\gamma_p^\star l_p} - e^{-\gamma_p^\star l_p} \right] \\ \frac{1}{Z_p^\star} \left[e^{\gamma_p^\star l_p} - e^{-\gamma_p^\star l_p} \right] & e^{\gamma_p^\star l_p} + e^{-\gamma_p^\star l_p} \end{bmatrix}. \tag{5.33}$$

Then, Equation 5.27 with S_{11} and S_{21} can be rewritten as follows:

$$\begin{bmatrix} a \\ b \end{bmatrix} = \mathbf{B} \begin{bmatrix} c \\ d \end{bmatrix}, \quad \begin{bmatrix} a \\ b \end{bmatrix} = \mathbf{A}^{-1} \begin{bmatrix} 1 \\ S_{11} \end{bmatrix}, \quad \begin{bmatrix} c \\ d \end{bmatrix} = \mathbf{C} \begin{bmatrix} S_{21} \\ 0 \end{bmatrix}. \tag{5.34}$$

Substituting $\mathbf{B}$ from Equation 5.33 into Equation 5.34 and eliminating the exponential terms, the $Z_S^\star$ of the sample results in:

$$Z_S^\star = \pm\sqrt{\frac{a^2-c^2}{b^2-d^2}}. \tag{5.35}$$

After eliminating the impedance expression, $\gamma_S^\star$ is found to be:

$$\gamma_S^\star = \pm a\cosh\left(\frac{ab+cd}{ad+bc}\right) l^{-1}. \tag{5.36}$$

All three quasi-analytical approaches are expressed in a general manner to allow the explicit determination of $Z_S^\star$ and $\gamma_S^\star$ based on the measured S_{ij}-parameters. Subsequently, it is possible to determine $\varepsilon_{r,\text{eff}}^\star$ based on one of the appropriate Equations 5.13 to 5.15.

The iterative method BJI uses the Levenberg-Marquardt algorithm [245, 246] to calculate $\varepsilon_{r,\text{eff}}^\star$ iteratively by finding the minimum difference, D, between the measured and numerical calculated scattering parameters [180, 243]:

$$D = \frac{W_2 f_1 + (1-W_2) f_2}{2}. \tag{5.37}$$

where, f_1 and f_2 are defined as:

$$f_1 = S_{11}S_{22} - S_{21}S_{12} - \frac{\Gamma^2-\Upsilon^2}{1-\Upsilon^2\Gamma^2}, \tag{5.38}$$

$$\begin{aligned} f_2 = &\frac{W_1(S_{21}+S_{12})+(1-W_1)(S_{11}+S_{22})}{2} \\ &- \frac{W_1\Upsilon(1-\Gamma^2)+(1-W_1)\Gamma(1-\Upsilon^2)}{1-\Gamma^2\Upsilon^2}. \end{aligned} \tag{5.39}$$

where, S_{ij} are measured scattering parameters, W_i are weighing factors with $0 \leq W_i \leq 1$, Γ is the ideal reflection factor and Υ is the ideal transmission factor. For a given sample length of l_B, Γ and Υ are defined according to Equations 5.25 and 5.26, with $Z_S^\star$ and $\gamma_S^\star$ given by Equation 5.13 and 5.14, respectively. However, in an initial step, the PM method in combination with Equation 5.15 is used to obtain an appropriate starting guess for the iterative computation. The calculation of the starting guess for the iteration process is modified after 1000 frequencies ($\approx$ 630 MHz), and the initial value for the iteration is then determined by the median of the previously calculated 100 results.

5.4 Numerical simulations of probes

5.4.1 OE probe

In order to understand the propagation characteristics of HF-EM waves, numerical simulations of the in-house-made OE probe on different MUT were conducted using High Frequency Structure Simulator (Ansoft HFSS). The numerically determined propagation characteristics of HF-EM waves in different MUT are necessary to know and understand the sensitive volume of the probe and the overall performance.

HFSS solves Maxwell's Equations 4.1 via a finite element method to determine the propagation of HF-EM waves in the MUT [137, 247]. Several electrically low-loss and high-loss dispersive materials with EM material properties were chosen to perform numerical simulations. The 3-D finite element structure of the OE probe was adopted from Wagner et al. [227]. Figure 5.5 shows the 3-D finite element structure of the OE probe implemented in the HFSS. The OE probe was designed exactly with the dimensions shown in Figure 5.3,

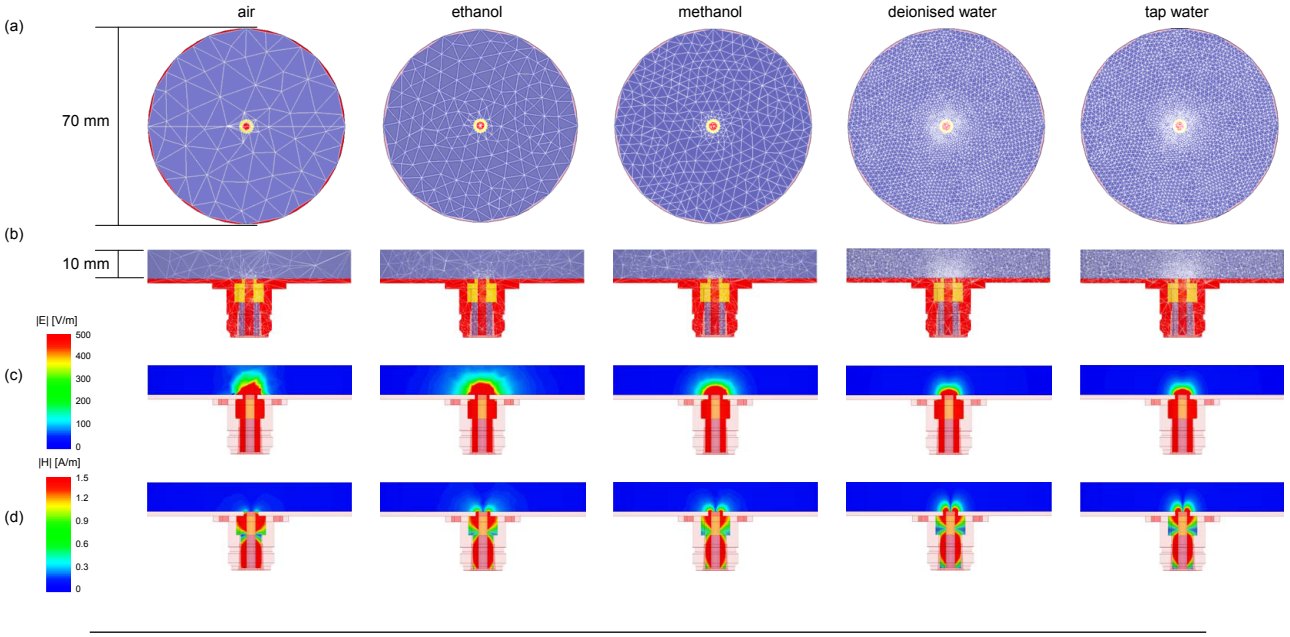

Figure 5.5: Numerical simulation of the OE probe for air, ethanol, methanol, deionised water, and tap water: (a) top view and (b) cross-sectional view on the 3-D finite element structure and tetrahedral mesh of the OE probe at 10 GHz, and cross-sectional view on the magnitude of the (c) electrical and (d) magnetic field distribution at 1 GHz.

with a 70 mm diameter of the outer conductor, 5 mm outer diameter of the dielectric and 3 mm diameter of the inner conductor. The height of the MUT was set to 10 mm. The simulated 3-D finite element structure was meshed by tetrahedral elements, as shown in Figure 5.5a and 5.5b. The mesh was generated automatically using 1/3 wavelength-based adaptive

mesh refinement at a solution frequency of 10 GHz [227]. Tangential vector basis functions interpolated field values from both nodal values at the vertices and edges. The outer surface of the MUT determined the boundary condition of the simulation domain [227]. The numerical simulations were run for air, ethanol, methanol, deionised water and tap water, with theoretically calculated input data obtained from [227]. Figure 5.5c and 5.5d present the propagation characteristics of the magnitude of the electrical and magnetic field distributions in a cross-sectional view. The electrical field distribution showed stable results, where the wave propagation or influencing zone was located in the simulated domain ($<$10 mm) without exceeding the height of the MUT. Further, the electrical field distributions of all MUTs were consistent in magnitude, indicating that the distribution was less dependent for these EM material properties. In contrast, the magnetic field distribution of the MUT showed a different trend, without consistent results. A negligibly low magnetic field distribution was observed for the simulation on air, whereas, for high-loss materials, such as tap water, a larger magnetic field distribution and higher radiation effect were noted. Based on the results of the numerical simulation, it was determined that the sensitive region of the electrical and magnetic field distribution was within 7 mm in height from the probe aperture and $\pm$10 mm in the lateral direction. Hence, the influence of the boundary layer can be neglected for a distance of 10 mm. Further, a minimum sample height of 10 mm was suggested for dielectric measurements on materials to ensure an electrical and magnetic field distribution in the MUT.

5.4.2 CT cell

In Section 5.3.3, three quasi-analytical approaches and an iterative method were introduced to calculate $\varepsilon^{\star}_{r,\text{eff}}$ based on 2-port CT measurements. Numerical simulations on CT cells filled with tap water were performed to evaluate and compare these three quasi-analytical approaches – namely NRW, BJ, PM – and the iterative method, BJI. The objective was to find the most accurate and appropriate method to calculate $\varepsilon^{\star}_{r,\text{eff}}$ based on 2-port measurements on a CT cell. Numerical simulations were conducted in the same order as with the OE probe, explained in Section 5.4.1, using HFSS. The dimension for the 3-D finite element structure of the CT cell was chosen according to Figure 5.4a, with a 50 mm cell length, 38.8 mm inner diameter of the outer conductor, and 16.9 mm outer diameter of the inner conductor. The structure was built and implemented with different excitation fields and boundary conditions. The mesh generation was performed automatically with 1/3 wavelength-based adaptive mesh refinement at a solution frequency of 10 GHz Wagner et al. [227]. The input spectra used for the numerical simulations on tap water were taken from the experimental results obtained in Wagner et al. [227]. The scattering S_{ij}=parameters were simulated in a

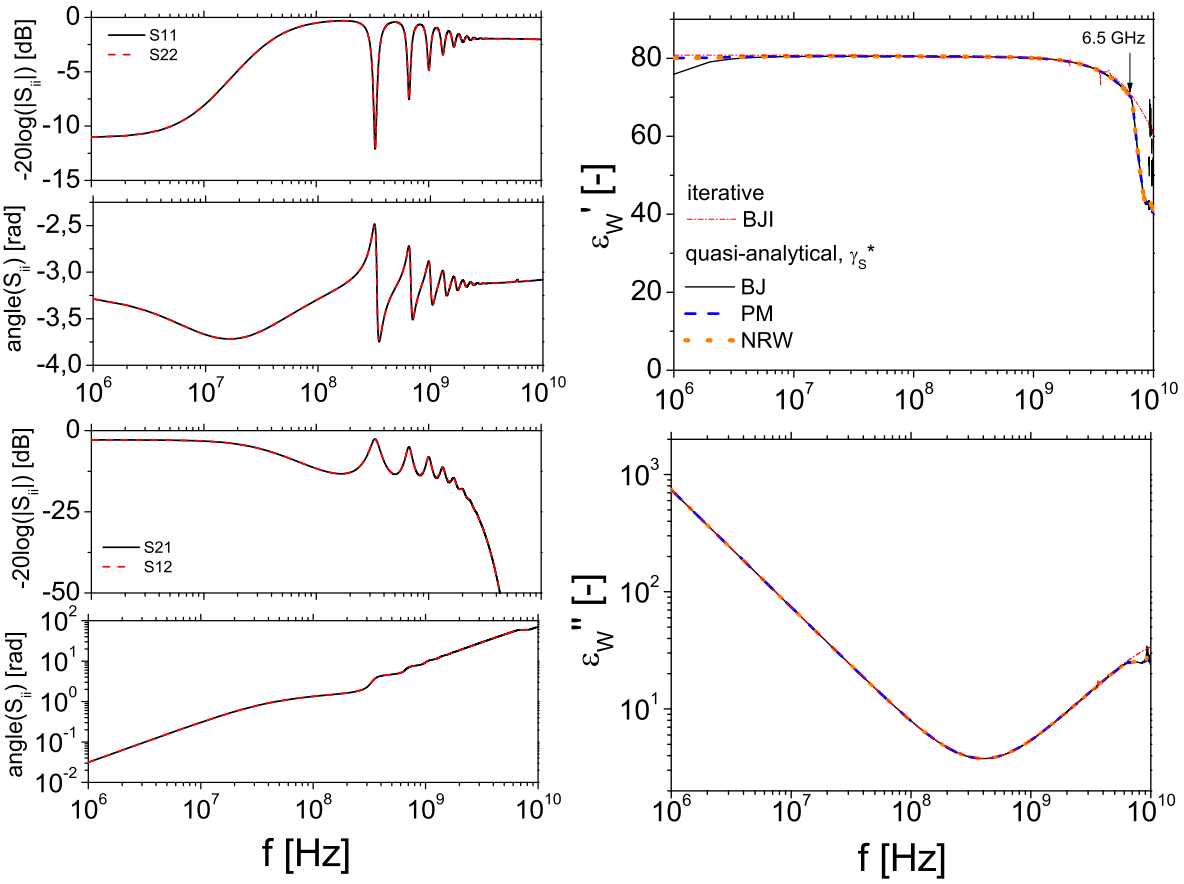

Figure 5.6: (left) Numerical determined full S-parameter set S_{ij} for tap water and (right) appropriate dielectric spectra obtained with the quasi-analytical approaches and iterative method based on the NRW, BJ, PM and BJI methods.

frequency range from 1 MHz to 10 GHz, including direct current conductivity extrapolation, as shown in Figure 5.6(left).

Based on the numerically calculated S_{ij} parameters, the real and imaginary parts of $\varepsilon^{\star}_{r,\mathrm{eff}}$ of tap water were computed with the three quasi-analytical approaches and the iterative method. Figure 5.6(right) shows a comparison of the results obtained by numerical simulations, where the real $\varepsilon'_{r,\mathrm{eff}}$ and imaginary part $\varepsilon''_{r,\mathrm{eff}}$ of $\varepsilon^{\star}_{r,\mathrm{eff}}$ are plotted. It can be seen that all methods gave nearly identical results in frequency range between 30 MHz to 6.5 GHz. While PM, NRW, and BJI still showed consistent results, the $\varepsilon^{\star}_{r,\mathrm{eff}}$ of the BJ method deviated from the other methods below 30 MHz. This indicated that the BJ approach failed for dielectric lossy materials, such as tap water, at frequencies lower than 30 MHz. In contrast, all three analytical approaches demonstrated an unexpected remarkable drop of $\varepsilon'_{r,\mathrm{eff}}$ and $\varepsilon''_{r,\mathrm{eff}}$ in the HF range from 6.5 GHz to 10 GHz. At the same time, BJI still showed stable results in this HF range. Therefore, it can be concluded that the BJI gave reasonable and stable results over the complete frequency range investigated in this study.

5.5 Preliminary experimental investigation

5.5.1 Calibration of OE probe

The OE probe needed to be calibrated by at least three different independent calibration standards in order to ensure accurate measurements. This calibration procedure had to be evaluated to ensure an accurate and successful calculation $\varepsilon^{\star}_{r,\text{eff}}$ of the MUT. To do so, two different calibration procedures were introduced in Section 5.3.2 [227]: (i) **OWS** and (ii) **OWL** calibration. In this thesis, six different standard calibration materials were tested:

1. air
2. short
3. ethanol
4. methanol
5. deionised water
6. tap water

Figure 5.7 illustrates an example of the calibration procedure performed in the case of the commercial Agilent P probe (see probe specification in Table 5.1 in upcoming Section 5.5.2). These six different calibration standards were tested and the absolute value and phase shift of the measured S_{11}-parameter were recorded over a frequency range from 10 MHz to 40 GHz. Subsequently, the dielectric spectra, $\varepsilon'_{r,\text{eff}}$ and $\varepsilon''_{r,\text{eff}}$, of the liquids were calculated based on the OWL calibration procedure. In addition to the measured dielectric spectra, the theoretically expected $\varepsilon^{\star}_{r,\text{eff}}$ for deionised water, ethanol and methanol [172] were plotted. The results showed that the measured dielectric spectrum of the deionised water, ethanol and methanol were characterised by stable and smooth curves, which agreed with the expected values in a frequency from 50 MHz to 40 GHz. Below 50 MHz, unstable measurement results were observed that deviated from the theoretically expected dielectric spectra. On the one hand, the deviation is caused by conductivity effects in the imaginary part. On the other hand, it can be seen in Figure 5.7 that the absolute values of the S_{11}-parameter show nearly identical measurement results below 50 MHz for all calibration reference materials which causes uncertainties in the determination of the complex permittivity. To minimise these uncertainties, a device such as the Agilent E5061B ENA VNA (coupled impedance analyser and VNA) is required with higher precision and better performance in the low frequency range. In order to obtain stable measurement results over the entire frequency range, a combined OWS and

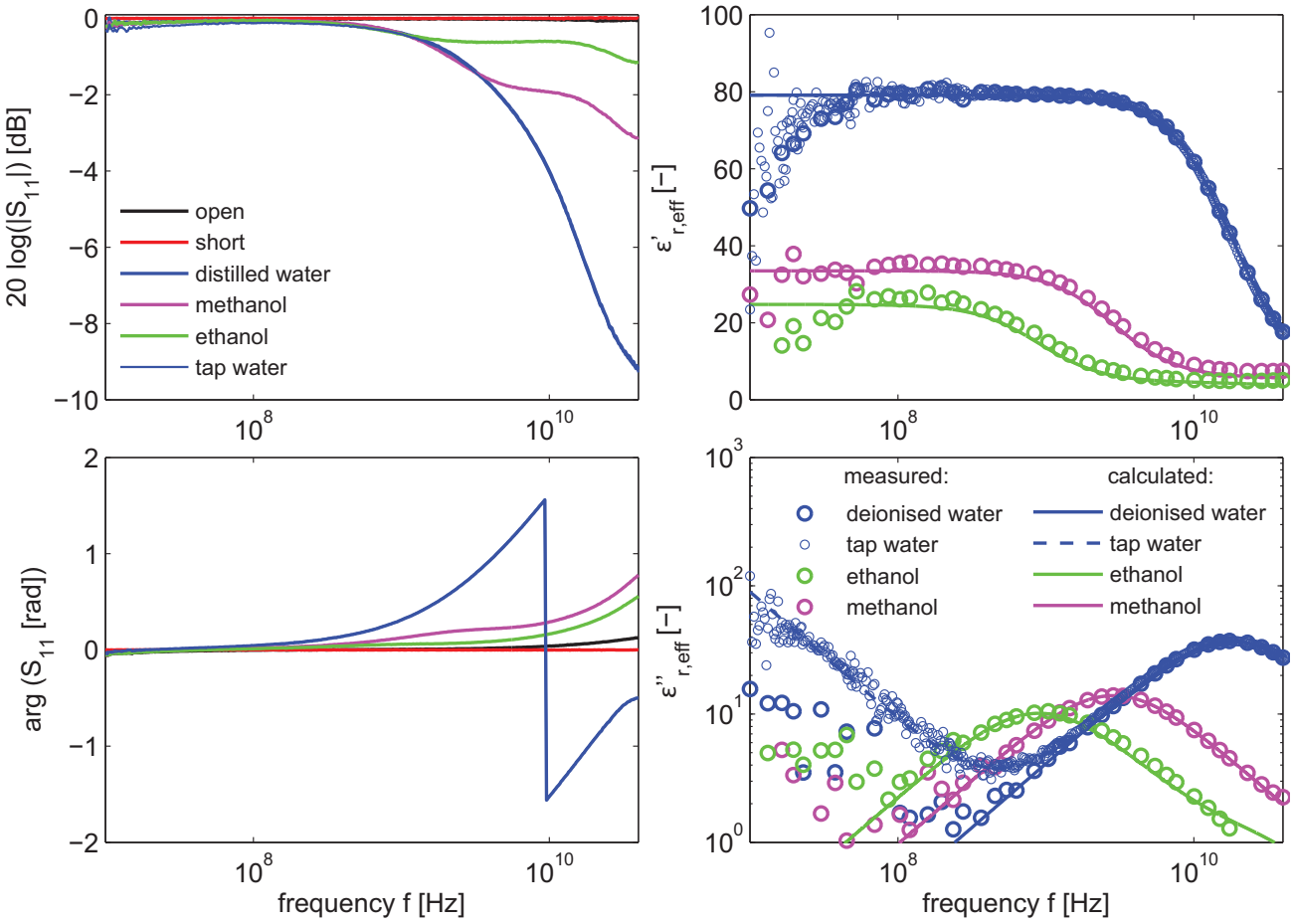

Figure 5.7: (left) Absolute value and phase shift of measured S_{11}-parameter, and (right) comparison of measured and theoretical expected dielectric spectrum with real, $\varepsilon'_{r,\text{eff}}$, and imaginary, $\varepsilon''_{r,\text{eff}}$, parts of calibration reference materials.

OWL calibration procedure was suggested, at which OWS covered the low frequency range and OWL the HF range. Minor probe and measurement errors are caused by radiation effects and probe geometry above 1 GHz. However, the OE probe generally measures accurately broadband frequency dependent dielectric properties. A detailed error estimation of the OE probe in the frequency range from 100 MHz to 10 GHz is provided in Wagner et al. [227] which shows that the mean error of the real and imaginary part of the complex permittivity is 1.1 % and 3.2 %, respectively.

5.5.2 Verification of probe performance

Different techniques and probes are available to measure the frequency dependent dielectric soil parameters [216]. Section 5.3.2 and 5.3.3 introduced the theoretical background of two different techniques based on 1-port and 2-port measurements. Different types of

probes based on these two techniques are available, which differ in their design, application, performance and applicable frequency range [234]. Table 5.1 compiles the probes and their features used for the experimental probe comparison. The in-house-made OE probe and CT cell (CC1 5/8), which were introduced in Section 5.3.2 and 5.3.3, were the probes primarily used for the experimental investigations of fine-grained soils in this study. In order to evaluate these probes, their performance was compared experimentally to commercially available probes – Agilent HT (HT), Agilent P (P) and Sequid SDM-10G (SDM) – and a smaller CT cell (CC7/8). Three different VNAs were used to test the probes on a fine-grained soil:

1. Rohde & Schwarz ZVR ('R&S'; 10 kHz to 4 GHz),
2. Agilent PNA E8363B ('PNA'; 10 MHz to 40 GHz),
3. Anritsu Handheld VNA Master^{TM} ('AHM'; 2 MHz to 6 GHz).

VNA 1 and 2 are high-precision laboratory devices that allow EM measurements in a broad frequency range with high sensitivity and precision. However, due to the precise and sensitive measurement properties of these devices, their application is normally restricted to a laboratory environment, where defined conditions prevail with constant temperature and humidity. Hence, an additional handheld VNA 3 was included, which is a frequently used laboratory and field device [234]. Table 5.1 lists the VNAs to show which VNA was combined with the probes. The dielectric measurements were performed on clay (C), whose soil parameters are listed in Table 6.1. Prior to the experiment, sieving with a mesh opening of 0.4 mm was conducted in order to segregate coarse particle sizes. In a following step, the soil was mixed with deionised water to reach a water content of 1.1 times the liquid limit. The soil was then left to settle for at least 24 hours in an airtight container to achieve sufficient homogenisation of the soil structure. After homogenisation, the soil was slowly air dried and frequently mixed until the desired water content of 44.0 % was achieved. This water content lay approximately in the middle of the plastic range between the liquid and plastic limit. Dielectric measurements were then undertaken on the same soil with different probes. However, different installation techniques had to be applied (details can be found in Schwing et al. [234]) to ensure full contact between the probes and soil samples, and to avoid evaporation of water. However, the exact water content was determined directly after each measurement, which fell in the range of 42.9 % to 45.0 % for all measured samples. It should be pointed out that the exact water content of the measured sample with different probes varied slightly due to uncontrolled water loss. Further, the microscopic soil structure of the sample could not be controlled and might be different for the different probes.

Table 5.1: Summary of used OE probes of which three are commercially available probes and one is an in-house manufactured probe.

Probe	Agilent HT	Agilent P	Sequid SDM-10G	in-house OE probe	CT cell
Abbreviation	HT	P	SDM	OE-N	CC7/8 / CC1 5/8
Frequency [GHz]	0.1 - 20	0.5 - 50	0.1 - 10	0.05 - 10	0.0001-10 / 0.0001-5
VNA	PNA	PNA	PNA	AHM	R&S / PNA
Inner conductor diameter [mm]	0.66	1.6	1.0	3.0	8.7 / 16.9
Outer conductor diameter [mm]	19.0	9.5	30.0	70.0	20.0 / 38.8

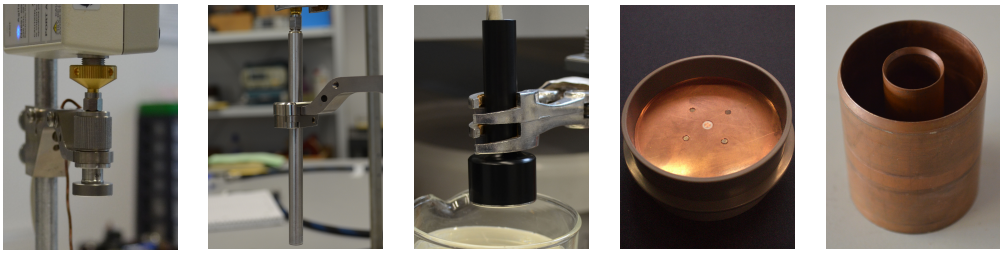

Figure 5.8 presents the results of the soil measurements showing the $\varepsilon'_{r,\text{eff}}$ and $\varepsilon''_{r,\text{eff}}$ obtained by using different probes and/or devices, as listed in Table 5.1.

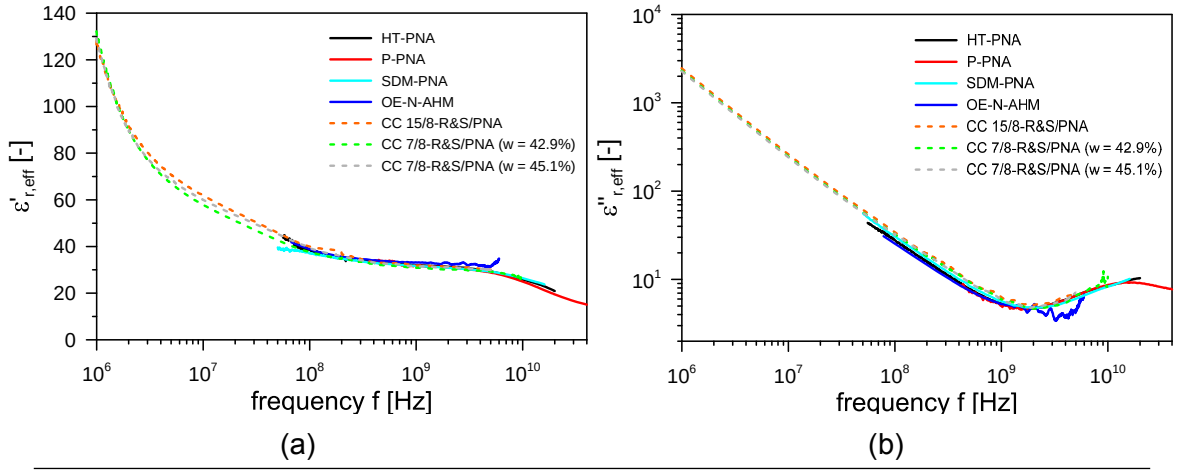

Figure 5.8: Comparison of dielectric spectrum of a fine-grained soils measured by different probes: (a) real part, $\varepsilon'_{r,\text{eff}}$, and (b) imaginary part, $\varepsilon''_{r,\text{eff}}$, of $\varepsilon^{\star}_{r,\text{eff}}$.

Despite slight differences in the water content in the samples, Figure 5.8 indicates that the measurement results were consistent and agreed well with each other, particularly for the frequency range between 100 MHz and 3 GHz. This result further supports the accuracy and validity of the data processing methods, as well as calibration procedures introduced in the previous sections. Moreover it can be seen that the measurement with commercial probes (HT-PNA, P-PNA and SDM-PNA) covered the HF range up to 40 GHz. At the same time, the in-house-made OE probe (OE-N-AHM), connected to the portable field device (AHM), suffered from noise and instable measurement for frequencies higher than 3 GHz, which resulted in slight inaccuracies, particularly in the imaginary part, $\varepsilon''_{r,\text{eff}}$, of $\varepsilon^{\star}_{r,\text{eff}}$. This was mainly caused by two reasons: (i) portable VNAs, such as AHM, are less accurate than high-precision laboratory VNAs, and (ii) a few imperfections in the manufacturing process of the probes might cause noise and signal disturbances in the sensitive HF range. However, as this HF range ($f > 3$GHz) is not the subject of this thesis, slight inaccuracies were acceptable and hence negligible. For the measurement using a CT cell in combination with the laboratory VNAs, the results were consistent for frequencies higher than 100 MHz, whereas obvious discrepancies could be seen in the frequency range between 2 MHz and 100 MHz. This was mainly due to the following three factors:

- slight differences in water content
- soil structure variation (such as in the density)
- inhomogeneity at the microscopic scale.

The observation indicated that the dielectric behaviour of fine-grained soil was sensitive to both soil microstructure and water content at frequencies lower than 100 MHz. This observation further supported the objective of the thesis to investigate the dielectric spectrum over a broad frequency range from 1 MHz to 3 GHz in consideration of soil structure and composition.

5.6 Conclusion

This chapter has extensively explained the broadband EM technique that was used for dielectric measurements in this study. It presented an in-house-manufactured probe that was designed and optimised for the experimental study. The in-house-made probe was based on a conventional coaxial line and modified N-type connector, and relies on the 1-port reflection OE technique. To evaluate the propagation characteristics of the EM waves and probe sensitivity, numerical simulations on the in-house-made OE probe using five different calibration

materials were performed. The results showed that the sensitive region can be localised within 7 mm in height and $\pm$ 10 mm in lateral direction from the probe aperture.

This chapter has extensively discussed the calibration procedure and data processing of 1-port reflection OE technique, and derived and presented relevant equations. The experimental investigation of the calibration procedure on six calibration materials showed good results in the aimed frequency window. The measured dielectric spectrum matched the theoretically expected dielectric spectrum of the selected calibration materials. However, a combination of OWS and OWL calibration is recommended to improve the probe performance over a broad frequency range.

In addition to the OE probe, this chapter intriduced a CT cell. It explained the principles of data processing of 2-port reflection and transmission measurements using CT cells. It presented three quasi-analytical approaches and an iterative technique, which can be used to process the measured S_{ij} parameters and calculate $\varepsilon^{\star}_{r,\text{eff}}$ as a function of frequency, f. Numerical simulations on the CT cell using tap water were performed to evaluate and compare the different approaches. The numerical simulation showed that the iterative technique (BJI) provided the most stable and reliable results. Therefore, the use of the iterative technique is strongly recommended and enforced in this thesis.

Finally, these two probes were experimentally compared against commercial probes. Dielectric measurements using each probe were performed on a fine-grained soil. The obtained $\varepsilon'_{r,\text{eff}}$ and $\varepsilon''_{r,\text{eff}}$ with different probes were compared to each other over the entire measured frequency range. The results showed good agreement in the frequency range between 100 MHz to 3 GHz, which generally suggests the use of the OE probe and CT cell.

Chapter 6

Experimental investigation

6.1 Introduction

To investigate the coupled mechanical, hydraulic, and dielectric aspects during soil densification, two different laboratory experiments were conducted. As explained in Section 2.5, the densification of fine-grained soils may be driven by internal stress, external stress or combination of both.

The study chose the shrinkage test to examine soil densification induced by internal stress. The shrinkage test basically follows the standardised procedure according to [1]. However, the objective of the shrinkage test is not only to measure densification, but also to measure SWCC and dielectric properties during shrinkage. Since coupled mechanical, hydraulic and dielectric soil characterisation during soil shrinkage has never been studied to this extent, the standardised shrinkage test was modified and enhanced to develop a test methodology and experimental procedure to enable the coupled investigation of these parameters. For these investigations, the novel in-house-manufactured OE probe was used to continuously measure the dielectric spectrum of the shrinking soil sample.

To examine the densification induced by external stress, this study chose to use the standardised compaction test, according to [4] and [5]. Similar to the shrinkage test, there is limited literature that simultaneously examines the mechanical, hydraulic, and dielectric aspects of standardised compacted fine-grained soils. Hence, a modified test methodology and experimental procedure, developed in this thesis, is proposed to perform coupled investigations during densification due to external stress conditions.

This chapter begins by introducing the fine-grained soils under investigation. It presents the preliminary work, including classification of the fine-grained soils and determination of standard geotechnical parameters. Subsequently, this chapter is divided into sections according to the compaction test and shrinkage test. For each test, the soil preparation, test setup, developed test methodology and experimental procedure are explained in detail.

6.2 Classification of soils under test

The soils investigated in this thesis were chosen depending on their plasticity in order to cover the range of high plastic soils. Prior to the actual experimental work, preliminary tests were conducted to classify the soils and obtain standard geotechnical parameters. Table 6.1 lists the selected soils together with the obtained parameters.

Table 6.1: Standard parameters and particle size fractions of the investigated soils, with abbreviations in parenthesis.

Soil	Clay (C)	Kaolin (KA)	Alluvial soil (AS)
Liquid limit (LL) [%]	61.70	89.95	52.50
Plastic limit (PL) [%]	23.90	35.66	22.31
Shrinkage limit (SL) [%]	17.59	34.76	14.74
Plasticity index (PI) [%]	37.80	54.28	30.19
Solid density [-]	2.707	2.615	2.713
Total specific surface area [m^2/g]	32.7	16.86	34.28
Cation exchange capacity [meq/100 g]	10	26.5	39.7
Particle size fraction			
Sand [%]	4.2	0	23.2
Silt [%]	18.0	13.9	30.9
Clay [%]	77.8	86.1	45.9

The consistency limits – namely liquid limit (LL) and plastic limit (PL) – were determined using the well-known methods established by Casagrande [248, 249], which were adopted as a standard procedure in ASTM D4318-10 [250]. The results showed that the highest LL and PL were measured for KA. Classification of the investigated soils was undertaken based on their plasticity range [251]. The consistency limits are generally a measure of the soil water retention behaviour and sensibility to water content changes. Hence, the plasticity chart was used to classify the soils based on the LL and plasticity index (PI). PI defines the

extent of the plasticity range, which is given by the difference between LL and PL. Figure 6.1 shows the classification of soils in the plasticity chart according to Casagrande [249] and ASTM D2487-11 [251].

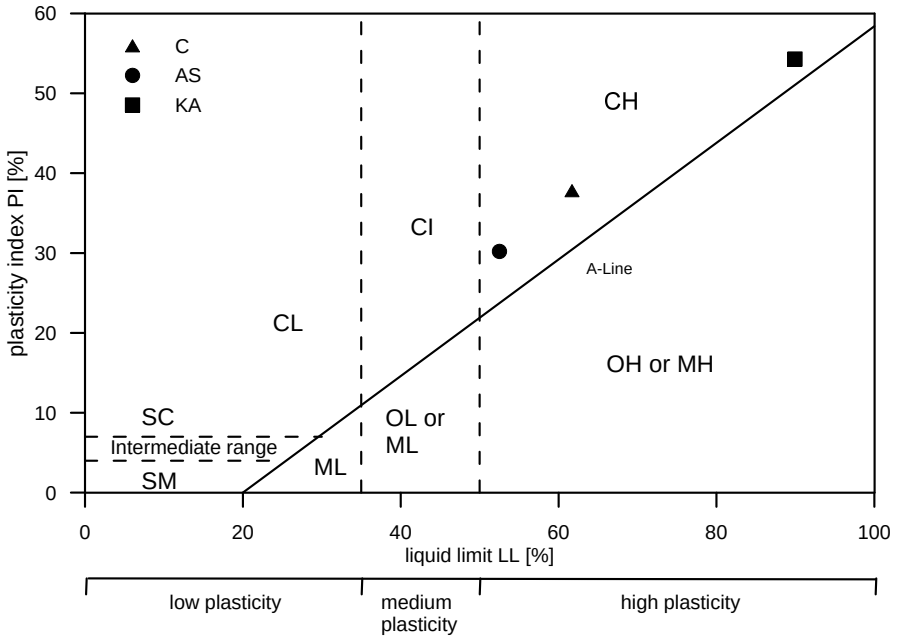

Figure 6.1: Classification of investigated soils in the plasticity chart according to Casagrande [249].

It can be seen that all soils were highly plastic because the measured LL values were higher than 50 % water content. Due to high plasticity indices, the selected soils were consistently located above the A-line, which separated inorganic soils from organic soils. Based on this observation, the soils were classified, according to ASTM D2487-11 [251], as inorganic clays with high plasticity. In addition to the LL and PL, the shrinkage limit (SL) was determined using the water displacement method [1]. The difference between LL and SL gives an idea about the extent of water content changes in which volume changes are expected. The result showed that the SL and PL are nearly identical in the case of the investigated KA. This meant that no volume change was expected at the lower limit of the plasticity range. In contrast, distinct differences between SL and PL were measured for C and AS. The solid density of each soil was determined by means of a gas pycnometer [252].

As mentioned in Section 2, the soil behaviour and plasticity of fine-grained soils strongly depend on the type and quantity of clay minerals and their particle surface area. However, it is not possible to obtain a reasonable quantitative description of the mineralogical composition on the basis of the consistency limits. As a result, the particle size distribution, soil mineralogy, total specific surface, and cation exchange capacity were separately determined. The total specific surface area was determined by measuring the amount of physically adsorbed

nitrogen according to the Brunauer-Emmett-Teller (BET) method, in combination with the single-point differential method [253, 254, 255]. The cation exchange capacity for AS and KA was determined by means of silver thiourea methods (for method details, see [256] and for soil C by means of Cu-Triethylentetramin (modified method of Meier and Kahr [257] – see Kaden [258]). Sedimentation tests using a hydrometer were conducted to determine the particle size distribution finer than 75 μm according to ASTM D422-63 [259]. Figure 6.2 presents the results of the particle size distribution analysis. The KA and C showed the highest clay content, with a percentage of clay mass of 86.1% and 78.0%, whereas the AS revealed the most coarse-grained particles.

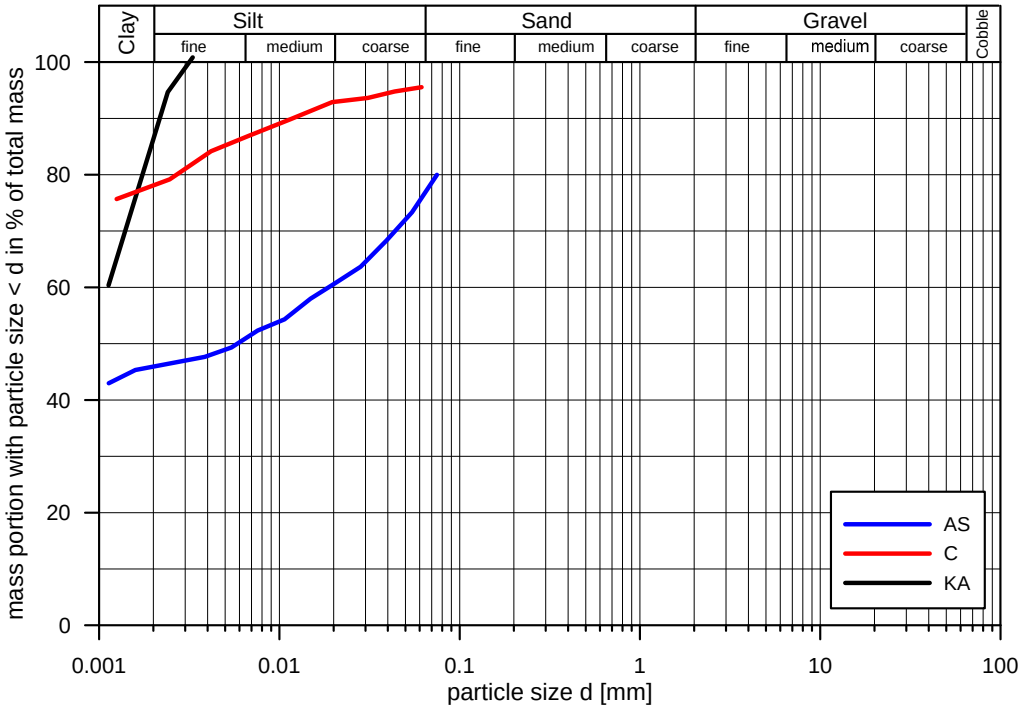

Figure 6.2: Particle size distribution of the three investigated soils determined using hydrometer tests according to ASTM D422-63 [259].

It is worth emphasising that, in order to avoid confusion, the term 'clay' in the particle size distribution determined by the sedimentation tests [259] relates to any particle of sufficiently small size. However, in this study the term 'clay' is considered only shrink-swell mineral particles of sufficiently small size. Due to this consideration, the mineralogical composition was determined to distinguish between clay particles contributing to the shrink-swell behaviour and non-clay particles. X-ray diffraction analysis, in combination with total elemental microwave digestion, was used to determine the mineralogical composition of the AS and KA soil (for details, see [256, 260]). In the case of C, X-ray diffraction method, in combination

with infrared spectroscopy, was applied to determine the mineralogy. Table 6.2 lists the obtained result of the mineralogical investigation of the soils, where the single mineral fractions are expressed in mass per cent.

Table 6.2: Overview of the results of the mineralogical composition of clay particles contributing to the shrink-swell behaviour and non-clay particles (in mass per cent).

Soil	Clay C	Kaolin KA	AS AS
Clay content [%]	45.0	72.7	26.1
Illite-mica [%]	19	20.0	0
Kaolinite [%]	23	52.7	26.1
Quartz [%]	41	26.6	64.8

The results in Table 6.2 show that the highest amount in mass per cent of shrink-swell clay minerals was found in KA, with 52.7% kaolinite and 20.0% illite-mica. This observation is definitely supported by the determined consistency limits, shown in Table 6.1, which also indicate that the most distinctive shrinkage behaviour, from LL to SL, was found for the soil AS. The lowest amount of shrink-swell clay minerals, with 26.1% mass per cent, was measured for AS. At the same time, the highest amount of non-clay minerals – mostly quartz – was determined for AS, whereas the lowest amount was for KA.

6.3 Compaction test

Standard and modified compaction tests, according to ASTM D698-12 [4] and ASTM D1557-12 [5], were chosen as an experimental standard procedure because these methods are widely used to determine the compaction behaviour of soils in laboratory investigations [261]. The standard and modified compaction tests were established in order to determine the optimum water content, w_{Pr}, at which a specific soil is compacted to be as dense as possible to an optimum dry density, $\rho_{D,Pr}$, under a given compaction energy [262]. These compaction characteristics are often used in field engineering applications [261, 262]. In this study, the standardised procedure was preferably used to obtain different soil compaction tests by applying a defined external compaction energy.

The compaction of soil influences not only the strength and compressibility [263], but also the hydraulic behaviour in terms of permeability and soil suction [264, 265, 266, 267]. In particular, in unsaturated soil conditions, the influence of compaction on the hydraulic behaviour – such as soil suction changes due to change in compaction – is not well understood [264, 268]. Hence, in order to cover a broad density and water content range, conventional and standardised compaction tests were conducted, together with measurements of hydraulic and

dielectric soil parameters, under controlled test conditions. The objective was to investigate the effect of the different density states – achieved by applying different external stress – on the soil suction and complex permittivity at different water contents.

The following section details the experimental methodology that was developed in this study, including the experimental setup and standard test procedure. This experimental methodology was used to systematically measure and analyse not only the soil compaction state, but also the hydraulic and dielectric soil properties.

6.3.1 Conventional standardised compaction tests

This section first presents a short review of the experimental concept of the standard and modified compaction tests. According to commonly used standards [4, 5], three different methods are available to conduct compaction tests. These methods differ in their sample mould dimension, number of compaction blows and soil pre-treatment in terms of particle segregation. Prior to testing, the soil is always pre-treated and segregated by sieving at a specific particle size, which depends on the chosen method. After soil pre-treatment and preparation, compaction tests are then conducted on soil materials which pass the mesh opening of the desired segregation particle size. In this study, in order to achieve comparable soil conditions, it was necessary to segregate all soils consistently at the identical particle size. Further, it was decided to use the same compaction mould dimension for all tests to develop an identical experimental investigation procedure, and prevent any possible influence of sample dimension on the experimental results. For these two reasons, Method A – as it is defined in the corresponding standards – was chosen for both the standard and modified compaction tests. The specifications for the compaction tests are listed in Table 6.3[1].

Table 6.3: Specification of the standard and modified compaction according to ASTM D698-12 [4] and ASTM D1557-12 [5].

	Standard compaction test	Modified compaction test
Method	A	A
Soil segregation [mm]	4.75	4.75
Mould diameter [mm]	101.6	101.6
Mould height [mm]	116	116
Rammer weight [kN]	24.5	44.5
Compaction energy [kN-m/m^3]	600	2700
Falling height [cm]	305	457.2
Number of blows [-]	25	25
Number of soil layers [-]	3	5

[1] listed values may differ minimally to ASTM D698-12 [4], ASTM D1557-12 [5] due to conversion from imperial to SI units

6.3.2 Soil preparation

The investigated soils were pre-treated and prepared in dry conditions after slowly air drying under controlled environmental conditions, as standardised in ASTM D698-12 [4] and ASTM D1557-12 [5]. When necessary, soil aggregates were carefully broken apart without crushing single mineral particles. The chosen method required segregation of the soil mass at 4.75 mm particle size. Prior to the sample preparation, a reasonable optimum water content for each soil and test was approximated. Based on this assumption, several soil samples were prepared with water content lower and higher than these approximated values. During the soil preparation, only deionised water was used to wet soil samples to the desired water content in order to avoid significantly influencing the hydraulic and dielectric soil properties (such as osmotic suction and pore water conductivity) and to avoid any unexpected and uncontrollable side-effects. The prepared soil samples were packed into plastic bags that were air-tightly sealed. The soil samples were stored and left to settle for at least three days to ensure homogenisation.

6.3.3 Experimental procedure of standardised compaction test

After soil pre-treatment and sample preparation, the soil was installed layer-wise into the compaction mould with defined dimensions of 101.6 mm in diameter and 116 mm in height (see Table 6.3). The standard and modified compaction tests differed in the number of layers, rammer weight and rammer falling height. Each soil layer was compacted by a number of certain rammer blows with a specific falling height. The standard compaction test required the soil to be installed into the mould in three layers, with each layer compacted by 25 rammer blows, with a weight of 24.5 kN and a falling height of 305 mm. Overall, the applied number of blows with the specified rammer weight and falling height resulted in a total compaction energy of 600 kN-m$/$m^3. In contrast to the standard compaction test, the modified compaction test was specifically designed to achieve a higher applied compaction energy. To do so, the soil was installed with five soil layers, instead of three, into the compaction mould with the same dimension. Further, the modified compaction tests employed a heavier rammer weight of 44.5 kN, with a higher falling height that applied a total compaction energy of 2700 kN-m$/$m^3.

(a) (b)

Figure 6.3: Dewpoint potentiameter WP4T used to measure soil suction, based on the chilled mirror hygrometer technique.

6.3.4 Test setup

To measure the hydraulic and dielectric soil properties during the compaction tests, appropriate measurement techniques and additional equipment were chosen. Further, it was necessary to develop a methodology and experimental procedure that enabled the measurement of these additional soil properties without influencing or altering the standardised compaction tests.

To measure the soil suction for the compacted soil samples, a suitable experimental method had to be chosen. As the optimum water content for soils is generally found at values much lower than the LL and located below the zero air void line, which means at unsaturated soil conditions (see data presented in Pandian et al. [263] and Birle et al. [127]), the soil suction was expected to be at a high suction range. Due to this expectation, the chosen method should be able to cover and measure the high suction range. Additionally, the intention was to choose a method that allowed quick measurements with high accuracy. Section 3.2 presented an extensive literature review on available methods for measuring soil suction, which differ in technique, applicable suction range and measurement time. Based on this literature review, it was decided to use the chilled mirror hygrometer technique to measure the soil suction of the compacted soil sample.

The device that was used for the experimental investigation was a commercially available **WP4T Dewpoint Potentiameter** from Decagon Devices, as shown in Figure 6.3. The WP4T Dewpoint Potentiameter uses the chilled mirror dewpoint technique, which measures soil suction based on the thermodynamic relationship (given by Kelvin's Equation 2.8) between relative humidity, temperature and water potential [118, 119]. The measured water potential, as a sum of the osmotic and matric potential, is determined by the equilibrium between the

vapour pressure of the water phase in the soil, and the air phase surrounding the soil sample [127]. The sample is equilibrated in the headspace of a sealed chamber. The sealed chamber contains a mirror and photoelectric cell for detecting condensation on the mirror. At equilibrium, the water potential of the air in the chamber is equal to the water potential of the sample. A dewpoint sensor measures the dewpoint temperature of the air, and an infrared thermometer measures the sample temperature. The WP4T Dewpoint Potentiameter allows precise and fast measurements of soil suction in a range from 0.1 to 100 MPa [127]. The WP4T measures temperature (in Celsius) and soil suction (in MPa and pF-value) as a sum of osmotic and matric potential, and visualises the measured values on a front screen (see Figure 6.3B). Since deionised water was used to prepare the samples (see Section 6.3.2), it is assumed that the influence of the osmotic potential is negligibly low.

In order to measure the dielectric parameters, an Agilent E5061B ENA VNA was employed in combination with the CT technique. The use of the CT technique was preferred because it is advantageous in investigating soil samples under a defined volume and compaction state. The design of the coaxial cell enables coring undisturbed soil samples; thus, it is suitable for both laboratory and field investigations. Commercially available copper tubes were purchased with diameter dimensions as shown in Figure 5.4A. The copper tubes were precisely cut into a length of 5 cm to obtain CT cells with an inner and outer conductor. One side of the cell was sharpened, as shown in the photograph in Table 5.1, in order to be able to core samples from the compacted soil specimen.

Based on this setup, the relative effective complex permittivity, $\varepsilon^{\star}_{r,\mathrm{eff}}$, was determined, under controlled environmental conditions and density, in a frequency range from 1 MHz to 3 GHz. Figure 6.4 shows the experimental setup used in this study to measure the dielectric parameters.

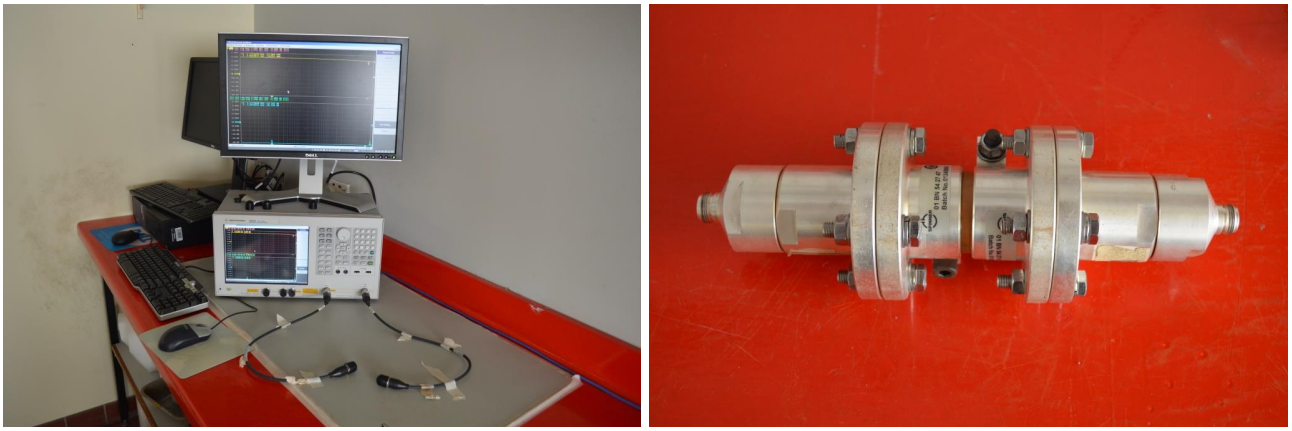

(a) (b)

Figure 6.4: Configuration of the experimental setup to measure the dielectric soil property: (A) Agilent E5061B ENA in combination with (B) CT technique. The CT cell was installed between two flange connectors which were connected via coaxial cable to the VNA.

Technically, the VNA covers the frequency range from 5 Hz to 3 GHz and can be used for both impedance and S-parameter measurements. However, as the low frequency limitation of the CT cell was at 1 MHz, the effective and usable frequency range for the dielectric measurement technique was restricted to 1 MHz to 3 GHz.

6.3.5 Experimental procedure

The methodology and experimental procedure were established and strictly followed during the experimental investigations. One objective was to develop a standard procedure that enabled determination of different soil parameters in one and the same experiment. Another important objective was to ensure the consistency of the procedure throughout the experiments, and minimise any possible and undesired experimental influences. In the following, a compaction test is described as an enumeration to provide a better and more understandable overview of the step-wise experimental procedure:

1. Prior to beginning the compaction tests, both the VNA and coaxial cable had to be calibrated. A mechanical calibration kit was used to eliminate systematic imperfections and errors in the VNA and coaxial cables. Figure 6.5A shows a photograph of the mechanical calibration kit used in this study.

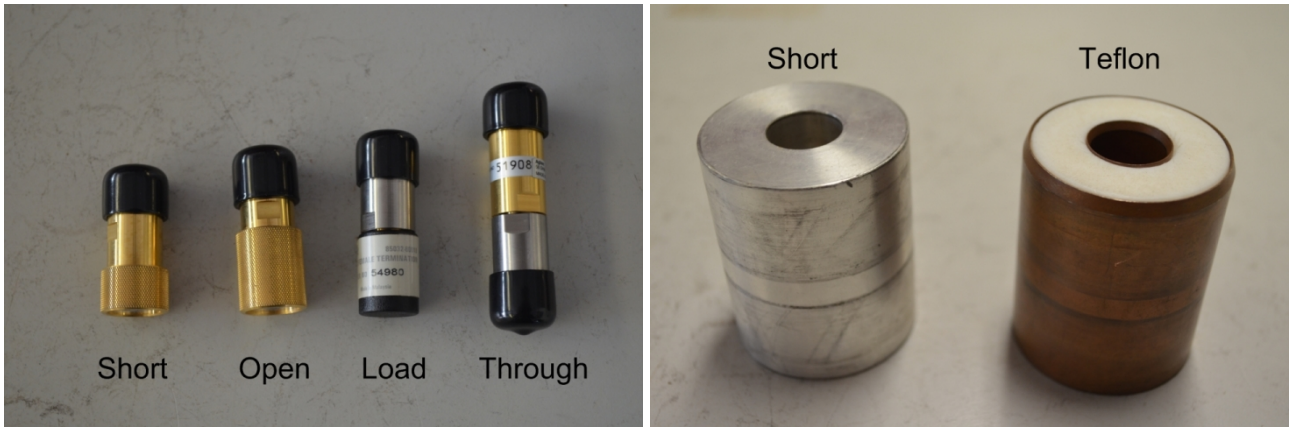

(a) (b)

Figure 6.5: (A) Mechanical calibration kit (Agilent type N 85032F) that includes open, short, load and through calibration standards and (B) additional two standard calibration materials – Teflon and short – used to check the performance and success of the VNA calibration.

The kit from Agilent, type N 85032F, included the open, short, load and through calibration standards. These calibration standards were connected at the end of the coaxial cables, one after the other, and measurements were taken. Based on the difference between the measured and theoretically expected values, the VNA software calibrated

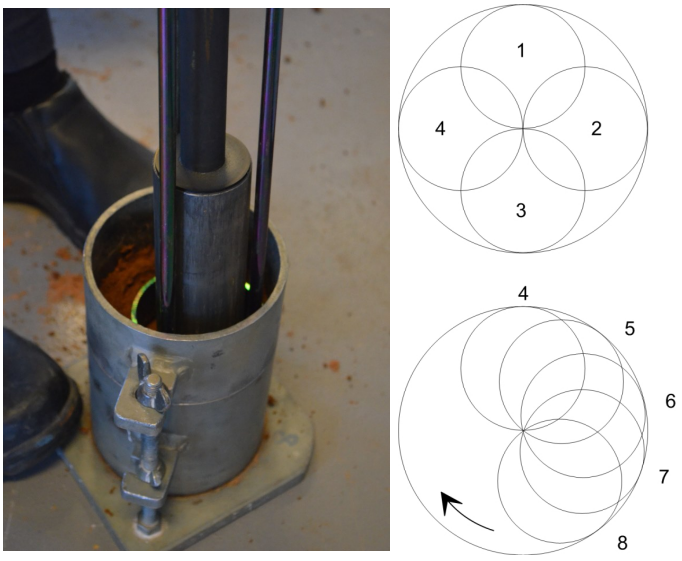

Figure 6.6: (A) standard compaction test with rammer compaction of the soil into the mould. (B) Compaction pattern proposed by ASTM D698-12 [4] and ASTM D1557-12 [5].

the network to remove any error and noise of the EM signal. Additionally, two other calibration materials – namely short and Teflon, as shown in Figure 6.5B – were measured to check the performance and success of the mechanical VNA calibration.

2. After successful calibration of the VNA and coaxial cables, the actual compaction test was prepared. Before compacting soil into the mould, the dimension and weight of the compaction mould were determined because these values were required for the later calculation of the soil dry density. The soil was layer-wise compacted into the mould. Special care must be taken on the soil layers, which should be compacted into equal thicknesses in the compaction mould. To do so, a special compaction pattern is proposed by ASTM D698-12 [4] and ASTM D1557-12 [5]. As Figure 6.6B indicates, the first four rammer blows should hit the soil layer equally in area. The following rammer blows then compact each soil layer equally, with a rotating compaction pattern. After 25 rammer blows, the next soil layer is filled into the mould, and the same procedure is repeated for each consecutive layer. Once all layers are installed into the mould, the excessive soil on top of the mould must be removed using a knife or other appropriate tool. The soil surface must be trimmed to be even with the top of the mould, using a straightedge scraper. This means that the volume of the compacted soil body equals the mould volume (see Figure 6.7A). Subsequently, the weight of the filled mould is determined to obtain the bulk soil mass of the compacted specimen.

3. Once the soil specimen was compacted into the mould, the coaxial cell was pushed into the specimen via a hydraulic jack in order to core a soil sample. Before coring the sample, the dimensions and weight of the empty CT cell were determined.

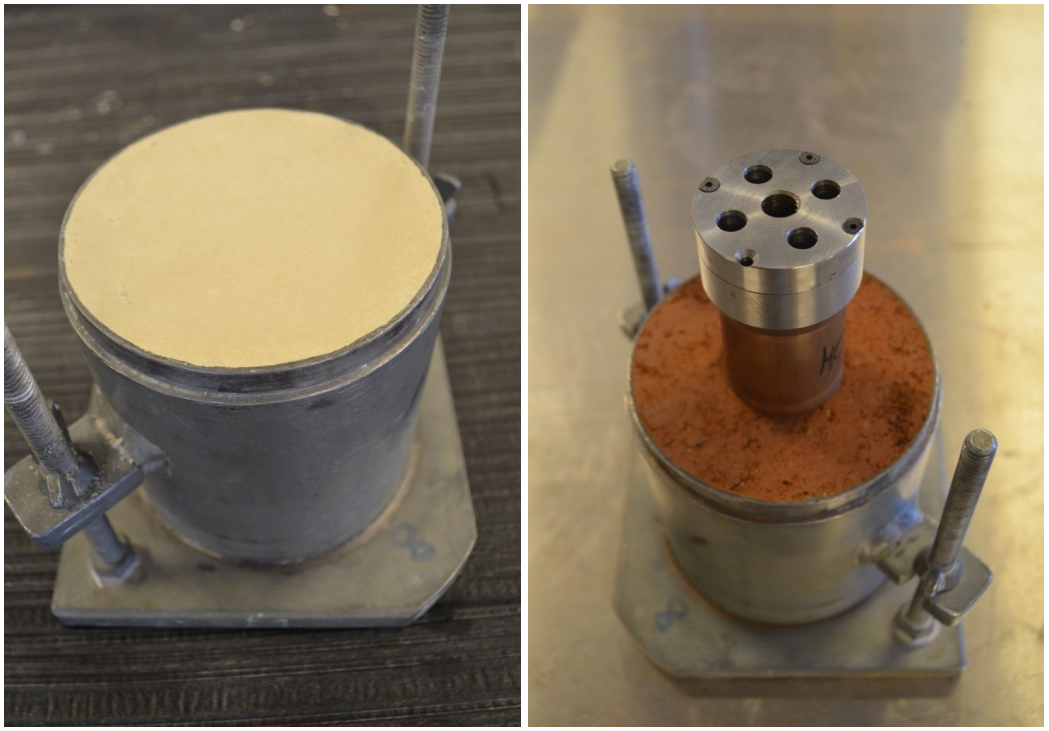

(a) (b)

Figure 6.7: (A) Compacted KA sample with trimmed soil surface even to the top of compaction mould and (B) AS sample compacted according to the standard compaction test [4], with the CT cell, including the sample holder, placed on the top center of the compacted soil specimen.

Figure 6.7B shows a photograph of the mould filled with compacted AS soil, where the CT cell is placed on the top centre. A special sample holder was manufactured to hold the inner and outer conductor of the CT cell, while pushing the cell into the compaction mould. The sample holder was necessary to place the inner conductor exactly in the centre of the outer conductor. In order to take accurate and successful dielectric CT measurements, the inner conductor must be perfectly centred and parallel with the outer conductor. In addition, the sample holder was important to keep the inner and outer conductor in centre position of the mould, while pushing the cell into the mould using a hydraulic jack, which applied the load onto the sample holder and not onto the cell itself. By employing this procedure, damage to the CT cell was minimised. As Figure 6.7B demonstrates, the sample holder contained small holes that were designed to observe the point at which the CT cell was filled completely with soil. As soon as the cell was filled, the applied load onto the sample holder was released to stop the cell being further pushed into the compaction mould. The sample holder was then removed and an appropriate cap was used to close the top end of the CT cell and prevent any water evaporation of the soil sample.

4. In the next step, the compaction mould was unscrewed and disassembled from the compaction base. The compaction mould was turned around and set upside down

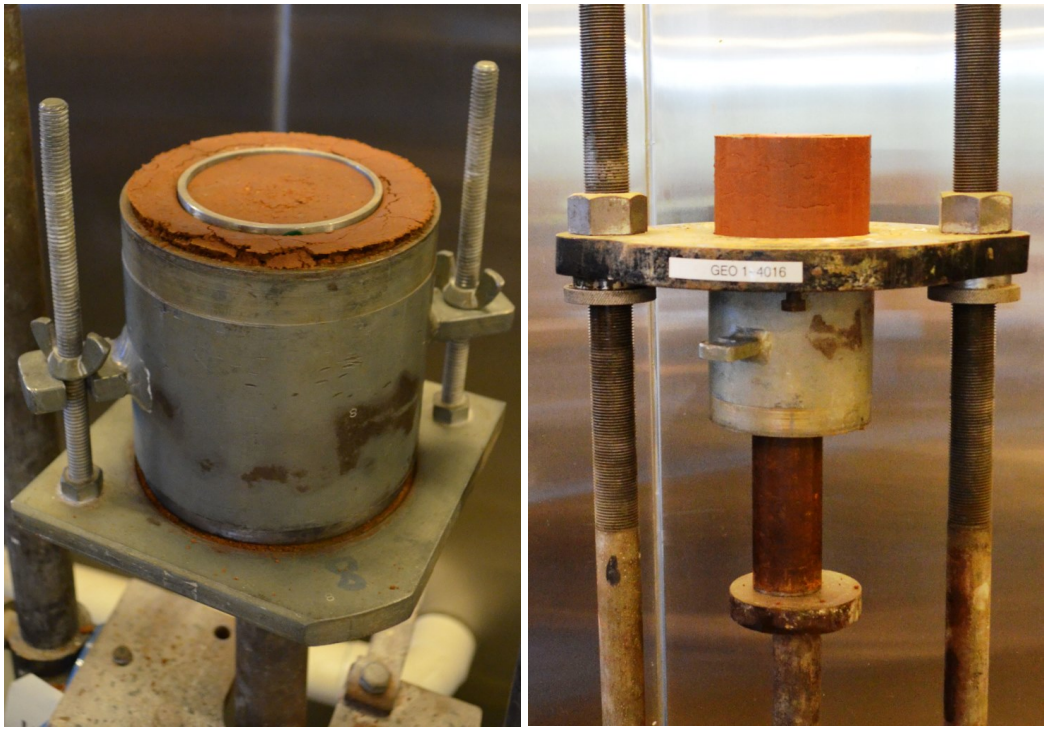

(a) (b)

Figure 6.8: (A) Standard compacted AS soil, in which the shrinkage rings were pushed into the bottom centre of the compaction mould, and (B) extraction process of standard compacted AS soil sample from compaction mould using a hydraulic jack.

onto the compaction mould. Then, a shrinkage ring of 70 mm in diameter and 14 mm in height was used to core the shrinkage test sample from the compacted soil specimen. Similar to the CT cell, one side of the shrinkage ring was sharpened prior to the test to allow the ring to be easily cut into the compacted soil specimen. Before cutting out the soil sample, the weight of the shrinkage ring was measured. Then, the shrinkage ring was placed on the centre of the compaction mould and an additional ring was placed on top of it. A metal plate was placed on top of both rings, which was used to transmit the applied load from the hydraulic jack to the shrinkage rings. By doing so, the shrinkage rings were slowly pushed into the compacted specimen. The second shrinkage ring was necessary to push the first shrinkage ring slightly deeper into the specimen without causing additional compaction of the samples. As soon as the second shrinkage ring was half-filled with soil, the hydraulic load was released and the metal plate and second shrinkage ring were removed. Figure 6.8A shows a compacted sample of AS soil, where the shrinkage rings were perfectly pushed into the bottom centre of the compacted specimen. It can be seen that the second shrinkage ring was only half-filled with compacted soil.

5. Once the CT cell and shrinkage ring were driven into the compacted specimen, the entire soil body was extracted from the compaction mould using the hydraulic jack.

Figure 6.8B shows a photograph during the extraction process. The compaction mould was positioned below the extraction plate, containing a tapered hole with an opening size of the inner diameter of the compaction mould. The compacted soil body was extracted upwards by applying the load to the bottom of the specimen.

6. As soon as the compacted soil specimen was extracted, three samples were taken according to ASTM D2216-10 [136] to determine the water content. Three samples were collected from different layers across the specimen, and the average water content value was calculated in order to obtain a representative water content over the entire compacted specimen. Subsequently, the dry density of the compacted sample was calculated based on the measured bulk soil mass and average water content.

7. In a further step, three additional samples were taken from the compacted soil specimen to measure the soil suction using the WP4T. The samples were collected from different sections of the compacted soil specimen with a minimum weight of 10 grams to achieve a representative suction value. Where possible, the three samples were cut out of the specimen to obtain more or less undisturbed samples. Special care was taken when preparing and placing the soil into the sample cups. To obtain good and satisfying measurement results, the bottom of the sample cup was completely covered by soil, and the cup should not filled more than halfway in height. Then, each prepared sample cup was placed into the draw of the WP4T, and the chamber was closed. The measurements were taken and the readings of soil suction and soil temperature were recorded. The temperature of the device was set as close as possible to the sample temperature in order to reduce the equilibrium time and speed up the measurement time. A low temperature difference between the device and soil sample may enhance the measurement accuracy. Two repetition measurements were additionally taken for each sample to calculate an average suction value. After the suction measurements were completed, the water content of each sample was determined by oven drying at 105 °C for 24 hours, according to ASTM D2216-10 [136].

8. The shrinkage ring was retrieved from the compacted soil specimen. Soil mass exceeding the ring dimension was removed. Both sides of the soil sample were carefully levelled to the edges of the ring in order to define the soil volume according to the ring volume, as shown in Figure 6.9A. After preparing the shrinkage test sample, the shrinkage sample was weighed to determine the bulk soil mass. Based on the averaged water content of the compaction test, the initial water content of the shrinkage test sample was known, and the dry density could be calculated based on the weight of the shrinkage ring, bulk soil mass and water content. Since the shrinkage test could not be started immediately after retrieving the sample, the soil samples had to be preserved temporarily in vacuum-sealed plastic bags.

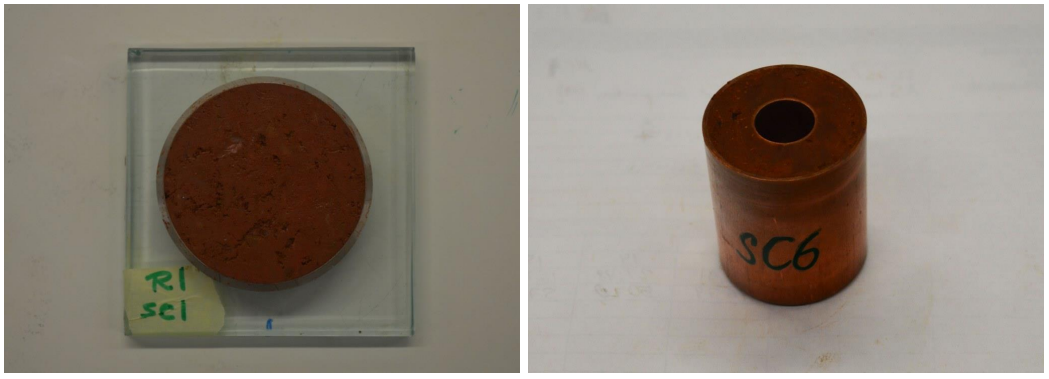

(a) (b)

Figure 6.9: (A) Compacted shrinkage test sample of AS soil after retrieving from compaction mould and preparation and (B) CT cell with cored soil sample after retrieving from the compaction mould and preparing for dielectric measurement.

9. The CT cell was retrieved from the compacted soil specimen directly after the shrinkage ring. Soil that was also cored into the inner conductor was removed, and the CT cell was carefully cleaned of excess soil covering the surface of the outer conductor, as shown in Figure 6.9B. Similar to the shrinkage ring, both sides of the soil sample in the CT cell were trimmed to form an even surface at the CT cell ends. A careful cleaning and preparation of the CT cell was required for two reasons: (i) to ensure a successful dielectric measurement and (ii) to determine precisely the soil volume and soil weight. By doing so, the soil volume could be calculated based on the dimensions of the CT cell, which were previously presented in Figure 5.4A in Section 5.3.3. The soil sample was weighed to determine the bulk mass. The dry density of soil in the CT cell was then calculated based on the soil volume, bulk soil mass and water content determined previously in the compaction mould. These dry density values of the soil in the CT cell could be compared to the values obtained in the compaction mould in order to assess the extent of soil disturbance due to coring the soil samples.

10. After preparing a sample in the CT cell, it was installed between flange connectors, as shown in Figure 6.4A. Then, the 2-port coaxial reflection and transmission measurements were taken using the VNA to measure the full set of S_{ij} parameters. The S_{ij} parameters were determined as an average of 50 measurements with a logarithmic sweep in a frequency range from 1 MHz to 3 GHz to reduce random noise in the measurements. Based on a MATLAB code, a post-processing phase shift correction was performed to eliminate the influence of the flange connectors. The iterative BJI method (introduced in Section 5.3.3) was employed to calculate the complex permittivity $\varepsilon^{\star}_{r,\text{eff}}$ from the measured and post-processed S_{ij} parameters for the covered frequency range.

11. Once the CT cell was measured with the VNA and the dielectric soil properties were obtained, the soil sample in the CT cell was used to measure the dry path of the SWCC

for the compacted sample. In order to collect several points of the SWCC, the soil in the CT cell was removed and portioned into subsamples of at least 10 grams mass. These subsamples were then air dried under controlled environmental conditions to slowly reduce the water content from the compaction water content to dry conditions. Successively, subsamples were taken at different time steps to measure the soil suction using the WP4T. Again, three suction measurements were performed on each subsample to obtain a representative average soil suction value. After the suction measurement, the water content of each subsample was determined. The SWCC of one compaction test, as a relationship of soil suction versus gravimetric water content, was then constructed by plotting the results of all measured subsamples.

12. A shrinkage test was performed on the soil sample cored with the shrinkage ring from the compaction mould. The soil sample was unpacked from the vacuum-sealed plastic bag and a control weighting was conducted to check whether water evaporation occurred. Then, the shrinkage test was begun under controlled environmental conditions, and mass and volume changes were recorded every two hours. The volume changes were measured with the direct determination of the sample geometry, as explained in Section 3.3.2. At the end of the shrinkage test, the final density beyond the SL ($w < \mathrm{SL}$) was additionally measured, with the water displacement method (see Section 3.3.2). The shrinkage curve was modelled based on the known initial soil conditions, as well as the continuous readings of mass and volume change.

13. This entire experimental procedure was implemented for each compaction test.

6.4 Shrinkage test

Shrinkage tests on fine-grained soils were conducted to investigate volume changes induced by internal stress due to pore water evaporation. Changes in water content result in changes in soil volume, particularly for fine-grained soils, which leads to different consistencies [30, 248]. The shrinkage test was designed to determine the SL, which describes the water content at the transition from semi-solid to solid state, where no further volume changes are expected [30]. A standardised procedure for conventional shrinkage tests was proposed by ASTM D4943-08 [1].

As explained in Section 2.4, mass and volume changes during shrinkage influence the hydraulic behaviour of fine-grained soils – such as soil suction for a given water content – and vice versa. However, changes in hydraulic behaviour are usually not investigated together

with soil shrinkage. Therefore, there is a need that has also been identified in the literature for coupled investigations of soil shrinkage and SWCC. In this study, shrinkage tests were conducted in parallel with determining the SWCC, starting with exactly the same initial conditions and comparable boundary conditions. Further, a broadband EM measurement technique was employed to measure the dielectric behaviour during soil shrinkage.

6.4.1 Conventional shrinkage test

ASTM D4943-08 [1] describes the standardised procedure for determining the water content at the SL for fine-grained soils. The soil under investigation was remoulded and prepared to a water content at approximately the LL. In this study, the initial water content at the shrinkage test was chosen to be 1.1 times the LL. In the next step, the soil slurry was placed in a shrinkage dish. Directly afterwards, the soil mass and volume were recorded to determine the water content and dry density at the beginning of the shrinkage test. Then, the soil sample was slowly air dried under controlled conditions to try to prevent soil cracking. The point of the SL was reached when the soil colour changed from dark to light. In the next step, the final volume at $w = 0\%$ was measured with the water displacement method. The SL was calculated based on the initial water content and volume, as well as the volume after reaching the SL. There were two major disadvantages observed for the conventional shrinkage test:

1. As explained in Section 2.5.2, different zones are generally observed in the shrinkage behaviour of fine-grained soils. However, volume and mass changes are usually not continuously recorded during the shrinkage test. The conventional shrinkage test is only used to determine the SL. Thus, it is not possible to model the shrinkage curve, for instance, as a function of w and ρ_D. As a result, the different shrinkage zones cannot be quantified.

2. Given that the whole shrinkage curve is not recorded, it is impossible to determine the exact SL. In the conventional shrinkage test, the SL is defined as the water content at which the imaginary shrinkage curve would theoretically leave the zero air void line. This is only valid under the assumption that the residual shrinkage zone does not exist. However, it is normally expected to have residual shrinkage, especially in highly plastic soils. Therefore, the exact SL is found to be somewhere at lower water content.

To obtain a quantitatively better description of the shrinkage behaviour and shrinkage zones of fine-grained soils, it is inevitable to determine the exact shrinkage curve. Thus, the standardised shrinkage test was modified to measure mass and volume changes during the shrinkage in order to model the entire shrinkage curve, starting from initial conditions ($w =$

1.1 LL) to the end state at $w = 0$, together with determining the SWCC for the same boundaries.

6.4.2 Test setup

It was necessary to develop a methodology for the simultaneous determination of the coupled behaviour. To do so, appropriate measurement techniques were selected in order to measure the hydraulic and dielectric parameters during soil shrinkage. Further, an experimental procedure was elaborated to quantify the coupled parameters simultaneously, without altering the standardised procedure of the shrinkage test.

The conventional shrinkage test on fine-grained soils starts at slurry condition, with a gravimetric water content of $w \geq$ LL. At this stage, the soil suction is predicted to be very low. In contrast, fine-grained soil is at almost completely dry conditions at the end of the shrinkage test. The soil suction at this stage can be expected to reach maximal values due to unsaturated conditions, with a gravimetric water content close to $w = 0.0\%$. As a result, the soil suction range is extremely large for the entire shrinkage process. Thus, in this study, appropriate experimental methods had to be selected and combined to measure the soil suction over a range that was as broad as possible. Based on the literature review given in Section 3.2, this study chose three different methods:

1. the hanging column test method
2. the axis translation technique using the pressure plate apparatus
3. the chilled mirror hygrometer

The **hanging column test** method was chosen to measure the low suction range between 0 kPa $\leq \Psi_t \leq$ 20 kPa. Figure 6.10 schematically illustrates the experimental setup for this hanging column test method. The soil sample under investigation is placed in a measuring glass on top of a saturated ceramic plate. The measuring glass, including the sample, is placed into a climate chamber to keep the environmental conditions controlled during the test. The climate chamber is located on a platform to elevate it to a height of about 2.0 m. The measuring glass inside the climate chamber is connected via a water pipe to a burette, which is located outside the climate chamber. The burette is fixed to a rack that is held by the platform. The burette can be vertically adjusted in height along the rack.

Prior to the test, it is necessary to completely saturate the ceramic plate. Once the ceramic plate is saturated, the burette needs to be adjusted so that the water level inside is at the

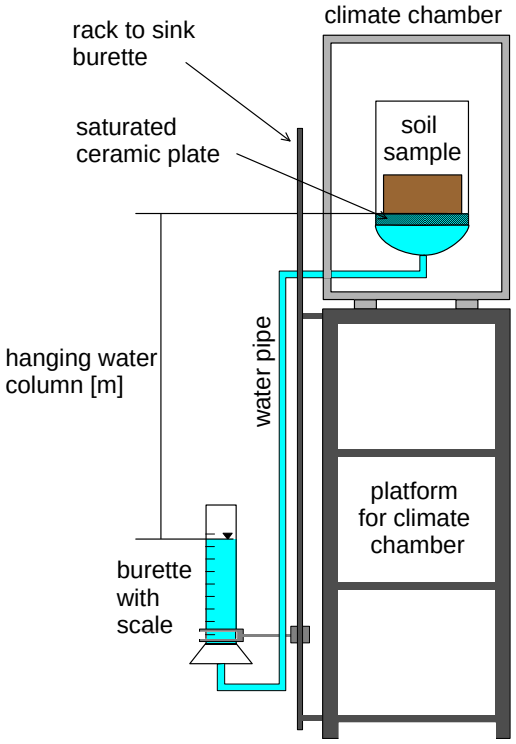

Figure 6.10: Schematic illustration of the setup for the hanging column test method.

same level as the top end of the ceramic plate. The water level inside the burette is recorded prior to the test. After that, the prepared soil sample is placed on top of the saturated ceramic plate. Then the actual test begins by lowering the elevation level of the burette. With lowering the elevation level, soil suction is induced in the soil sample due to the hanging water column. As a result, the soil starts draining water and the water level rises accordingly in the burette. The soil drains until the hanging water column is in equilibrium for the given induced suction in the soil sample. Equilibrium is indicated when the water level in the burette stops rising and a constant value is reached. At this point, it can be assumed that the induced soil suction equals the applied negative water pressure below the ceramic plate applied as the height difference of the actual water level in the burette and the top of the ceramic plate. The corresponding gravimetric water content is found by balancing the water levels in the burette before and after lowering the burette. The burette is step-wise lowered to further decrease the water pressure by the hanging water column. Each time, the gravimetric water content is determined by balancing the water level in the burette at equilibrium. By doing so, several points of the SWCC are determined in a range from 0 kPa $\leq \Psi_t \leq$ 20 kPa by combining the induced soil suctions with the corresponding gravimetric water contents.

The **axis translation technique using the pressure plate apparatus** was employed to measure the intermediate suction range from 25 kPa $\leq \Psi_t \leq$ 400 kPa. Figure 6.11 presents a schematic illustration of the used setup. The soil sample is placed on a saturated ceramic

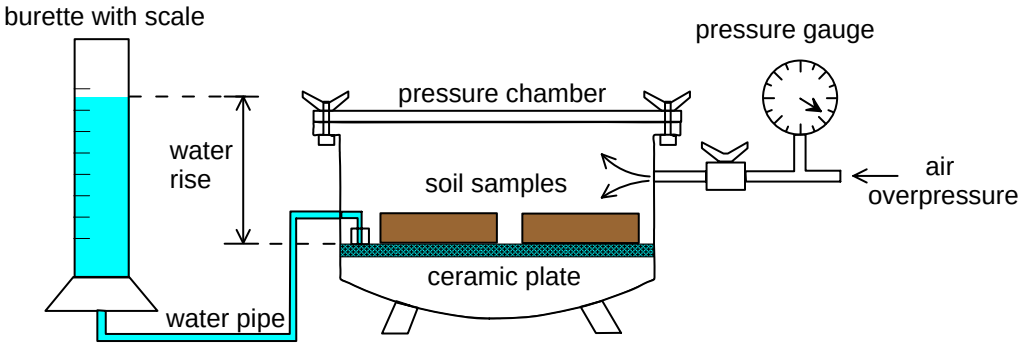

Figure 6.11: Schematic illustration of the axis translation technique setup using a conventional pressure plate apparatus.

membrane plate at known initial water content and dry density. The ceramic membrane plate, including the soil samples placed on it, is installed into a pressure chamber that is air-tightly closed. The ceramic membrane plate is connected via water pipe to a burette outside the pressure chamber. The water in the burette is balanced at the top of the ceramic membrane plate to keep the plate saturated. Prior to the test, the water level is recorded to obtain an initial value. In contrast to the hanging column test, the pressure plate apparatus uses air overpressure to induce suction in the soil samples. A pressure gauge is used to apply a defined air overpressure that forces the soil samples to drain water. As the soil samples start draining, the water flows through the water pipes out of the chamber into a burette. The drainage of water causes the water level in the burette to rise. The water drainage continues until equilibrium is reached. At equilibrium conditions, the soil suction compensates the applied air overpressure, which is indicated by a constant water level in the burette. The water levels before and after application of the air-overpressure are used to balance the amount of drained water, and to calculate the actual gravimetric water content based on the initial water content. Then, the air overpressure is step-wise increased to obtain several points on the SWCC in a suction range from 25 kPa $\leq \Psi_t \leq$ 400 kPa.

The **chilled mirror hygrometer** method was used to determine the high suction range from 400 kPa $\leq \Psi_t \leq$ 100 MPa. As with the compaction test, a WP4T Dewpoint Potentiameter from Decagon Devices was employed to measure the soil suction (see Section 6.3).

The measurement principles of the methods used for soil suction below 400 kPa and the chilled mirror hygrometer are very different. The literature review showed that these methods even measure different water potentials. As shown in Table 3.1, the hanging column test and pressure plate apparatus measure the matric suction, Ψ_M. In contrast, the chilled mirror hygrometer measures the total suction, Ψ_t, which includes the Ψ_M and osmotic suction, Ψ_O. However, since deionised water for pre-treatment and preparation of the soil samples was used, it can be assumed that the influence of osmotic suction was negligibly low. Under

this assumption, the matric suction was equal to the total suction, $\Psi_t = \Psi_M$. By combining these three experimental methods, the measurable suction range was maximised from 0 kPa $\leq \Psi_t \leq$ 100 MPa.

To measure the dielectric behaviour of the soil under shrinkage, the VNA technique was employed in combination with 1-port reflection measurements. An Agilent E5061 ENA VNA (see Figure 6.4A) was used with an in-house-made OE probe to measure the reflection S_{11}-parameter in a frequency range from 1 MHz to 3 GHz. As no appropriate commercial probes were available, the in-house-made probe was specifically designed for the shrinkage test of fine-grained soils. Figure 6.12 shows a photograph of the in-house-made OE probe.

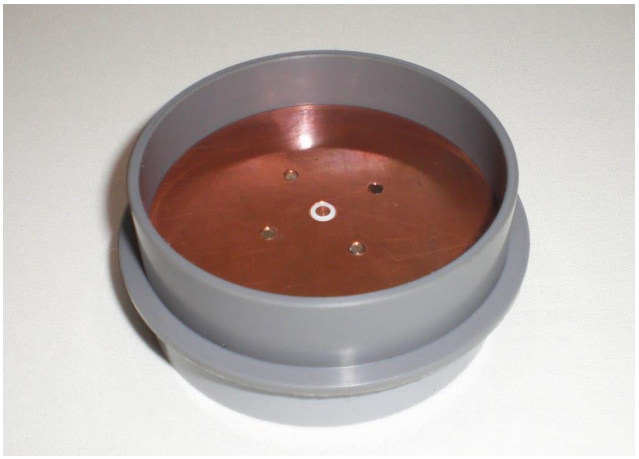

Figure 6.12: Photograph of the in-house made OE probe based on a modified N-type connector. On top of the probe, a copper plate and sealed sample holder were assembled to serve as a cup to contain liquids and other materials.

The OE probe was connected via a conventional coaxial cable to the VNA. The soil samples were installed into the container of the OE probe. While the soil was shrinking, the reflection S_{11}-parameter was measured under controlled environmental condition in a frequency range from 1 MHz to 3 GHz. Based on the S_{11}-parameter measurement, the relative effective complex permittivity, $\varepsilon^{\star}_{r;\text{eff}}$, could be determined for this frequency range.

6.4.3 Soil preparation and experimental procedure

A methodology and experimental procedure were developed that had to be strictly followed to correctly test the soils to determine the coupled mechanical, hydraulic and dielectric soil parameters. Since the experiments were run individually, starting from the same initial conditions and with similar boundary conditions, several factors could influence the success of the

subsequent combined analysis. Thus, it was of paramount importance to maintain consistency throughout the experiments. The following conditions were identical for the shrinkage test, soil suction measurements and dielectric measurements:

- Soil pre-treatment, such as segregation of coarse-grained particles, was conducted according to ASTM D4943-08 [1].
- Soil sample preparation plays an important role because several parameters can affect the shrinkage behaviour and SWCC, such as initial water content and density [127, 269]. Therefore, the procedure for soil sample preparation was identical for all experiments in order to ensure exactly the same initial conditions at the beginning of the tests. Special care was taken during soil sample preparation to guarantee well-defined and reproducible initial conditions.
- The same sample sizes were chosen for all experiments to avoid any effect caused by the geometry on the results. The shrinkage ring, sample ring for the SWCC determination, and sample holder of the OE probe were identical in dimension, with the same diameter and height.
- The tests all used the same technique to install the soil mass into the sample ring and sample holder.
- The environmental conditions were controlled and kept constant throughout the experimental process, at 23 °C temperature and 55 % relative humidity.

The initial water content was chosen to be 1.1 times the LL for all tests. Prior to the shrinkage test, the investigated soils, AS and KA, were pre-treated and prepared according to ASTM D4943-08 [1]. The soils were pre-treated at dry conditions after slowly air drying under controlled environmental conditions. The dried soil was sieved with a mesh opening of 425 μm to segregate possible coarse-grained particles. Samples were prepared from soil fraction passing through the mesh opening. The soil was wetted with deionised water to a water content of 1.1 times the LL to obtain slurry soil consistency. The soil at slurry state was left to settle for 72 hours in a sealed container in order to ensure homogenisation of the soil.

In the following, the test methodology is explained and the experimental procedure is summarised to provide a better overview of the overall experimental process:

1. Six shrinkage tests on each sample with the same initial condition were performed to determine the average and deviation of the shrinkage curve. A plastic plate was used as a base for the shrinkage test. The shrinkage ring, with dimensions according to

Figure 3.1, was placed on top of the plastic plate. Prior to the test, the inside of the shrinkage ring and surface of the shrinkage plate were slightly lubricated with grease to prevent soil sticking to the surface, which may have caused shrinkage cracks or irregular and asymmetric volume changes. The mass and volume of the greased shrinkage ring and shrinkage plate were regularly weighed and recorded. Then, the prepared soil mass was carefully installed into the shrinkage ring using a spatula. A small amount of soil was first placed into the shrinkage ring and distributed to the ring edges by slightly tapping the base on the preparation table. Then, more soil mass was added and the procedure was repeated until the soil mass was equally distributed and slightly overfilled the shrinkage ring. Special care had to be taken to avoid any air bubbles and air gaps in the soil sample. The soil mass should fill the complete volume of the shrinkage ring to obtain a regular cylindrical shape. By doing so, the soil sample volume corresponds to the shrinkage ring volume. A straight edge was used to level the soil surface to the top of the shrinkage ring, and excess soil was removed. Following that, the base and outer face of the shrinkage ring were cleaned ofadhering soil. Once, the shrinkage sample was prepared, the initial weight was immediately determined. Additionally, three samples were taken from the remaining prepared soil mass to check and determine the initial water content. The soil sample was then air dried under controlled conditions. To do so, the shrinkage test was conducted in a climate chamber (MRC

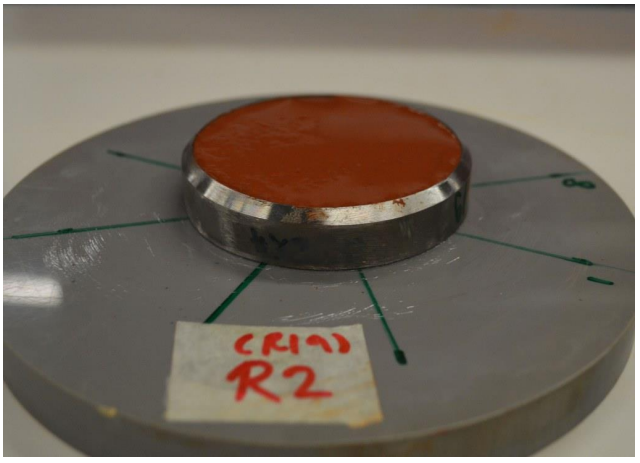

Figure 6.13: Photograph of the AS sample in the early stage of the shrinkage test.

CCG-250) to keep the environmental conditions controlled and constant, as explained before. The mass and geometrical changes while shrinking were recorded continuously in two-hours intervals. To do so, the sample was taken out of the climate chamber and the soil mass was weighed. Figure 6.13 shows a photograph taken during the early stage of a shrinkage test on AS. Geometrical changes were measured using direct determination of sample geometry (see Section 3.3.2). After that, the sample was placed back into the climate chamber. At night, a cap was placed onto the shrinkage ring to

cover the sample in order to minimise the water evaporation and slow the shrinkage process of the sample. The shrinkage test was finished when the sample mass was constant with time. After finishing the shrinkage test, the soil samples were dried completely in an oven at 105°C for 24 hours, and then the final dry density of the samples was determined by the water displacement method (see Section 3.3.2). The final dry density measured by the water displacement method and the directly measured dry density were compared to evaluate and assess the accuracy of the dry density resulting from the direct measurements.

2. The soil suction was tested parallel to the shrinkage tests. The hanging column test was prepared similarly to the shrinkage test. A sample ring was placed on a saturated filter paper. The weights of the sample ring and wet filter paper were recorded. Then, the sample ring and filter paper were placed on a plastic plate to prepare the sample. The sample preparation followed exactly the procedure explained previously for the shrinkage test. Figure 6.14A shows a soil sample prepared in a sample ring that was placed on the saturated filter paper and plastic plate.

(a) (b) (c)

Figure 6.14: Photographs of hanging column test on KA: (A) soil sample prepared in a sample ring placed on a saturated filter paper; (B) close-up view of measuring cylinder containing a KA sample, which is placed on top of the saturated ceramic plate; and (C) view of the entire setup, as schematically shown in Figure 6.10.

After sample preparation, the sample ring with soil was weighed and recorded. Three samples were taken from the remaining prepared soil mass to determine the initial water content. Then, the prepared sample, including the filter paper, was installed into the measuring cylinder. As shown in Figure 6.14B, the sample was placed on top of the

saturated ceramic plate in the measuring cylinder. The filter paper between the sample and ceramic plate prevented fine soil particles from blocking the micro-pores in the ceramic plate. Further, it was absolutely necessary to ensure good hydraulic contact between the sample and saturated ceramic plate. A foil was used to close the measuring cylinder and prevent water evaporation of the sample. Figure 6.14C illustrates the entire test setup of the hanging column test, which indicates the climate chamber located on the platform. The burette was fixed to the left of the climate chamber, which was elevated to the level of the saturated ceramic plate. Once the sample was accurately installed into the measuring cylinder, the actual hanging column test began, as explained in Section 6.4.2. Different soil suctions were induced by the hanging water column up to 2 m, which was equal to $\Psi_t = 20\,\text{kPa}$. The gravimetric water content was balanced for each hanging water column level. After finishing the hanging column test, the soil sample was removed and the volume change was determined by the water displacement method, according to Section 3.3.2.

3. The pressure plate apparatus available for this study had the capacity to install four membrane plates at the same time. As the use of the pressure plate apparatus was extremely time consuming, four sets of soil samples were tested simultaneously. Figure 6.15B illustrates the entire setup of the pressure plate apparatus.

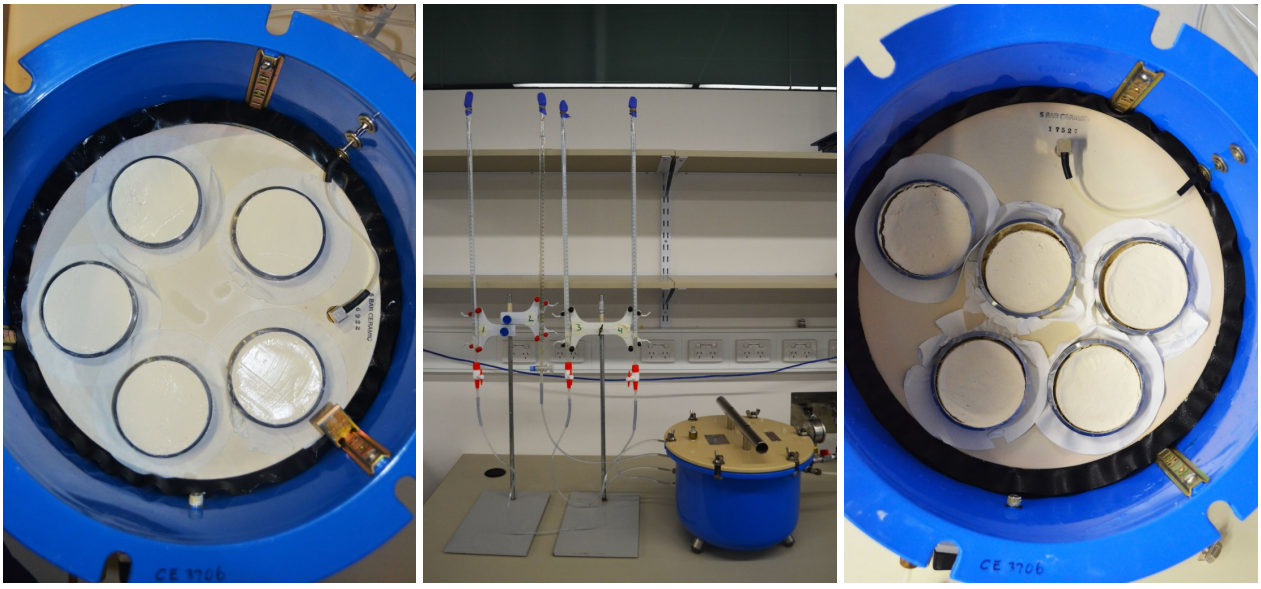

(a) (b) (c)

Figure 6.15: Photographs of axis translation technique on KA using the pressure plate apparatus: (A) photograph prior to the test, showing five prepared soil samples placed on saturated ceramic membrane plate; (B) view of the entire setup during axis translation technique test, showing the pressure plate apparatus with four burettes; and (C) five soil samples placed on saturated ceramic membrane plate after the 400 kPa pressure step, indicating that the volume changes occurred during the test.

Four burettes were used to balance the water drainage during the test for each ceramic membrane plate. The sample preparation procedure basically followed the procedure for the hanging column test, with the difference being that many more samples needed to be prepared. To obtain a representative average value of the soil suction measurements, five soil samples were tested on each ceramic membrane plate (see Figure 6.15A). The ceramic membrane plate was connected via water tube to a burette that balanced the water drainage as a sum of the five samples. The pressure plate apparatus held a pressure gauge that allowed accurate adjustment of the desired air overpressure. Once all soil samples were prepared onto the ceramic membrane plate, the pressure chamber was air-tightly closed and the first pressure step of 25 kPa was applied. Once the water level in the burettes indicated a constant level, equilibrium was reached. At this point, the water level was recorded and the gravimetric water content corresponding to the pressure step was balanced using the initially measured water content. The magnitude of the further pressure steps were doubled each time, up to 400 kPa. Figure 6.15C shows soil samples of KA on a ceramic membrane plate after the 400 kPa pressure step was applied. Comparing the sample before the test in Figure 6.15A and after the test in 6.15C, it is obvious that the soil samples underwent remarkable volume changes due to water drainage. In order to quantify the extent of volume changes, a ceramic membrane plate was removed from the pressure chamber after each pressure step of 100, 200 and 400 kPa, and the volume of the removed samples was determined with the water displacement method.

4. As aforementioned, three ceramic membrane plates were removed from the pressure plate apparatus and used to measure the volume changes during the axis translation technique. Thus, one ceramic membrane plate was left after the test to measure soil suction up to 100 MPa using the chilled mirror hygrometer. The five remaining soil samples were divided into subsamples with a minimum weight of 10 g, similar to the soil suction measurement on the compacted samples in Section 6.3.5. These subsamples were air dried under controlled environmental conditions to slowly reduce the water content. Successively, the subsamples were taken at different time steps to measure the soil suction using the WP4T Dewpoint Potentiameter. Three measurements were performed on each subsample to obtain an average soil suction value. The gravimetric water content corresponding to the suction measurement was measured on each subsample.

5. Dielectric measurements on shrinking samples were taken using the VNA in combination with the OE probe. Since dielectric measurements are extremely sensitive to any movement and disturbance of the OE probe, it was not possible to measure mass and volume changes of the sample in the OE probe. Hence, three reference samples

were prepared to representatively measure mass changes during shrinkage, parallel to the dielectric measurements. Further, the test needed to be conducted under absolutely controlled environmental conditions because dielectric measurements (or $\varepsilon^{\star}_{r;\text{eff}}$) are strongly temperature dependent. To achieve this, the dielectric measurements on soil samples were undertaken in a climate chamber (MRC CCG-250) with 23 °C temperature and 55 % relative humidity. Figure 6.16A illustrates the entire setup for the combined investigation of the dielectric properties and shrinkage behaviour. The VNA was located on the right side of the climate chamber during the test. The coaxial cables of the VNA were led through an air-tightly sealed opening into the climate chamber. The VNA was featured with a PC screen to observe the changing dielectric spectrum during the shrinkage test. Further, a PC located on the left side of the climate chamber was used to control the balance inside the climate chamber. Figure 6.16B shows a close-up view of the inside of the climate chamber. On the right, two OE probes are shown containing the sample at which the dielectric properties were measured during the shrinkage. The balance (Ohaus Pioneer$^{\text{TM}}$) can be seen on the left side of Figure 6.16B. Three samples were placed on the top of the balance as reference to the samples in the OE probes. The balance was connected via a RS-232 interface to the PC, which was located on the left to the climate chamber. A MATLAB based code was written to control the balance via the PC. This code allowed continuous measurement of mass changes during shrinkage. A Visual Basic code was used to control the VNA and to take continuous dielectric measurements at defined time intervals. The PC and VNA were synchronised in order to take dielectric measurement and sample weight readings at the same time in 10-minute intervals.

Prior to the test, the VNA and coaxial cable were calibrated using a mechanical calibration kit from Agilent, type N 85032F. As explained in Section 5.3.1, 1-port reflection measurements using a VNA require an open, short, and load calibration. After this first calibration step, the OE probe was connected to the end of the coaxial cable. The second calibration step, for the OE probe itself, included measuring six additional calibration materials, as explained in Section 5.5.1. Once the entire setup was calibrated, the two samples were prepared in the OE probes. The OE probes with the soil sample were weighed to determine the soil mass. Three samples were prepared as reference samples, and placed on the balance. The test began by simultaneously running the MATLAB code and Visual Basic code. Then, three samples were taken from the remaining soil mass to determine the exact water content at the beginning of the test. The experiment was stopped when the output of the continuous mass measurements indicated a constant value. The soil samples were then removed from the climate chamber, as shown in Figure 6.16C. It can be seen that the samples shrunk similarly in dimension. The soil samples of the OE probe were visually investigated in detail to check

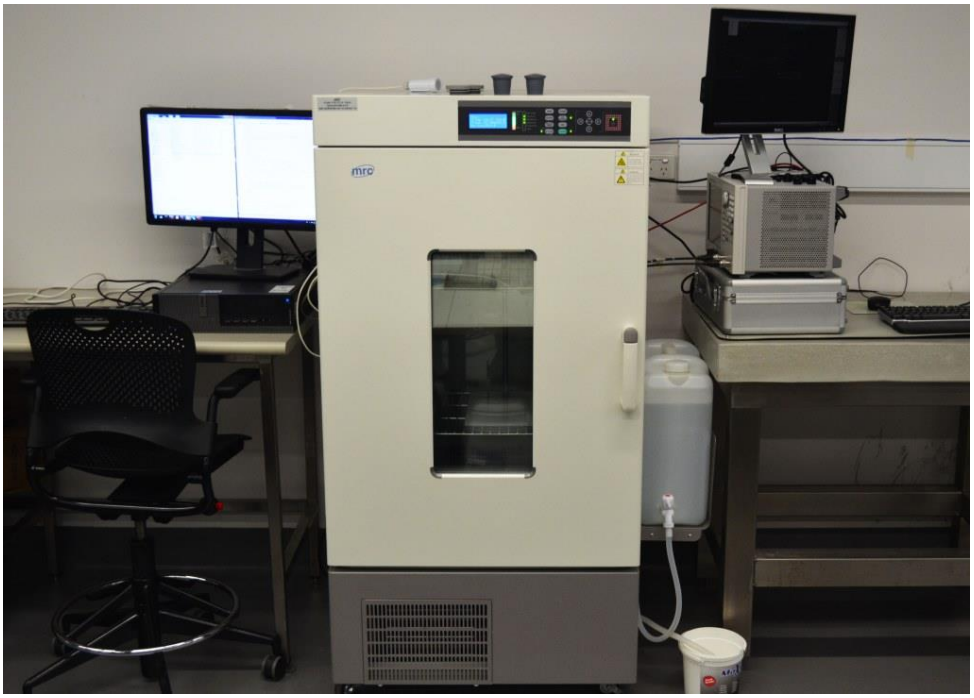

(a)

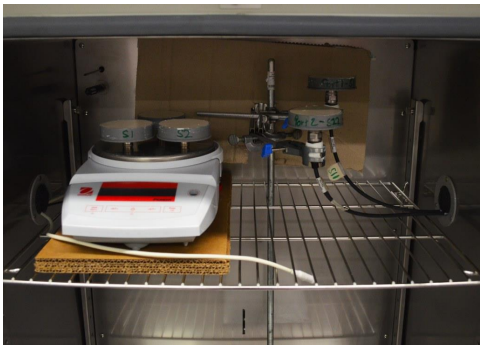

(b)

(c)

Figure 6.16: Photographs of the combined dielectric measurement and shrinkage test on KA: (A) view of the entire setup – PC controlling the balance on the left, climate chamber containing the samples under test in the mid, and VNA on the right; (B) view inside the climate chamber, showing the balance with three reference samples on the left, and two OE probe containing samples on the right; (C) five soil samples after the test was finished.

whether there was good contact between the soil sample and probe aperture. The importance of this investigation will be discussed in detail later. In a final step, the volume of samples was measured with the water displacement method to determine the dry density and to compare them in regard to value consistency.

6.5 Summary

This chapter introduced the soils under investigation and the related standard soil parameters, including mineralogy. It determined the particle size distribution and consistency limits in preliminary experimental investigations. Based on the standard parameters, the soils under investigation were classified as inorganic clays with extremely high plasticity.

This chapter extensively explained the developed methodology and experimental procedure of coupled soil characterisation during the compaction test and shrinkage test. A step-wise procedure had to be developed, together with the development of setups for the combined investigation of the shrinkage curve, SWCC and dielectric behaviour.

The following chapter focuses on the results and analysis of the experimental data.

Chapter 7

Results and analysis

7.1 Introduction

This chapter presents the results of the experimental investigations explained in the previous chapter. This chapter is divided into two sections with similar structure – compaction test and shrinkage test. The first section presents the results of the compaction tests, including analysis of the compaction curve itself. The second section presents the results of the shrinkage test. In both sections, the measured experimental data are first explained and discussed. Subsequently, appropriate models are taken from the literature to quantitatively describe and parameterise the experimental results. The shrinkage curve and SWCC of compacted and shrinking soil samples are established and parameterised. In a further step, the measured dielectric spectra are analysed and, for selected frequencies, compared against existing material-specific empirical calibration equations and theoretical mixture approaches. The results of the dielectric spectrum prediction, based on enhanced theoretical mixture approaches coupled with the shrinkage curve and SWCC, are shown and compared to the dielectric measurements. Finally, the results of the spectrum analysis of the frequency dependent dielectric soil parameters during compaction and shrinkage are presented.

7.2 Compaction test

7.2.1 Compaction curve

The experimental procedure, as explained in the previous chapter, was performed on all prepared soil samples of AS and KA. Thus, the analysis of the experimental data for each

compaction test followed the same principle and analysis pattern. The compaction curve for each test was constructed based on the record of the bulk soil mass, compaction mould volume and water content determination after the compaction procedure. The compaction curve results of each tests, both standard and modified, are illustrated in Figure 7.1, in which the dry density is plotted against the gravimetric water content. The compaction tests were conducted in nearly 2.0% water content steps. A slightly larger gap of compaction tests can be observed for the standard compaction tests on KA in the water content range from 36.0% to 40.0%.

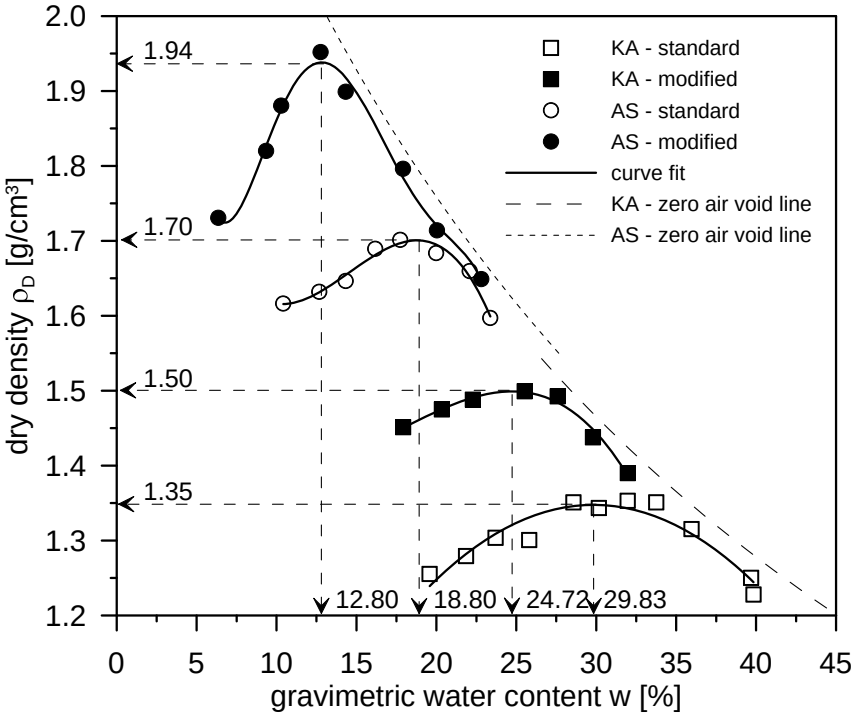

Figure 7.1: Standard and modified compaction curve determined on AS and KA according to ASTM D698-12 [4] and ASTM D1557-12 [5]. The curve fits are indicated, which were used to determine the optimum water content, w_{Pr}, and optimum dry density, $\rho_{D,Pr}$, for each compaction curve.

It can be seen that the obtained compaction curves satisfied the typical curve trend of compaction tests, with distinct peak values that are widely known as optimum water content, w_{Pr}, and optimum dry density, $\rho_{D,Pr}$. Figure 7.1 shows additionally the curve fits for the compaction tests on AS and KA, based on polynomial fitting equations (see Appendix A.1). Based on these curve fits, both w_{Pr} and $\rho_{D,Pr}$ were determined for each compaction curve as they are shown in Figure 7.1. The region with water content lower than w_{Pr} is defined as the dry side of the compaction curve. The region with higher water content than w_{Pr} is considered the wet side. For water content higher than w_{Pr} on the wet side of the compaction curve, the curve runs along the zero air void line at nearly saturated soil conditions. On the

dry side of the compaction curve with $w \leq w_{Pr}$, the curve runs in highly unsaturated soil conditions, with a saturation degree of $S \ll 1.0$. The appearance of a peak in the compaction curve can be explained from microstructural considerations. As schematically shown in Figure 2.7 in Section 2.5.2, fine-grained soils form a pore structure consisting of intra-aggregate and inter-aggregate pores. Soil prepared with a water content located on the dry side of the compaction curve exhibits a continuous air phase [265]. Menisci between the air and water phase are built at contact points between the clay aggregates. When applying compaction energy to the soil, these menisci resist aggregate slippage, which results in a decrease of densification, with dry density lower than the optimum dry density [265]. In contrast, a continuous water phase with included air bubbles is found on the wet side of the compaction curve, at which the soil is nearly saturated. When soil prepared on the wet side is subject to compaction, the water is restricted in draining out of the soil. This effect creates partially undrained conditions [265] at which pore water pressure increases under compaction, which prevents further densification of the soil located on the wet side [265].

In general, it is expected that tests with enhanced compaction effort result in higher densification of soil. As a result, the modified compaction tests showed higher values of ρ_D at a given water content than did the standard compaction tests. As can be seen in Figure 7.1, the modified compaction tests on AS and KA showed a curve that was clearly located above the standard compaction curves. Moreover, the modified compaction curves shifted to lower water content, relative to the standard compaction curves. As a result, the w_{Pr} values of the modified compaction curves were found for both AS and KA at lower water content than the w_{Pr} values of the standard compaction curves. The $\rho_{D,Pr}$ of the modified compaction curves for AS and KA were generally higher than those of the standard compaction curves. Comparing the compaction tests between KA and AS, it can be noted that the optimum dry densities of standard and modified compaction tests of KA showed lower values than those of AS. This is reasonable because KA soil consists of a much higher clay content than does AS; thus, KA is less compactible. In addition, the compaction curves of KA shifted relative to higher water content compared to the compaction curves of AS. This resulted in higher w_{Pr} values of the compaction curves of KA.

It was observed, particularly in the case of KA, that the soil surface of samples on the dry side and wet side of the compaction curve looked different in terms of the visual soil texture. High-resolution photographs of the soil texture were taken with a digital single-lens reflex camera. Figure 7.2 shows high-resolution photographs of soil texture of two KA samples that were compacted with modified compaction effort. Figure 7.2A is a photograph of a sample at 22.3% water content that was located on the dry side of the compaction curve. Figure 7.2B shows a photograph of a sample at 32.0% water content that was located on the wet side of the compaction curve. Despite the same soil preparation and experimental procedure for

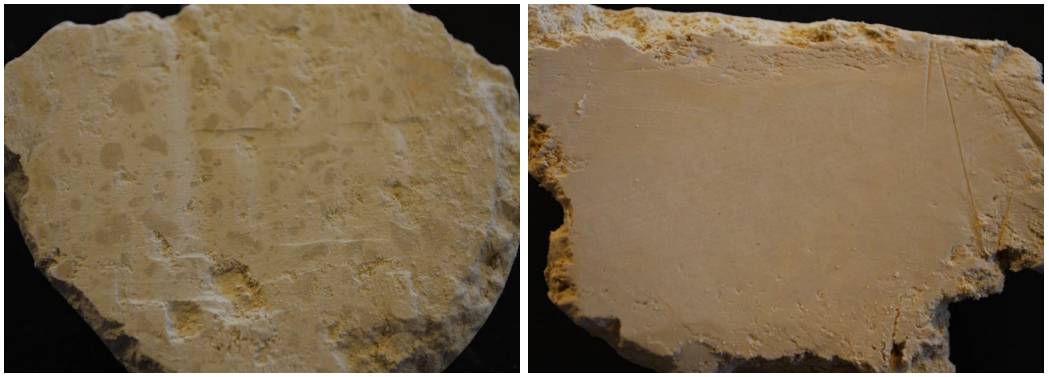

(a) (b)

Figure 7.2: High-resolution photographs of the texture of soil samples after compaction test with modified effort: (A) modified compacted KA sample at 22.3% water content on the dry side of the compaction curve, with water content lower than the optimum water content. (B) modified compacted KA sample at 32.0% water content on the wet side of the compaction curve, with water content higher than the optimum water content.

both samples, it is clearly visible that the soil textures differed remarkably. The soil texture on the dry side of the compaction curve exhibited distinct inhomogeneities that were visible as distinguishable shaded spots on the soil surface. Darker shaded spots indicate areas with higher water content, while lighter spots are areas with lower water content. Thus, these observed inhomogeneities suggest that unequally distributed soil water phase was present in more unsaturated soil conditions. In contrast, the soil texture on the wet side of the compaction seemed to be more homogeneous. As can be seen in Figure 7.2B, no inhomogeneities were identifiable, and the same soil colour was found all over the sample surface. This indicated that an equally distributed soil water phase could be assumed to exist for nearly saturated soil samples on the wet side of the compaction curve close to the zero air void line.

One might argue that this phenomenon was caused by inappropriate soil preparation and different sample water content. Hence, it should be further noted that the soil texture can differ even if the water content of two samples is the same. For instance, two soil samples of KA were prepared in the same manner with nearly identical water contents ($w = 25.5\%$ and $w = 25.8\%$). Thus, it can be assumed that the water distribution in the loose soil state before compaction was exactly the same for both samples. Then, the sample with $w = 25.8\%$ was compacted with standard compaction effort, and the sample with $w = 25.5\%$ was compacte with modified compaction effort. Figure 7.1 shows that the standard compacted sample was located on the dry side of the compaction curve, with $w = 25.8 < w_{Pr} = 29.83\%$. The modified compacted sample with $w = 25.5\%$ was located on the wet side of the compaction curve, but close to $w_{Pr} = 24.72\%$. Both samples were visually inspected and, again, the same pattern of soil textures was identified, regardless of the water content. The sample on the dry side of the compaction curve showed a soil texture with a visually inhomogeneous soil water distribution

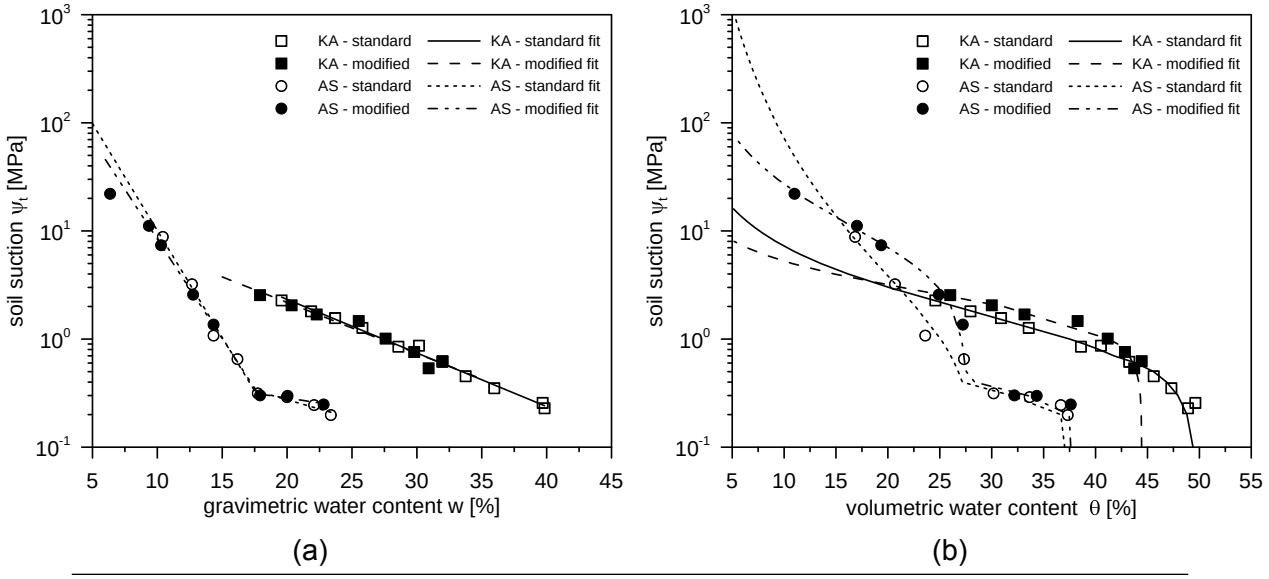

Figure 7.3: SWCC of drying path for standard and modified compaction curve of KA and AS measured by the WP4T: (A) SWCC in a semi-logarithmic illustration of soil suction related to the measured gravimetric water content, and (B) SWCC in a semi-logarithmic illustration of soil suction related to the calculated volumetric water content.

similar to Figure 7.2A. The soil texture on the wet side of the compaction curve was found to be more homogeneous with equal water distribution, similar to Figure 7.2B. It can be said that, regardless of the water content, homogeneous soil texture and water distribution were found for compaction tests close to the zero air void line, where a nearly saturated condition was expected. Thus, homogeneous soil texture with equal water distribution can be determined by appropriate compaction effort and soil densification to achieve almost saturated conditions for a given water content.

In addition to the compaction tests, the soil suction was measured using the WP4T to obtain the SWCC for each compaction curve. Figure 7.3 shows the obtained SWCCs for both the standard and modified compaction curves of KA and AS. Figure 7.3A illustrates the SWCCs in a semi-logarithmic relationship of soil suction and gravimetric water content. It was observed for all SWCCs that the lowest soil suction values were measured for the highest water content. Consistently for all SWCCs, the soil suction increased with decreasing gravimetric water content. The highest soil suction was measured at the lowest water content. It became obvious when comparing the SWCCs dependent on the gravimetric water content of AS and KA that the curves differed in their trends and shapes. In the case of KA, the SWCCs of both the standard and modified compaction curves followed a nearly linear relationship in a semi-logarithmic plot. Both SWCCs of KA were almost identical, with no distinct difference observed. In contrast to the SWCCs of KA, the SWCCs of AS followed a different trend that seemed to indicate a more bilinear relationship with the gravimetric water content. In both curves of AS, a water content could be observed that could be considered the intersection

of the bilinear relationship. The intersection point was found at a water content of $w = 17.5\%$. For water content below this intersection point, the slope of the SWCC was much steeper, resulting in much higher suction changes with varying water content. For water content above this intersection point, the slope of SWCCs was low, which resulted in little suction changes with varying water content.

The SWCCs of AS and KA in Figure 7.3A can be directly compared to each other in an overlapping gravimetric water content range from 18% to 24%. In this water content range, the SWCCs of KA were located above the SWCCs of AS. The soil suctions at a given water content in this range were higher for KA than AS. This might be for two reasons:

1. The clay content of KA was much higher than for AS; thus, an increased interaction between the solid particle surface and water phase was expected, as theoretically explained in Section 2.4. This increased interaction results in higher capillary and adsorptive forces, which dominate the SWCC of natural soils (with low salinity at which osmotic suction is reasonably neglected).

2. This water content range is lower than the w_{Pr} of the standard and modified compaction curve of KA. Looking at Figure 7.1, it can be seen that this water content range is located on the dry side of both compaction curves of KA, which means unsaturated soil conditions were expected. At unsaturated soil conditions, the amount of interfaces between the water and air phase increases with a decreasing degree of saturation as more air enters the water-filled pore space. As discussed in Section 2.4.2, these interfaces between the water and air phase are described by capillarity. Thus, an increased amount of interfaces results in higher soil suction due to increased capillary forces.

A quantitative description of the SWCC for the compaction curves based on the gravimetric water content is not realisable because the SWCC equations (previously introduced in Section 2.4.3) describe the soil suction as a function of the volumetric water content. Therefore, Figure 7.3B shows the soil suction of the compaction tests related to the volumetric water content, which is calculated based on Equation 2.10, with ρ_D measured in the compaction mould. As can be seen, the shape and curve trends of the SWCC change when depending on the volumetric water content. Instead of a linear relationship, as in Figure 7.3A, the SWCCs of KA depending on θ show a curvilinear relationship. Comparing the SWCCs in Figure 7.3B, it can be seen that the SWCCs of KA and AS show different curve shapes. The SWCCs of KA show a smooth progression over the entire curve, whereas the SWCCs of AS show distinct points in a water content range from $25 \leq w \leq 30$, where the curve progression changes abruptly. In order to deliver a quantitative description and investigate the difference of curve shapes, the SWCCs were parametrised using a bimodal van Genuchten equation,

according to Equation 2.14 in Section 2.4.3. Two assumptions were made to enable a successful and accurate parametrisation of the SWCCs:

1. In order to set upper and lower limits to model the SWCCs, θ_S and θ_R were approximated. The experimental data measured with highest water content were taken as θ_S to limit the low suction range of the SWCC. In a first approach, this assumption was justifiable because the highest water content was located on the wet side of the compaction curve, where nearly saturated soil conditions prevail.

2. θ_R was taken to be zero for all investigated soils. Even though the low suction range was not fully covered by the SWCCs, it was reasonable to assume that $\theta_R = 0$ for sufficiently high soil suction.

Based on these two assumptions, the SWCCs of both AS and KA were modelled with two weighting factors, W_i, representing the bimodal relationship between Ψ_t and θ. Table 7.1 gives a tabular overview of the fitting parameters obtained by modelling the SWCCs.

Table 7.1: Tabular overview of parameters obtained by fitting the SWCCs of the standard and modified compaction tests on KA and AS.

Soil		AS		KA	
Compaction test		Standard	Modified	Standard	Modified
	θ_S	37.32	37.62	49.62	44.45
	θ_R	0	0	0	0
Mode 1	W	0.77	0.73	0.98	0.99
	a_{vG}	0.958	0.162	0.854	0.449
	n_{vG}	1.248	1.665	1.858	2.658
	m_{vG}	0.199	0.399	0.462	0.624
Mode 2	W	0.23	0.27	0.02	0.01
	a_{vG}	3.342	3.254	1.640	1.010
	n_{vG}	25.583	0.000	44.363	45.319
	m_{vG}	0.961	0.900	0.977	0.978

The results of this parameterisation are shown in Figure 7.3B. It can be seen that the parametrised models perfectly fitted the experimental data of the SWCCs. To illustrate the fundamental difference of the SWCCs between AS and KA, Figure 7.4 shows the SWCC modelling results with different modes for the modified compaction tests. It should be mentioned at this point that almost identical trends were obtained for the SWCCs of the standard compaction test. Figure 7.4A shows the parameterisation of the SWCC for AS. A distinct change in curve shape was observed at $\theta \approx 27.5\%$. Two explicit modes were observed for the SWCC of AS with weighting factors, as shown in Table 7.1. For low water content, associated with the dry side of the compaction curve, the soil suctions were perfectly described by Mode 1

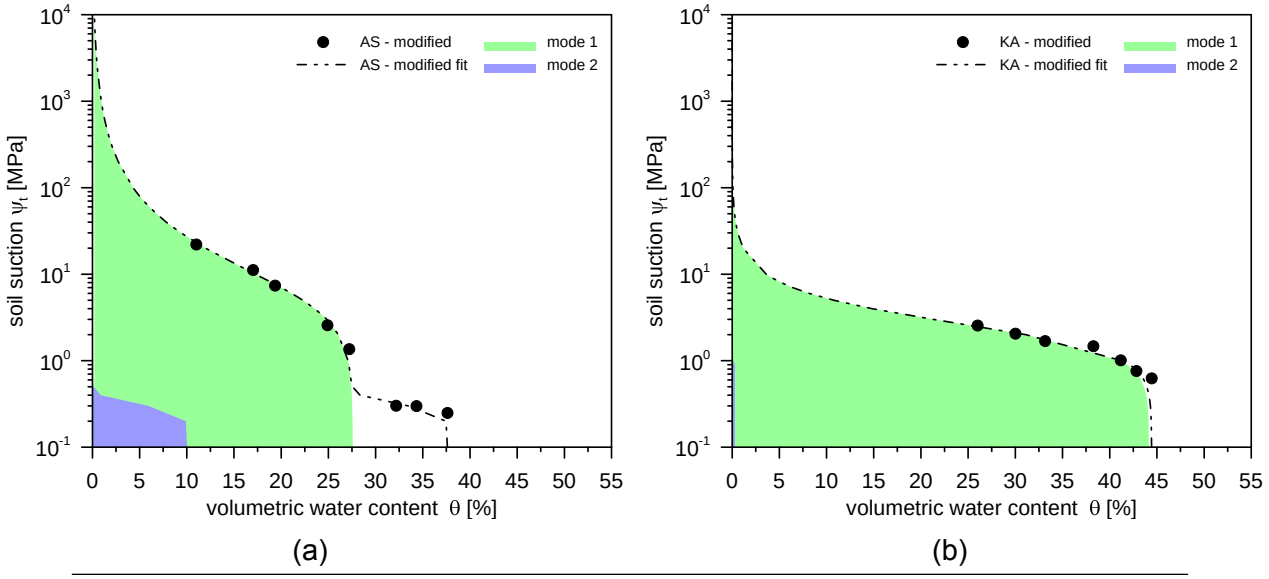

Figure 7.4: Fitting result of the SWCC for modified compaction curves of KA and AS using bimodal van Genuchten model. Shaded areas indicate the different modes observed in the SWCC.

of the van Genuchten equation (see the green shaded area in Figure 7.4A). For high water content located on the wet side of the compaction curve, a second mode was required to parametrise the soil suction as a bimodal relationship. This result indicated that the compacted soil samples of AS were characterised by a heterogeneous pore system over the entire compaction curve, which caused the bimodal character of the SWCC [68]. In contrast, the parameterisation of the SWCC of KA in Figure 7.4B showed a completely different result. The weighting factor of the second mode was $W = 0.01$, and was significantly lower than the first mode. As a result, the influence of the second mode on the SWCC was negligibly low. Subsequently, the SWCC of KA revealed an unimodal relationship over the entire SWCC. The result demonstrated that the compacted KA soil exhibited a homogeneous pore structure. This observation was reasonable and can be reinforced by Figure 6.2 in Section 6.2, which shows the particle size distribution of the investigated soils. Soil KA is mainly composed of clay with similar particle sizes. Therefore, packing solids with similar size should produce a pore structure with unique dimensions. In contrast, the AS is composed of both clay and silt, which have different particle sizes. A broad range of particle sizes create a more heterogeneous pore system with different pore sizes and dimensions.

To attain more detailed explanations of this finding, additional experiments were required to provide better insight to the pore structure of soils. Possible techniques enabling this insight – such as mercury porosimetry and scanning electron microscopy – have already been proposed and introduced to measure pore size distribution [268, 270, 271, 272, 273, 274, 275, 276]. However, this additional experimental investigation was not the aim of this work; thus, this finding needs to be addressed and further investigated in future research.

7.2.2 Shrinkage behaviour of compacted soil

The shrinkage curve of each compaction soil sample was determined according to the technique and experimental procedure explained in the previous Section 3.3.2. Due to time restrictions in this study, it was not possible to determine the shrinkage curves of the standard compacted KA samples. Figure 7.5 shows the shrinkage curves measured on the compacted soil samples, in which the dry density is plotted against the gravimetric water content.

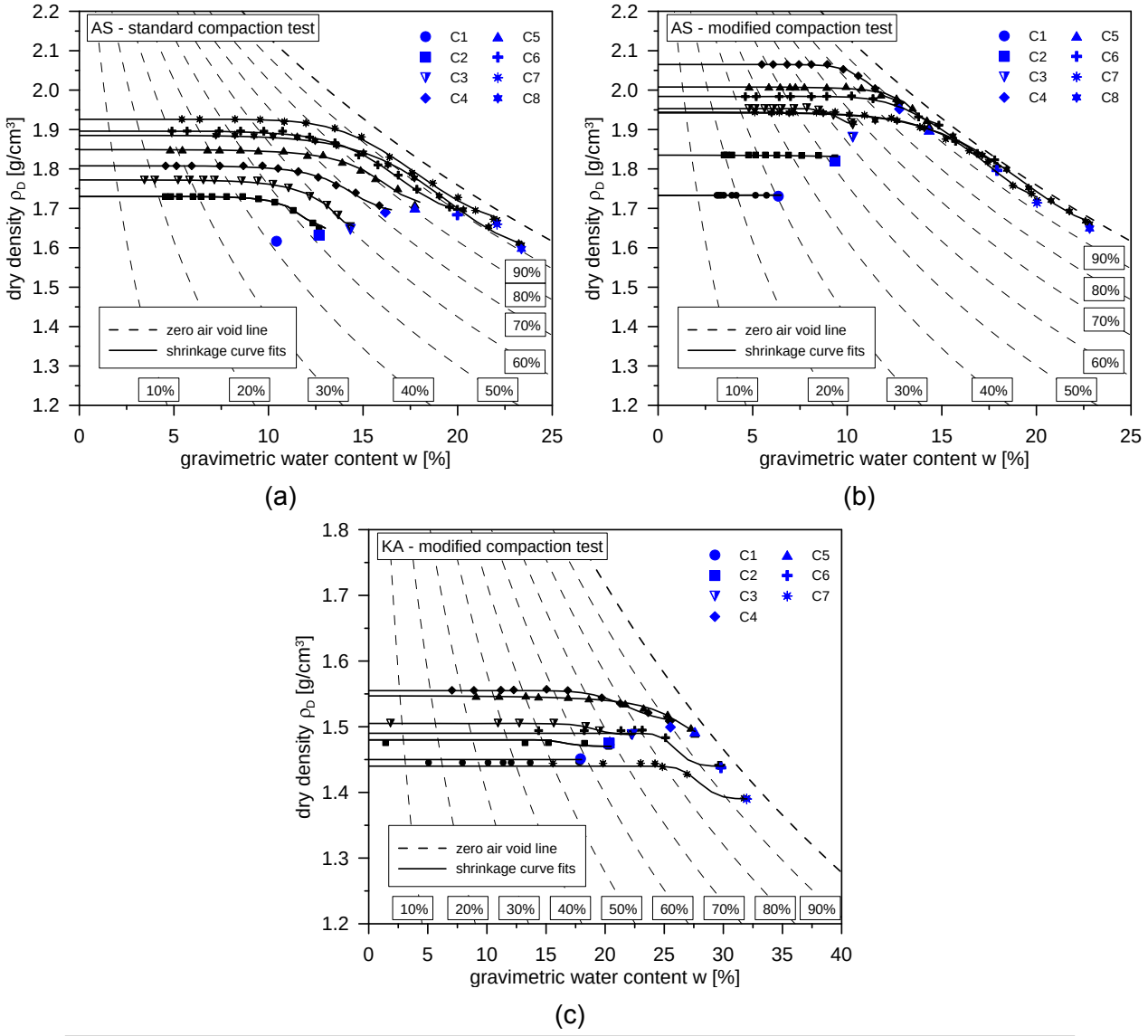

Figure 7.5: Standard and modified compaction curves of AS and KA, including shrinkage curves. The blue symbols indicate the compaction tests and black symbols show the corresponding shrinkage curve. The zero air void line and saturation lines are indicated by the dashed lines. Additionally, shrinkage curves are parameterised using the fitting equation proposed by Peng and Horn [6].

The shrinkage tests were run as long as the SL was reached and no volume changes were observed. In addition to the compaction and shrinkage curves, the zero air void lines and

saturation lines are indicated by dashed lines. The compaction tests are illustrated by blue symbols, and their corresponding shrinkage curves with smaller black symbols. All shrinkage curves started with an initial water content and density close to the compaction test. This confirmed that the shrinkage test samples were not disturbed much when cored from the compaction mould. With ongoing desiccation, the soil lost water content due to water evaporation. The soil volume reduced with decreasing water content, which resulted in increasing dry density. As theoretically explained in Section 2.5.2, the SL was reached when no further soil volume changes occurred. These SLs were observed for all soils, regardless of soil type and compaction effort. The trend of the shrinkage curves indicated that the samples on the wet side of the compaction curve tended to show more distinct shrinkage behaviour than did samples on the dry side of the compaction curve. Further, it was observed for the modified compaction tests that soil compacted on the dry side of the compaction curve presented only minimal or nearly zero shrinkage. This indicated that the higher compaction effort on the soil resulted in lower shrinkage behaviour on the dry side of the compaction curve.

To obtain a quantitative description of the shrinkage behaviour of the compacted soil, the shrinkage curves were parameterised by the fitting Equation 2.17, proposed by Peng and Horn [6] (Section 2.5.3). A MATLAB script was coded that fitted the shrinkage curve based on an algorithm of nonlinear least-squares problems. Figure 7.6 shows two fitting results of AS samples after modified compaction. Sample C8 was located on the wet side of the compaction curve, while C3 was on the dry side. The fitting results of the shrinkage curve are presented in the $\vartheta - e$ - relationship, as proposed by Peng and Horn [6], which can be transferred into the $w - \rho_D$ - relationship (see Section 2.5.2). However, it is more convenient to present the shrinkage curve and its derivatives in the $\vartheta - e$ - relationship.

Figures 7.6A and 7.6C shows the measured shrinkage data indicated by the symbols. To allow optimal comparison of the results, the scale of axis coordinates is kept identical. When comparing the measured shrinkage curves, it is obvious that sample C8 that was compacted on the wet side of the compaction curve showed much more distinct shrinkage behaviour than did C3, which was compacted on the dry side. In addition to the experimental data, the shrinkage curve fits, $e(\vartheta)$, are illustrated by the black line. For both samples, the obtained fits agreed perfectly with the measured experimental data over the entire shrinkage curve. Based on the fitting results, the first three derivatives of the shrinkage curve – $e'(\vartheta)$, $e''(\vartheta)$ and $e'''(\vartheta)$ – were developed. Figure 7.6B and 7.6D show the curve progression of $e'(\vartheta)$, $e''(\vartheta)$ and $e'''(\vartheta)$. The derivatives were used to determine the different shrinkage zones of the shrinkage curves (see the shaded areas in Figure 7.6A and 7.6C). The shrinkage zones were found by the intersections of tangents e_0, e_1 and e_2 (see details in Section 2.5.3). The tangent points of e_0, e_1 and e_2 were determined by finding the roots of the $e''(\vartheta)$ and $e'''(\vartheta)$ in a water content from $0 \leq \vartheta \leq \vartheta_1$. Figures 7.6B and 7.6D present the calculated roots of these

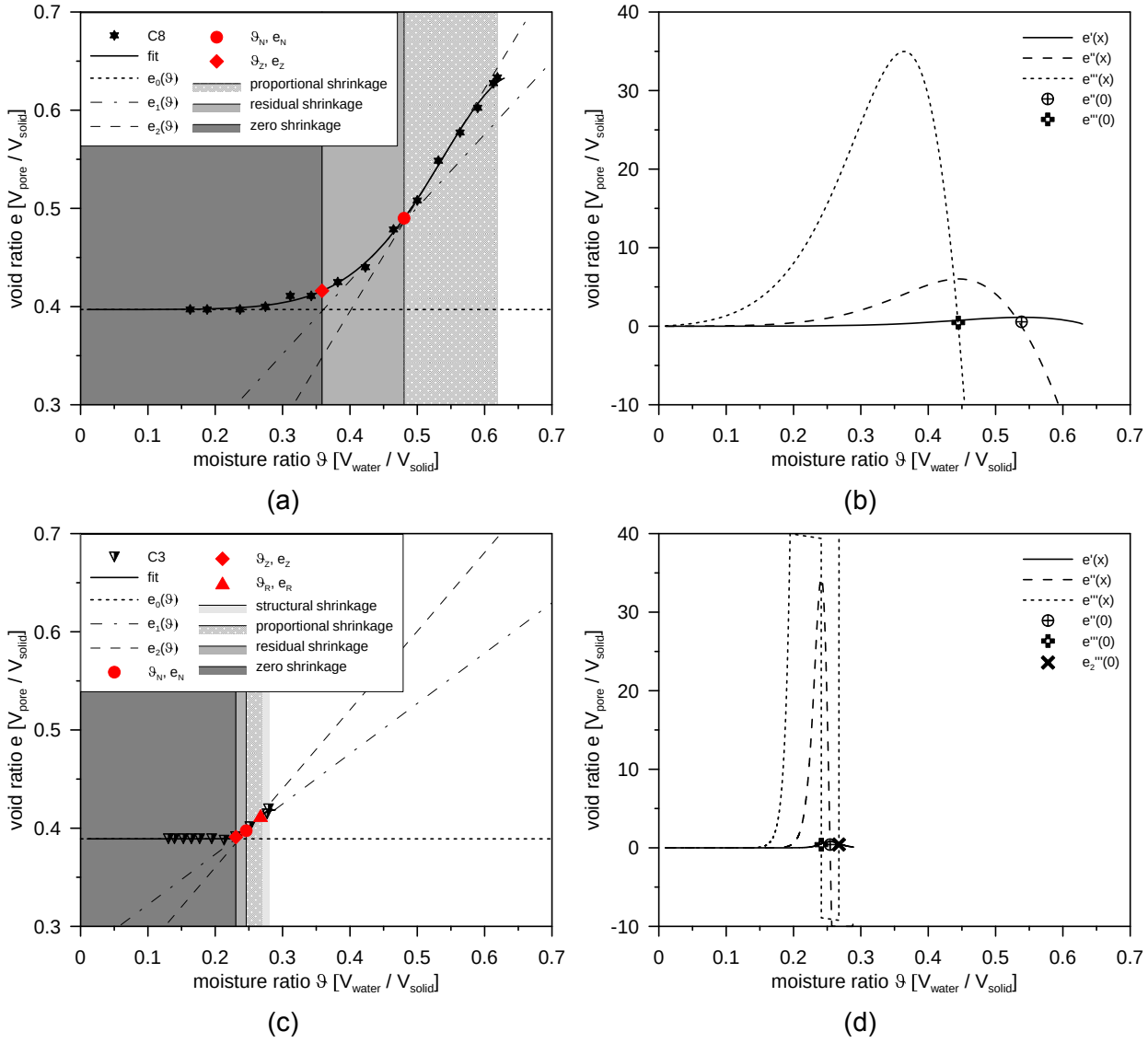

Figure 7.6: Example of two shrinkage curves of AS from modified compaction tests that are modelled with fitting equation proposed by Peng and Horn [6]: (A) and (C) shrinkage curves and fits of sample C3 and C8, including the observed shrinkage zones and their intersection points between the shrinkage zones, and (B) and (D) derivatives of fitted parametrised shrinkage curve equations that are used to determine the inflection points and extremes of the shrinkage curve.

functions, $e''(\vartheta)$ and $e'''(\vartheta)$, in the observed moisture ratio range ($0 \leq \vartheta \leq \vartheta_1$). It can be seen that, for sample C8, one root was only detected for $e'''(\vartheta)$, whereas two roots of $e'''(\vartheta)$ were observed for sample C3.

In both cases, one root was calculated for $e''(\vartheta)$. The slope of the tangents, presented in Figure 7.6A and 7.6C, were calculated using $e'(\vartheta)$. By constructing the tangents to the shrinkage curve, the transition moisture ratios could be calculated from proportional to residual and residual to zero shrinkage. The transition moisture ratio from structural to proportional shrinkage was found at the maximum curvature of $e(\vartheta)$ on the wet side of the shrinkage curve

([6, 86], see details in Section 2.5.3). It can be seen in Figure 7.6A and 7.6C that four shrinkage zones were determined for C3. Similar results with four distinct shrinkage zones for compacted samples were presented in Dhawan et al. [277]. However, the shrinkage curves in Dhawan et al. [277] were not parametrised by an equation, and the shrinkage zones were approached by the geometrisation of straight lines. For sample C8, only three shrinkage zones (proportional, residual, and zero) were detected. Similar results were presented in Birle et al. [127], who observed three shrinkage zones for the shrinkage of standardised compacted soil samples. As stated before, the $e'''(\vartheta)$ of sample C8 revealed only one root that was located on the dry side of the shrinkage curve. As $e'''(\vartheta)$ did not show a second root on the wet side at high moisture ratios, the maximum curvature of the shrinkage curve was missing, which was required to determine the structural shrinkage zone. For sample C3, a maximum curvature of the shrinkage curve was found with a second root of $e'''(\vartheta)$. As a result, sample C3 showed potential structural shrinkage.

Two observations that were made when fitting the shrinkage curve with the proposed model, are worthy of discussion:

1. It was occasionally found that the mathematical determination of the transition moisture ratio from residual to zero shrinkage zone was imprecise. Theoretically, the zero shrinkage zone defines the area where soil should not expose any volume changes. For example, as shown in Figure 7.6A, the intersection of the tangents e_0 and e_1 was located at a moisture ratio of $\vartheta \approx 0.36$. However, it can be seen that the zero shrinkage zone was visually not reached at this moisture ratio. Further volume changes and thus void ratio changes were observed with ongoing moisture ratio decrease below $\vartheta \approx 0.36$.

2. It is noted that the determination of the shrinkage zone of the low shrinking sample located on the dry side of the compaction curve (such as sample C3 in the modified compaction curve of AS) required special discussion. As shown in Figure 7.6B, four shrinkage zones were theoretically identified. Three shrinkage zones – structural, proportional and residual – were determined in an extremely narrow moisture ratio range, where few measurement data existed. When looking at the shrinkage curve of C3 in Figure 7.5C, it seems that the shrinkage curve exhibited only two shrinkage zones: zero and residual shrinkage. It is questionable to expect a proportional shrinkage of soil on the dry side of the compaction curve, where volume changes are extremely low and the shrinkage curve does not proportionally follow a saturation line. The determination of shrinkage zones for soil on the dry side of the modified compaction curve suffered inaccuracies due to the negligibly low shrinkage behaviour. Therefore, it is reasonable to assume that compacted soil with low shrinking behaviour, normally found on the dry side of the compaction curve, is only subject to residual and zero shrinkage modes.

Despite inaccuracies in the determination of the shrinkage zones, the fitting equation proposed by Peng and Horn [6] delivered a perfect fit of the experimental shrinkage curve. Table 7.2 provides a tabular overview of the parameters obtained by fitting the shrinkage curve. It can be seen that the fitting parameters of sample C1 of the modified compaction test on AS and KA is $a_p = n_p = m_p = 1$. Since the shrinkage curve of these samples essentially represents a straight horizontal line, the fitting algorithm could not optimise the parameters to predict a curve. Because e_Z and e_I were nearly identical, the second term of Equation 2.17b was zero and the shrinkage curve reduced to $e(\vartheta) = e_Z$. Reasonable fitting results were obtained for all other shrinkage curves.

Table 7.2: Overview of the parameters obtained by fitting the shrinkage curves of the standard and modified compaction tests on KA and AS using the model of Peng and Horn [6].

Soil	Compaction test	Test No.	e_Z	e_I	a_p	n_p	m_p	resnorm
AS	standard	C1	-	-	-	-	-	-
		C2	0.5682	0.6452	0.9218	26.0683	0.1996	3.71E-5
		C3	0.531	0.6403	0.6698	45.0673	0.0779	4.08E-5
		C4	0.5006	0.6034	0.4775	7.2959	0.4427	1.24E-4
		C5	0.4673	0.5875	0.3047	5.2951	0.4961	2.23E-4
		C6	0.4309	0.611	0.3882	2.6712	1.2352	2.33E-4
		C7	0.4086	0.6246	0.9934	1.6376	5.4839	2.46E-4
		C8	0.4393	0.6988	0.4232	2.2253	1.4227	3.79E-5
AS	modified	C1	0.5655	0.5637	1	1	1	-
		C2	0.4785	0.4841	0.6165	3.7455	0.4359	1.44E-5
		C3	0.3891	0.4197	0.6833	9.3945	1.5322	1.36E-5
		C4	0.3138	0.38	0.3101	3.2609	1.6902	1.30E-5
		C5	0.3511	0.4204	0.1304	4.0701	0.5566	8.76E-5
		C6	0.3674	0.5022	5.7133	1.4153	73.667	1.37E-4
		C7	0.3956	0.5773	0.2722	2.2002	1.161	1.85E-4
		C8	0.397	0.6334	0.5644	1.5107	2.6556	1.41E-4
KA	modified	C1	0.8034	0.8034	1	1	1	-
		C2	0.7669	0.7789	1.1915	7.2417	13.6663	3.24E-6
		C3	0.7375	0.7574	0.5073	8.2341	0.8679	4.48E-7
		C4	0.6817	0.7341	0.5634	2.4936	4.0171	3.89E-5
		C5	0.6904	0.7562	0.1101	2.4765	0.6232	5.78E-5
		C6	0.755	0.816	0.2897	4.8473	4.6614	4.52E-8
		C7	0.816	0.8813	0.2881	4.6678	3.7805	3.37E-7

The fitting equations were used to determine the SL for all shrinkage curves. The SL was determined based on the moisture ratio at the transition from the residual to zero shrinkage zone, according to Peng and Horn [6]. Figure 7.7A compares the SL to the initial gravimetric water content at the beginning of the shrinkage tests for the shrinkage curves of AS and KA. It can be observed that the SL increased with increasing gravimetric water content, regardless of the compaction state and soil type. The higher the initial water content at the beginning of the shrinkage test, the higher is the SL.

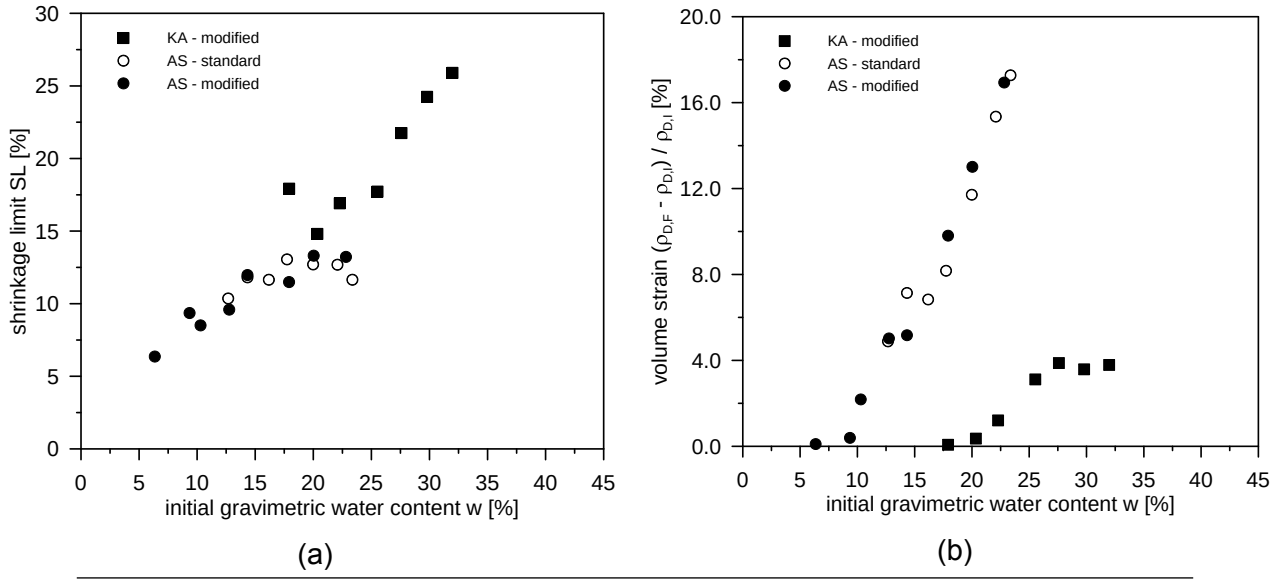

Figure 7.7: Shrinkage behaviour of sample from standard compaction tests on KA and AS, and modified compaction test on AS: (A) relationship between SL and initial gravimetric water content at the beginning of the shrinkage test, and (B) relationship between volume strain of shrinkage and initial gravimetric water content at the beginning of the shrinkage test.

In addition, the extent of the shrinkage behaviour of the compacted soil sample was investigated based on the shrinkage ratio. The shrinkage ratio was defined in this study as $\frac{\Delta\rho_D}{\rho_{D,I}}$, with the shrinkage area $\Delta\rho_D = \rho_{D,F} - \rho_{D,I}$, in which $\rho_{D,I}$ is the initial dry density and $\rho_{D,F}$ is dry density at the SL. Figure 7.7B shows the volume strain or shrinkage ratio plotted over the initial gravimetric water content at the beginning of the shrinkage tests. It can be seen that the trends of the shrinkage behaviour of the standard and modified compacted samples of AS were similar. Generally, the volume strain continuously increased with the increasing initial gravimetric water content. The higher the initial gravimetric water content, the higher is the volume stain. In both tests, the relationship between volume strain and initial gravimetric water content was nearly identical. A difference of volume strain dependent on the compaction effort could hardly be found. For an initial gravimetric water content of $\approx$ 13.0%, the volume strain ratio was even identical for both standard and modified compaction. For higher initial gravimetric water content, differences in volume strain between standard and modified compacted conditions were found. The relationship of volume strain and initial gravimetric water content for AS was nearly linear, regardless of the imposed compaction effort. For the modified compacted KA, the observed trends differed to AS. First, the volume strain increased with initial gravimetric water content up to $\approx 25.0\%$, which is close to the $\rho_{D,Pr}$. Second, the volume strain remained constant for an initial gravimetric water content higher than $\rho_{D,Pr}$. Therefore, the relationship of volume strain and initial gravimetric water content was nonlinear. Similar results were reported in Osinubi and Nwaiwu [278] and Daniel and Wu [279]. However, those observations were made on lateritic soils and low plastic soils, which differ to KA. As a result, a general description and prediction of the influence of initial

water content on volume strain is not clear and requires further experimental research.

7.2.3 SWCC of compacted soil

As explained in Section 6.3.5, the drying path of the SWCC was determined for each individual compaction test. Due to time restrictions in this study, it was not possible to determine the SWCC of the standard compacted KA samples.

The soil in the CT cell was taken and divided into subsamples. Then, soil suction was measured at different water contents. After each suction measurement, the gravimetric water content of the investigated subsamples was determined. Figure 7.8 shows the results of the suction measurements for the standard and modified compaction tests on AS, and the modified compaction tests on KA, as a relationship of soil suction and gravimetric water content. The initial conditions for all samples were defined by the initial gravimetric water content and dry density existing after compaction. The soil suction increased continuously with the decreasing water content. Regardless of the investigated soil, the SWCCs showed similar trends. At the beginning, with high water content and low soil suction, the SWCCs followed different relationships in all three compaction test sets. This indicated that, at the low suction range, the initial water content of the compacted soil strongly influenced the evolution of the SWCC. The SWCCs converged with further decreasing water content, and met at one specific water content. After this water content, the SWCCs were nearly identical and followed one curve. Below this water content, the SWCCs remained identical, approaching almost complete dry conditions with extremely high soil suctions.

Similar results were presented in Romero et al. [273] and Birle et al. [127]. Romero et al. [273] investigated the SWCC and microstructure of unsaturated clay compacted on the dry side of the optimum compaction point. The authors defined a delimiting water content of the converging SWCCs for statically compacted soil samples. This delimiting water content essentially divided the SWCCs into regions that were governed either by intra-aggregate or inter-aggregate pore structure. In the region at low water content below the delimiting point, the influence of the dry density on the SWCC was negligibly low. Instead of dry density, the SWCC was influenced by the specific particle surface and microstructure of intra-aggregate pores. Generally, this observation seems reasonable for the dry side of the compaction curve, with previous porosimetry experiments reporting that soil samples compacted on the dry side of the compaction curve showed a bimodal pore structure [127]. This structure is associated with intra-aggregate and inter-aggregate pores [35, 127]. Further, it has been shown in porosimetry investigations on high plastic clay that the intra-aggregate pore structure is not influenced when subject to compaction on the dry side of the curve [270, 272, 273].

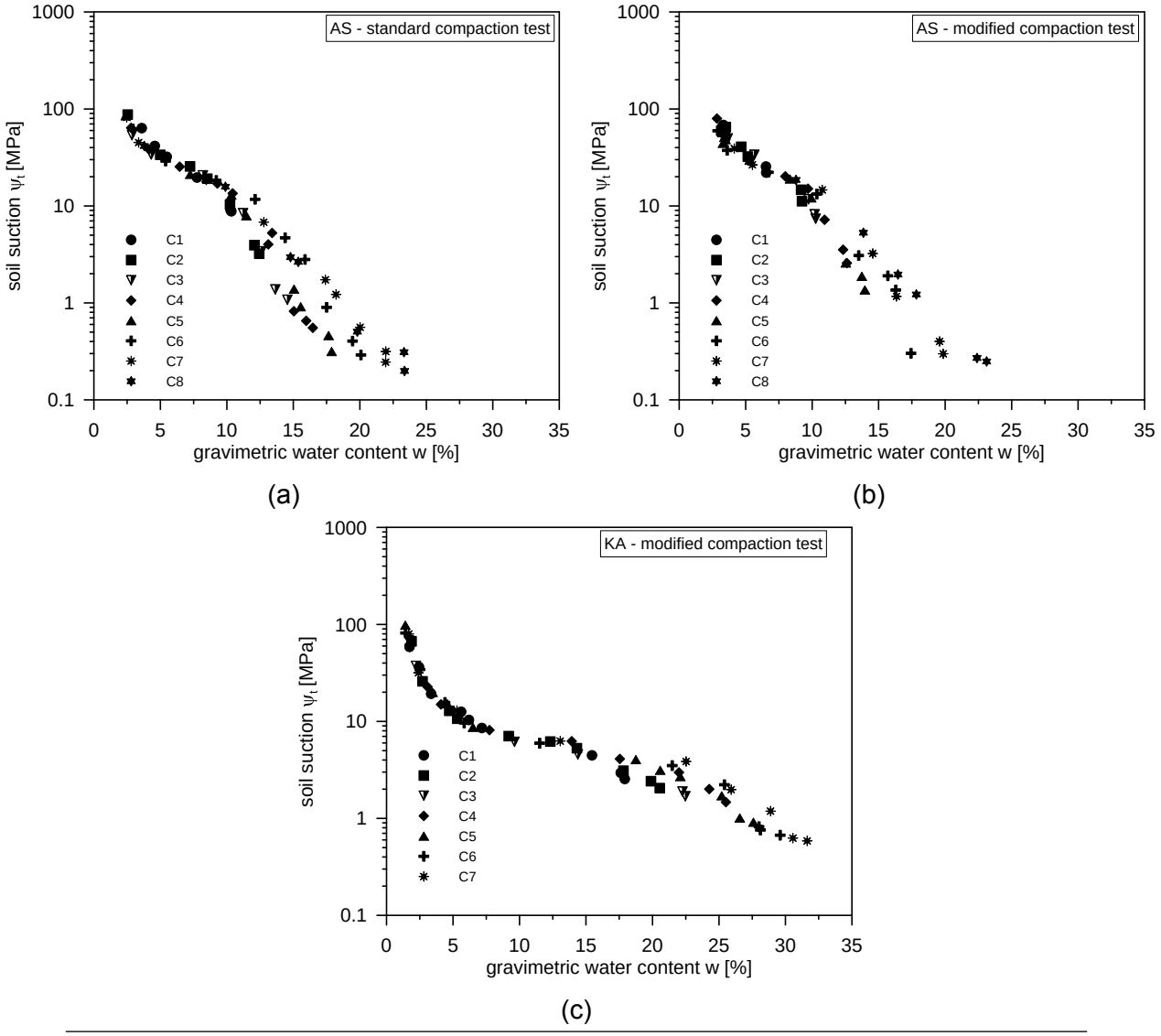

Figure 7.8: SWCC as relationship of soil suction, Ψ_t, dependent on the gravimetric water content: (A) SWCC of standard compaction test on AS, (B) SWCC of modified compaction test on AS and (C) SWCC of modified compaction test on KA.

One possible explanation for this is that, at lower water content on the dry side of the compaction curve, the soil aggregates reveal an enhanced stiffness that results in insensitivity of the intra-aggregate pore structure under compaction [280]. This essentially implies that the SWCC must be equal for the same intra-aggregate pore structure. Moreover, Romero et al. [273] identified a region at water content higher than the delimiting point, in which the SWCC is influenced by the initial dry density and inter-aggregate pore structure. This observation is supported by the results presented in [281], which reports that the initial dry density influences the SWCC of unsaturated compacted soil specimen. This means that changes in macro-porosity (in terms of inter-aggregate pores) caused by compaction affect the SWCC at high water content. Birle et al. [127] showed in experimental investigations that compacted soil samples with different gravimetric water contents and similar dry densities exhibit converging SWCCs, which also highlights the influence of the initial water content on the SWCC.

Tinjum et al. [282] also explained that the shape of the SWCC changes with pore structure, which is strongly influenced by initial water content and compaction effort.

By comparing the measurement results obtained in this study to the results reported in the literature, two major differences were identified:

1. Diamond [276] found that the microstructure of the soil compacted on the dry side of the compaction curve is different than it is for soil compacted on the wet side of the compaction curve. This justifies that SWCCs generally differ at high water content close to the initial water content after compaction. Similar to Romero et al. [273], a delimiting point can be observed at which the SWCCs converge. However, in contrast to Romero et al. [273], the current study found that the SWCCs converged with decreasing water content, regardless of whether the samples had been compacted on the dry or wet side of the compaction curve.
2. Changes in the shape and slope of the SWCCs were observed at the delimiting point. This essentially indicates that the soil structure or the origin for suction governing the SWCC at low water content beyond the delimiting point, is different for high water content.

This observation leads to the following questions:

1. Why do the SWCCs of compacted soil converge at the delimiting point?
2. Why does the shape of the SWCCs change at the delimiting point?

The SWCCs were parameterised to allow the development of answers to these questions. It was found in the literature that the SWCC of compacted fine-grained soil was mostly described qualitatively, without quantitative description or parametrisation. One of the few quantitative descriptions of the SWCCs of compacted soil samples is presented in Tinjum et al. [282]. The SWCCs were parameterised by the unimodal van Genuchten Equation 2.12 and the empirical statistical Equation 2.11 proposed by Brooks and Corey [64]. Yet, the investigated soil suction was constrained with an upper suction limit of 1.35 MPa and, because of that, convergence of SWCCs was not measured. Given that the SWCC equations (introduced in Section 2.4.3) describe the soil suction as a function of the volumetric water content, a quantitative description based on the gravimetric water content was not possible. Therefore, the SWCCs needed to be related to the volumetric water content in order to enable a quantitative description of the SWCC measured for the compaction curves. The drying path of the SWCC of the compacted soil samples arose with significant volume changes due

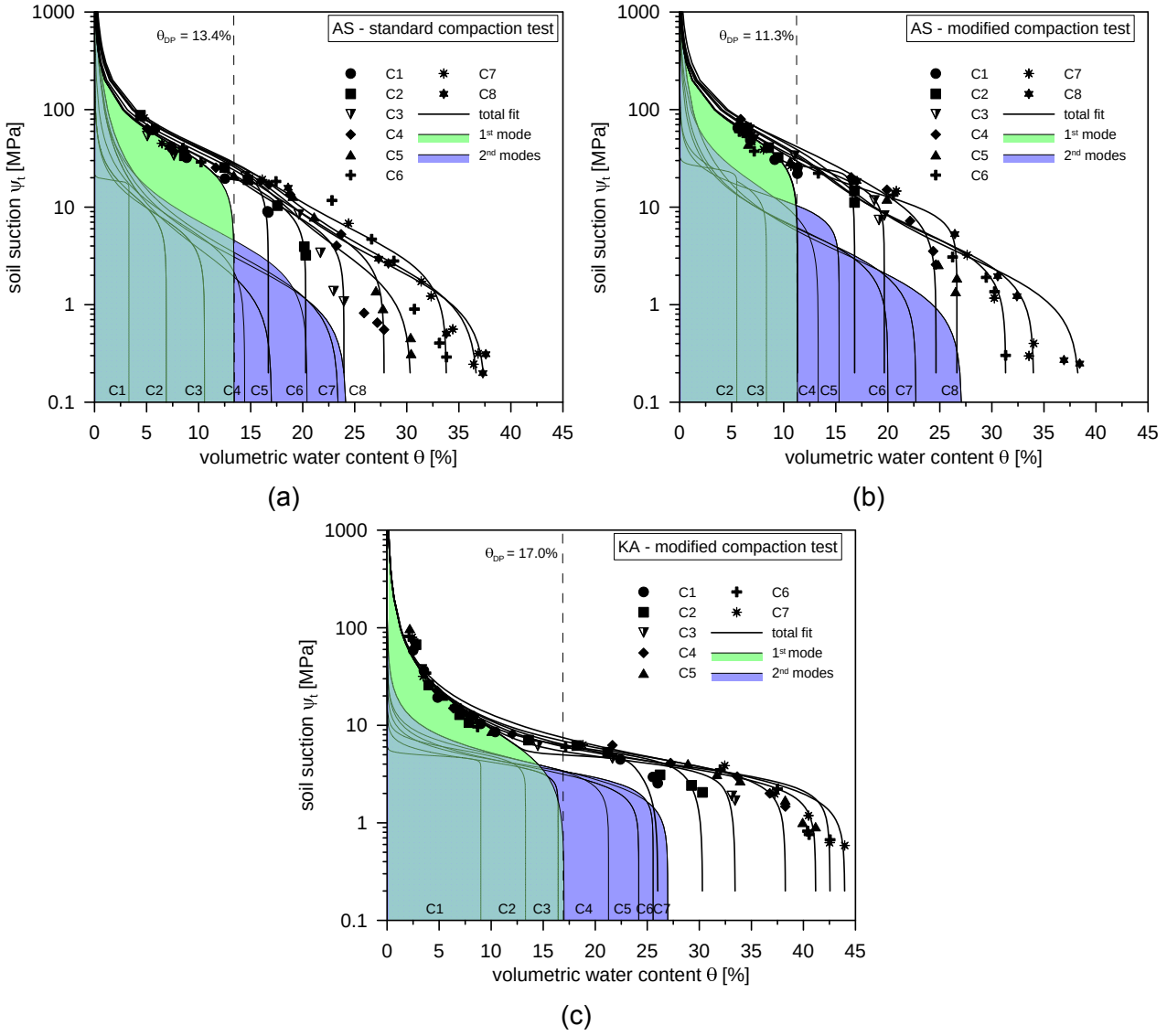

Figure 7.9: SWCCs and parameterisation as relationship of soil suction, Ψ_t, dependent on the volumetric water content: (A) SWCC of standard compaction test on AS, (B) SWCC of modified compaction test on AS, and (C) SWCC of modified compaction test on KA. The dashed line shows the delimiting point. The solid lines present the total fit using the bimodal van Genuchten Equation 2.14. The shaded areas indicate the determined individual modes of the compacted soil samples.

to shrinkage. However, the volume changes, in terms of dry density changes, were not directly determined when measuring the soil suction. As a result, the parameterised shrinkage curves of the compacted soil samples (see Table 7.2 in Section 7.2.2) were used to calculate the volumetric water content. This approach seems reasonable under the assumption that the volume changes in the SWCCs correspond to the measured shrinkage behaviour of the compacted soil. This assumption will be addressed and further discussed later.

Figure 7.9 shows the SWCCs of standard and modified compaction tests on AS and KA, dependent on the volumetric water content. In contrast to the gravimetric water content, the

volumetric water content considers volume changes indirectly by using the dry density to calculate the volume of pore water. Even though the volume changes are indirectly considered, the SWCCs dependent on the volumetric water content converge at a pronounced delimiting point, similar to Figure 7.8. Figure 7.9 shows the identified delimiting points, θ_{DP}, with the indicated dashed lines. In order to parameterise the soil suction measurements, θ_R and θ_S needed to be determined for each individual SWCC. As explained in Section 2.4.3, θ_S originally describes the upper boundary of the SWCC at high water content, at which saturated soil conditions are expected [127]. In this case, θ_S is used as a mathematical boundary to define the asymptote for the highest observed water content. The lower boundary, θ_R, limits the SWCC to a residual water content. Two assumptions were made in this study:

1. For the compacted soil on the dry side of the compaction curve, the drying path of the SWCC started with a maximum volumetric water content that was measured at unsaturated soil conditions. As a result, the actual θ_S of the SWCC of the compacted soil did not exist from the physical point of view. Despite this, θ_S was used only to establish an upper boundary water content to fit the SWCC. This assumption needs to be further evaluated, yet this was not the aim of this research. However, the assumption is certainly reasonable as a first approach.

2. Due to a lack of soil suction measurements at extremely low water content, the residual water content, θ_R, was always taken to zero. This was justified by the assumption that no water remains in the soil under sufficiently high soil suction. An equivalent soil suction for $\Psi_t = 10^3$ MPa for $\theta_R = 0$ was approximated according to Fredlund and Xing [8].

The bimodal van Genuchten equation, according to Equation 2.14, was used to parameterise the SWCCs. The applied parameterisation process of the SWCC was divided into a two-step procedure:

1. Since SWCCs are identical beyond the identified delimiting point, it was suggested in this study that the **first mode** needed to be same for the SWCCs in each test. In order to achieve the best results, the data of all measured SWCCs were collected together for measurements at water content lower than the delimiting point. Then, in the first step, a unimodal van Genuchten Equation 2.12 was used to parameterise the common mode below the delimiting point, with $\theta_S = \theta_{DP}$.

2. As the second step, the **second mode** was added to the van Genuchten equation according to Equation 2.14. with weighting factors, W_i. The determined fitting parameters of the first mode were included, and then the fitting parameters and weighting factors W_i for the second mode were approached.

For both steps, a MATLAB script was coded that fitted the SWCC based on an algorithm of nonlinear least-squares problems. The fitting parameter, m_{vG}, is frequently written in terms of n_{vG} according to $m_{vG} = 1 - 1/n_{vG}$ [282]. This relationship constrains the flexibility of the van Genuchten Equation 2.14, yet enhances the stability of the fitting process [282]. As a bimodal van Genuchten equation was employed to fit the SWCC, the n_{vG}-m_{vG}-relationship was used to reduce the number of fitting parameters. Further, upper and lower boundaries were set to minimise the value range of the fitting parameters. Based on the previous fitting results found in Tinjum et al. [282], the lower and upper limits of a_{vG} for both modes were set to zero and one, respectively. The lower and upper limits of n_{vG} were set to zero and infinite. A secondary condition was implemented with $\sum_{i=1}^{2} W_i = 1$.

The entire dataset of the determined fitting parameters is compiled in Table A.1 in the appendix of this thesis. In Figure 7.9, the parametrisation results of the SWCCs are graphically presented for the standard and modified compacted AS, as well as the modified compacted KA. The solid lines represent the total fit of the bimodal van Genuchten equation. It can be noted that reasonable fits of the SWCCs were obtained. The shaded areas indicate the individual modes of the parameterisation. As previously suggested, the first mode was identical for each SWCC. It is found that the first mode (with $\theta_{DP} = 11.3\%$) of the SWCCs of the modified compacted AS was the smallest, whereas the largest first mode (with $\theta_{DP} = 17.0\%$) was determined for the SWCCs of the modified compacted KA. An interesting finding was observed when comparing the delimiting point as a gravimetric water content and the SL. The gravimetric water content, w_{DP}, of the delimiting point could be calculated for each SWCC based on the volumetric water content, θ_{DP}, and the void ratio, e_Z, at the SL determined by the shrinkage curve parameterisation (see values in Table 7.2). Figure 7.10 compares the gravimetric water contents of the delimiting point, w_{DP}, and the SL, also determined by the shrinkage curve parameterisation. The solid line defines the 1:1 line with a slope of $45°$. The area below the 1:1 line highlights the area of the zero shrinkage zone. It can be seen that all delimiting points were located in the zero shrinkage zone. This result demonstrates that no volume changes were expected in the water content range $0 \leq \theta \leq \theta_{DP}$, where SWCC were identical. This subsequently signifies that the influence of volume changes on the SWCC was expected to be low.

Following the explanation of Romero et al. [273], it was further suggested that a bimodal van Genuchten equation was suitable to parameterise the SWCC of compacted soils. It was assumed in this study that the second mode represented the inter-aggregate pore structure that governed the soil suction at water content higher than θ_{DP}. With decreasing water content, the influence of the first mode became more dominant. This also seems reasonable because inter-aggregate pores are associated with larger pore sizes, which are expected to drain first. Then, at the delimiting water content and below, the SWCC was only governed by the first

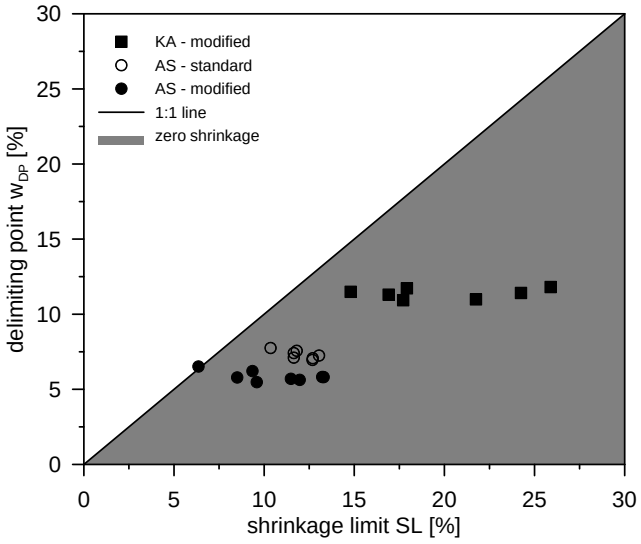

Figure 7.10: Comparison of gravimetric water content at the SL and delimiting point of the SWCC. The solid line indicates the 1:1 line with a 45° slope. The shaded area below the 1:1 line represents the zero shrinkage area.

mode, regardless of whether it was initially compacted on the dry or wet side of the compaction curve. This first mode is always located in the zero shrinkage zone of the shrinkage curve. Thus, it was assumed in this study that the first mode refers to the intra-aggregate pore structure, which is characterised by a constant void ratio for $\theta \leq \theta_{DP}$. These suggestions require further research work – particularly investigations of the pore structure variations in the SWCCs and shrinkage curves of compacted soils – in order to provide evidence for these assumptions. However, this was beyond the scope of the present study.

7.2.4 Dielectric behaviour of compacted soil

CT measurements were conducted on the standard and modified compacted soil samples of KA and AS. CT cells were used to core samples from compacted soil in the compaction mould. Prior to the dielectric measurement, the mass of the soil in the CT cell was determined to obtain the dry density of the soil. By doing so, it was possible to compare the dry density values in the compaction mould and CT cell in order to evaluate the degree of disturbance while coring the soil samples. Figure 7.11 shows a comparison of the results, in which the dry density values in the CT cell are plotted against the values in the compaction mould. The black line defines the slope of unity (1:1) at which the dry density values are identical. The comparison shows that the largest differences in dry density values were measured for the standard compaction tests on AS. However, the overall results showed only minimal differences in the dry density values between the compaction mould and CT cell. In general, the dry density values in the CT cell tended to be slightly higher. This trend can be simply

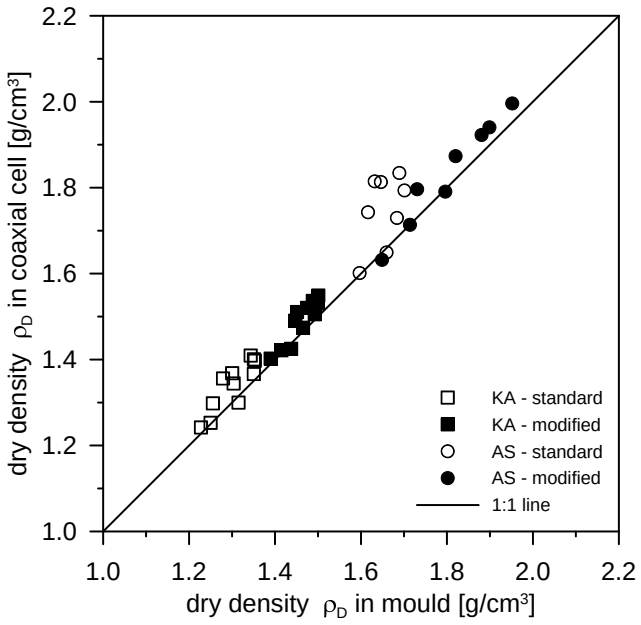

Figure 7.11: Comparison of dry density values measured in the compaction mould and CT cell for standard and modified compaction tests on AS and KA.

explained by the fact that soil became additionally compacted when pushing the CT cell into the compaction mould. Nevertheless, the comparison shows good agreement between the dry density values in the compaction mould and CT cell. This result further suggests the practical use of coring more or less undisturbed samples by means of a CT cell. Since the differences were negligibly low, the dry density measured in the CT cell was used in the further analysis.

The S_{ij}-parameters, both for the signal reflection and transmission, were measured in a frequency range from 1 MHz to 3 GHz. As the CT cell was assembled between two flange connectors (see Figure 5.4B), the measured S_{ij}-parameters included not only soil information, but also the influence of the flange connectors. To eliminate this influence, the measured S_{ij}-parameters on each compacted soil sample were post-processed. A phase shift correction was performed on the measured S_{ij}-parameters over the entire frequency range. Figure 7.12 shows an example of a post-processing phase shift correction on the $S_{\mathrm{i,j}}$-parameter of a dielectric measurement on sample C1 of the standard compacted AS. Figures 7.12A and 7.12C compare the measured and corrected values of the magnitude of reflection S_{ii}-parameters and transmission S_{ij}-parameters, respectively. It can be seen that the measured reflection parameters, S_{11} and S_{22}, were nearly identical. Given that it did not matter from which end of the CT cell the measurement was taken, this indicated that sample C1 of the standard compacted AS was homogeneous. Similarly, the transmission parameters, S_{21} and S_{12}, were identical. Further, it was observed that the measured and corrected values were

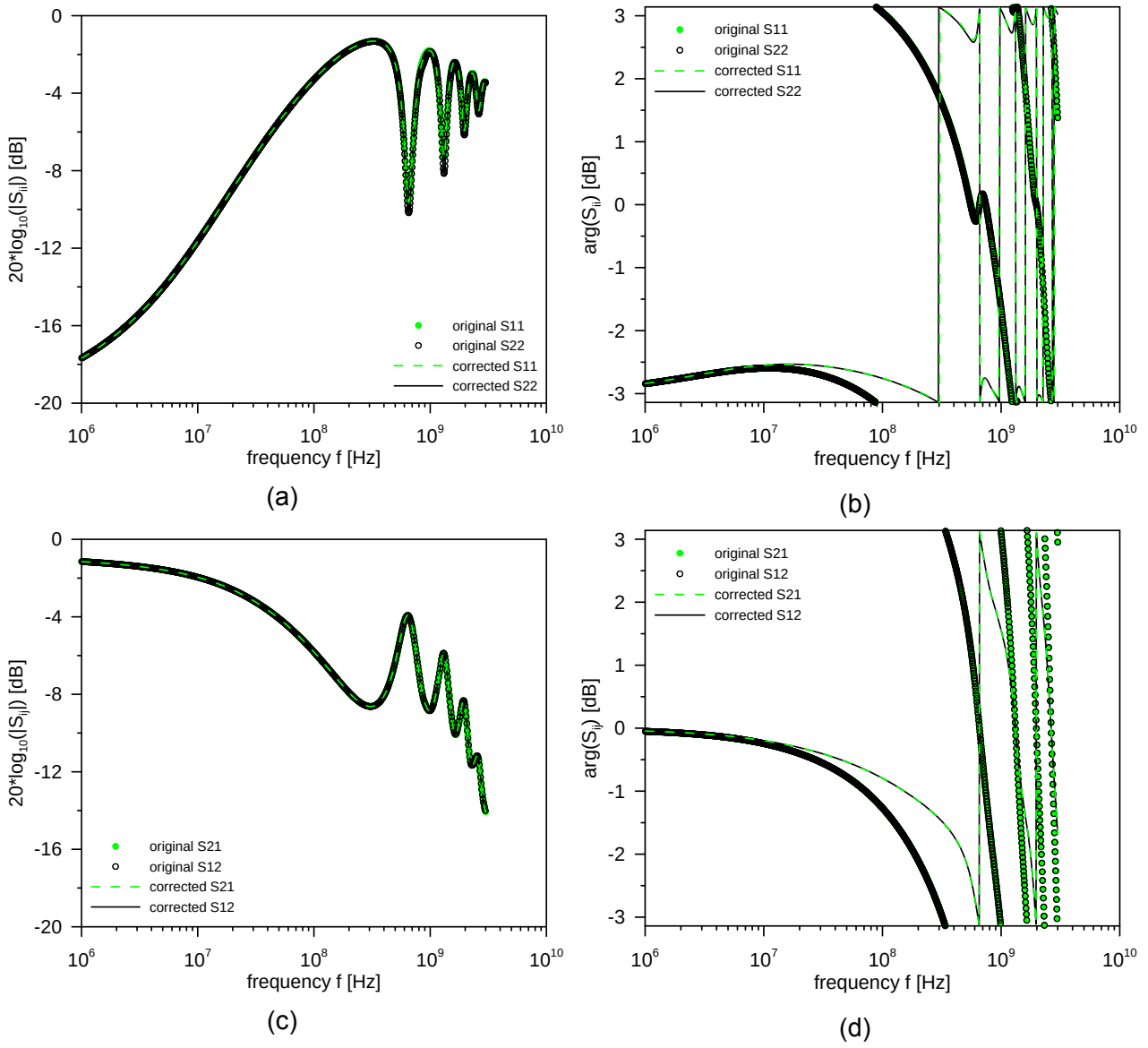

Figure 7.12: Example of post-processing phase shift correction on $S_{i,j}$-parameter of a dielectric measurement on sample C1 of standard compacted AS. Shown is comparison of measured and corrected values of: (A) magnitude of reflection S-parameters (S_{11} and S_{22}), (B) phase shift of reflection S-parameters, (C) magnitude of transmission S-parameters (S_{21} and S_{12}) and (D) phase shift of transmission S-parameters.

identical, which meant that the flange connector did not influence the magnitude of the measured reflected and transmitted signal. Figures 7.12B and 7.12D compare the measured and corrected phase shift of reflection S_{ii}-parameters and transmission S_{ij}-parameters, respectively. Similar to Figure 7.12A and 7.12B, the reflection parameters, S_{11} and S_{22}, and transmission parameters, S_{21} and S_{12}, were the same in each case. However, it should be also noted that there was a distinct difference between the measured and corrected values of the phase shift, which essentially highlights the influence of the flange connectors.

Following the post-processing, the corrected S-parameters were used to calculate the complex permittivity, $\varepsilon^{\star}_{r,\mathrm{eff}}$, for each individual compacted soil sample. To do so, the iterative

method (BJI) was employed to calculate the permittivity, $\varepsilon^{\star}_{r,\text{eff}}$, as a function of the frequency from 1 MHz to 3 GHz. As an example, the results of the iteratively determined $\varepsilon^{\star}_{r,\text{eff}}$ are presented in Figure 7.13 for standard compacted samples C1 to C8 on AS. Figures 7.13A and 7.13B show the real part, $\varepsilon'_{r,\text{eff}}$, and imaginary part, $\varepsilon''_{r,\text{eff}}$, as a 3-D plot dependent on the frequency, f, and volumetric water content, θ. The figures of the dielectric measurements of the standard and modified compacted KA samples, as well as the modified compacted AS samples, are included in Appendix A.3.

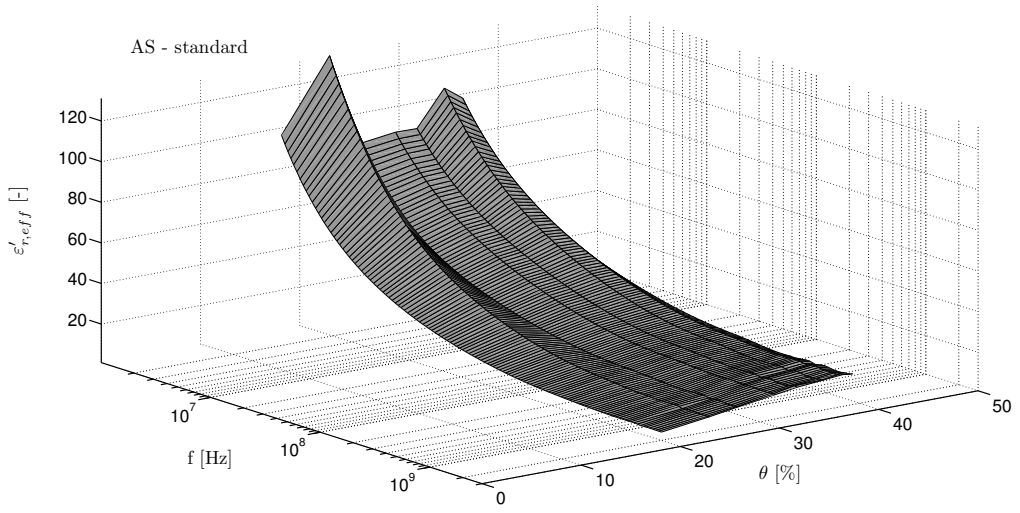

(a)

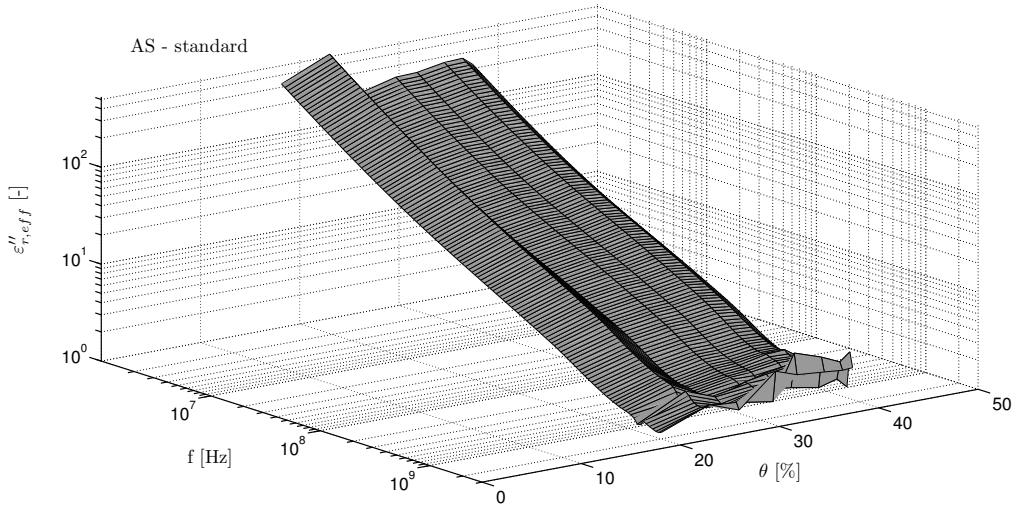

(b)

Figure 7.13: 3-D illustration of complex permittivity, $\varepsilon^{\star}_{r,\text{eff}}$, of standard compacted AS dependent on the frequency, f, and volumetric water content, θ: (A) real part, $\varepsilon'_{r,\text{eff}}$, of complex permittivity and (B) imaginary part, $\varepsilon''_{r,\text{eff}}$, of complex permittivity.

It can be seen that the $\varepsilon'_{r,\text{eff}}$ of a single measurement varied only slightly at high frequencies ($f > 500$ MHz) close to the GHz range. As shown in Figure 4.2, the $\varepsilon'_{r,\text{eff}}$ was expected to

be nearly constant due to dipolar polarisation of the pore water in the soil matrix. With decreasing frequency below $f < 500$ MHz, the $\varepsilon'_{r,\text{eff}}$ changed remarkably. $\varepsilon'_{r,\text{eff}}$ revealed much higher values at frequencies near the low MHz range. The frequency dependence of $\varepsilon'_{r,\text{eff}}$ is also known as 'dispersion' [283]. This frequency dependence is explained by two different effects. An additional different polarisation mechanism occurs in the low range of MHz. This mechanism is associated with interfacial polarisation, which occurs at the interface of heterogeneous multiple-phase material, such as soils. This interfacial polarisation superimposes the dipolar polarisation at lower frequency, which results in an increase of the $\varepsilon'_{r,\text{eff}}$. Another effect is related to the dipolar polarisation. In the theory of dipolar polarisation, the dispersion is caused by particle surface forces obstructing water molecules to rotate in phase with the applied frequency of the EM field [42, 284]. For low frequency at MHz range, water molecules may be easily polarised, which results in an increase of $\varepsilon'_{r,\text{eff}}$. For higher frequencies at GHz, water molecules – particularly bound water molecules – are restricted in their mobility to rotate in the EM field, which leads to minimised permittivity. As a result, the dispersion might be associated with different water phases and the binding forces acting on them [42, 284].

Similar effects were observed for the $\varepsilon''_{r,\text{eff}}$ of a single measurement. However, in contrast to $\varepsilon'_{r,\text{eff}}$, it should be noted that $\varepsilon''_{r,\text{eff}}$ does not reach a constant value at HF. Moreover, a slight increase of $\varepsilon''_{r,\text{eff}}$ can be seen for $f > 1$ GHz due to dipolar relaxation. With decreasing frequency, $\varepsilon''_{r,\text{eff}}$ is similar to $\varepsilon'_{r,\text{eff}}$, also increasing due to the possible presence of interfacial polarisation. However, much higher values of $\varepsilon''_{r,\text{eff}}$ were observed than for $\varepsilon'_{r,\text{eff}}$ at a given frequency at low MHz range. This effect is described by the contribution of direct current conductivity, σ_{DC}, to the low-frequency range.

By carefully examining the relationship between $\varepsilon'_{r,\text{eff}}$ and θ at one given HF close to the GHz range, it can be seen that the real part varied with water content. $\varepsilon'_{r,\text{eff}}$ showed its maximum value at the highest water content, then $\varepsilon'_{r,\text{eff}}$ decreased with decreasing water content. A similar trend was identified for the relationship of $\varepsilon''_{r,\text{eff}}$ and θ. This relationship is explained by the fact that less water was available in the soil matrix at which dipolar polarisation can occur. As a result, the contribution of the complex permittivity of water, $\varepsilon^{\star}_{\text{W}}$, to the overall complex permittivity of the soil, $\varepsilon^{\star}_{r,\text{eff}}$, as a mixture of phases, became less dominant, which led to a decrease of both $\varepsilon'_{r,\text{eff}}$ and $\varepsilon''_{r,\text{eff}}$. Thus, it can be stated that there was a strong relationship between $\varepsilon^{\star}_{r,\text{eff}}$ and θ at HF close to the GHz range.

In contrast, a different behaviour was observed at frequencies near the low MHz range. It can be seen that there was no distinct relationship between θ and $\varepsilon'_{r,\text{eff}}$ or θ and $\varepsilon''_{r,\text{eff}}$. Nevertheless, the strong increase of $\varepsilon'_{r,\text{eff}}$ and $\varepsilon''_{r,\text{eff}}$ at the low MHz range needs to be further investigated and discussed later. First, the focus is on the dielectric soil behaviour at a HF at 1 GHz. Figure 7.14 compares the measured real part, $\varepsilon'_{r,\text{eff}}$, with material-specific empirical

calibration equations and theoretical mixture approaches. As most empirical equations and mixture approaches refer to a frequency range close to GHz, the measured $\varepsilon'_{r,\text{eff}}$ was taken at 1 GHz.

Two material-specific empirical calibration equations were chosen for comparison – the well-known equations proposed by Topp et al. [15] and Wensink [196]. As shown in Figure 7.14, the dielectric measurements were additionally modelled with two theoretical mixture approaches.

In a first step, $\varepsilon'_{r,\text{eff}}$ was calculated based on a 3-phase model according to Equation 4.24, in which the complete pore water was considered free water. In this 3-phase model, the permittivity of the solid phase, $\varepsilon_{r,G}$, was approached by the previously introduced empirical fitting Equation 4.9. The complex permittivity of the pore water, $\varepsilon^{\star}_{r,W}$, as a function of temperature and frequency was approached based on a Debye model, according to Equation 4.6. To do so, the literature values for $\varepsilon_{\text{S,W}}$, $\varepsilon_{\infty,\text{FW}}$ and τ_{FW} were adopted from Wagner et al. [227] to calculate the $\varepsilon^{\star}_{r,W}$ at a frequency of 1 GHz and temperature of 23°C. The structure parameter was suggested to be $\alpha = 0.5$, according to Birchak et al. [201]. The volume fractions of the individual phases, expressed in terms of porosity, n, and volumetric water content, θ, were known parameters from the compaction tests.

In a second step, $\varepsilon'_{r,\text{eff}}$ was calculated using a 4-phase model that included the bound water as an additional phase. In this model, the water phase was divided into the free water and bound water phase, in which the bound water was considered with a thickness of two water molecule layers. The complex permittivity of the solid phase, $\varepsilon_{r,G}$, and free water, $\varepsilon^{\star}_{r,W}$, were calculated according to the 3-phase model. Similar to the $\varepsilon^{\star}_{r,W}$, the frequency and temperature dependent complex permittivity of bound water, $\varepsilon^{\star}_{\text{BW}}$, was modeled by the Debye equation (see Equation 4.6) at a frequency of 1 GHz and temperature of 23°C. $\varepsilon_{\infty,\text{FW}}$ was assumed to be the same value as for the 3-phase model. The static permittivity of bound water, $\varepsilon_{\text{S,BW}}$, in the first and second water molecule layers was taken from the literature presented in Wagner and Scheuermann [19]. The corresponding relaxation time, τ_{BW}, for the first and second water molecule layers was calculated based on Eyring's Equation 4.35, with literature values for Gibbs energy, $\Delta G^{\ddagger}_{w}$, taken from Wagner and Scheuermann [19]. The volumetric water content of the first and second bound water layer was predicted by Equation 4.26 [205]. As for the 3-phase model, the structure parameter was set to $\alpha = 0.5$.

In a final step, the frequency dependent dielectric spectrum was predicted based on two theoretical mixture approaches in combination with a phenomenological relaxation model, which were coupled with the ρ_D/Ψ_t-information derived from the parameterised shrinkage curve and SWCC. One of the approaches, called the Hil-model, is the theoretical mixture Equation 4.30 proposed by Hilhorst [48], previously introduced in Section 4.5.3. The other

approach – the WS-model – is based on an extended version of the complex refractive index model model presented by Wagner and Scheuermann [19], according to Equation 4.32. For both models, the parameterised SWCC for each compacted soil sample was used to predict the complex permittivity for free and bound water, using Equation 4.31 for the Hil-model, and the set of Equations 4.33 to 4.38 for the WS-model. Then, the theoretical mixture approaches according to Equations 4.32 and 4.30, in combination with the information provided by the shrinkage curve, were applied to calculate $\varepsilon^{\star}_{r,\text{eff}}$ in frequency range from 1 MHz to 3 GHz. To be consistent with 3-phase model and 4-phase models, the permittivity of the solid phase, $\varepsilon_{r,G}$, was also calculated with Equation 4.9. The results of $\varepsilon'_{r,\text{eff}}$ at 1 GHz are presented in Figure 7.14 with the solid red line for the WS-model, and dashed red line for the Hil-model. In Figure 7.14, the results of the approaches are shown in comparison to the measured $\varepsilon'_{r,\text{eff}}$ for the standard and modified compacted samples on KA and AS. Since the shrinkage curve and SWCC for the standard compaction tests on KA were not measured, it was not possible to predict the dielectric spectrum using the Hil-model and WS-model.

In general, it can be seen that the material-specific empirical calibration equation proposed by Topp et al. [15] tended to overestimate the real part, $\varepsilon'_{r,\text{eff}}$, of KA, particularly at high volumetric water content, θ, and underestimated the $\varepsilon'_{r,\text{eff}}$ of AS at low water content. In contrast, the equation by Wensink [196] gave a slightly better prediction, but still tended to overestimate $\varepsilon'_{r,\text{eff}}$ in the low volumetric water content range of the standard compaction test. Essentially, the material-specific empirical calibration equations gave a quick approximation of the relationship between $\varepsilon'_{r,\text{eff}}$ and θ. However, the results emphasised that a universal approach of the dielectric behaviour dependent only on the water content does not reproduce the behaviour for all soils. The results further highlighted that not only water content influences the permittivity at 1 GHz, but also mineralogy [204], soil structure [285] and particularly soil suctions acting on the bound water phase [19, 23, 212].

Therefore, theoretical mixture approaches for cohesive soils should be more suitable to better reproduce the dielectric measurement for fine-grained soils. In Figure 7.14, it can be seen that the Hil-model tended to overestimate the dielectric spectrum, resulting in serious deviations from the experimental data. Further, it was observed that the Hil-model showed decreasing $\varepsilon^{\star}_{r,\text{eff}}$-values at the high water content range. A considerable disadvantage of the theoretical mixture equation was found for soils at high water content close to saturated conditions. In Equation 4.29, the depolarisation factor of water, $S_{\text{dep,W}}$, was defined as a function of the volumetric water content, θ, and porosity, n. At saturation with $n = \theta$, the depolarisation factor became to $S_{\text{dep,W}} = 1/(3\theta)$. Hilhorst et al. [25] assumed a fixed value of 28.5 for the real part of the saturated permittivity. Due to this assumption, the first term in Equation 4.30 is independent of θ with $\Omega^{\star}_1/(3\theta) = \varepsilon^{\star}_{\text{W}}/3$ for saturated soil conditions. Hence, $\varepsilon^{\star}_{r,\text{eff}}$ in

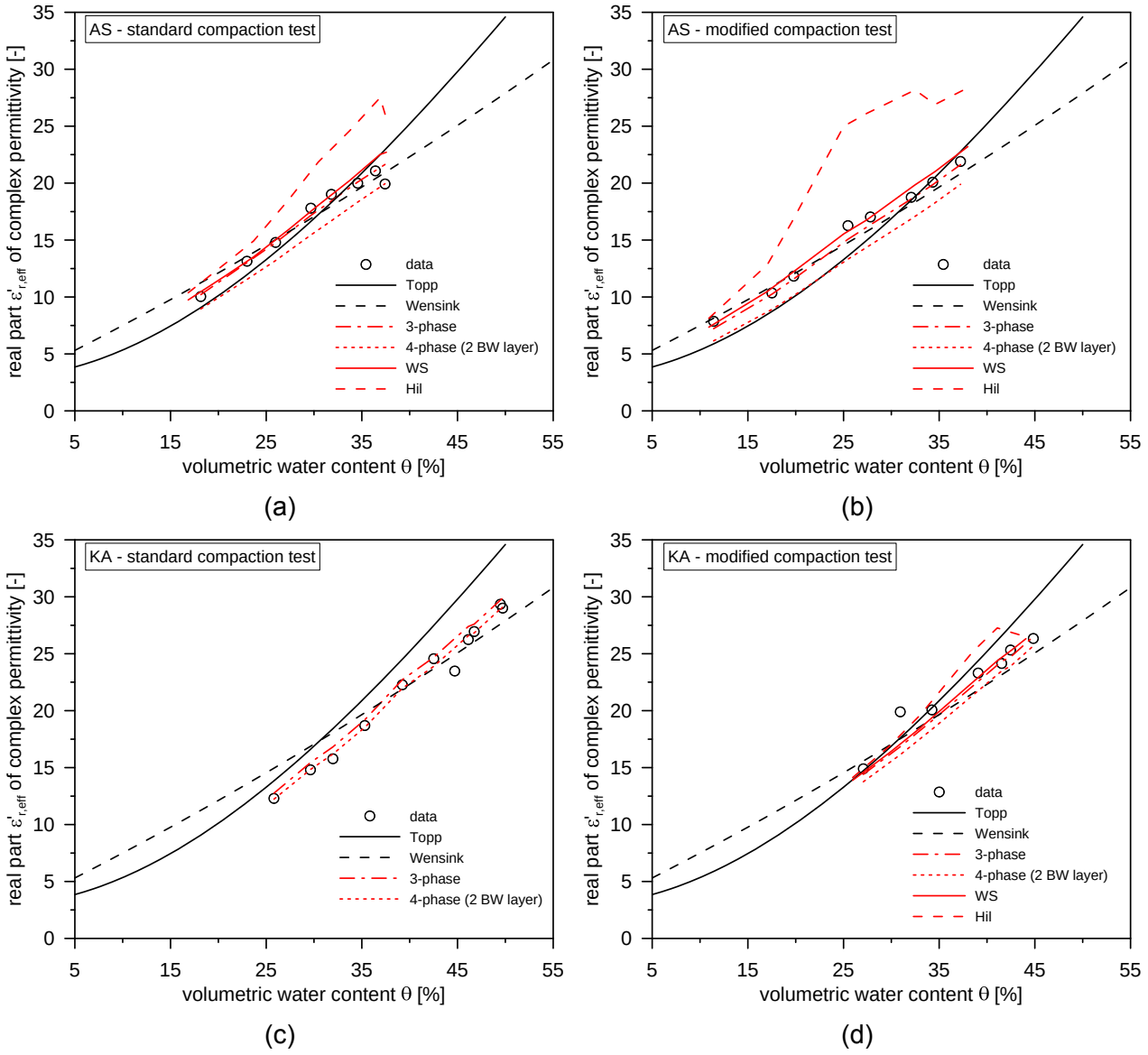

Figure 7.14: Comparison of dielectric measurements with material-specific empirical calibration equations and theoretical mixture approaches. The real part, $\varepsilon'_{r,\mathrm{eff}}$, at 1 GHz is plotted versus the volumetric water content, θ.

Equation 4.30 reduces to following expression:

$$\varepsilon^{\star}_{r,\mathrm{eff}}(\omega, T, \theta) = \frac{\varepsilon^{\star}_{\mathrm{W}}}{3} + (1-\theta)\cdot\varepsilon_{r,G} \tag{7.1}$$

Equation 7.1 demonstrates that $\varepsilon^{\star}_{r,\mathrm{eff}}$ decreases with increasing volumetric water content, θ. Controversially, it is generally assumed that $\varepsilon^{\star}_{r,\mathrm{eff}}$ increases with increasing volumetric water content. Therefore, it is likely that the Hil-model fails with increasing water content due to its inability to take into account changes in porosity.

The results of the other theoretical mixture approaches gave a much better prediction over nearly the entire water content range. In the case of the AS, the best approach was found for the 3-phase model and WS-model. An interesting feature was observed for the 4-phase

model with two water molecule layers. It can be seen that the results of the 4-phase model deviated more from the dielectric measurements with an increasing number of water molecule layers. This essentially highlighted that the bound water phase does not influence the dielectric behaviour of AS at a frequency of 1 GHz.

In contrast to AS, it should be noted that, for KA, the theoretical mixture approaches gave nearly the same results, regardless of the type of mixture approaches. The results of the 4-phase model deviated only minimally from the results of the 3-phase model and WS-model. This effect was explained by the lower specific particle surface and dry density in comparison to AS. According to equation 4.26, a lower specific particle surface and dry density lead to lower volumetric water content of the bound water phase. This subsequently reduces the influence of the bound water phase on the dielectric soil behaviour when considering a 4-phase model.

Figure 7.14 only shows a comparison of the measured dielectric spectrum and approaches for $\varepsilon'_{r,\text{eff}}$ at 1 GHz frequency. However, as shown in Figure 7.13, the dielectric spectrum is strongly frequency dependent in the range from 1 MHz to 3 GHz. Hence, the aim of this study was to predict the dielectric properties at different frequencies based on the theoretical mixture approaches. Since the Hil-model overestimated the dielectric soil properties of compacted soil samples (see Figure 7.14), only the WS-model was applied to predict the dielectric spectrum in the observed frequency range. Figure 7.15 presents the results in which the prediction of the WS-model is compared to the dielectric measurements. The predicted and measured real, $\varepsilon'_{r,\text{eff}}$, and imaginary, $\varepsilon''_{r,\text{eff}}$, part are compared as a function of the volumetric water content at 1 GHz, 100 MHz, 10 MHz and 1 MHz frequency. The comparison of the real $\varepsilon'_{r,\text{eff}}$ and imaginary, $\varepsilon''_{r,\text{eff}}$, part of AS is shown in Figures 7.15A and 7.15B, in which the results of the standard and modified compaction tests are highlighted with red and black, respectively. The comparisons for KA soil are shown in Figure 7.15C and 7.15D.

It can be seen that the dielectric spectra for the standard and modified compaction tests varied slightly. At high volumetric water content, close to saturation, the dielectric spectra were similar, only showing minor deviations. In contrast, differences in dielectric spectra were observed with decreasing volumetric water content. The dielectric spectrum of modified compaction tests tended to exhibit higher values, which can distinctly be seen in the case of $\varepsilon''_{r,\text{eff}}$ of KA soil.

The WS-model accurately predicted the real part, $\varepsilon'_{r,\text{eff}}$, of the dielectric measurements at 1 GHz and 100 MHz. For KA, the entire dielectric spectrum of the modified compaction test was predicted well, even at low frequency 10 MHz to 1 MHz. For AS, the WS-model slightly overestimated $\varepsilon'_{r,\text{eff}}$ with decreasing frequency. This led to increasing deviations with reducing frequency from 10 MHz to 1 MHz. A different trend was observed for the imaginary part, $\varepsilon''_{r,\text{eff}}$,

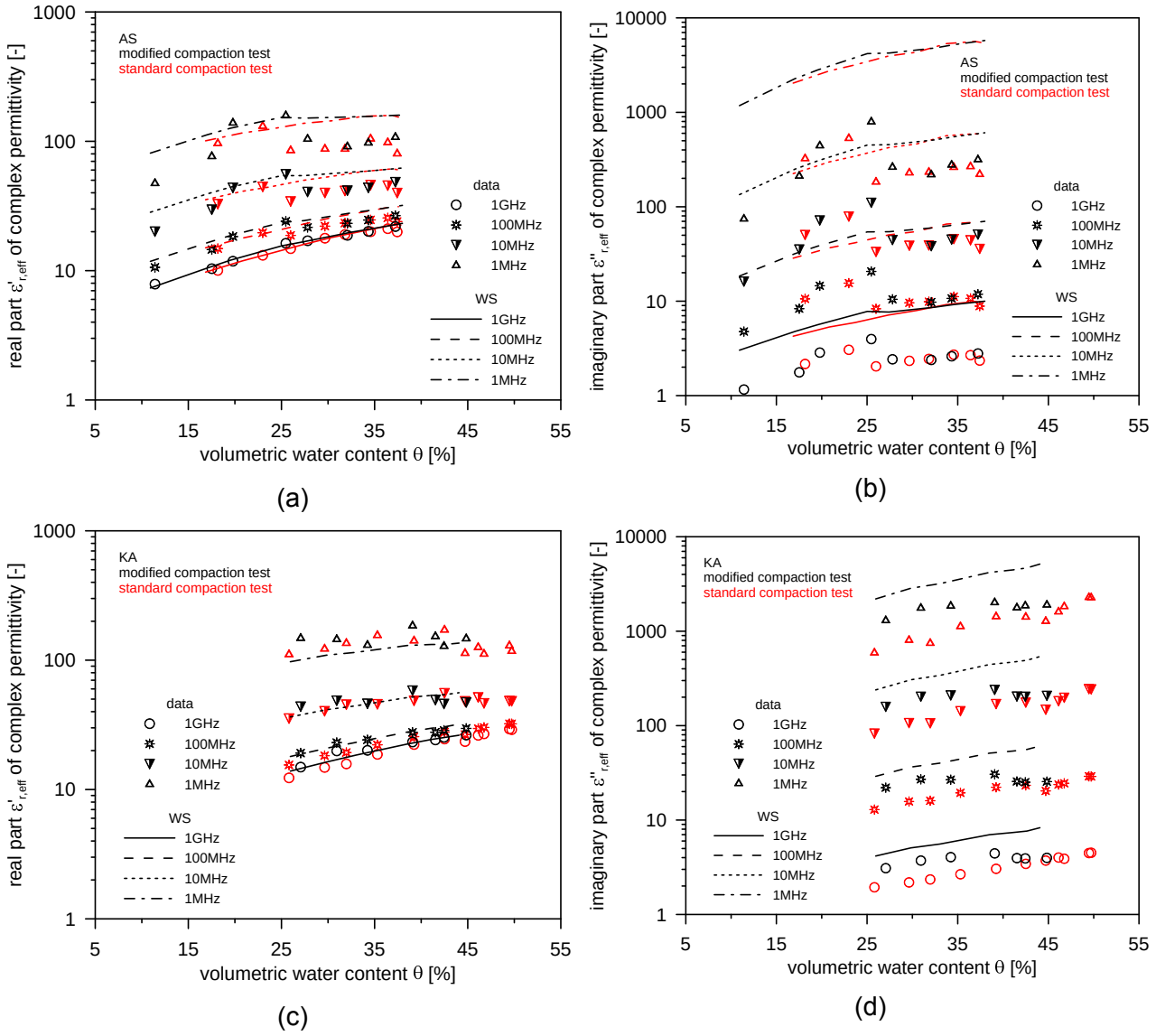

Figure 7.15: Comparison of dielectric measurements with the results of the WS-model at specific frequencies of 1 GHz, 100 MHz, 10 MHz and 1 MHz: (A) to (B) comparison of real, $\varepsilon'_{r,\text{eff}}$, and imaginary, $\varepsilon''_{r,\text{eff}}$, parts of standard (red) and modified (black) compaction test on AS, and (C) to (D) comparison of real $\varepsilon'_{r,\text{eff}}$ and imaginary, $\varepsilon''_{r,\text{eff}}$, parts of standard (red) and modified (black) compaction test on KA. The WS-model could not be used for the standard compaction test because the shrinkage curve and SWCC were not available.

of the dielectric spectrum. In general, the prediction of $\varepsilon''_{r,\text{eff}}$ was higher than the measured values for $\varepsilon''_{r,\text{eff}}$. The results of the WS-model deviated more with decreasing frequency. The reason for this was found in the direct current conductivity of the pore water, which was estimated based on Equation 4.38. In this equation, the values of the empirical coupling parameters – $\sigma_{w,U} = 10^{-0.36}$ and $B = 0.572$ – were taken from the literature [140]. However, it is likely that these two empirical coupling parameters are material-specific parameters that should be investigated in detail in future studies to find better predictions of $\varepsilon''_{r,\text{eff}}$. However, the WS-model is the only approach available that enables prediction of the dielectric spectrum based on the shrinkage curve and SWCC. The results showed that the WS-model sufficiently

predicted the $\varepsilon'_{r,\text{eff}}$ as a function of frequency.

The distinct increase of complex permittivity with decreasing frequency below 100 MHz indicated that dielectric relaxation processes occur due to certain polarisation mechanisms. It was interesting to find that the measured $\varepsilon'_{r,\text{eff}}$ and $\varepsilon''_{r,\text{eff}}$ at low frequency, such as at 1 MHz, did not monotonically decrease with decreasing volumetric water content. Furthermore, the measured $\varepsilon''_{r,\text{eff}}$ does not show a clear trend with variations of water content due to following reason. On the one hand, the pore water conductivity which contributes to the complex permittivity is a function of water content which generally decreases with an increase of water content [140, 143]. On the other hand, the $\varepsilon''_{r,\text{eff}}$ also depends on the water content according to Archie's law [140]. However, in contrast to the pore water conductivity, the $\varepsilon''_{r,\text{eff}}$ generally increases with increasing water content. Because of that reason, there are two competing factors which complicate the interpretation of an obvious trend in the $\varepsilon''_{r,\text{eff}}$ of the complex permittivity. In particular, for AS soil, there was a sudden increase of the measured $\varepsilon'_{r,\text{eff}}$ and $\varepsilon''_{r,\text{eff}}$ observable at low frequency. This observation must be connected to the density and/or structural changes of the soil. However, this type of data illustration is not suitable for quantitative description of soil states, and only allows a qualitative interpretation of the frequency dependence of complex permittivity. In order to investigate the underlining mechanisms causing the dielectric dispersion and the relation to soil states, the measured dielectric spectrum was analysed using an empirical relaxation model, as discussed in the following section.

7.2.5 Spectrum analysis of frequency dependent dielectric behaviour

As the measured dielectric spectrum ranged from 1 MHz to 3 GHz, it was expected that not only a single relaxation process occurs, but multiple superimposed relaxation processes characterise the dielectric spectrum in the considered frequency range. According to Figure 4.2, three relaxation processes can be assumed in the measured frequency window:

- HF relaxation due to dipolar polarisation
- intermediate-frequency relaxation due to interfacial polarisation
- low-frequency relaxation associated with counterion polarisation

In order to fit the dielectric spectra measured on the compacted soil samples, a three-term Cole-Cole model was employed, according to Equation 4.8. Since a three-term Cole Cole model is highly complex, with a large number of unknown fitting parameters, it is practically impossible to calculate analytically the solution one by one. As a result, a Markov Chain

Monte Carlo (MCMC) algorithm was used to optimise the fitting results. There are many different MCMC algorithms available in the literature [286, 287]. The algorithm used in this study is the Random Walk Metropolis-within-Gibbs (RW-MWG) algorithm. The RW-MWG algorithm is based on the original work of Metropolis et al. [288] and Hastings [289], which was further improved by Tierney [290], with the implementation of the Gibbs sampler into the original algorithm to increase the acceptance ratio. Figure 7.16 schematically illustrates the operation principle of the algorithm, in which N is the number of unknown parameters and K is the maximum of iteration steps. If $\mathbf{x} \in \mathbb{R}^N$ is the set of unknown parameters of interest and

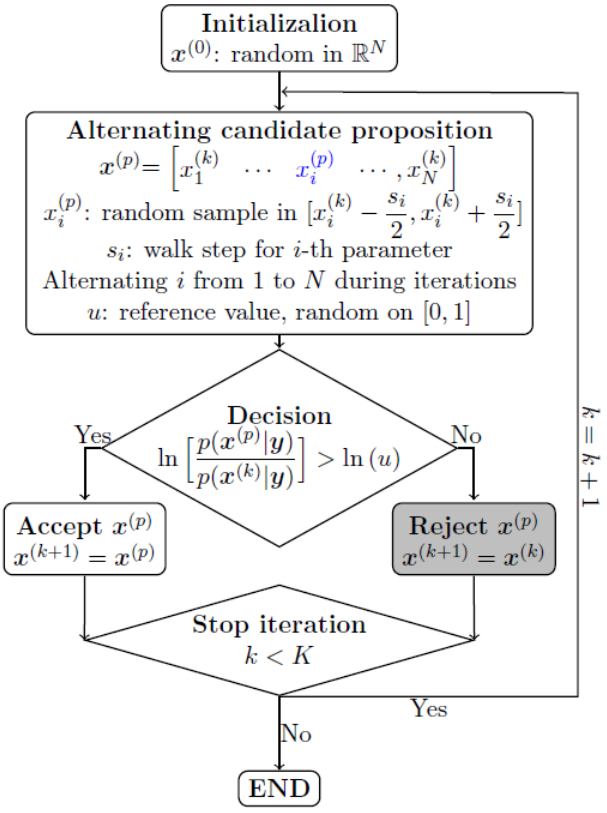

Figure 7.16: Diagram of the RW-MWG method. N is the number of unknown parameters, K is the maximum number of iterations, and s_i defines the size of the neighbourhood in which a new candidate will be proposed, based on [290, 291].

$\mathbf{y} \in \mathbb{C}^M$ is the set of observation points, the objective of an inverse problem is the estimate $\mathbf{x}$ from $\mathbf{y}$ [290]. The mathematical problem can be formulated as an independent, identically distributed, Gaussian noise model according to [286]:

$$\mathbf{y} = f(\mathbf{x}) + \varepsilon, \quad \text{with} \quad \varepsilon \sim \mathcal{N}(0, \Sigma), \tag{7.2}$$

where, $f(\mathbf{x})$ models the mathematical function from $\mathbf{x}$ to $\mathbf{y}$, excluding noise, and ε accounts for the Gaussian noise. The expected value of the posterior distribution is calculated based

on the posterior mean estimation method according to Tierney [290]:

$$\hat{\mathbf{x}} = \int\limits_{\mathbf{x}\in\mathbb{R}^N} \mathbf{x}\, p(\mathbf{x}|\mathbf{y})\, \mathrm{d}\mathbf{x} = \int\limits_{\mathbf{x}\in\mathbb{R}^N} \mathbf{x}\, p(\mathbf{y}|\mathbf{x})\, p(\mathbf{x})\, \mathrm{d}\mathbf{x}, \tag{7.3}$$

where, $p(\mathbf{x}|\mathbf{y})$ is the posterior distribution, $p(\mathbf{y}|\mathbf{x})$ is the likelihood, and $p(\mathbf{x})$ is the prior distribution, which is assumed to be a uniform distribution without further prior information. In this case, the posterior mean estimation was equivalent to the likelihood. However, due to the high complexity of the integral in Equation 7.3, the mathematical problem was solved using the RW-MWG algorithm.

A RW-MWG algorithm allows the generation of samples in the parameter space that follow an objective distribution up to a normalised constant. If the posterior distribution, $p(\mathbf{x}|\mathbf{y})$, is denoted as the objective distribution, the posterior mean estimator can be predicted by averaging all samples in the algorithm. The RW-MWG algorithm began with a random initial guess, $\mathbf{x}^{(0)}$, in the parameter space. For each iteration step, k, a new candidate, $\mathbf{x}^{(p)}$, was predicted in the direction nearby of the active parameter, $\mathbf{x}^k$, with a walk step, s_i. When $\mathbf{x}^{(p)}$ gave a better likelihood than the previous candidate, the active parameters, $\mathbf{x}^k$, was accepted. Otherwise, $\mathbf{x}^k$ was only accepted subject to a probability. After warming up the algorithm, the generated samples followed the posterior distribution. The fundamental criterion of the RW-MWG algorithm is the calculation of the logarithmic ratio of the posterior distributions between the actual candidate, $\mathbf{x}^{(p)}$, and the active parameter, $\mathbf{x}^k$, according to Tierney [290]:

$$\ln\left[\frac{p(\mathbf{x}^{(p)}|\mathbf{y})}{p(\mathbf{x}^{(k)}|\mathbf{y})}\right] = \ln\left[\frac{p(\mathbf{y}|\mathbf{x}^{(p)})\, p(\mathbf{x}^{(p)})}{p(\mathbf{y}|\mathbf{x}^{(k)})\, p(\mathbf{x}^{(k)})}\right] = \ln\left[\frac{p(\mathbf{y}|\mathbf{x}^{(p)})}{p(\mathbf{y}|\mathbf{x}^{(k)})}\right]. \tag{7.4}$$

As mentioned above, with uniform prior distribution, $p(\mathbf{x})$, the logarithmic ratio of the posterior distribution equals the logarithmic likelihood ratio. As a result, the expectation value of the posterior distribution can be approximated at the end of the RW-MWG algorithm as follows:

$$\hat{\mathbf{x}} = \int\limits_{\mathbf{x}\in\mathbb{R}^N} \mathbf{x}\, p(\mathbf{x}|\mathbf{y})\, \mathrm{d}\mathbf{x} \approx \frac{1}{K - K_w} \sum_{k=K_w}^{K} \mathbf{x}^k, \tag{7.5}$$

where, K_w is the number of warming up iterations.

The unknown parameters, $\mathbf{x}$, of interest in the three-term Cole-Cole model were ε_∞, σ_{DC}, $\Delta\varepsilon_i$, τ_i and $\beta_{\mathrm{CC,i}}$, with $i = 1,2,3$ for the number of relaxation processes. The stretching parameter, β_{CC}, of HF relaxation associated with dipolar polarisation, was set to one. The measured dielectric spectrum was denoted as the observations point, $\mathbf{y}$, in the RW-MWG algorithm. The number, K, of maximum number of iteration steps was set to $5 \cdot 10^5$ in order to ensure best convergence of the algorithm.

Figure 7.17 presents two fitting examples on two modified compacted samples of AS: C3 is located on the dry side of the compaction curve, and C8 is located on the wet side. Figures 7.17A and 7.17C show the fitting results for C3 for the real, $\varepsilon'_{r,\text{eff}}$, and imaginary, $\varepsilon''_{r,\text{eff}}$, parts of the complex permittivity, respectively. The results for C8 are presented in Figures 7.17B and 7.17D.

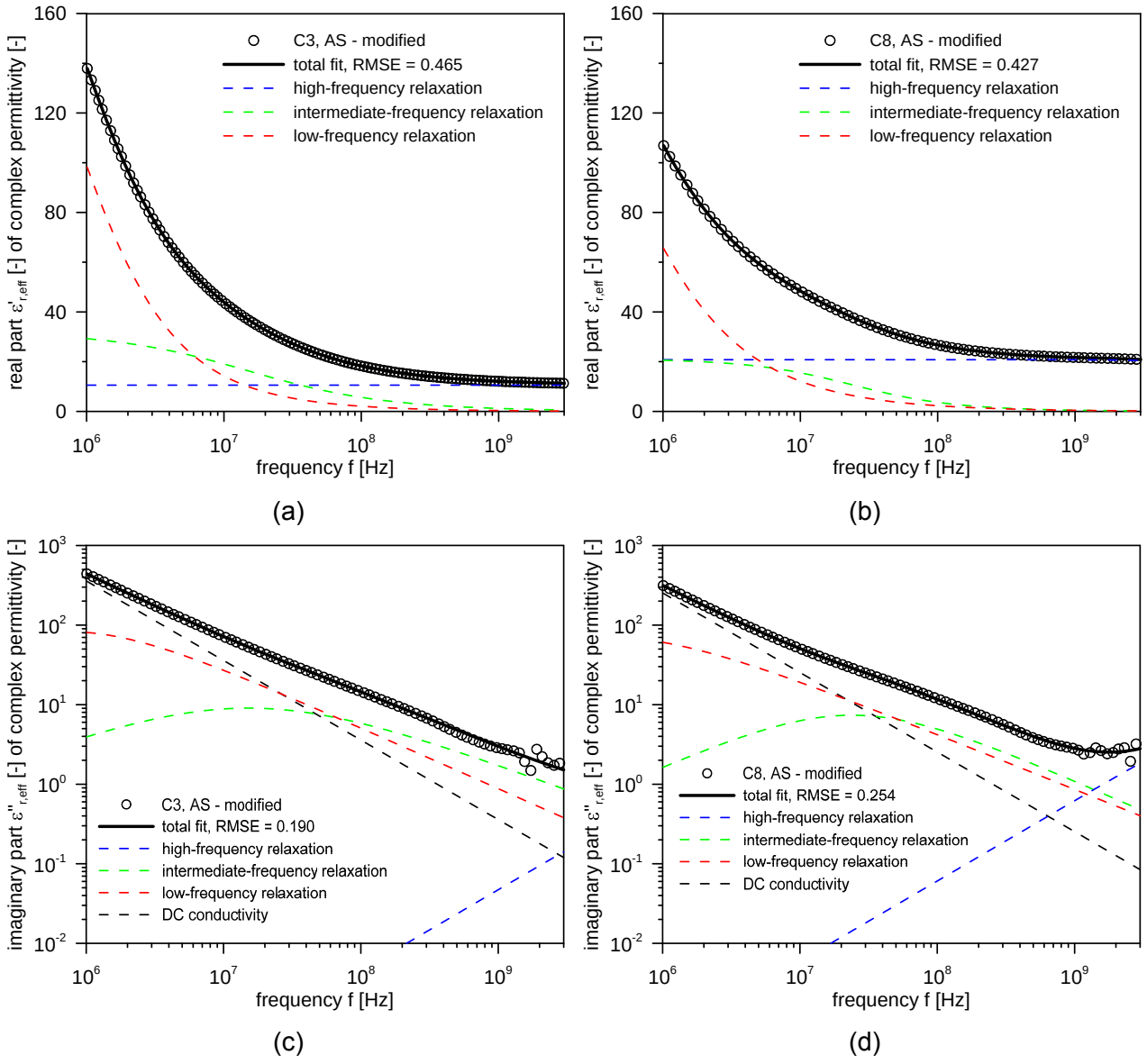

Figure 7.17: Fit of relaxation processes on the dielectric spectrum of compacted samples of AS using a 3-term Cole-Cole model optimised using the RW-MWG algorithm: (A) relaxation magnitude, $\Delta\varepsilon$; (B) relaxation time, τ; (C) stretching exponent, β_{CC}; and (D) direct current conductivity, σ_{DC} ,as function of volumetric water content, θ. The results of high-frequency (HF) relaxation, intermediate-frequency relaxation and low-frequency relaxation are highlighted by various colours.

The total fit of the three-term Cole-Cole agreed perfectly with the measured dielectric spectrum. The fits on the $\varepsilon'_{r,\text{eff}}$ and $\varepsilon''_{r,\text{eff}}$ gave an extremely low RMSE < 0.5. This essentially suggests that the assumptions of the three superimposed relaxation processes were reasonable

in the measured frequency range from 1 MHz to 3 GHz. The extent of the individual relaxation processes is indicated with coloured dashed lines, and the σ_{DC} contribution in the imaginary part is indicated by a black dashed line. It should be noted that the low-frequency relaxation and HF relaxation can only be partly revealed, which indicates that measurements should be undertaken with even broader frequency range to cover the entire relaxation spectrum. The low-frequency relaxation was found to be in the kHz range, whereas the HF relaxation was found at a frequency range of several tens of GHz. In contrast, Figure 7.17 demonstrates that the intermediate-frequency relaxation was around 20 MHz which was completely covered in the measured frequency window. The fits on the other compacted soil samples showed similar trends, but with different fitting parameter values.

Figure 7.18 summarises the obtained fitting parameters, including the standard deviation, of the Cole-Cole model as a function of the volumetric water content. The relaxation magnitude, $\Delta\varepsilon$, of each relaxation process is illustrated in Figure 7.18A, and its corresponding relaxation time, τ, is shown in Figure 7.18B. The obtained stretching exponents, β_{CC}, and direct conductivity, σ_{DC}, are shown in Figures 7.18C and 7.18D. The results of the direct current contribution in Figure 7.18D show a couple of points that are shifted to lower values and deviate from the other fitting results. A possible reason for this shift in σ_{DC} can be found in the quality of the deionised water used for the soil preparation. In general, the σ_{DC} contribution is significantly affected by the ionic concentration of the pore water solution, temperature and molecular composition [42]. Hence, little changes in water quality will affect the chemistry of the pore water solution, which subsequently influences the dielectric properties, particularly the σ_{DC} contribution. However, apart from this deviation, there was still a trend observable. In Figure 7.18D, the fitting results of the σ_{DC} contribution demonstrated a constant value at high volumetric water content. Then the σ_{DC} decreased with decreasing water content as less pore water existed in the soil matrix, which can contribute to direct current conductivity.

A similar trend was observed for the HF relaxation magnitude in Figure 7.18A, which shows a distinct linear relationship with volumetric water content, indicated by the black trend line. Regardless of the soil type or compaction test, the HF relaxation magnitude decreased with decreasing volumetric water content, which accompanied minimal decrease in relaxation time, τ (see Figure 7.18B). This suggests that the HF relaxation magnitude purely depends on the volume fraction of the available water in the soil matrix.

In comparison to the HF relaxation magnitude, there was no clear trend observable in the relationship between low-frequency relaxation magnitude and volumetric water content, as the obtained data points were too scattered. A similar scattering effect can be seen for the stretching exponent in Figure 7.18C, with variation of $0.6 < \beta_{CC} < 1$. However, as aforementioned, only a part of the frequency range covering the low-frequency relaxation processes

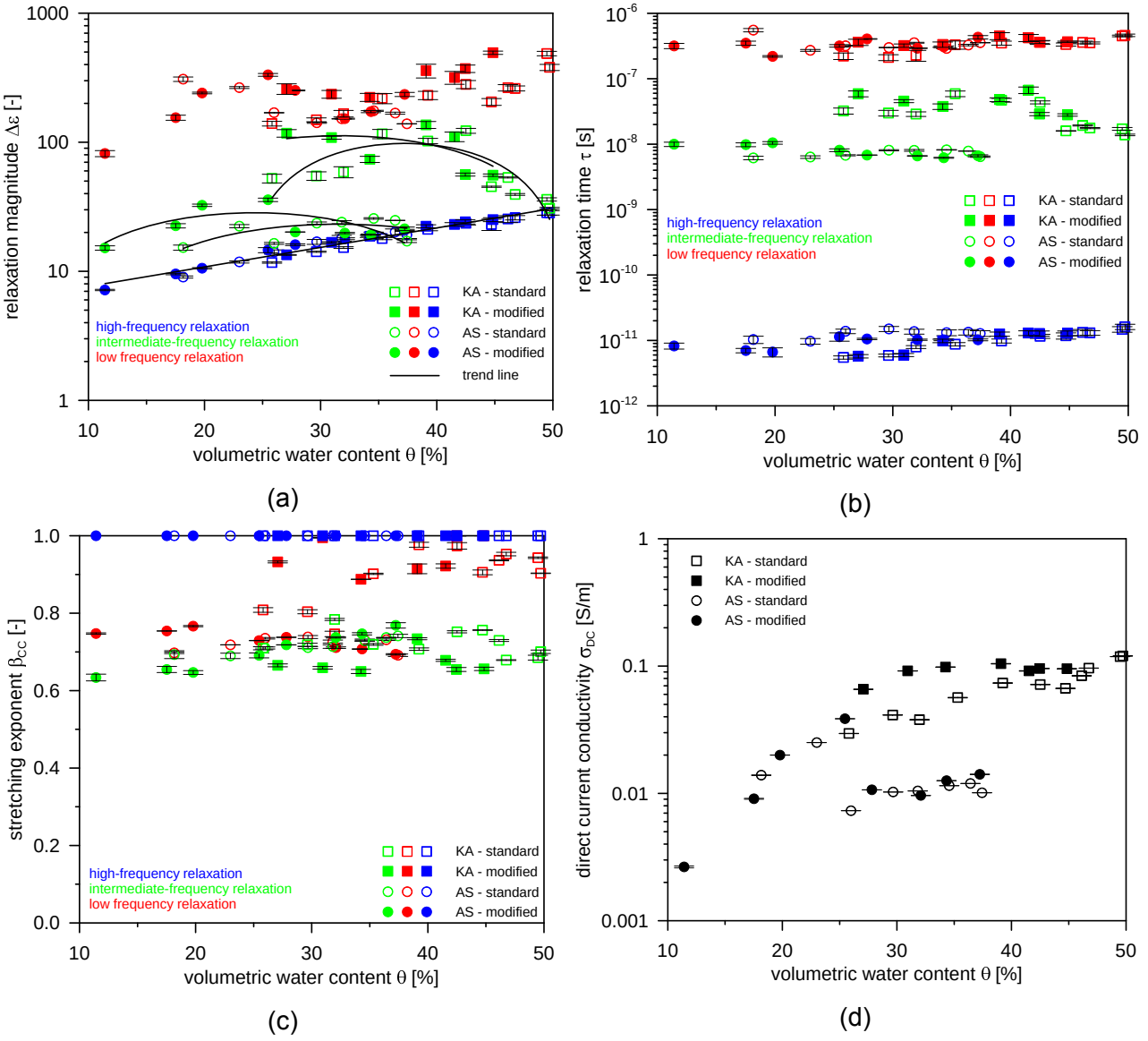

Figure 7.18: Relaxation parameters for the measured dielectric spectrum of compacted samples of AS using 3-term Cole-Cole model combined with MCMC algorithm.

was measured with the given frequency range of 1 MHz to 3 GHz. As a result, the fitting on the low-frequency relaxation suffered uncertainties, despite the good fitting results for the relaxation time, which showed constant values with low RMSE (Figure 7.18B).

Further, Figure 7.18A shows the intermediate-frequency relaxation magnitude, in which the trend of each compaction test is indicated by the black trend line. It was interesting to find that the variation of the relaxation magnitude with volumetric water content had a similar tendency to that of the compaction curve, shown in Figure 7.1. Similar to the compaction curve, the relaxation magnitude demonstrated a peak value. The peak value of the relaxation magnitude of the modified compacted soil samples showed higher values than did the standard compacted soil samples, which was also consistent with the compaction curves.

This result indirectly implies that the magnitude of intermediate relaxation has a strong correlation with the compaction state of a soil. As aforementioned, the intermediate-relaxation may include bound water polarisation and Maxwell-Wagner polarisation. However, in the present study, the intermediate polarisation occured at a low-frequency range at several tens of MHz. This frequency is normally considered too low for polarisation processes connected to the bound water relaxation and, as a result, the Maxwell-Wagner polarisation is assumed to be overwhelming dominant [292]. The Maxwell-Wagner polarisation arises from the accumulation of space charges at the interfaces between two phases with different electrical properties. For clay minerals, it has been found that the magnitude of the Maxwell-Wagner polarisation is strongly dependent on the total surface area of the clay minerals [48]. This is unsurprising because the clay surface is actually the interface that induces the Maxwell-Wagner polarisation. This essentially explains the observed trend for the intermediate-frequency relaxation in Figure 7.18A, similar to that of the compaction curve. With the increasing dry density of the compacted soil sample, the weight and thus the amount of solids in a unit volume increases, which results in a larger total specific surface area. As a result, the magnitude of the Maxwell-Wagner polarisation – the relaxation strength of the intermediate-frequency relaxation – increases.

At first glance, one feature that seemed not to correlate with the compaction curves was the relaxation magnitudes of AS soil, which was lower than that of the KA soil. In contrast, the compaction density of AS was generally higher than that for KA (see Figure 7.1). One may argue that the explanation given above is wrong because, otherwise the relaxation magnitude of AS must be higher than it is for KA due to its higher compaction density, and thus specific particle surface area. However, the specific particle surface area is dominated by the clay fraction. As shown in the particle size distribution in Figure 6.2, the amount of clay particles in AS was less than 50%, whereas KA consisted of nearly pure clay. As a result, the average total particle surface area of KA was higher than that for AS. Thus, the magnitude of the intermediate-frequency relaxation was expected to be higher for KA than for AS.

7.2.6 Summary

This section performed standard and modified compaction tests on AS and KA, in combination with shrinkage tests, soil suction measurements and dielectric measurements. As such, the following observations and findings need to be highlighted:

- The shrinkage tests were parameterised with an empirical fitting equation that was also used to predict different shrinkage zones. In general, the empirical fitting equation was suitable to provide a sufficient fit of the entire shrinkage curve. However, it was

also found that soil compacted on the dry side showed negligibly low shrinkage behaviour, which complicated interpretation of the fitted shrinkage zones. However, soil compacted on the wet side exhibited distinct shrinkage behaviour, and hence allowed better interpretation of the shrinkage modes.

- The SWCCs of each compacted soil sample were measured as a function of the gravimetric water content. The shrinkage curve was used to define the SWCCs dependent on the volumetric water content. The SWCCs of each set of compaction tests were quantified and parameterised using a bimodal fitting equation. A delimiting water content for each set of compaction tests was found at which the SWCCs converged, regardless of the soil compaction state. These delimiting water contents were compared to the parameterised shrinkage curve with the obtained shrinkage zones. It was found that the SWCCs beyond this delimiting water content were associated with the intra-aggregate pore structure, and the delimiting water contents were all located in the zero shrinkage zone.

- Dielectric measurements using the CT cell in a frequency range from 1 MHz to 3 GHz were presented. It was found that the CT cell only minimally varied the density when coring soil samples. This suggests that the use of the CT cell is suitable for both in laboratory and field investigations, where it becomes important to core undisturbed soil samples for subsequent laboratory investigations. The dielectric measurements were compared to existing material-specific calibration equations and theoretical mixture approaches. Moreover, two novel theoretical mixture approaches – WS-model and Hil-model – were applied in combination with the parameterised shrinkage curve and SWCC to predict the dielectric spectrum on the compacted soil samples. The results showed that material-specific calibration equations gave a satisfying approximation of the measured dielectric parameters. However, theoretical mixture approaches were more suitable to consider the structural composition of the soil. Further, it was found that the coupled Hil-model overestimated the dielectric parameters and failed at high water content due to its instability in accurately predicting the porosity. The WS-model was successfully applied to predict the real part, $\varepsilon'_{r,\mathrm{eff}}$, at 1 GHz of the compacted soil samples. Moreover, the real part, $\varepsilon'_{r,\mathrm{eff}}$, was sufficiently predicted at four specific frequencies in a range from 1 MHz to 1 GHz. In contrast to $\varepsilon'_{r,\mathrm{eff}}$, the imaginary part, $\varepsilon''_{r,\mathrm{eff}}$, was generally overestimated by the WS-model, which needs to be investigated in more detail and adjusted in future research.

- The frequency dependence of the complex permittivity of compacted soil was investigated. Three underlining mechanisms causing dielectric dispersion were elaborated by means of a three-term Cole-Cole relaxation model. A MCMC model was applied

to successfully fit the dielectric spectrum. The results showed that the high-frequency relaxation magnitude, associated with dipolar polarisation, was purely dependent on the volumetric water content. In addition, it was found that the intermediate relaxation magnitude, predominantly influenced by Maxwell-Wagner polarisation, showed a similar trend to the compaction curve. Hence, the intermediate relaxation is not only related to the water content, but also to the compaction state due to the influence of the particle surface area on the underlining polarisation processes. The low-frequency relaxation suffered from inaccuracies and insufficient coverage of the low-frequency range and thus requires measurements in a broader frequency range to enable better interpretation.

7.3 Shrinkage test

Densification of soil can be induced by internal stress due to desiccation, as discussed in Section 2.5.2. In order to investigate volume changes caused by pore water evaporation, shrinkage tests on fine-grained soils were conducted in parallel with the dielectric measurements and determination of the SWCC. The methodology and experimental procedure was introduced in Section 6.4; thus, the following sections will focus on the results.

7.3.1 Shrinkage curve

Figure 7.19 shows the results of the shrinkage tests conducted on AS and KA, in which the shrinkage curve is presented in w-ρ_D-relationship. Six shrinkage tests with identical initial conditions were performed for each soil. The shrinkage tests started at an initial water content of 1.1 times the LL, which was found at $w_l = 58.0\%$ for AS and $w_l = 99.0\%$ for KA. It can be seen that the six measured shrinkage curves were consistent and nearly identical.

Minor deviations of the shrinkage curves were only observed for KA for water content below $w = 40\%$. The final dry density of the shrinkage curves ($w = 0\%$) was additionally determined with the water displacement method and compared to the values obtained by the direct measurement method. Based on that, RMSE was calculated to give the standard error of the final density of the direct measurement method to the average value obtained by water displacement method. As shown for both soils in Figures 7.19A and 7.19B, the RMSE values were extremely low, thereby suggesting reliable and consistent results from measuring the shrinkage curve using the direct measurement method.

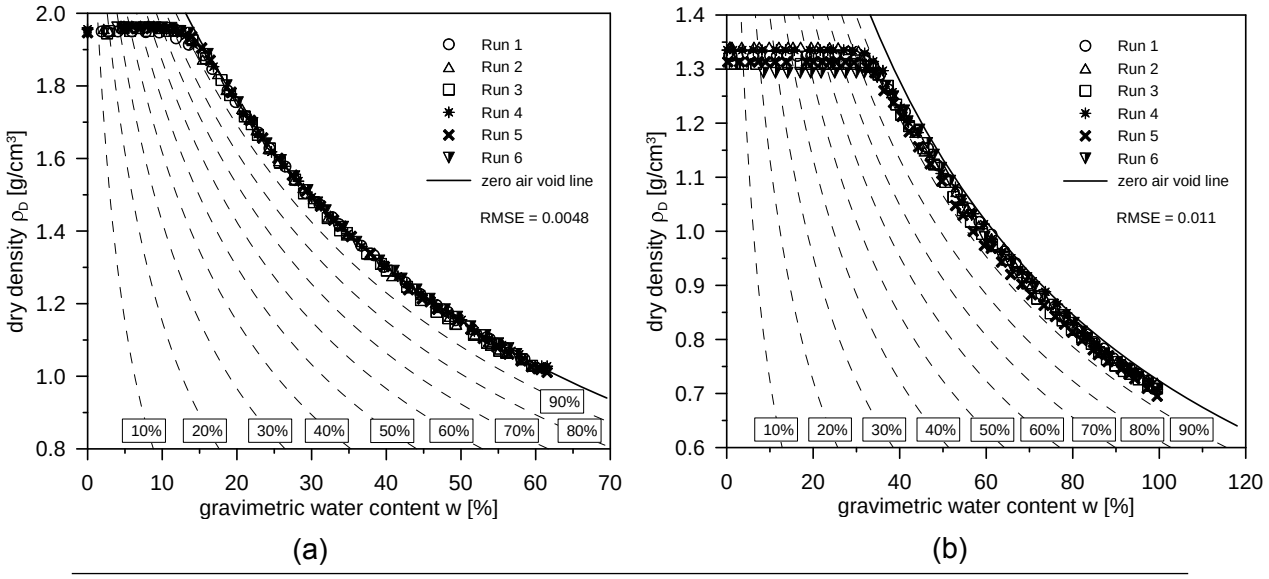

Figure 7.19: Shrinkage curves obtained from shrinkage tests on AS and KA with initial water content of 1.1 times the LL. RMSE gives deviation of the final dry density by direct measurement to the average final density determined by the water displacement method. Shown are the shrinkage curves of (A) AS and (B) KA.

Two different geometrical deformation behaviours could be observed during the shrinkage process. In the first stage of the shrinkage test, the soil only experienced a one-dimensional deformation in sample height. At the beginning of the shrinkage tests, the soil samples were nearly saturated. With the beginning of desiccation of the soil samples, the dry density increased with the decreasing gravimetric water content. Further, the shrinkage curve ran along the zero air void line, which meant that the volumetric loss of water was compensated by the volume changes of the sample. This behaviour is commonly referred to as 'proportional shrinkage', as explained in Section 2.5.2 [3, 87, 97]. A structural deformation mode was not observed for AS or KA, which highlights that the clay content of both soils was sufficiently high, so that intra-aggregate pores dominated the pore structure [88, 96]. Then, in a second stage, the one-dimensional deformation turned into isotropic deformation mode, in which radial deformations occurred. In this stage, the soil shrinkage was still subject to proportional shrinkage. With continuing soil shrinkage, the measured curves left the zero air void line, which can be associated with the residual shrinkage zone. With sufficient loss of water content, the zero shrinkage zone was reached, at which no further volume deformations were observed. Qualitatively, it can be said that the zero shrinkage zone of AS appeared at a lower water content than that of KA.

This phenomenological description of the shrinkage process based on observations given in Figure 7.19 is only qualitative. Thus, the shrinkage curves were subsequently parametrised in order to deliver a quantitative description of the shrinkage behaviour and shrinkage modes. To do so, three facts should be pointed out:

- The shrinkage test started at an extremely high water content of 1.1 times the LL at which soil is seen as 'liquid'. At this water content, the soil consistency is like a clay paste.
- Prior to the test, the samples were remoulded. In contrast to the shrinkage test samples in Section 6.3, the samples were not subject to mechanical stress (such as static compaction).
- During the shrinkage test, crack development could not be visually detected in the samples. This means that desiccation occurred sufficiently slowly during soil shrinkage, given the appropriately chosen sample size. As the samples were crack free, the obtained experimental data could be considered the reference shrinkage curve.

The model proposed by Chertkov [3] for modelling soil clay pastes was used to parameterise the shrinkage curve and determine the shrinkage zones of the different shrinkage curves (see Section 2.5.3). Figure 7.20 shows an example of the parameterised shrinkage curve for Run 1 of KA.

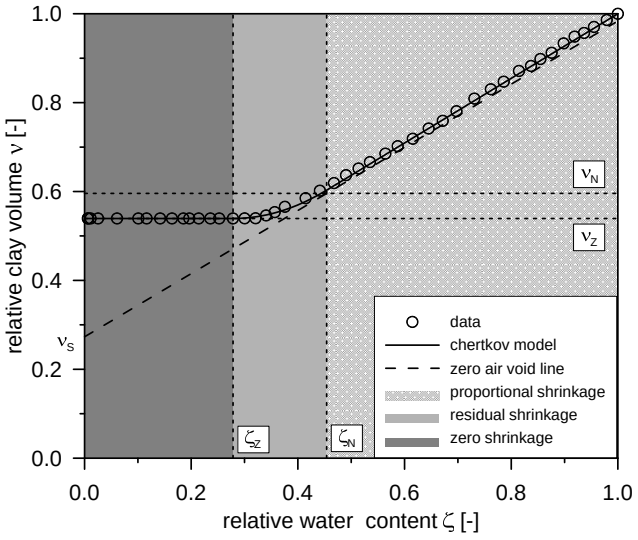

Figure 7.20: Shrinkage curve of Run 1 of KA parameterised by the model proposed by Chertkov [3]. The macro-parameters are indicated by symbols. The obtained shrinkage modes are indicated by shaded areas.

For convenience, the results are shown in ζ-v-dependence, as the model was originally based on this relationship. To do so, the experimental data of the shrinkage curve – originally measured in w and ρ_D – had to be converted into ζ and v, respectively. A MATLAB based code was written to model each individual shrinkage test on AS and KA. First, the zero air void line was calculated dependent on ζ and v. By doing so, the macro-parameter, v_S, was found at $\zeta = 0$. The v_Z parameter was simply determined by the measured final dry density of

the shrinkage test. The transition from proportional to residual shrinkage was determined by finding the point (ζ_N,v_Z), at which the shrinkage curve leaves the zero air void line. Similarly, the transition from residual to zero shrinkage was determined with the relative water content, v_Z, at which relative clay volume remained constant. Figure 7.20 illustrates the obtained macro-parameters that were used to highlight the different shrinkage zones (shaded areas). Based on the obtained macro-parameters, the shrinkage behaviour was modelled by the previously introduced set of Equations 2.27. It can be seen from Figure 7.20 that the model perfectly reproduced the experimental data in the case of the shrinkage test Run 1 of KA. Each individual shrinkage curve of AS and KA was modelled by the model of Chertkov. The results of this parameterisation are compiled in the Table B.1 of the appendix.

Based on the model results shown in Table B.1, the standard deviation of the individual shrinkage curves for AS and KA was calculated. In addition, the standard deviation was calculated for the transition water content, ζ_Z and ζ_N, between the shrinkage zones. Figure 7.21 shows the standard deviation of the shrinkage curves of AS and KA in w-ρ_D-relationship, in which the standard deviation is multiplied by factor 2 in order to highlight the deviation zone. The mean values of the macro-parameters were used to model the average shrinkage

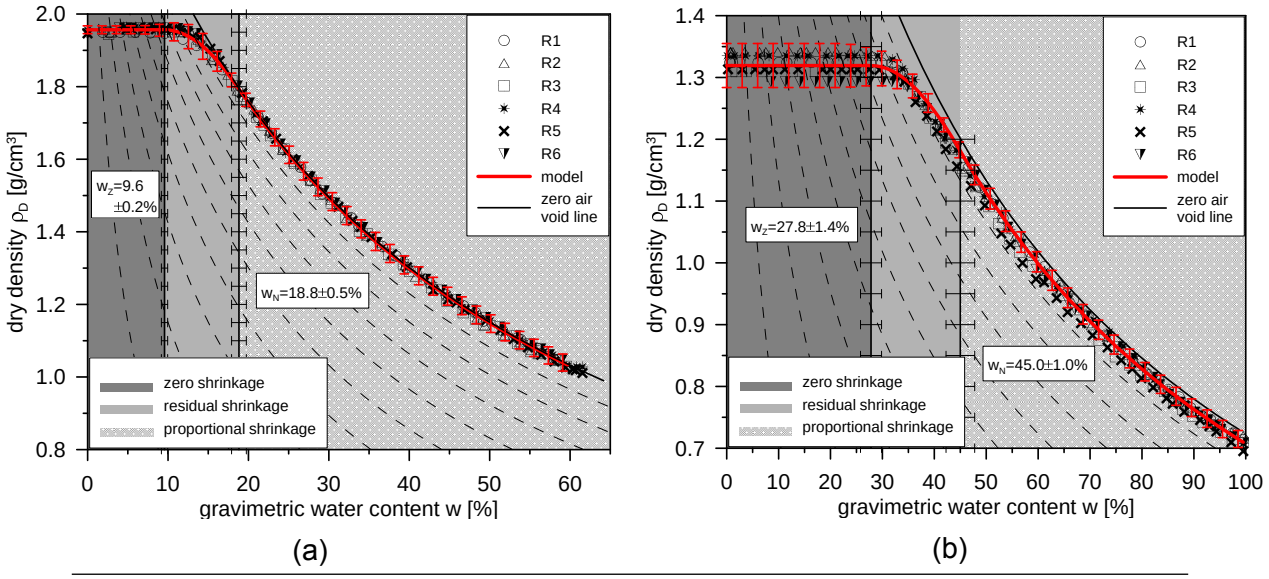

Figure 7.21: Standard deviation of model according to Chertkov [3] used to parameterise the shrinkage curves of AS and KA. Shrinkage curves are shown in w-ρ_D-relationship. The shrinkage zones are indicated by shaded areas, including transition water content, with standard devation.

curve of the entire experimental dataset of the shrinkage tests, as shown by the red line in Figure 7.21. As qualitatively observed in Figure 7.19B, the standard deviation of the modelled shrinkage curves of KA confirmed that a larger uncertainty of the shrinkage curves could be expected at water content lower than $w = 30\%$. This uncertainty began in the residual shrinkage zone, but was mainly located in the zero shrinkage zone. The uncertainty may

be explained by the fact that, for KA, the samples did not shrink uniformly in sample height. Rather, the sample's top surface shrank in a parabolic profile, with larger deformations in the sample centre. Thus, the calculation of the volume change during soil shrinkage based on a cylindrical sample shape may cause inaccuracies. In contrast to KA, minor deviations were only observed in the shrinkage curve of AS at a water content of around $w = 15\%$. For AS, it was observed that the sample surface nearly shrunk uniformly in sample height, which satisfied the assumption of a shrinking cylindrical sample.

It can be seen that the actual SL – considered as the transition from residual to zero shrinkage – was found at a much higher water content for KA ($w_Z = 27.8\%$) than for AS ($w_Z = 9.6\%$). As a result, the zero shrinkage zone for KA covered a much broader water content range. Similar to the SL, the transition from proportional to residual shrinkage was measured at a much higher water content for KA ($w_N = 45.0\%$) than for AS ($w_N = 18.8\%$). Based on the parameters, w_Z and w_N, the water content range of the residual shrinkage zone was localised, which suggested that KA showed a more distinct residual shrinkage zone with a water content range of $w = 17.2\%$. The mean value and standard deviation of the shrinkage zones were quantified. It can be noted that the standard deviation of the transition water contents, w_N and w_Z, was generally low. A minimally larger deviation of w_N and w_Z was observed for KA, which was simply a result of slightly higher uncertainties and deviation of the shrinkage curves. However, it can be seen that the model of Chertkov accurately reproduced the experimental data. This suggests that determination of the shrinkage curve by the direct measurement method was reliable and that the model proposed by Chertkov [3] successfully reproduced the shrinkage curve of fine-grained soils.

7.3.2 SWCC

The soil suction, Ψ_t, was measured dependent on the gravimetric water content, w, using different measurement techniques. Figure 7.22 shows the result of the soil suction measurements for AS and KA, which were used to establish the SWCC as a function of w. The result shows the drying path of the SWCC measured by the combined use of hanging column test ($0 \leq \Psi_t \leq 20$kPa), pressure plate apparatus (25kPa $\leq \Psi_t \leq 400$kPA) and chilled mirror hygrometer (400kPa $\leq \Psi_t \leq 10^5$kPa; WP4T). As aforementioned (see Section 6.4.2 and Table 3.1), the applied methods vary in their measurement principles, and even measure different water potentials. Based on that, critical reviews of the combined working principles and error in soil suction measurements have previously been discussed in the literature [49, 118, 119]. However, the results in Figure 7.22 show a smooth transition at the points where the measurement methods were changed. This strongly suggests that the SWCC can be reliably

measured in a broad soil suction range, when the osmotic potential is negligibly low, by preparing soil samples with deionised water.

The initial water content was prepared to be $w = 59.9\%$ and $w = 99.5\%$ for AS and KA, respectively. It can be seen in Figure 7.22 that soil suction increases with decreasing water content. Considering Equation 2.9 for the capillary rise of pore water, it becomes obvious that capillary suction is strongly dependent on the pore size. With this in mind, it can be suggested that the largest pore size starts to drain first. With increasing suction, smaller pore sizes are also subject to air entry. As a result of the higher bonding forces on the water phase in smaller pore sizes, the applied pressure to drain the pores also increases significantly. For low water content, the soil suction increases rapidly because the fact that water is mostly present in the finest pore sizes. As seen in Figure 7.22, the SWCC of AS and KA

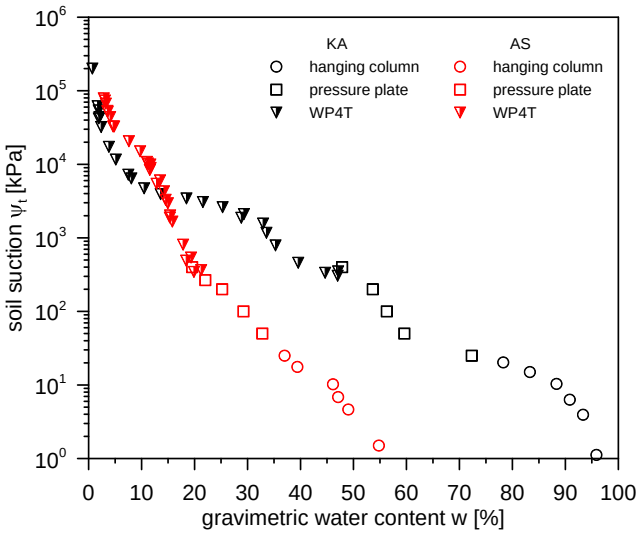

Figure 7.22: SWCC of AS and KA measured using the hanging column test, pressure plate apparatus and WP4T dewpoint potentiameter. The drying path of SWCC is shown starting from a gravimetric water content of 1.1 times the LL, with $w = 59.9\%$ and $w = 99.5\%$ for AS and KA, respectively.

showed an overlapping water content range from $0 \leq w \leq 55\%$. Comparing both SWCCs, it can be qualitatively observed that KA generally demonstrated higher soil suction at the same water content than did AS in the range from $15\% \leq w \leq 55\%$. This observation can be essentially explained by the soil composition. Referring to the mineralogy and particle size distribution (Section 6.2), it was found that KA is composed of a higher amount of clay particles, which results in a finer pore system. A finer pore system, in turn, leads to a higher soil suction, according to Equation 7.22. A change in this trend was observed for a water content lower than $w \leq 15\%$ at which higher soil suction was measured for AS. As adsorptive water is subject to the strongest binding forces to the particle surface, the highest soil suction is reached when only adsorptive water phase is present. Therefore, it was expected that the

SWCC was influenced by adsorptive water in the low water content range. According to the soil investigation in Section 6.2, AS has a clay fraction with higher specific particle surface than does KA, which explains why a higher soil suction was measured below $w \leq 15\ \%$ water content.

However, soil suction measurements dependent on the gravimetric water content do not consider the influence of volume changes on the SWCC due to soil shrinkage. Further, one must consider that the SWCC equations give a quantitative description of the SWCC that is only dependent on the volumetric water content (see Section 2.4.3). In conflict with this, the introduced test methods are usually designed in a manner that makes the determination of volume changes during the test impossible. To overcome this shortcoming, it was assumed that volume changes in the SWCC and shrinkage curve were identical for the entire water content range. Under this assumption, the parameterised reference shrinkage curve was used to match the corresponding dry density for a given water content. In order to justify this assumption, all four samples of soil suction measurements for AS and KA were taken to determine the volume by the water displacement method (see Section 6.4.3). Subsequently, the dry density was calculated and compared to the values obtained by the shrinkage curve. Figure 7.23 demonstrates the comparison between the dry density obtained by the shrinkage curve and the dry density measured by the water displacement method after soil suction measurements.

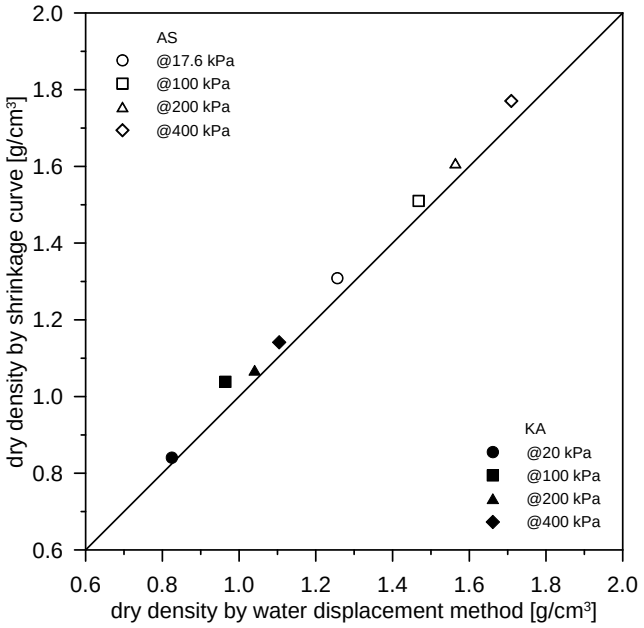

Figure 7.23: Comparison of sample densities measured with the water displacement method and density values obtained by the shrinkage curve based on the measured gravimetric water content and geometrically measured volume.

The result shows that the measured values were nearly identical. The dry density defined by the shrinkage curve tended to be slightly higher than the values during the soil suction measurement. A possible reason can be found in the difference in the testing procedures. There are certainly differences in the boundary conditions, leading to the dewatering of the samples in the shrinkage and SWCC tests. It is obvious that the shrinkage test represents a process of continuous desiccation of the soil samples depending on the prevailing atmospheric conditions. In contrast, the measurement using the hanging column test method and pressure plate apparatus is a discontinuous, yet monotonous, process in which the soil suction is determined step-wise by applying a pressure step in the water or air phase, and awaiting equilibrium conditions between both phases. This discontinuous process of dewatering soils may lead to slightly lower values than those measured in the shrinkage test. This must be investigated in more detail in future experiments. However, based on the results shown in Figure 7.23, it can be concluded, that the assumptions of the same volume changes in the shrinkage and SWCC tests were reasonable.

Figure 7.24 shows the SWCCs of AS and KA dependent on the volumetric water content, which implicitly considers volume changes during the test. Further, the parameterised shrinkage curve of each soil used to convert the SWCC into volumetric water content is also illustrated. The initial volumetric water content of the SWCCs was found to $\theta = 61.8\%$ and $\theta = 70.6\%$ for AS and KA, respectively. Similar to Figure 7.22, a smooth transition is given between the different experimental measurement methods. It can be seen that the SWCCs of AS and KA revealed bumps at which the curve shape changed. These bumps indicate a heterogeneous pore system [68], which seems plausible when considering the distinct shrinkage behaviour of fine-grained soils. However, comparing the SWCC with the shrinkage curve, it can be seen that these bumps are located in the residual shrinkage zone, whereas, in the range of the proportional and zero shrinkage zones, the SWCCs exhibit a smooth shape without significant bumps.

Three different equations were applied to describe and parameterise the SWCC quantitatively. Due to the lack of soil suction measurement at a water content close to $\theta = 0\%$, the residual water content was assumed to be θ_R, with an equivalent soil suction of $\Psi_t = 10^6$kPA [8]. The initial volumetric water contents, as aforementioned, were taken as θ_S. First, the experimental data were fitted by two unimodal van Genuchten equations with two unknown fitting parameters (a_vG and n_vG), in which m_vG was expressed by n_vG according to $m_\mathrm{vG} = 1 - 1/n_\mathrm{vG}$. Second, a unimodal van Genuchten equation with three unknown fitting parameters (a_vG, n_vG and m_vG) was used. In order to respect the observed heterogeneous pore system, a 4-modal van Genuchten equation was applied, according to 2.14. For the 4-modal van Genuchten equation, m_vG was also expressed by $m_\mathrm{vG} = 1 - 1/n_\mathrm{vG}$ to reduce the number of unknown fitting parameters and ensure sufficient stability of the fitting process.

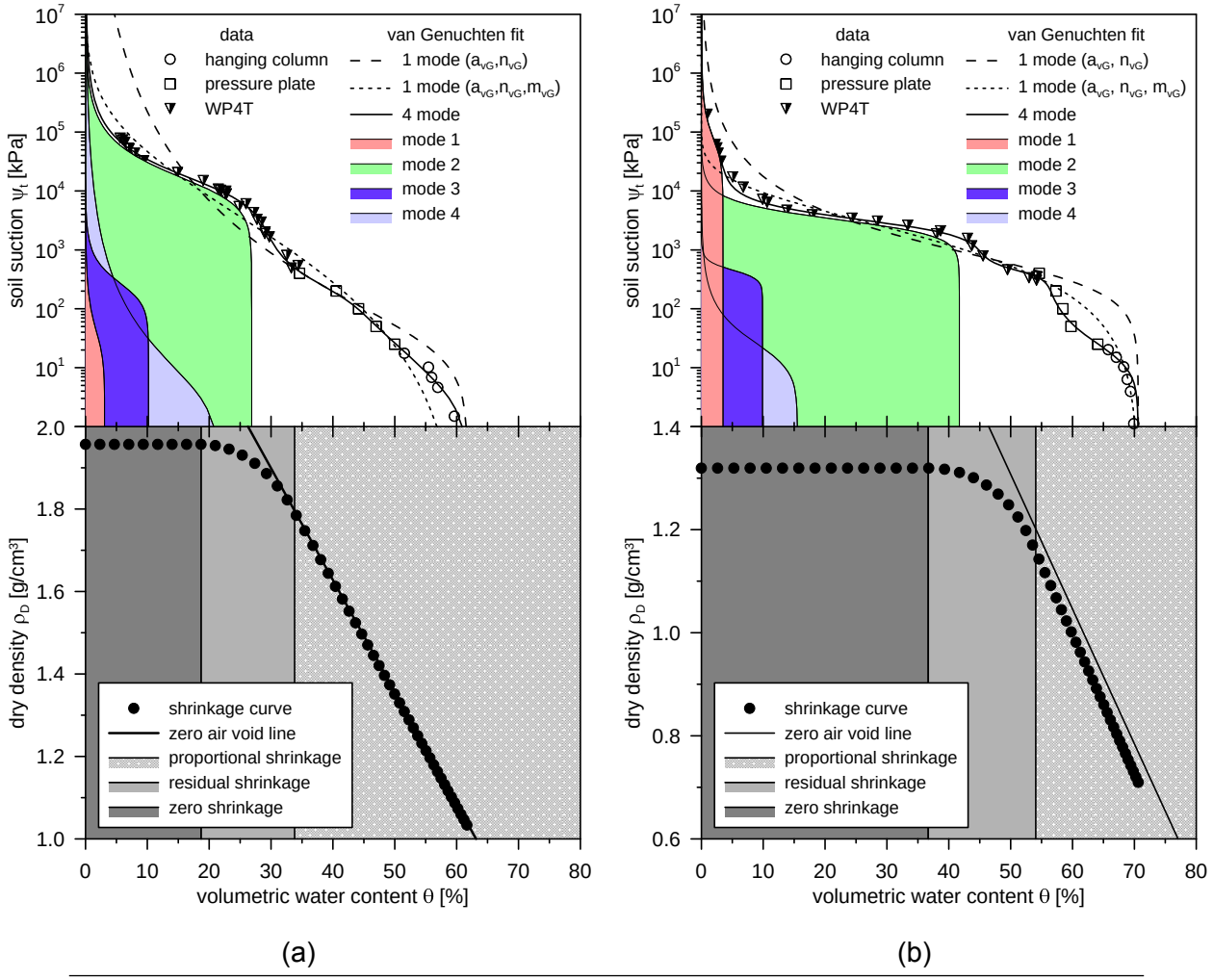

Figure 7.24: Combination of SWCC and shrinkage curve of (A) AS and (B) KA – (Top) SWCCs parameterised by (i) a multimodal van Genuchten model (solid line), and a unimodal van Genuchten with (ii) two unknown fitting parameters and (iii) three unknown parameters. The individual modes of the multimodal van Genuchten model are indicated by the shaded areas. Experimental data were determined by a combination of the hanging column test method (hanging column), pressure plate apparatus (pressure plate), and chilled mirror hygrometer (WP4T). (Bottom) Parameterised shrinkage curves, including shrinkage zones.

All three equations were fitted by the RW-MWG algorithm, introduced in Section 7.2.5. The fitting parameters, including RMSE, are compiled in Table B.3 and B.2.

The solid lines in Figure 7.24 represent the total fit of the 4-modal van Genuchten model for AS and KA. The shaded areas in Figure 7.24 represent the individual modes that were obtained by weighting the four subsystems of the SWCC. The dashed and dotted lines show the results of the unimodal van Genuchten models, with two and three unknown parameters, respectively. It can be seen that the 4-modal van Genuchten model best reproduces the observed bumps in the curve and provides a perfect fit for AS and KA with the lowest RMSE (see Table B.2). In contrast, the fitting results of the unimodal van Genuchten models reveal higher RMSE, which indicates greater deviations from the experimental data. In addition, it

can be seen that the unimodal van Genuchten model with two unknown parameters varies particularly at the high soil suction range with low water content. This is due to the expression $m_{vG} = 1 - 1/n_{vG}$, which additionally constrains the flexibility of the model at high suction range. In comparison, the unimodal van Genuchten model with three unknown parameters agrees better with a experimental data, especially at a high soil suction range, where only minor deviations were observed.

The importance of the accuracy of the SWCC fitting process and influence when modelling the dielectric spectrum will be discussed at a later stage in this thesis.

7.3.3 Dielectric behaviour of shrinking soil

Shrinkage tests on AS and KA were conducted in combination with continuous dielectric measurements. In parallel, three reference samples were prepared to record continuously the gravimetric water content changes during the shrinkage process. A MATLAB based code was developed to control the balance and automatically measure the weight changes of the three reference samples. Since the weight of the sample cups was known a priori, the total bulk soil weight of all reference samples could be plotted over the test time. Figure 7.25A shows the results of the recordings on the reference samples.

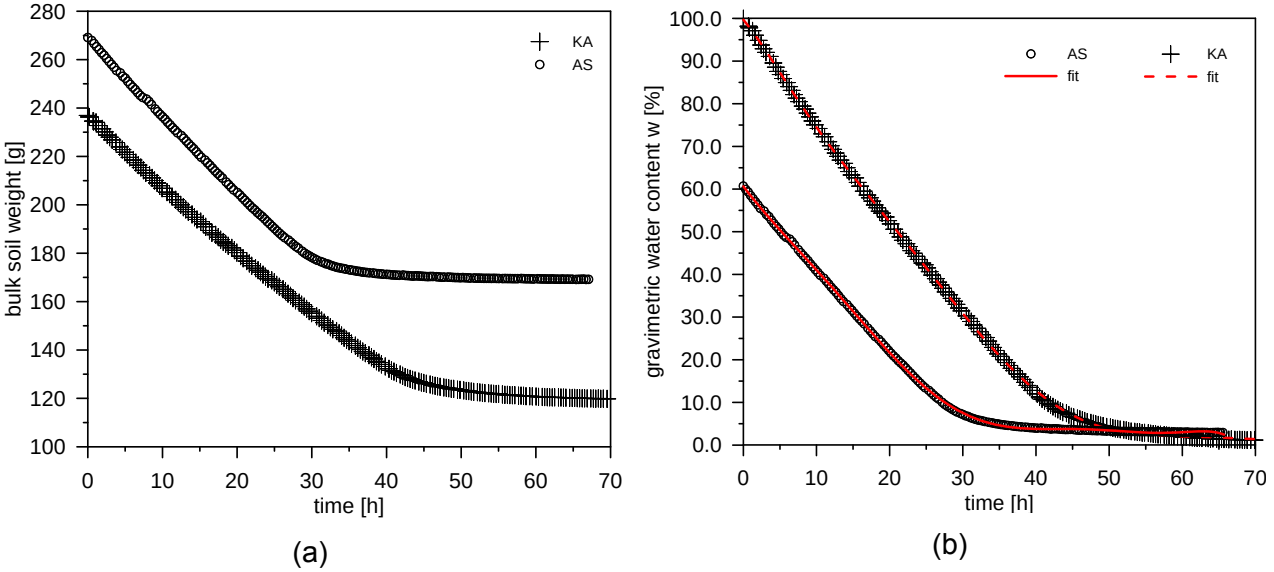

Figure 7.25: Continuous balance measurement on reference samples during shrinkage tests on AS and KA. (A) bulk soil weight as function of time, and (B) gravimetric water content as function of time including fit using a 9^{th} degree polynomial.

The experiments were performed in a climate chamber; thus, the environmental conditions were perfectly controlled to prevent any external influence on the soil shrinkage behaviour.

The result of the measurements on AS and KA showed a smooth curve over the entire measurement time. The soil weight was continuously decreasing with ongoing test time. At the beginning of the shrinkage test, there was a clear linear relationship between soil weight and time. This linear relationship turned into a nonlinear evolution with increasing time. At this point, the soil weight reduction significantly slowed down. Towards the end of the experiments, the soil weight reached a constant value.

The initial gravimetric water content of the reference samples was determined before starting the shrinkage test, and was found to $w_{\mathrm{I}} = 60.3\,\%$ and $w_{\mathrm{I}} = 99.7\,\%$ for AS and KA, respectively. Based on w_{I} and the measured bulk soil weight, the gravimetric water content changes during the shrinkage test could be determined. Figure 7.25B illustrates the gravimetric water content as a function of time. The trend of the curves followed the ones in Figure 7.25A. Subsequently, a ninth degree polynomial was used to fit the gravimetric water content evolution as a function of time. As shown in Figure 7.25B, the fit reproduced the experimental data perfectly.

Another MATLAB based code was used to calculate automatically the permittivity, $\varepsilon^{\star}_{r,\mathrm{eff}}$, from the 1-port reflection measurements based on the technique introduced in Section 5.3.2. As previously explained in the experimental procedure (Section 6.4.3), six calibration materials were measured prior to the shrinkage test. By doing so, both OWS and OWL calibrations were combined, as recommended in Section 5.5.1. The OWS calibration was applied to calculate the $\varepsilon^{\star}_{r,\mathrm{eff}}$ in a frequency range from $1\,\mathrm{MHz} \leq f \leq 400\,\mathrm{MHz}$, whereas the OWL calibration was used to calculate $\varepsilon^{\star}_{r,\mathrm{eff}}$ at HF range ($400\,\mathrm{MHz} < f \leq 3\,\mathrm{GHz}$). That meant that each individual dielectric measurement was analysed to calculate $\varepsilon^{\star}_{r,\mathrm{eff}}$ in a frequency range from 1 MHz to 3 GHz. As balance weight measurements and dielectric measurements ran simultaneously and were synchronised, the calculated $\varepsilon^{\star}_{r,\mathrm{eff}}$ could be directly related to the measured gravimetric water content changes during shrinkage. Figure 7.26 and 7.27 show the result of dielectric measurements during the shrinkage tests on AS and KA.

In these figures, the dielectric spectra with the real part, $\varepsilon'_{r,\mathrm{eff}}$, and imaginary part, $\varepsilon''_{r,\mathrm{eff}}$, of $\varepsilon^{\star}_{r,\mathrm{eff}}$ are illustrated in a 3-D plot as a function of frequency, f, and gravimetric water content.

Two aspects should be highlighted concerning the evolution of the dielectric spectra of AS and KA:

1. Minor noise and small ripples were observed in the imaginary part, $\varepsilon''_{r,\mathrm{eff}}$, for the frequency range, $f \geq 1\,\mathrm{GHz}$. This unwanted artefact may have been caused by two reasons. First, calibration materials (such as deionised water and methanol) have dielectric parameters with strong temperature dependence. Accurate determination of the temperature is required during the calibration measurement with accuracy of 0.1°C [293].

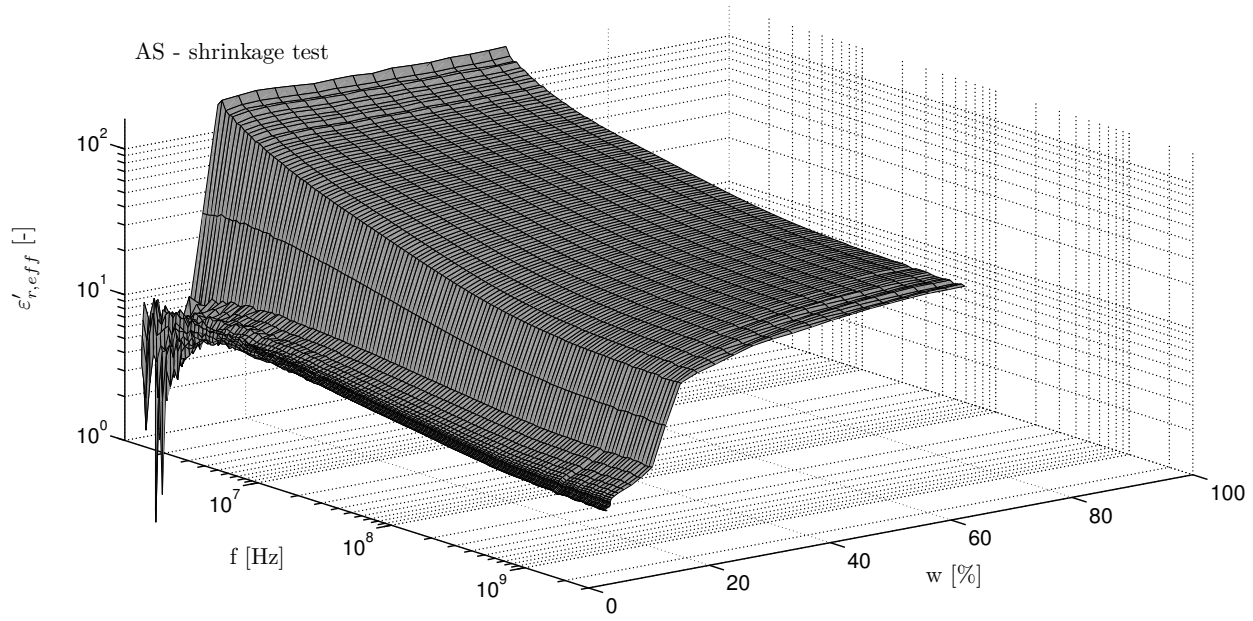

(a)

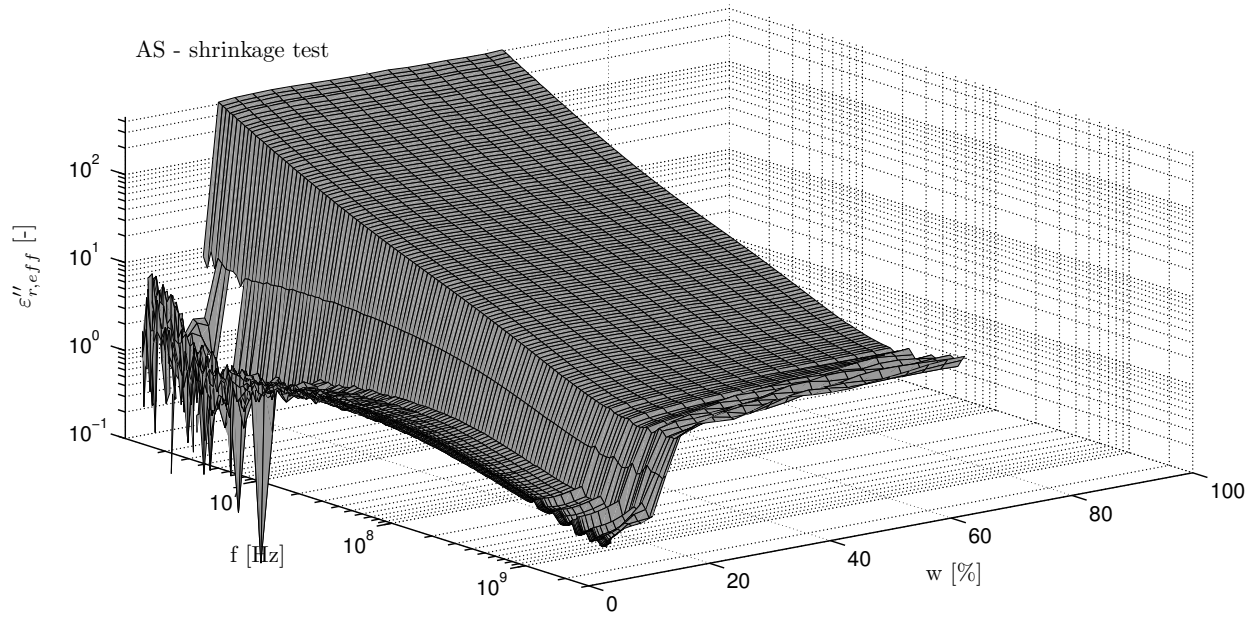

(b)

Figure 7.26: 3-D illustration of complex permittivity measured during the shrinkage tests on AS. Shown are (A) $\varepsilon'_{r,\text{eff}}$ and (B) $\varepsilon''_{r,\text{eff}}$ as a function of frequency and gravimetric water content.

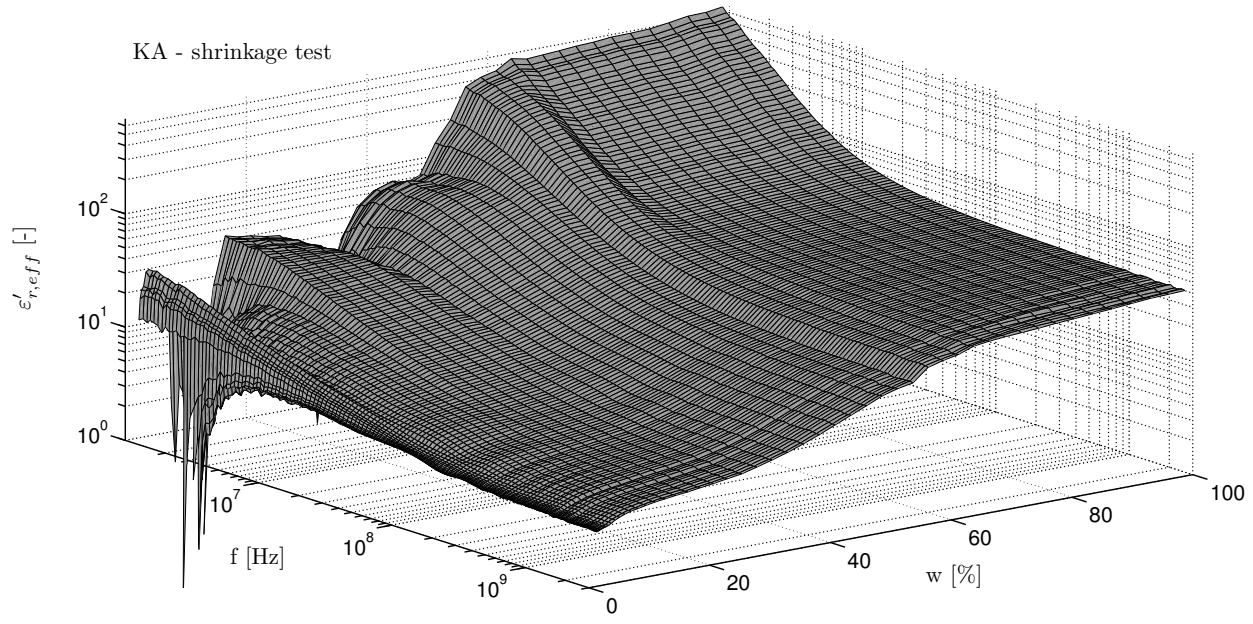

(a)

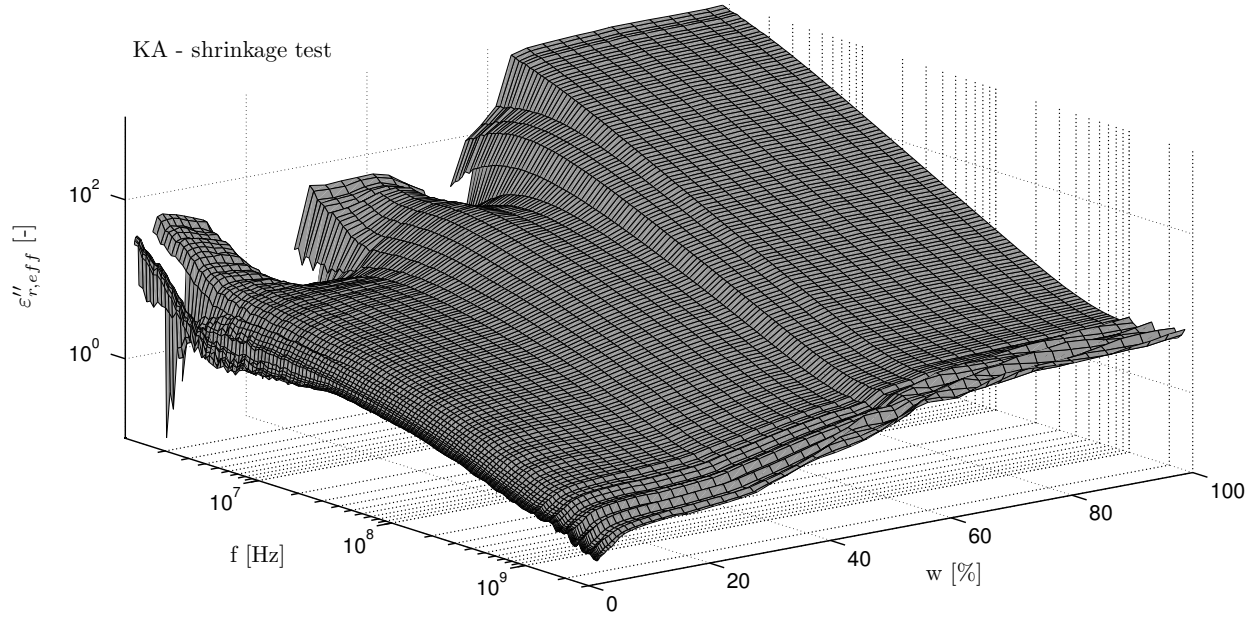

(b)

Figure 7.27: 3-D illustration of complex permittivity measured during the shrinkage tests on KA. Shown are (A) $\varepsilon'_{r,\text{eff}}$ and (B) $\varepsilon''_{r,\text{eff}}$ as a function of frequency and gravimetric water content.

Hence, an imprecise temperature determination when measuring the dielectric parameters of calibration materials may cause inaccuracies in the subsequent calculation of the permittivity. Second, calibration materials (such as methanol and ethanol) have a hygroscopic nature. As a result, potential contamination of the calibration liquids may influence the results of the dielectric measurements [293].

2. Remarkable noise was obtained in both the real and imaginary part for the low frequency range $f \leq 10\,\text{MHz}$ at lower water content. The value of the complex permittivity is generally expected to be smaller in the low water content range. At low permittivity, the sensitivity of permittivity from the measured reflection coefficient, S_{11}, was higher. Hence, minor inaccuracies in measuring the reflection coefficient may cause remarkable noise in the computation of the dielectric spectrum.

Looking at the relationship between $\varepsilon^{\star}_{r,\text{eff}}$ and f at given water content, it can be noted that the real part only varied slightly at the HF range of $0.5\,\text{GHz} \leq f \leq 3\,\text{GHz}$, which essentially demonstrates the area of dipolar polarisation of water molecules. In contrast, the real part increased strongly with frequency lower than 500 MHz. This was a result of the additional presence of other polarisation mechanisms (such as interfacial and counterion polarisation) that superimpose at a low-frequency range. A different trend was observed when examining the relationship of $\varepsilon''_{r,\text{eff}}$ and f at given water content. In a logarithmic plot, $\varepsilon''_{r,\text{eff}}$ exhibited higher values at 3 GHz frequency than at 1 GHz, which may already indicate dipolar relaxation. Further, $\varepsilon''_{r,\text{eff}}$ steadily increased with decreasing frequency, which is caused by the same polarisation mechanisms as mentioned for $\varepsilon'_{r,\text{eff}}$. However, direct conductivity may also contribute to the magnitude of $\varepsilon''_{r,\text{eff}}$ at a low-frequency range. When carefully examining the relationship between $\varepsilon'_{r,\text{eff}}$ and w at a given frequency (such as 1 GHz), it should be noted that the real part varied with the water content. The highest values of $\varepsilon'_{r,\text{eff}}$ were measured at the highest water content. Then, $\varepsilon'_{r,\text{eff}}$ decreased with a reduction of water content due to soil shrinkage. A similar trend was observed for $\varepsilon''_{r,\text{eff}}$. However, in contrast to $\varepsilon'_{r,\text{eff}}$, the imaginary part generally had much lower values in the frequency range of GHz.

A characteristic phenomenon was observed in the dielectric spectra measured on AS and KA during the shrinkage test. For AS, a remarkable drop of both dielectric parameters, $\varepsilon'_{r,\text{eff}}$ and $\varepsilon''_{r,\text{eff}}$, was found at a volumetric water content range around $\theta = 25\,\%$, and a minor drop was observed for KA at a water content near to $\theta = 58\,\%$. To provide a better view of this phenomenon, Figure 7.28 illustrates the real, $\varepsilon'_{r,\text{eff}}$, and imaginary, $\varepsilon''_{r,\text{eff}}$, parts of complex permittivity at selected frequencies (1 GHz, 100 MHz, 10 MHz and 1 MHz) as a function of volumetric water content.

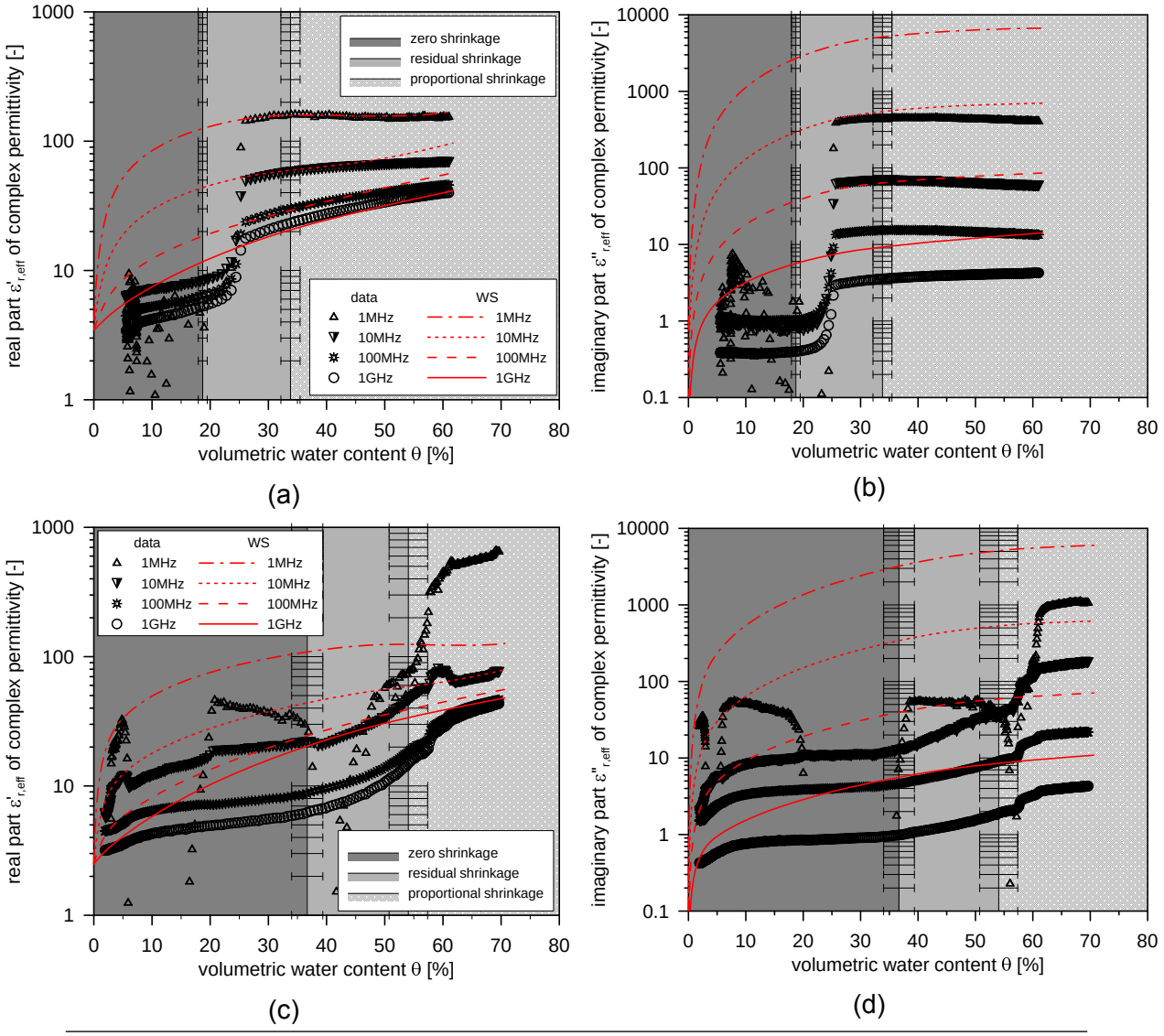

Figure 7.28: Dielectric measurements at frequencies of 1 GHz, 100 MHz, 10 MHz and 1 MHz during soil shrinkage of AS and KA as a function of volumetric water content, θ, with predictions of WS-model: (A) to (B) measured real, $\varepsilon'_{r,\mathrm{eff}}$, and imaginary, $\varepsilon''_{r,\mathrm{eff}}$, parts on AS in comparison with prediction using the WS-model, and (C) to (D) measured real, $\varepsilon'_{r,\mathrm{eff}}$, and imaginary, $\varepsilon''_{r,\mathrm{eff}}$, parts on KA in comparison with prediction using the WS-model. Additionally, the shrinkage zones, including standard deviations, are illustrated.

The prediction of the theoretical mixture approach WS is also shown for comparison. The prediction of $\varepsilon^{\star}_{r,\mathrm{eff}}$ using the WS-model followed the same scheme as previously explained in Sections 4.5.2 and 7.2.4. The SWCC modelled with 4-modal van Genuchten equation and the parameterised shrinkage curve were used as input for the WS-model.

In the case of AS at 1 GHz, it can be seen prior to the drop ($\theta > 25.0\,\%$) that $\varepsilon'_{r,\mathrm{eff}}$ was slightly underestimated by the WS-model. After the drop, the trend changed significantly and the measured $\varepsilon'_{r,\mathrm{eff}}$ was much lower than predicted, which meant the permittivity, $\varepsilon'_{r,\mathrm{eff}}$, was overestimated by the model. For lower frequencies, the WS-model approached $\varepsilon'_{r,\mathrm{eff}}$ sufficiently

well prior to the drop. In particular, a good estimation was found for $\varepsilon'_{r,\text{eff}}$ at 1 MHz, where the measurement showed nearly constant value for water content prior to the drop ($\theta > 25\,\%$).

For KA, the WS-model tended to overestimate $\varepsilon'_{r,\text{eff}}$ at 1 GHz over the entire volumetric water content range. With decreasing volumetric water content, the prediction of the model deviated more and more from the measured $\varepsilon'_{r,\text{eff}}$. Especially at 1 MHz, a reliable prediction was not possible. Prior to the drop ($\theta > 58\,\%$), the measured $\varepsilon'_{r,\text{eff}}$ at 1 MHz showed much higher values than were predicted using the WS-model, which suggests that additional polarisation effects may occur. Further, the $\varepsilon'_{r,\text{eff}}$ at 1 MHz exhibited extreme noise after the drop ($\theta < 58\,\%$), which indicated that the measurement results could not be considered reliable at this low-frequency range.

It was interesting to find in this analysis three different aspects which need to be discussed further:

1. The influence of soil suction, Ψ_t, and dry density, ρ_D, on the WS-model seemed unclear. The question to be addressed is how the prediction of the WS-model varies with a changing shrinkage curve and SWCC. For example, as shown in Figure 7.24, the SWCCs were fitted by various van Genuchten models, which gave a different quality of fitting results, at which the best fit was obtained with a 4-modal van Genuchten equation. The question is how the accuracy of the SWCC fit influences the prediction of the WS-model.

2. The WS-model essentially cannot reproduce the measured drop of $\varepsilon^{\star}_{r,\text{eff}}$. This suggests that the drop is not directly related to changes in water content, density or soil suction. In Figure 7.28, the shrinkage zones obtained by the Chertkov model are illustrated together with their standard deviations. It was interesting to find that the drop of $\varepsilon'_{r,\text{eff}}$ for AS fell exactly in the range of the residual shrinkage zone. For KA, the drop of $\varepsilon'_{r,\text{eff}}$ was located in the residual shrinkage zone, including standard deviation. This drop will be numerically investigated and further discussed in Section 7.3.4.

3. It can be seen that $\varepsilon'_{r,\text{eff}}$ at 1 GHz for AS and KA decreased with decreasing volumetric water content. However, a different trend was observed at 1 MHz and 10 MHz for AS, at which $\varepsilon'_{r,\text{eff}}$ and $\varepsilon''_{r,\text{eff}}$ showed a constant value prior to the drop. This observation will be further investigated in Section 7.3.5.

In order to study the influence of the shrinkage curve and SWCC on the performance of the WS-model, two sensitivity analyses were separately performed. To gain a representative and meaningful result from this sensitivity analyses, two different scenarios were considered. In the first step, only the measured standard deviation of the shrinkage curve was taken into

account, as shown in Figure 7.21, in combination with the SWCCs of AS and KA parameterised by the 4-modal van Genuchten equation. The SWCC and shrinkage curve, including the standard deviation, were used to predict the dielectric spectrum of AS and KA using the WS-model in a frequency range from 1 MHz to 3 GHz. Then, in a second step, only the SWCC was varied using the different parameterisation based on the used van Genuchten equations, as shown in Figure 7.24, in combination with a fixed averaged shrinkage curve. The shrinkage curve and variation in the SWCCs were used to predict the dielectric spectrum of AS and KA in a frequency range from 1 MHz to 3 GHz.

Figure 7.29 illustrates the results of the sensitivity analysis. The grey shaded area shows the sensitivity of $\varepsilon'_{r,\text{eff}}$ and $\varepsilon''_{r,\text{eff}}$ at specific frequencies (1 GHz, 100 MHz, 10 MHz and 1 MHz) as a function of the volumetric water content due to variations in the SWCC. The red shaded areas show the sensitivity due to standard deviation of the shrinkage curve. Figures 7.29A and 7.29B present the results for AS, while Figures 7.29C and 7.29D present the results for KA.

It can be seen that, at 1 GHz, the $\varepsilon'_{r,\text{eff}}$ was identical for both soils. This indicates that the WS-model was insensitive to the deviations in SWCC and shrinkage curve, which means that the influence of Ψ_t and ρ_D was negligibly low. As a direct result, one can conclude that, at 1 GHz, $\varepsilon'_{r,\text{eff}}$ is proposed to be only a function of water content. Another trend in Figure 7.29B and 7.29D is found for $\varepsilon''_{r,\text{eff}}$ at 1 GHz, which seemed to be more sensitive to changes in SWCC, but not so much to changes in the shrinkage curve. Analogue trends were obtained for $\varepsilon''_{r,\text{eff}}$ at lower frequencies (100 MHz, 10 MHz and 1 MHz). The influence of the standard deviation of the shrinkage curve on the modelled permittivity was relatively low. It seems that the sensitivity to the variations in the SWCC is much higher than it is to the standard deviation of the shrinkage curve. Similar results were obtained for $\varepsilon'_{r,\text{eff}}$ at low frequency. The results showed that the SWCC had the dominating influence because the $\varepsilon'_{r,\text{eff}}$ varied more with SWCC variations.

To conclude, the sensitivity analysis showed that the $\varepsilon'_{r,\text{eff}}$ at 1 GHz was insensitive to soil suction, Ψ_t, and dry density, ρ_D, when predicted by the WS-model. With lower frequencies, $\varepsilon'_{r,\text{eff}}$ became increasingly sensitive to Ψ_t and ρ_D; however, the influence of changes in Ψ_t definitely dominated. Further, the sensitivity analysis demonstrated that the $\varepsilon''_{r,\text{eff}}$ was sensitive to soil suction over the entire illustrated frequency. Generally, the sensitivity of $\varepsilon''_{r,\text{eff}}$ to variations in ρ_D was much lower than it was to variations in Ψ_t. Of course, Ψ_t and ρ_D were strongly correlated, and the considered variations may not represent natural variability. While ρ_D was varied based on observed deviations during the test, the SWCCs were varied based on the usage of different parameterisations. Nevertheless, this study could demonstrate the

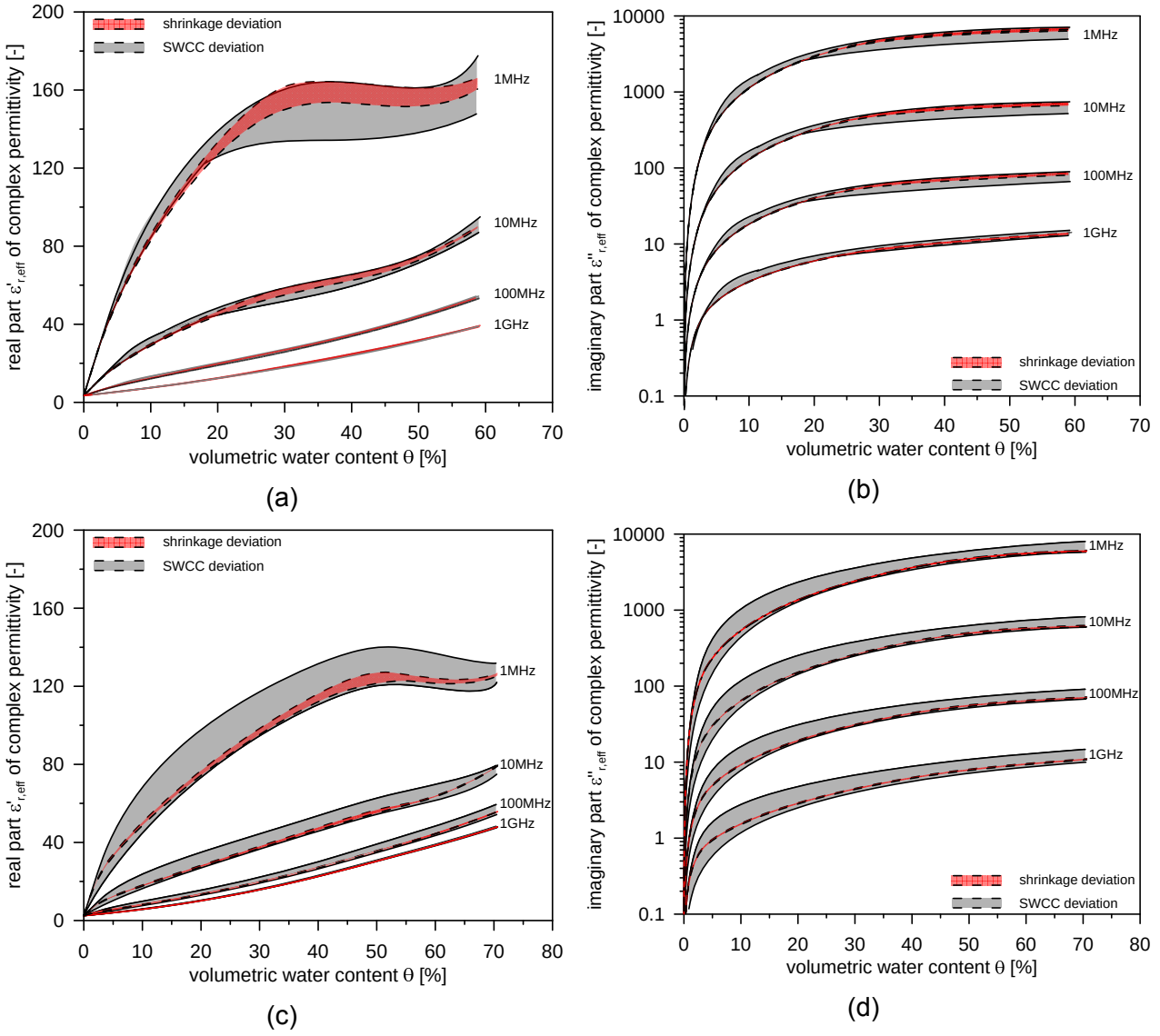

Figure 7.29: Frequency dependent sensitivity analysis on WS-model applied on AS and KA based on parameterised SWCCs and shrinkage curve standard deviation: (A) to (B) show the sensitivity of $\varepsilon'_{r,\text{eff}}$ and $\varepsilon''_{r,\text{eff}}$ at 1 GHz, 100 MHz, 10 MHz and 1 MHz on AS, and (C) to (D) show the sensitivity of $\varepsilon'_{r,\text{eff}}$ and $\varepsilon''_{r,\text{eff}}$ at 1 GHz, 100 MHz, 10 MHz and 1 MHz on KA.

influence of both, Ψ_t and ρ_D, on the performance of the WS-model. It will be a task of future studies to systematically investigate, also experimentally, the influence of Ψ_t and ρ_D on $\varepsilon^{\star}_{r,\text{eff}}$.

7.3.4 Numerical simulation

A possible scenario that might have caused the sudden drop in the complex permittivity, is illustrated in Figure 7.30. The soil sample in the OE probe was subject to volume changes due to soil shrinkage. Figure 7.30 schematically shows stages of geometrical changes during the shrinkage test, which might have caused the observed drops in $\varepsilon'_{r,\text{eff}}$ and $\varepsilon''_{r,\text{eff}}$. As reported in Section 7.3, at the beginning of the shrinkage test, the soil sample shrank only

one-dimensionally in sample height, which is highlighted by Stage I in Figure 7.30. With ongoing shrinkage, the soil experienced isotropic geometrical changes at which the sample shrank not only in height, but also in radial direction, as indicated by Stage II. In the last stage (Stage III), the soil sample also shrank minimally in a one-dimensional direction, but this time from the bottom upwards. At this stage, soil started detaching from the base, which was the copper plate of the OE probe, as shown Figure 7.30.

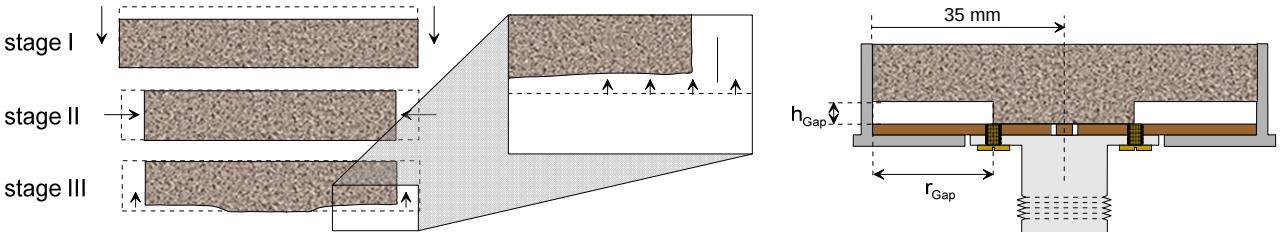

Figure 7.30: Schematic illustration of air gap between soil sample and OE probe: (left) geometrical changes detected during the shrinkage test in which Stage III causes an air gap between soil sample and OE probe and (right) definition of dimension of air gap propagation, starting from the sample outside to the OE probe aperture.

This Stage III created an air gap between the soil and copper plate of the OE probe, which approached the probe aperture with advancing shrinkage. Theoretically, a complete loss of contact would create an air gap between soil and probe aperture. Water has a complex permittivity with the real part in the range of $78 \leq \varepsilon'_{r,\text{eff}} \leq 80$ at a frequency of $f = 1\,\text{GHz}$ (see measurement in Figure 4.4). The permittivity of solid particles was found to be between 3 to 15 [175]. In contrast, air has much lower permittivity than water and solid particles, which is commonly known as $\varepsilon_A = 1$ (see Figure 4.2). As a result, an air gap due to complete loss of contact between the probe aperture and soil certainly influences the dielectric measurement. However, shrinkage Stage III in Figure 7.30 does not represent a complete loss of contact. Hence, two fundamental questions arise when considering the scenario of this shrinkage Stage III:

1. Does an air gap between the soil and copper plate influence the dielectric measurement of the soil sample?
2. What are the dimensions of an acceptable air gap that does not influence the measurement result?

To address these questions, numerical simulations using HFSS were performed to conduct a sensitivity analysis on the influence of an air gap between the soil sample and copper plate of the OE probe. The 3-D finite element structure of the OE probe was adopted from Wagner et al. [227]. The adopted 3-D finite element structure was modified in this study by adding

an artificial air gap between the soil sample and copper plate. As shown in Figure 7.30, the artificially introduced air gap was described by two variables: h_{Gap} and r_{Gap}. h_{Gap} defines the height of the air gap, while r_{Gap} is the length of the air gap.

In the first step, a virtual calibration of the OWL calibration materials (air, methanol and water) was conducted over the entire frequency range from 1 MHz to 3 GHz. The theoretically calculated $\varepsilon^{\star}_{r,\text{eff}}$ of the OWL calibration materials was taken from [227] and used as an input for the numerical calculations. The reflection parameter, S_{11}, of the OWL calibration materials was numerically computed. Subsequently, the complex calibration constants, c_i, required according to Equation 5.6 were calculated for the virtual calibration.

Then, in the second step, the dielectric spectra for $\varepsilon'_{r,\text{eff}}$ and $\varepsilon''_{r,\text{eff}}$ as a function of f, measured with the OE probe on AS and KA, were used as input data to investigate the effect of a propagating air gap. For AS, the drop of the complex permittivity, $\varepsilon^{\star}_{r,\text{eff}}$, during the shrinkage test was observed in a water content range of $10.5\% \leq w \leq 15.9\%$. Figure 7.31A shows the dielectric measurements that were used for the numerical simulations on AS.

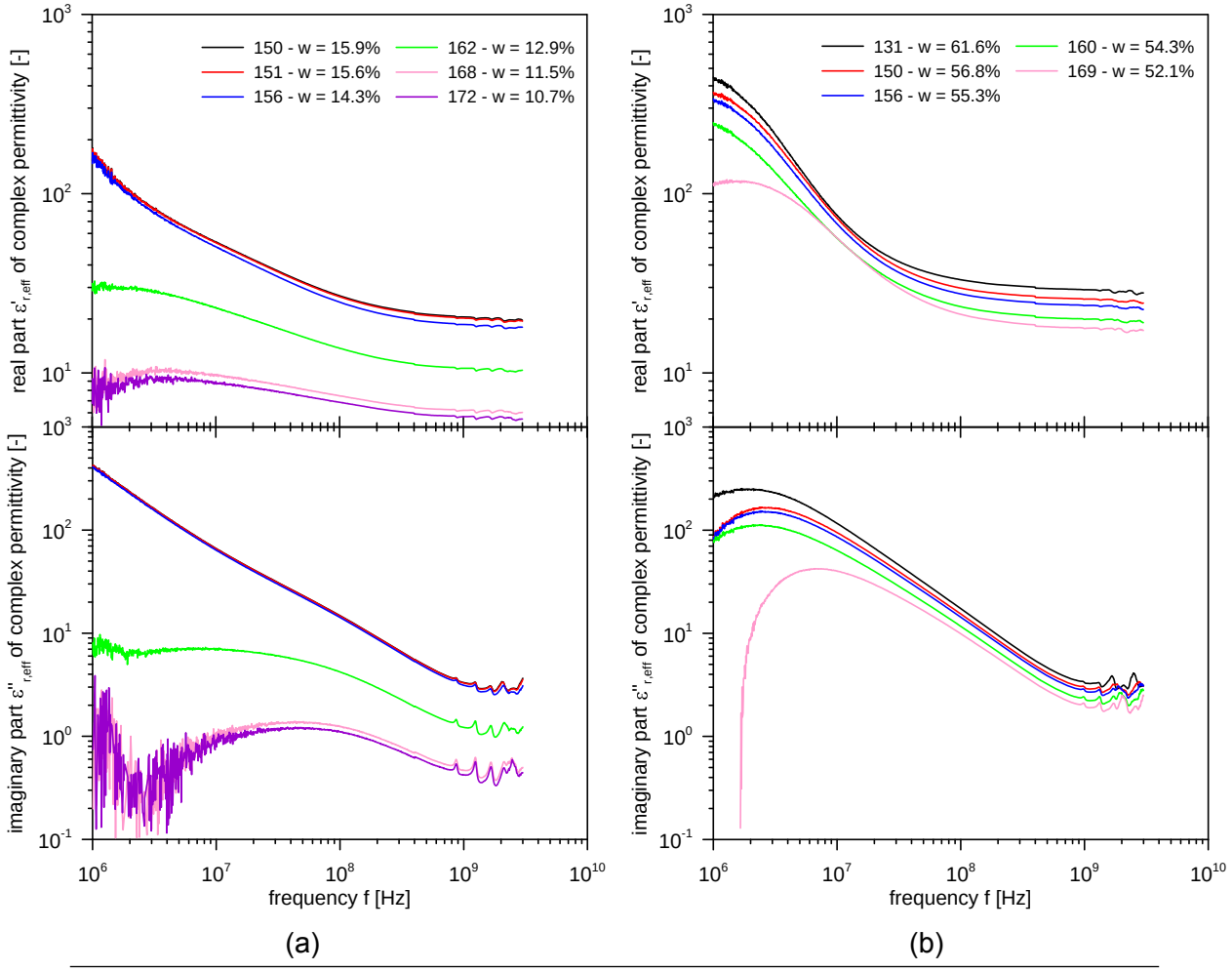

Figure 7.31: Dielectric spectra, $\varepsilon'_{r,\text{eff}}$ and $\varepsilon''_{r,\text{eff}}$ as a function of f at selected water contents characterising the drops of $\varepsilon^{\star}_{r,\text{eff}}$, used as input data for numerical simulations on (A) AS and (B) KA.

In total, six dielectric spectra were selected to cover the entire drop of $\varepsilon^{\star}_{r,\text{eff}}$. Figure 7.31B shows the selected dielectric spectra for KA. In this case, only five measurements covered the drop in $\varepsilon^{\star}_{r,\text{eff}}$ and were taken for the numerical simulations in a water content range between $52.1\% \leq w \leq 61.6\%$. The dielectric spectrum of the selected measurements were used to back-calculate the reflection parameter, S_{11}, in consideration of the presence of an air gap with dimensions characterised by r_{Gap} and h_{Gap}. The reflection S_{11} parameter was used in combination with the previously virtually determined calibration constants, c_i, to compute $\varepsilon^{\star}_{r,\text{eff}}$, based on Equation 5.6, under the influence of the air gap. A parametric study on h_{Gap} and r_{Gap} was performed to systematically investigate the influence of a propagating air gap on the dielectric spectrum, $\varepsilon^{\star}_{r,\text{eff}}$. The propagation of the air gap was simulated starting from the sample outside, and propagating towards the probe aperture. The length of the air gap was simulated in a range of $0 \leq r_{\text{Gap}} \leq 35\,\text{mm}$, with a propagation rate of 0.5 mm towards the probe aperture. The height of the air gap was set to $h_{\text{Gap}} = 1\,\text{mm}$ and $2\,\text{mm}$.

The results of the numerical simulations on AS are presented in Figure 7.32A and for KA in Figure 7.32B. The results show the real part of the complex permittivity, $\varepsilon'_{r,\text{eff}}$, at 1 GHz as a function of air gap length, r_{Gap}, with a fixed height of $h_{\text{Gap}} = 1.0\,\text{mm}$.

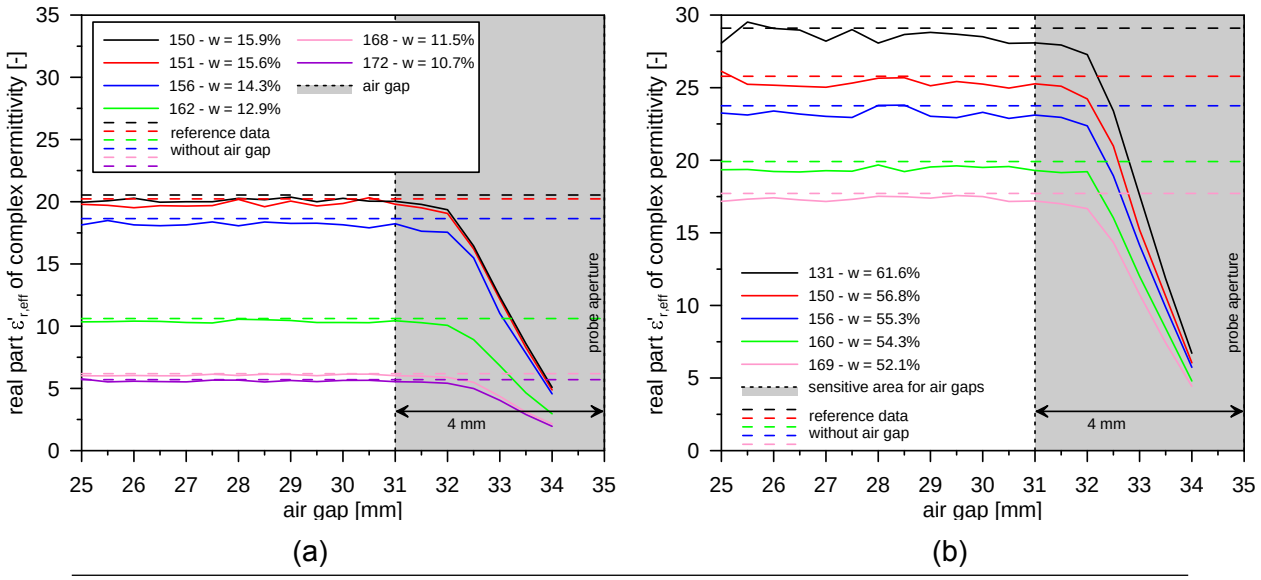

Figure 7.32: Results of numerical simulations on air gap between soil sample and OE probe aperture. Air gap effect on (A) six measurement on AS and (B) five measurement on KA, at selected gravimetric water contents. Shown is $\varepsilon'_{r,\text{eff}}$ at 1 GHz as function of air gap length r_{Gap}, with a fixed height of $h_{\text{Gap}} = 1.0\,\text{mm}$. The propagation of the air gap length r_{Gap} starts from sample outside to OE probe aperture (at 35 mm, see Figure 7.30).

The dashed lines represent the dielectric measurements without the gap as reference data. The solid lines show the result of the parametric study in consideration of a propagating air gap. Since there is no influence of an air gap below 25 mm length, the results are only shown for an air gap length in the range from 25 mm to the OE probe aperture at 35 mm.

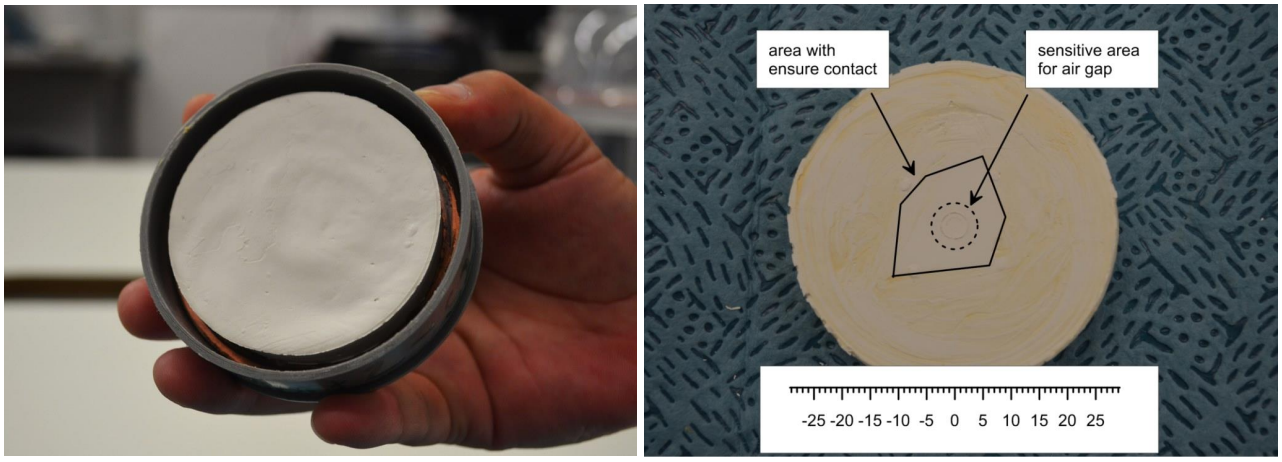

Figure 7.33: High-resolution photographs of soil sample KA in the sample holder of an OE probe after shrinkage test: (A) soil sample in the OE demonstrating that contact existed after the shrinkage test, and (B) footprint of the OE probe showing the contact zone between the probe aperture and soil (area indicated by solid line). The sensitivity zone for air gaps is demonstrated by a circle with a dashed line.

It can be observed that the influence only became significant when the air gap propagated close to the OE probe aperture. Further, it can be noted that the influence of the air gap was independent of the gravimetric water content because the $\varepsilon'_{r,\mathrm{eff}}$ of all curves dropped nearly at the same air gap length. Similar results were obtained for $\varepsilon''_{r,\mathrm{eff}}$ at 1 GHz, which can be found in Appendix B.4. Further, the numerical simulations with an air gap height of $h_{\mathrm{Gap}} = 2.0\,\mathrm{mm}$ showed similar results (see results attached in Appendix B.4). This suggests that h_{Gap} influences the dielectric measurements less than r_{Gap}. Based on the numerical simulation results, the influence of an air gap on the dielectric measurement can be confined to a sensitive zone with 4 mm distance from probe aperture, as indicated in Figure 7.30 by the grey shaded area.

Figure 7.33A shows a high-resolution photograph of a KA soil sample in the sample holder of an OE probe. It shows that the soil sample underwent significant volume changes during the shrinkage test, and demonstrates that the sample stuck to the OE probe. This implies that there was still contact between the probe and sample. The soil sample was removed from the OE probe, and the sample bottom was visually inspected in order to determine the contact area. Figure 7.33B shows the footprint of the OE probe aperture in the contact area between the soil and OE probe, which is highlighted by the solid line. In addition, the sensitive zone of the influence of the air gap is indicated by a dashed line. It can be seen that the observed contact area was significantly larger than the numerically determined sensitive zone of the air gap. It is unlikely that an air gap caused the drop of $\varepsilon^{\star}_{r,\mathrm{eff}}$. as observed in Figure 7.26 and 7.27.

As a consequence of this sensitivity analysis, this study could conclude that the drop of $\varepsilon^{\star}_{r;\text{eff}}$ must have another origin as an air gap between the soil sample and OE probe aperture. As previously shown in Figure 7.28, the drop of $\varepsilon^{\star}_{r;\text{eff}}$ was located in the residual shrinkage zone of the shrinkage curve. The residual shrinkage zone is designated as the zone at which air begins entering the intra-aggregate pore structure for the first time, as the water volume reduction exceeds the pore volume reduction [96], which changes soil state from saturated to unsaturated conditions. In his model for the shrinkage curve, Chertkov [3] assumed a discontinuous air phase with isolated bubbles in the intra-aggregate pores in the residual shrinkage zone. With ongoing shrinkage, successively more air enters the soil matrix, resulting in an enhanced accumulation of isolated air bubbles. With this enhanced accumulation, air bubbles merge, which leads to a partly continuous air phase. Chertkov [3] assumed that a continuous air phase throughout the pore system is given at the transition water content from residual to the zero shrinkage zone.

The hypothesis proposed in the present study is that the drop of $\varepsilon^{\star}_{r;\text{eff}}$ is caused by this entry of the air phase into the intra-aggregate pores in the soil matrix during the residual shrinkage zone. The intra-aggregate pore water is associated with bound water, whose permittivity at 1 GHz ranges within $\varepsilon'_{\text{BW}} \approx 3 - 35$ (see Section 4.4.3). The entry of air with $\varepsilon_A = 1$ changed the phase composition and structure. Thus, the bulk permittivity of soil must decrease significantly with decreasing water content in the residual shrinkage zone. However, further and more detailed experimental investigations are required to exactly determine the continuous air phase in order to reinforce this hypothesis.

7.3.5 Spectrum analysis of frequency dependent dielectric behaviour

As shown in Figure 7.28, the dielectric properties measured during soil shrinkage were strongly frequency dependent in a range from 1 MHz to 3 GHz. It was demonstrated in Section 7.2.5 that it is reasonable to assume three relaxation processes in this frequency range. However, OE measurements may suffer inaccuracies and noise at frequencies lower than $f < 50\,\text{MHz}$ (see Figures 7.26 and 7.27), which impede successful detection of the low-frequency relaxation. Hence, frequencies lower than $f < 50\,\text{MHz}$ were not considered, and only the frequency range from 50 MHz to 3 GHz was investigated. As a consequence, only two relaxation processes – intermediate-frequency and HF relaxation – were determined, as the low-frequency relaxation was expected to be in the kHz-range, which was far from the observed frequency window. In order to fit the dielectric spectrum using the two relaxation processes, a 2-term Cole-Cole model was considered, including direct current conductivity contribution. Similar to the spectrum analysis in Section 7.2.5, the RW-MWG algorithm was

used in the same manner to fit the unknown parameters in the 2-term Cole-Cole model (details of the algorithm are presented in Section 7.2.5). Due to the enormous amount of data, the number of measurements to be fitted was reduced to 62 for AS and 79 for KA.

Figures 7.34 and 7.35 show the fitting results of the spectrum analysis on AS and KA. To avoid any confusion, it should be mentioned that the magnitude of HF relaxation in Figures 7.34A and 7.34B is a sum of ε_∞ and $\Delta\varepsilon$, which is in contrast to the actual definition of the relaxation magnitude. However, this is justified for illustration purposes.

It was interesting to find that all fitting parameters showed a sudden change in trend that fell together with the observed drop for $\varepsilon'_{r,\text{eff}}$ and $\varepsilon''_{r,\text{eff}}$ in Figure 7.28. Prior to the drop, it can be seen in Figure 7.34A and 7.34B that the HF relaxation magnitude, both for AS and KA, decreased monotonically with water content, which agreed with the results presented in Ishida et al. [174]. At the same time, the HF relaxation in Figure 7.34C and 7.34D was the same for AS and KA. The initial relaxation time for both soils was found to be around $f = \cdot 10^{-11}$ s which fell in the range observed in Escorihuela et al. [43]. This further indicates that the HF relaxation is dependent on neither the mineralogy nor the soil suction. The stretching exponent of the HF relaxation in Figures 7.34E and 7.34F was located between $0.7 < \beta_{\text{CC}} < 1$ prior to the drop, and showed a remarkable change to $\beta_{\text{CC}} \approx 0.1 - 0.2$ after the drop. Yet, the HF relaxation, due to dipolar polarisation of free water, can be modelled by a modified Debye equation [43], which implies a stretching exponent equal to $\beta_{\text{CC}} = 1$. However, the results in Figure 7.34C differed remarkably to $\beta_{\text{CC}} = 1$. An entirely accurate interpretation of HF relaxation was not possible because the measured frequency range was too narrow. The effectively measured frequency was between 50 MHz to 3 GHz, and the HF relaxation was located around 10 GHz. As a result, the fitting of the HF relaxation may suffer inaccuracies due to lack of data at frequencies $f > 3\,\text{GHz}$. This becomes more obvious in Figures 7.34C and 7.34D, in which intermediate-frequency relaxation time after the drop tended to approach values of $f \approx 10^{-13}\,\text{s}$, which were not reasonable.

In contrast, the fitted relaxation time of the intermediate-frequency relaxation in Figures 7.34C and 7.34D was found between $10^{-7}\,\text{s} < f < 10^{-8}\,\text{s}$, which agrees with the results from literature [174]. In general, it can be seen that the magnitude of intermediate-frequency, prior to the drop, was much higher than that for HF relaxation. However, there were two differences observed between AS and KA. One difference was that the magnitude was higher for KA than for AS, which means that the contribution of interfacial polarisation was more dominant. This seems to correlate to the results obtained for the spectrum analysis on compacted soil, and can be explained by the same reasons already presented in Section 7.2.5. The other difference was that the intermediate-frequency relaxation of AS decreased slightly with volumetric water content prior to the drop, whereas the intermediate-frequency relaxation of KA

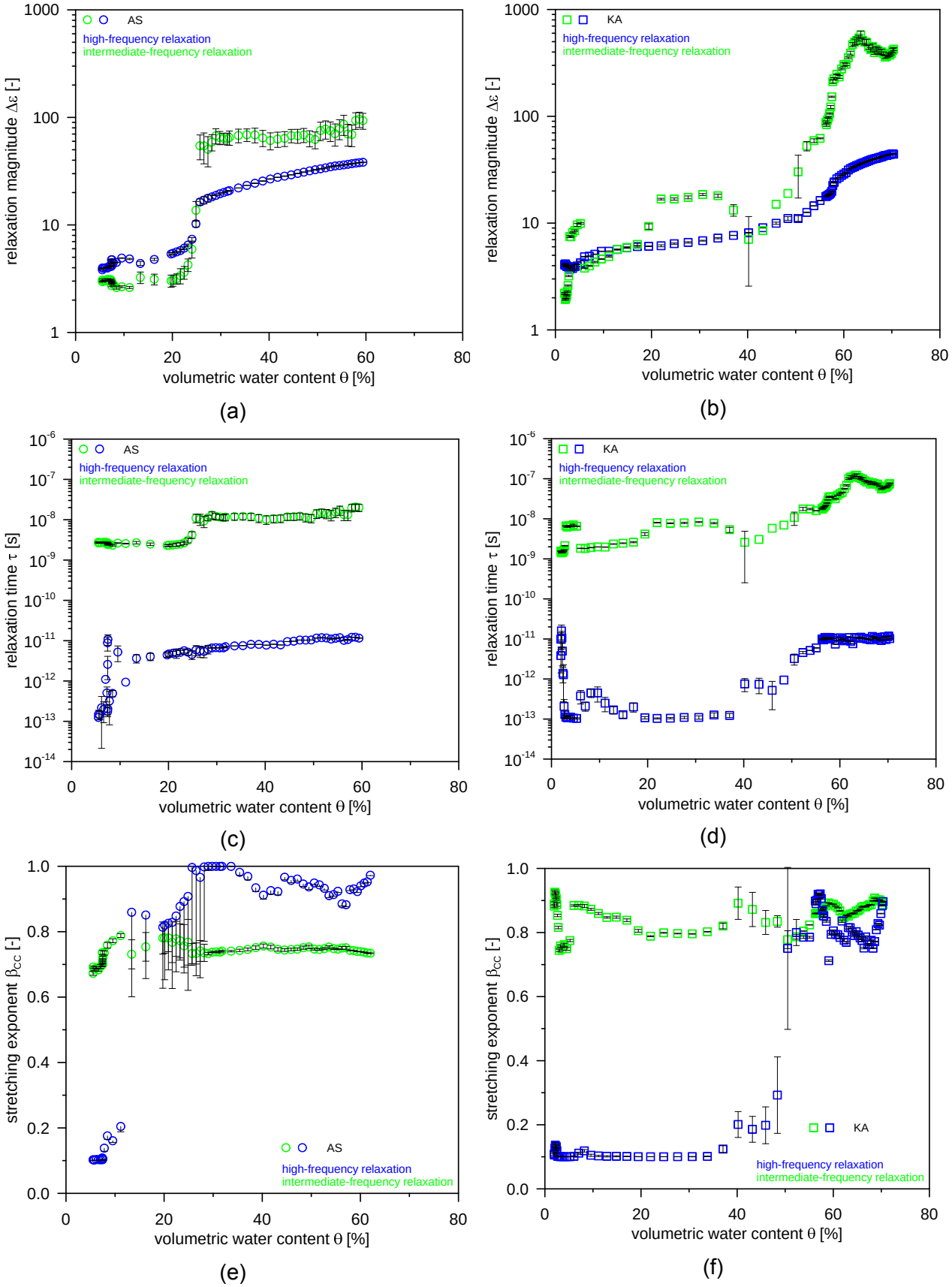

Figure 7.34: Fit of relaxation processes on the dielectric spectrum of shrinkage samples of AS and KA using a 2-term Cole-Cole model combined with the RW-MWG algorithm: (A) relaxation magnitude $\Delta\varepsilon$ of AS, (B) relaxation magnitude $\Delta\varepsilon$ of KA, (C) relaxation time τ of AS, (D) relaxation time τ of KA, (E) stretching exponent β_{CC} of AS, and (F) stretching exponent β_{CC} of KA. The results of high-frequency (HF) relaxation and intermediate-frequency relaxation are highlighted in various colours.

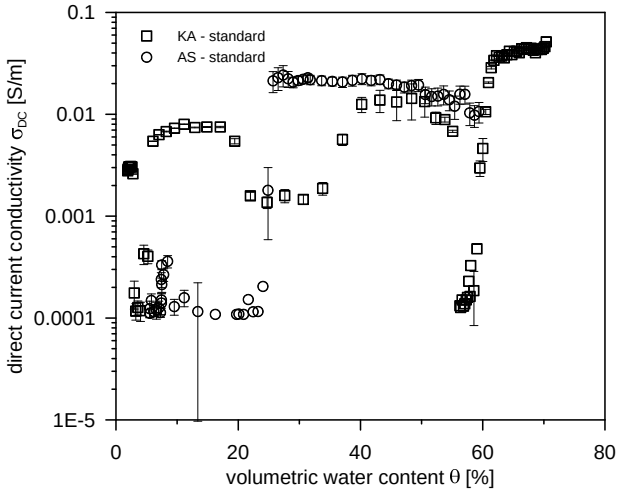

Figure 7.35: Result of the fit of direct current conductivity contribution on the dielectric spectrum of shrinkage samples of AS and KA.

increased with reducing volumetric water content. This result is actually in contrast with the result obtained for compacted soil. However, there is a fundamental difference between this spectrum analysis and the spectrum analysis applied to the results of compacted soils in Section 7.2.5 – the number of fitted relaxation processes. The dielectric spectra of compacted soil was analysed with a 3-term Cole-Cole model, whereas this spectrum was fitted with a 2-term Cole-Cole model, without considering the low-frequency relaxation, which may still contribute to the dielectric spectra analysed for the shrinkage tests. Hence, a direct comparison to the spectrum analysis shown in Section 7.2.5 was only possible in limited manner.

After the drop, a meaningful interpretation of the results was difficult because the frequency range of trustworthy and accurate data was too narrow. As shown in the 3-D illustrations in Figures 7.26 and 7.27, the measured permittivity at low-frequency range, particularly of $\varepsilon''_{r,\mathrm{eff}}$, suffered inaccuracies from noise. These inaccuracies cause an unsuccessful fit of the relaxation parameters, as well as the direct current conductivity, as shown in Figure 7.35, as indicated by high standard deviations.

Nevertheless, the low-frequency range of the dielectric spectra is of enormous interest. However, the broadband EM method is limited to a low-frequency limit of $f \approx 1\,\mathrm{MHz}$. To have a better success in measuring the dielectric spectrum in this frequency range, other measurement methods need to be adopted. For example, as shown in Figure 5.1, the parallel plate method based on impedance measurements is a feasible way to measure the dielectric spectrum in the kHz-range. Therefore, it is recommended to take advantage of the combined use of different measurement setups and methods (such as broadband EM method in line with the parallel plate method) to enlarge the frequency range and achieve a broadband dielectric characterisation.

7.3.6 Summary

This section introduced the results of novel experiments in performing shrinkage tests in combination with dielectric measurements, together with soil suction measurements. The following observations and finding were made:

- The shrinkage curve of two fine-grained soils was accurately determined by the direct determination of sample geometry. An analytical model derived based on the physics of shrinkage was successfully used to parameterise the shrinkage curve and define the shrinkage zones, thereby characterising the entire shrinkage behaviour.
- Soil suction measurements were performed to determine the drying path of the SWCC. Three different measurement methods were used to cover the entire soil suction range. The results of the measurements were subsequently combined to establish the entire SWCC. The results showed a smooth curve, which strongly suggests that combined usage of suitable methods enables measurement of the entire soil suction range. However, the soil suctions were measured together with the loss of water weight, which only enabled establishment of the SWCC as a function of the gravimetric water content. In this study, the parameterised shrinkage curve was taken to convert the SWCC as a function of the gravimetric water content into a function of the volume water content. It was experimentally found that it was reasonable to convert the SWCC using the shrinkage curve. Further, the SWCC was modelled with different van Genuchten equations. A 4-modal van Genuchten equation was required to obtain the best fits for the measured SWCC.
- This chapter presented the results of the shrinkage tests in combination with the continuous dielectric measurements using an in-house-manufactured OE-probe. The gravimetric water content and dielectric properties in a frequency range from 1 MHz to 3 GHz were automatically recorded during the soil shrinkage process. The useful frequency range of the dielectric properties was restricted to 50 MHz$< f <$3 GHz due to noise that is caused by the design and performance of the probe in the low-frequency range.
- The theoretical mixture approach, WS-model, was coupled with the parameterised shrinkage curve and SWCC and used to predict the dielectric spectrum of shrinking soil at 4 specific frequencies. The predictions of the real part, $\varepsilon'_{r,\text{eff}}$, of the permittivity were reasonable, particularly for AS. In contrast, the imaginary part, $\varepsilon''_{r,\text{eff}}$, suffered inaccuracies, among others connected to the representation of the direct current conductivity in the model (Section 7.2). In addition, the result of a sensitivity analysis on the WS-model from 1 MHz to 1 GHz showed that the $\varepsilon'_{r,\text{eff}}$ at 1 GHz was insensitive to reasonable deviations of soil suction, Ψ_t, and dry density, ρ_D. For frequencies lower than

$f < 1$ GHz, $\varepsilon'_{r,\text{eff}}$ became increasingly sensitive to changes of Ψ_t and ρ_D; however, the dominating parameter seemed to be the soil suction, Ψ_t. The imaginary part, $\varepsilon''_{r,\text{eff}}$, was sensitive to soil suction, Ψ_t, over the entire investigated frequency range, with minor sensitivity to the dry density, ρ_D.

- A remarkable phenomenon was observed in the measured dielectric spectra during soil shrinkage. A drop in $\varepsilon^{\star}_{r,\text{eff}}$ was found, which could be located inside the residual shrinkage zone. It was numerically shown that it is unlikely that this drop was caused by an air gap between the soil sample and OE probe, which might propagate from the sample outside towards the probe aperture due to soil shrinkage. A hypothesis explaining the observed phenomenon was proposed, stating that this is caused by the air phase entering the soil matrix during the residual soil shrinkage. However, this explanation requires further experimental investigations in order to reinforce the hypothesis.

- The frequency dependent (50 MHz$< f <$3 GHz) dielectric properties of the shrinking soil were investigated with a 2-term Cole-Cole model in combination with a MCMC algorithm. It was found that the HF relaxation magnitude, due to dipolar polarisation, during shrinkage was independent of mineralogy and soil suction, and seemed only a function of the volumetric water content. The intermediate-frequency relaxation magnitude during shrinkage did not show a clear trend, as observed for the spectrum analysis on compacted soil. This might be because the spectrum could only be fitted by a 2-term Cole-Cole model due to the narrow frequency range. Hence, it is highly recommended that future research enlarge the frequency range of dielectric measurement to achieve better broadband dielectric soil characterisation.

Chapter 8

Conclusion and Outlook

8.1 Conclusion

Geophysical radio and microwave EM methods are increasingly and successively applied in geotechnical and geo-environmental engineering because these methods offer the potential to explore and investigate soil parameters. However, successful application of these methods requires a profound knowledge of the multi-physical processes involved in EM wave propagation, which are currently far from being well understood. In order to contribute to a better knowledge of these processes, this thesis has focused on an experimental investigation to characterise fine-grained soils mechanically, hydraulically and dieletrically and has considered their interconnection during shrinkage and compaction.

This study first selected a suitable broadband EM technique to determine the dielectric parameters of soils in a frequency range from 1 MHz to 3 GHz. Two different probes were introduced, based on the OE and CT technique. As commercial probes for standard geotechnical tests barely exist, an in-house-manufactured OE probe was proposed and specifically designed to measure the dielectric properties of fine-grained soils during shrinkage. The propagation characteristics of EM waves and the probe sensitivity were numerically simulated on calibration materials to define the sensitivity volume and minimum sample height. In addition, a combination of calibration procedures was developed to ensure stable and reliable measurement results. A CT cell was also introduced, and three quasi-analytical approaches and iterative analysis techniques were proposed to calculate the permittivity from the measured S-parameters. Based on the numerical simulation, it was found that the iterative technique provided the best results. Subsequently, these two probes were experimentally compared to commercial probes and showed satisfying agreement in the observed frequency window.

The experimental investigation focused on the compaction and shrinkage of fine-grained soils, which represented different soil densification scenarios. In the first test series, standard and modified compaction tests, in combination with CT measurements, were conducted. It was found that the CT cells were suitable and practical for coring undisturbed soil samples. In addition, the shrinkage curve and SWCC of these compacted samples were measured and parameterised with existing models. It was interesting to find delimiting points in the SWCCs for each set of compaction tests, at which the curves converged, regardless of the initial soil compaction state. Further, this study assumed that this delimiting point must be associated with intra-aggregate pore structure because it is located in the zero shrinkage area. This observation requires further investigations on the pore structure to reinforce this assumption. Two theoretical mixture approaches – the Hil-model and WS-model – in combination with a phenomenological relaxation model, were coupled with the parameterised shrinkage curve and SWCC to predict the frequency dependent dielectric properties of compacted fine-grained soil based on its mechanical and hydraulic characterisation. It was generally found that the Hil-model overestimated the dielectric properties and failed at high water contents due its instability when predicting the porosity. For the WS-model, it was found that $\varepsilon'_{r,\mathrm{eff}}$ of compacted soils could be predicted reasonably in a frequency range from 1 MHz to 1 GHz. However, the prediction of $\varepsilon''_{r,\mathrm{eff}}$ suffered inaccuracies due to empirical coupling parameters, which also need to be further investigated in future studies. The frequency dependence of the dielectric properties of compacted soil was additionally investigated. Three underlining relaxation processes causing dielectric dispersion were fitted with a 3-term Cole-Cole model in combination with a MCMC algorithm. It was found that the HF relaxation magnitude was purely dependent on the volumetric water content. The intermediate-frequency relaxation magnitude could be associated to the compaction state.

In a second test series, a novel experimental setup was suggested to automatically perform shrinkage tests in combination with OE measurements, using the in-house-manufactured OE probe. In parallel, the drying path of the entire SWCC was successfully determined using a combination of three measurement methods, covering the entire suction range. The shrinkage curve was coupled with the SWCC to express soil suction as a function of the volumetric water content. It was experimentally proven that coupling of the shrinkage curve and SWCC is a valid procedure to determine the SWCC as a function of the volumetric water content, which is usually not possible with conventional measurement methods. For the shrinkage test, only the WS-model was coupled with the parameterised shrinkage curve and SWCC to predict the dielectric properties of shrinking samples. The real part, $\varepsilon'_{r,\mathrm{eff}}$, of shrinking soil could be predicted reasonably well in a frequency range from 1 MHz to 1 GHz. Similar to the compaction tests, the imaginary part, $\varepsilon''_{r,\mathrm{eff}}$, suffered inaccuracies due to the same restrictions on the model mentioned above. Further, a sensitivity analysis was

conducted to characterise the influence of soil suction, Ψ_t, and dry density, ρ_D, on the results of the WS-model. The results of the analysis showed that the real part, $\varepsilon'_{r,\text{eff}}$, at 1 GHz was insensitive to changes in Ψ_t and ρ_D, which was not observed for the imaginary part, $\varepsilon''_{r,\text{eff}}$. At lower frequencies, both $\varepsilon'_{r,\text{eff}}$ and $\varepsilon''_{r,\text{eff}}$, are sensitive to Ψ_t and ρ_D. However, it was also generally found that the dominating parameter in the sensitivity analysis seemed to be the Ψ_t. The measured dielectric spectra during shrinkage showed a distinct drop in $\varepsilon^{\star}_{r,\text{eff}}$, which could be located in the residual shrinkage zone. This thesis hypothesised that the drop in $\varepsilon^{\star}_{r,\text{eff}}$ was originated from air entry in the intra-aggregate pore structure, causing a continuous air phase. This hypothesis is a possible explanation of this; however, future research is required to prove this idea. Finally, the frequency dependent dielectric parameters of shrinking soil were fitted with a 2-term Cole-Cole model analysis using the MCMC algorithm. Similar to the compaction tests, the high-frequency relaxation magnitude was found to be a function of the water content. In contrast, the intermediate-frequency relaxation magnitude was difficult to interpret because it did not show a distinct trend, as given for the compaction test. The reason for this might be the dielectric spectrum measured during the shrinkage test, which was too narrow to allow a reasonable fit using the 3-term Cole-Cole model. As a result, it is recommended that future research modifies and extends the EM measurement technique to increase the dielectric spectra to the low-frequency range and achieve better broadband dielectric soil characterisation.

8.2 Outlook and recommendations

The objective of this thesis was the mechanical, hydraulic, and broadband dielectric characterisation of fine-grained soils. In addition, the objective was to investigate different densification scenarios of fine-grained soils. The results showed that a novel experimental methodology and procedure could successfully be established to characterise fine-grained soils, during standardised geotechnical compaction and shrinkage tests. Further, it could be shown that broadband dielectric measurements from 1 MHz to 3 GHz are suitable to investigate compaction and shrinkage behaviour of fine-grained soils. A theoretical mixture approach, coupled with the shrinkage curve and SWCC, was established to predict the measured dielectric spectrum, which showed promising results in describing the frequency dependent permittivity. The results signify the potential of EM measurement methods to investigate and characterise mechanical and hydraulic behaviour of fine-grained soils.

However, it was found that this type of experimental investigations is complex and requires interdisciplinary expertise. Especially, the establishment of the SWCC of fine-grained soils

is found to be highly time consuming. Further, the dielectric characterisation of the fine-grained soils was restricted from 1 MHz to 3 GHz due to the equipment available. Higher and lower frequencies could not be considered; hence, it was not possible to access a broader frequency range. On the one hand, the proposed probes are applicable only to a minimum frequency of 1 MHz. On the other hand, the probes could theoretically measure higher than 3 GHz frequency, but it was not possible due to the limitations of the used VNA. The challenge is to find an ideal compromise between probe and VNA. As a consequence from the results and findings of the presented study and these shortcomings of the measuring technique, the following future works are suggested across the disciplines:

- The low-frequency dielectric spectrum provides more information than does water content only (such as soil compaction, particle surface area and mineralogy). Future work in electrical engineering could include the development of probes, specifically designed for standard test methods, to allow measurements at lower frequencies than 1 MHz in order to enable a better broadband dielectric soil characterisation.
- Potential future work for soil scientists and geophysicists should focus on the broadband dielectric spectrum analysis because it offers the potential to better understand the underlining mechanisms of multi-phase and multi-physical processes.
- The shrinkage tests in combination with dielectric measurements showed that broadband dielectric characterisation is able to provide more information on soils than can water content alone. The observed drop in permittivity during the shrinkage could be a significant finding, proving the hypothesis that residual shrinkage is accompanied by an entry of the air phase into the intra-aggregate pore system. This hypothesis requires further experimental work, which might be of interest to all soil-related scientific disciplines. It will be a future task to further develop and modify the setups used in geotechnical engineering to better understand and employ this additional information.
- The theoretical mixture approach, WS-model, was extensively studied and coupled with the parameterised shrinkage curve and SWCC. The empirical coupling relationships – such as the direct current conductivity – need to be further investigated to improve predictions of the dielectric soil behaviour based on mechanical and hydraulic soil characterisation.

Bibliography

[1] ASTM D4943-08. Standard test method for shrinkage factors of soils by the wax method. American Society for Testing and Materials, ASTM International, West Conshohocken, Pa, 2008.

[2] ASTM D7263-09. Standard test method for laboratory determination of density (unit weight) of soil specimens. American Society for Testing and Materials, ASTM International, West Conshohocken, Pa, 2009.

[3] V. Y. Chertkov. Modelling the shrinkage curve of soil clay pastes. *Geoderma*, 112(1–2): 71--95, 2003.

[4] ASTM D698-12. Standard test methods for laboratory compaction characteristics of soil using standard effort. American Society for Testing and Materials, ASTM International, West Conshohocken, Pa, 2007.

[5] ASTM D1557-12. Standard test methods for laboratory compaction characteristics of soil using modified effort. American Society for Testing and Materials, ASTM International, West Conshohocken, Pa, 2009.

[6] X. Peng and R. Horn. Modeling soil shrinkage curve across a wide range of soil types. *Soil Science Society of America Journal*, 69(3):584--592, 2005.

[7] P. F. Low. Viscosity of interlayer water in montmorillonite. *Soil Sci. Soc. Am. J.*, 40(4): 500--505, 1976.

[8] D. G. Fredlund and A. Xing. Equations for the soil-water characteristic curve. *Canadian Geotechnical Journal*, 31(4):521--532, 1994.

[9] A. M. Thomas, D. N. Chapman, C. D. F. Rogers, and N. Metje. Electromagnetic properties of the ground: Part ii – the properties of two selected fine-grained soils. *Tunnelling and Underground Space Technology*, 25(6):723--730, 2010.

[10] D. Moret-Fernandez, J. L. Arrue, V. Perez, and M. V. Lopez. A tdr-pressure cell design for measuring the soil-water retention curve. *Soil and Tillage Research*, 100(1–2): 114--119, 2008.

[11] Z. Chen, M. Schwing, J. Karlovšek, N. Wagner, and A. Scheuermann. Broadband dielectric measurement methods for soft geomaterials: Coaxial transmission line cell and open-ended coaxial probe. *International Journal of Engineering and Technology*, 6(5):373--380, 2014.

[12] D. A. Boyarskii, V. V. Tikhonov, and N. Yu Komarova. Model of dielectric constant of bound water in soil for applications of microwave remote sensing. *Electromagnetic waves (Cambridge, Mass.)*, 35:251--269, 2002.

[13] M. Loewer, N. Wagner, and J. Igel. Prediction of gpr performance in soils using broadband dielectric spectroscopy. In *Near Surface Geoscience 2013*, 2013.

[14] A. Revil. Effective conductivity and permittivity of unsaturated porous materials in the frequency range 1MHz-1GHz. *Water Resources Research*, 49(1):306--327, 2013.

[15] G. C. Topp, J. L. Davis, and A. P. Annan. Electromagnetic determination of soil water content: Measurements in coaxial transmission lines. *Water Resources Research*, 16 (3):574--582, 1980.

[16] K. Roth, R. Schulin, H. Fluhler, and W. Attinger. Calibration of time domain reflectometry for water-content measurement using a composite dielectric approach. *Water Resources Research*, 26(10):2267--2273, 1990.

[17] S. Dasberg and J. W. Hopmans. Time domain reflectometry calibration for uniformly and nonuniformly wetted sandy and clayey loam soils. *Soil Science Society of America Journal*, 56(5):1341, 1992.

[18] M. A. Hilhorst. A pore water conductivity sensor. *Soil Sci. Soc. Am. J.*, 64(6):1922--1925, 2000.

[19] N. Wagner and A. Scheuermann. On the relationship between matric potential and dielectric properties of organic free soils: A sensitivity study. *Canadian Geotechnical Journal*, 46(10):1202--1215, 2009.

[20] M. A. Malicki, R. Plagge, and C. H. Roth. Improving the calibration of dielectric TDR soil moisture determination taking into account the solid soil. *European Journal of Soil Science*, 47(3):357--366, 1996.

[21] S. I. Siddiqui, V. P. Drnevich, and R. J. Deschamps. Time domain reflectometry development for use in geotechnical engineering. *Geotechnical Testing Journal*, 23(1): 9--20, 2000.

[22] V. P. Drnevich, A. K. Ashmawy, X. Yu, and A. M. Sallam. Time domain reflectometry for water content and density of soils: study of soil-dependent calibration constants. *Canadian Geotechnical Journal*, 42(4):1053--1065, 2005.

[23] M. A. Hilhorst, C. Dirksen, F. W. H. Kampers, and R. A. Feddes. Dielectric relaxation of bound water versus soil matric pressure. *Soil Sci. Soc. Am. J.*, 65(2):311--314, 2001.

[24] M. Schwing, Z. Chen, A. Scheuermann, D. J. Williams, and N. Wagner. Experimental study on the relationship of mechanic and hydraulic state variables, and the dielectric properties of clays. In *Unsaturated Soils: Research & Applications*, pages 247--253. CRC Press, 2014.

[25] M. A. Hilhorst, C. Dirksen, F. W. H. Kampers, and R. A. Feddes. New dielectric mixture equation for porous materials based on depolarization factors. *Soil Sci. Soc. Am. J.*, 64(5):1581--1587, 2000.

[26] D. G. Fredlund and H. Rahardjo. *Soil mechanics for unsaturated soils*. John Wiley & Sons, 1993.

[27] M. Budhu. *Soil Mechanics and Foundations (3rd Edition)*. John Wiley & Sons, 2011.

[28] R. E. Grim. Clay mineralogy. *Science*, 135(3507):890--898, 1962.

[29] J. C. Santamarina, K. A. Klein, and M. A. Fam. *Soils and waves*. Wiley, 2001.

[30] R. F. Craig. *Soil mechanics*. Chapman & Hall, London, 1992.

[31] M. Duquette. *Surface charge evaluation of soils, clays and oxides*. Nn72128, Department of Renewable Resources, 1991.

[32] H. Van Olphen. Unit layer interaction in hydrous montmorillonite systems. *Journal of Colloid Science*, 17(7):660--667, 1962.

[33] H. Van Olphen. *An introduction to clay colloid chemistry: for clay technologists geologists, and soil scientists*. John Wiley and Sons, Inc., New York, 1977.

[34] J. C. Santamarina, K. A. Klein, A. Palomino, and M. S. Guimaraes. *Micro-scale aspects of chemical-mechanical coupling interparticle forces and fabric*, pages 47--64. A. A. Balkema, Lisse, Maratea, Italy, 2002.

[35] J. K. Mitchell and K. Soga. *Fundamentals of soil behavior*. John Wiley & Sons, Hoboken, NJ, 2005.

[36] K. L. Babcock. *Theory of the chemical properties of soil colloidal systems at equilibrium*, volume 34 of *Hilgardia*. Hilgardia, Berkeley, 1963.

[37] M. C. Dobson, F. T. Ulaby, M. T. Hallikainen, and M. A. El-Rayes. Microwave dielectric behavior of wet soil-part II: Dielectric mixing models. *IEEE Transactions on Geoscience and Remote Sensing*, GE-23(1):35--46, 1985.

[38] A. Scheuermann. *Instationaere Durchfeuchtung quasi-homogener Erddeiche*. Ph.d. thesis, 2005.

[39] J. N. Israelachvili. *Intermolecular and surface forces (3rd Edition)*. Elsevier Science & Technology, Saint Louis, MO, USA, 3 edition, 2010.

[40] B. V. Derjaguin, N. V. Churaev, and V. M. Muller. *Surface Forces*. Springer, New York, 1987.

[41] M. Tuller, D. Or, and L. M. Dudley. Adsorption and capillary condensation in porous media: Liquid retention and interfacial configurations in angular pores. *Water Resources Research*, 35(7):1949--1964, 1999.

[42] T. Saarenketo. Electrical properties of water in clay and silty soils. *Journal of applied geophysics*, 40(1–3):73--88, 1998.

[43] M. J. Escorihuela, P. de Rosnay, Y. H. Kerr, and J. C. Calvet. Influence of bound-water relaxation frequency on soil moisture measurements. *IEEE Transactions on Geoscience and Remote Sensing*, 45(12):4067--4076, 2007.

[44] H. A. Dinulescu. Thermodynamic state functions of the soil water system. *Heat and Mass transfer*, 12(3-4):243--259, 1979.

[45] S. Iwata, T. Tabuchi, and B. P. Warkentin. *Soil-water interactions: mechanisms and applications*. Dekker, 1995.

[46] D. Or and M. Tuller. Liquid retention and interfacial area in variably saturated porous media: Upscaling from single-pore to sample-scale model. *Water Resources Research*, 35(12):3591--3605, 1999.

[47] R. Baker and S. Frydman. Unsaturated soil mechanics: Critical review of physical foundations. *Engineering Geology*, 106(1–2):26--39, 2009.

[48] M. A. Hilhorst. *Dielectric characterisation of soil*. Ph.d. thesis, 1998.

[49] S. S. Agus and T. Schanz. *Errors in total suction measurements*, volume 112 of *Springer Proceedings in Physics*, chapter 6, pages 59--70. Springer Berlin Heidelberg, 2007.

[50] S. Frydman and R. Baker. Theoretical soil-water characteristic curves based on adsorption, cavitation, and a double porosity model. *International Journal of Geomechanics*, 9(6):250--257, 2009.

[51] N. Lu and W. J. Likos. *Unsaturated soil mechanics*. John Wiley & Sons, 2004.

[52] M. D. Fredlund, G. W. Wilson, and D. G. Fredlund. Use of the grain-size distribution for estimation of the soil-water characteristic curve. *Canadian Geotechnical Journal*, 39(5):1103--1117, 2002.

[53] M. Pettenati, L. Mercury, and M. Azaroual. Capillary geochemistry in non-saturated zone of soils. water content and geochemical signatures. *Applied Geochemistry*, 23 (12):3799--3818, 2008.

[54] L. M. Skinner and J. R. Sambles. The Kelvin equation - A review. *Journal of Aerosol Science*, 3(3):199--210, 1972.

[55] F. A. M. Marinho, W. A. Take, and A. Tarantino. Measurement of matric suction using tensiometric and axis translation techniques. *Geotechnical and Geological Engineering*, 26(6):615--631, 2008.

[56] A. Scheuermann and A. Bieberstein. *Determination of the soil water retention curve and the unsaturated hydraulic conductivity from the particle size distribution experimental unsaturated soil mechanics*, volume 112 of *Springer Proceedings in Physics*, pages 421--433. Springer Berlin Heidelberg, 2007.

[57] V. K. S. Thakur, S. Sreedeep, and D. N. Singh. Parameters affecting soil-water characteristic curves of fine-grained soils. *Journal of Geotechnical and Geoenvironmental Engineering*, 131(4):521--524, 2005.

[58] H. Q. Pham, D. G. Fredlund, and S. L. Barbour. A study of hysteresis models for soil-water characteristic curves. *Canadian Geotechnical Journal*, 42(6):1548--1568, 2005.

[59] H. Q. Pham and Delwyn G. Fredlund. Equations for the entire soil-water characteristic curve of a volume change soil. *Canadian Geotechnical Journal*, 45(4):443--453, 2008.

[60] E. C. Leong and H. Rahardjo. Review of soil-water characteristic curve equations. *Journal of Geotechnical and Geoenvironmental Engineering*, 123(12):1106--1117, 1997.

[61] F. A. M. Marinho. Nature of soil-water characteristic curve for plastic soils. *Journal of Geotechnical and Geoenvironmental Engineering*, 131(5):654--661, 2005.

[62] S. B. Jones and D. Or. Surface area, geometrical and configurational effects on permittivity of porous media. *Journal of Non-Crystalline Solids*, 305(1–3):247--254, 2002.

[63] A.C. Resurreccion, P. Moldrup, M. Tuller, T. P. A. Ferré, K. Kawamoto, T. Komatsu, and L. W. de Jonge. Relationship between specific surface area and the dry end of the water retention curve for soils with varying clay and organic carbon contents. *Water Resources Research*, 47(6):W06522, 2011.

[64] R. H. Brooks and T. Corey. *Hydraulic properties of porous media*, volume 3, pages 1--27. Colorado State University, Fort Collins, Colorado, 1964.

[65] C. Miller, N. Yesiller, K. Yaldo, and S. Merayyan. Impact of soil type and compaction conditions on soil water characteristic. *Journal of Geotechnical and Geoenvironmental Engineering*, 128(9):733--742, 2002.

[66] M. T. van Genuchten. A closed-form equation for predicting the hydraulic conductivity of unsaturated soils. *Soil Sci. Soc. Am. J.*, 44(5):892--898, 1980.

[67] W. Durner. Predicting the unsaturated hydraulic conductivity using multi-porosity water retention curves. *Indirect methods for estimating the hydraulic properties of unsaturated soils*, pages 185--202, 1992.

[68] W. Durner. Hydraulic conductivity estimation for soils with heterogeneous pore structure. *Water Resources Research*, 30(2):211--224, 1994.

[69] E. Priesack and W. Durner. Closed-form expression for the multi-modal unsaturated conductivity function. *Vadose Zone Journal*, 5(1):121--124, 2006.

[70] S.-E. Parent, A. Cabral, and J.. Zornberg. Water retention curve and hydraulic conductivity function of highly compressible materials. *Canadian Geotechnical Journal*, 44(10):1200--1214, 2007.

[71] R. Hu, Y. F. Chen, H. H. Liu, and C. B. Zhou. A water retention curve and unsaturated hydraulic conductivity model for deformable soils: Consideration of the change in pore-size distribution. *Geotechnique*, 63(16):1389--1405, 2013.

[72] D. Gallipoli, S. J. Wheeler, and M. Karstunen. Modelling the variation of degree of saturation in a deformable unsaturated soil. *Geotechnique*, 53(1):105--112, 2003.

[73] D. Gallipoli. *Constitutive and numerical modelling of unsaturated soils (BL)*. Ph.d., 2000.

[74] R. Horn and T. Baumgartl. *Dynamic properties of soils*, page p. 389. CRC Press, Boca Raton, FL, 2002.

[75] K. Terzaghi. *Theoretical soil mechanics*. J. Wiley and sons, inc. ; London, New York, 1943.

[76] A. W. Bishop. The principle of effective stress. *Teknisk Ukeblad*, 106:859--863, 1959.

[77] T. Baumgartl and B. Kock. Modeling volume change and mechanical properties with hydraulic models. *Soil Science Society of America Journal*, 68(1):57--65, 2004.

[78] L. F. Vesga. Equivalent effective stress and compressibility of unsaturated kaolinite clay subjected to drying. *Journal of Geotechnical and Geoenvironmental Engineering*, 134(3):366--378, 2008.

[79] A. W. Bishop and G. E. Blight. Some aspects of effective stress in saturated and partly saturated soils. *Géotechnique*, 13(3):177--197, 1963.

[80] C. R. Clarke and J. B. Nevels Jr. Shrinkage and suction properties of pledger-roebuck alluvial clay. *Transportation Research Record*, (1546):162--173, 1996.

[81] V. A. Snyder and R. D. Miller. Tensile strength of unsaturated soils. *Soil Science Society of America Journal*, 49:58--65, 1985.

[82] H. Peron, L. Hu, T. Hueckel, and L. Laloui. *The influence of the pore fluid on desiccation of a deformable porous material experimental unsaturated soil mechanics*, volume 112 of *Springer Proceedings in Physics*, pages 413--420. Springer Berlin Heidelberg, 2007.

[83] G. Crescimanno and G. Provenzano. Soil shrinkage characteristic curve in clay soils: Measurement and prediction. *Soil Science Society of America Journal*, 63(1):25--32, 1999.

[84] E. Braudeau, J. P. Frangi, and R. H. Mohtar. Characterizing nonrigid aggregated soil–water medium using its shrinkage curve. *Soil Sci. Soc. Am. J.*, 68(2):359--370, 2004.

[85] P. Boivin, P. Garnier, and M.l Vauclin. Modeling the soil shrinkage and water retention curves with the same equations. *Soil Science Society of America Journal*, 70(4):1082--1093, 2006.

[86] P. H. Groenevelt and C. D. Grant. Re-evaluation of the structural properties of some british swelling soils. *European Journal of Soil Science*, 52(3):469--477, 2001.

[87] V. Y. Chertkov. Modeling the pore structure and shrinkage curve of soil clay matrix. *Geoderma*, 95(3–4):215--246, 2000.

[88] V. Y. Chertkov. The reference shrinkage curve at higher than critical soil clay content. *Soil Science Society of America Journal*, 71(3):641--655, 2007.

[89] M. A. Fam, M. A. Fam, and M. B. Dusseault. Determination of the reactivity of clay-fluid systems using liquid limit data. *Canadian Geotechnical Journal*, 36(1):161--165, 1999.

[90] V. Y. Chertkov. The reference shrinkage curve of clay soil. *Theoretical and Applied Fracture Mechanics*, 48(1):50--67, 2007.

[91] V. Y. Chertkov. An integrated approach to soil structure, shrinkage, and cracking in samples and layers. *Geoderma*, 173–174(0):258--273, 2012.

[92] C. W. Lauritzen. Apparent specific volume and shrinkage characteristics of soil materials. *Soil science*, 65(2):155--180, 1948.

[93] M. J. Reeve and D. G. M. Hall. Shrinkage in clayey subsoils of contrasting structure. *Journal of Soil Science*, 29(3):315--323, 1978.

[94] G. B. Stirk. Some aspects of soil shrinkage and the effect of cracking upon water entry into the soil. *Australian Journal of Agricultural Research*, 5(2):279, 1954.

[95] V. Y. Chertkov. The physical effects of an intra-aggregate structure on soil shrinkage. *Geoderma*, 146(1–2):147--156, 2008.

[96] W. M. Cornelis, J. Corluy, H. Medina, J. Diaz, R. Hartmann, M. Van Meirvenne, and M. E. Ruiz. Measuring and modelling the soil shrinkage characteristic curve. *Geoderma*, 137(1–2):179--191, 2006.

[97] G. Sposito. Volume changes in swelling clays. *Soil science*, 115(4):315--320, 1973.

[98] V. Y. Chertkov. Shrinkage anisotropy characteristics from soil structure and initial sample/layer size. *Geoderma*, 200–201(0):1--8, 2013.

[99] V. Y. Chertkov. The soil reference shrinkage curve. *Open Hydrology Journal*, 1(1): 1--18, 2007.

[100] J. J. B. Bronswijk. Relation between vertical soil movements and water-content changes in cracking clays. *Soil Sci. Soc. Am. J.*, 55(5):1220--1226, 1991.

[101] J. V. Giraldez, J. V. Giraldez, G. Sposito, and C. Delgado. A general soil volume change equation: I. the two-parameter model. *Soil Science Society of America Journal*, 47(3): 419--422, 1983.

[102] A. Tariq and D. S. Durnford. Analytical volume change model for swelling clay soils. *Soil Science Society of America Journal*, 57(5):1183, 1993.

[103] P. A. Olsen and L. E. Haugen. A new model of the shrinkage characteristic applied to some norwegian soils. *Geoderma*, 83(1):67--81, 1998.

[104] D. McGarry and K. W. J. Malafant. The analysis of volume change in unconfined units of soil. *Soil Science Society of America Journal*, 51(2):NP, 1987.

[105] A. R. Mitchell and A. R. Mitchell. Shrinkage terminology: Escape from “normalcy”. *Soil Science Society of America Journal*, 56(3):993, 1992.

[106] P. H. Groenevelt and G. H. Bolt. Water retention in soil. *Soil science*, 113(4):238--245, 1972.

[107] V. Y. Chertkov. Non-fitted prediction of clay soil aggregate shrinkage. *International Journal of Physical Sciences*, 1(1):34--46, 2006.

[108] V. Y. Chertkov. Physical modeling of the soil swelling curve vs. the shrinkage curve. *Advances in Water Resources*, 44:66--84, 2012.

[109] ASTM D6836-02. Test methods for determination of the soil water characteristic curve for desorption using a hanging column, pressure extractor, chilled mirror hygrometer, and/or centrifuge. American Society for Testing and Materials, ASTM International, West Conshohocken, Pa, 2002.

[110] ASTM D5298-10. Standard test method for measurement of soil potential (suction) using filter paper. American Society for Testing and Materials, ASTM International, West Conshohocken, Pa, 2010.

[111] ASTM D3152-72. Standard test method for liquid limit, plastic limit, and plasticity index of soils. American Society for Testing and Materials, ASTM International, West Conshohocken, Pa, 2000.

[112] R. J. Mitchell. The eleventh annual r.m. hardy keynote address, 1997: Centrifugation in geoenvironmental practice and education. *Canadian Geotechnical Journal*, 35(4): 630--640, 1998.

[113] S. S. Agus and T. Schanz. Comparison of four methods for measuring total suction. *Vadose Zone J.*, 4(4):1087--1095, 2005.

[114] R. Bulut and E. C. Leong. Indirect measurement of suction. *Geotechnical and Geological Engineering*, 26(6):633--644, 2008.

[115] E. C. Leong, L. He, and H. Rahardjo. Factors affecting the filter paper method for total and matric suction measurements. *Geotechnical Testing Journal*, 25(3):322--333, 2002.

[116] S. W. Park, J. W. Button, and R. L. Lytton. Forensic investigation of pavement distortions using soil suction. *Journal of Transportation Engineering*, 125(1):60--66, 1999.

[117] J. Krahn and D. G. Fredlund. On total, matric and osmotic suction. *Soil science*, 114 (5):339--348, 1972.

[118] P. H. Shah, S. Sreedeep, and D. N. Singh. Evaluation of methodologies used for establishing soil-water characteristic curve. *Journal of ASTM International*, 3(6):11, 2006.

[119] S. Sreedeep and D.N. Singh. Critical review of the methodologies employed for soil suction measurement. *International Journal of Geomechanics*, 11(2):99--104, 2011.

[120] D. N. Singh and Sneha J. Kuriyan. Estimation of unsaturated hydraulic conductivity using soil suction measurements obtained by an insertion tensiometer. *Canadian Geotechnical Journal*, 40(2):476--483, 2003.

[121] S Sreedeep and DN Singh. A study to investigate the influence of soil properties on suction. *Journal of Testing and Evaluation*, 33(1):579--584, 2005.

[122] W. J. Likos and N. Lu. Automated humidity system for measuring total suction characteristics of clay. *Geotechnical Testing Journal*, 26(2):179--190, 2003.

[123] F. Shuai and D. G. Fredlund. *Use of a new thermal conductivity sensor to measure soil suction*, volume 287, pages 1--12. Geo-Denver 2000, Denver, 2000.

[124] P. Sattler and D. G. Fredlund. Use of thermal conductivity sensors to measure matric suction in the laboratory. *Canadian Geotechnical Journal*, 26(3):491--498, 1989.

[125] E. C. Leong, S. Tripathy, and H. Rahardjo. Total suction measurement of unsaturated soils with a device using the chilled-mirror dew-point technique. *Géotechnique*, 53(2): 173--182, 2003.

[126] V. S. Thakur, S. Sreedeep, and D. N. Singh. Laboratory investigations on extremely high suction measurements for fine-grained soils. *Geotechnical & Geological Engineering*, 24(3):565--578, 2006.

[127] E. Birle, D. Heyer, and N. Vogt. Influence of the initial water content and dry density on the soil–water retention curve and the shrinkage behavior of a compacted clay. *Acta Geotechnica*, 3(3):191--200, 2008.

[128] R.M. Reis, F. Saboya, S. Tibana, C. R. Marciano, and A. B. Ribeiro. Determination of soil-water retention curve for a young residual soil using a small centrifuge. In *Proceedings of the 18th International Conference on Soil Mechanics and Geotechnical Engineering, Paris 2013*, pages 1175--1178, 2013.

[129] A. Tariq and D. S. Durnford. Soil volumetric shrinkage measurements: a simple method. *Soil science*, 155(5):325--330, 1993.

[130] R. D. Stewart, M. R. A. Najm, D. E. Rupp, and J. S. Selker. An image-based method for determining bulk density and the soil shrinkage curve. *Soil Science Society of America Journal*, 76(4):1217--1221, 2012.

[131] R. D. Berndt and K. J. Coughlan. The nature of changes in bulk density with water content in a cracking clay. *Soil Research*, 15(1):27--37, 1976.

[132] W. M. Schafer and M. J. Singer. A new method of measuring shrink-swell potential using soil pastes. *Soil Science Society of America Journal*, 40(5):805--806, 1976.

[133] E. Braudeau and P. Boivin. *Transient determination of shrinkage curve for undisturbed soil samples: A standardized experimental method*. Kluwer Academic, Norwell, MA, 1995.

[134] E. Braudeau, J. M. Costantini, and G. Bellier. New device and method for soil shrinkage curve measurement and characterization. *Soil Science Society of America Journal*, 63 (3):525, 1999.

[135] H. Peron, T. Hueckel, and L. Laloui. An improved volume measurement for determining soil water retention curves. *Geotechnical Testing Journal*, 30(1):1--8, 2007.

[136] ASTM D2216-10. Standard test methods for laboratory determination of water (moisture) content of soil and rock by mass. American Society for Testing and Materials, ASTM International, West Conshohocken, Pa, 2010.

[137] J. C. Maxwell Garnett. Colours in metal glasses and in metallic films. *Philosophical Transactions of the Royal Society of London. Series A, Containing Papers of a Mathematical or Physical Character*, 203:385--420, 1904.

[138] F. T. Ulaby. *Fundamentals of applied Electromagnetics*. Pearson Prentice Hall, 5th edition, 2007.

[139] A. P. Annan. *Chapter 1 - Electromagnetic principles of ground penetrating radar*, pages 1--40. Elsevier, Amsterdam, 2009.

[140] N. Wagner, T. Bore, J. C. Robinet, D. Coelho, F. Taillade, and S. Delepine-Lesoille. Dielectric relaxation behavior of callovo-oxfordian clay rock: A hydraulic-mechanical-electromagnetic coupling approach. *Journal of Geophysical Research: Solid Earth*, 118(9):4729--4744, 2013.

[141] D. A. Robinson. Calculation of the dielectric properties of temperate and tropical soil minerals from ion polarizabilities using the Clausius-Mosotti equation. *Soil Sci. Soc. Am. J.*, 68(5):1780--1785, 2004.

[142] A. R. Von Hippel. *Dielectrics and waves*. John Wiley & Sons, Inc., New York, 1954.

[143] N. Wagner, K. Emmerich, F. Bonitz, and K. Kupfer. Experimental investigations on the frequency- and temperature-dependent dielectric material properties of soil. *IEEE Transactions on Geoscience and Remote Sensing*, 49(7):2518--2530, 2011.

[144] N. J. Cassidy. *Chapter 2 - Electrical and magnetic properties of rocks, soils and fluids*, pages 41--72. Elsevier, Amsterdam, 2009.

[145] K. Klein and J. C. Santamarina. Soft sediments: Wave-based characterization. *International Journal of Geomechanics*, 5(2):147--157, 2005.

[146] L. F. Chen, C. K. Ong, C. P. Neo, V. V. Varadan, and V. K. Varadan. *Microwave electronics - Measurement and materials characterization*. John Wiley & Sons, 2004.

[147] R. Chen, V. P. Drnevich, X. Yu, R. L. Nowack, and Y. Chen. Time domain reflectometry surface reflections for dielectric constant in highly conductive soils. *Journal of Geotechnical and Geoenvironmental Engineering*, 133(12):1597--1608, 2007.

[148] J.-P. Frangi, D.-C. Richard, X. Chavanne, I. Bexi, F. Sagnard, and V. Guilbert. New in situ techniques for the estimation of the dielectric properties and moisture content of soils. *Comptes Rendus Geoscience*, 341(10–11):831--845, 2009.

[149] R. Zajicek, J. Vrba, and K. Novotny. Evaluation of a reflection method on an open-ended coaxial line and its use in dielectric measurements. *Acta Polytechnica*, 5:50--54, 2006.

[150] F. M. Francisca and V. A. Rinaldi. Complex dielectric permittivity of soil-organic mixtures (20 MHz-1.3 GHz). *Journal of environmental engineering (New York, N.Y.)*, 129 (4):347--357, 2003.

[151] D. A. Robinson, S. B. Jones, J. M. Wraith, D. Or, and S. P. Friedman. A review of advances in dielectric and electrical conductivity measurement in soils using time domain reflectometry. *Vadose Zone Journal*, 2(4):444--475, 2003.

[152] Y. Chen and D. Or. Effects of maxwell-wagner polarization on soil complex dielectric permittivity under variable temperature and electrical conductivity. *Water Resources Research*, 42(6):W06424, 2006.

[153] Y. Chen and D. Or. Geometrical factors and interfacial processes affecting complex dielectric permittivity of partially saturated porous media. *Water Resources Research*, 42(6):W06423, 2006.

[154] K. Klein and J. C. Santamarina. Methods for broad-band dielectric permittivity measurements (soil-water mixtures, 5 Hz to 1.3 GHz). *Geotechnical Testing Journal*, 20 (2):168--178, 1997.

[155] G.P. de Loor. Dielectric properties of heterogeneous mixtures containing water. *IEEE Transactions on Geoscience and Remote Sensing*, 21(3):364--369, 1983.

[156] N. Wagner, K. Kupfer, and E. Trinks. A broadband dielectric spectroscopy study of the relaxation behaviour of subsoil. In S Okamura, editor, *7th International Conference on Electromagnetic Wave Interaction with Water and Moist Substances*, pages 31--38, 2007.

[157] M. Fam and C. Santamarina. *Study of geoprocesses with complementary mechanical and electromagnetic wave measurements in an oedometer*, volume 18 of *Geotechnical Testing Journal*. ASTM, West Conshohocken, PA, 1995.

[158] N. Wagner, E. Trinks, and K. Kupfer. Determination of the spatial TDR-sensor characteristics in strong dispersive subsoil using 3D-FEM frequency domain simulations in combination with microwave dielectric spectroscopy. *Measurement Science and Technology*, 18(4):1137, 2007.

[159] T. Ishida and T. Makino. Microwave dielectric relaxation of bound water to silica, alumina, and silica–alumina gel suspensions. *Journal of Colloid and Interface Science*, 212(1):144--151, 1999.

[160] M. Fam and J. C. Santamarina. A study of consolidation using mechanical and electromagnetic waves. *Géotechnique*, 47:203--219, 1997.

[161] R. Alvarez. Complex dielectric permittivity in rocks. A method for its measurement and analysis. *Geophysics*, 38:920--940, 1973.

[162] T. L. Chelidze and Y. Gueguen. Electrical spectroscopy of porous rocks: A review-I. Theoretical models. *Geophysical Journal International*, 137(1):1--15, 1999.

[163] B. Rotenberg, A. Cadene, J. F. Dufreche, S. Durand-Vidal, J. C. Badot, and P. Turq. An analytical model for probing ion dynamics in clays with broadband dielectric spectroscopy. *The Journal of Physical Chemistry B*, 109(32):15548--15557, 2005.

[164] T. Ishida and T. Makino. Effects of pH on dielectric relaxation of montmorillonite, allophane, and imogolite suspensions. *Journal of Colloid and Interface Science*, 212(1): 152--161, 1999.

[165] T. Ishida, M. Kawase, K. Yagi, J. Yamakawa, and K. Fukada. Effects of the counterion on dielectric spectroscopy of a montmorillonite suspension over the frequency range 10^5 - 10^{10} Hz. *Journal of Colloid and Interface Science*, 268(1):121--126, 2003.

[166] H. P. Schwan, G. Schwarz, J. Maczuk, and H. Pauly. On the low-frequency dielectric dispersion of colloidal particles in electrolyte solution. *The Journal of Physical Chemistry*, 66(12):2626--2635, 1962.

[167] Gerhard Schwarz. A theory of the low-frequency dielectric dispersion of colloidal particles in electrolyte solution. *The Journal of Physical Chemistry*, 66(12):2636--2642, 1962.

[168] P. Debye. Part I. Dielectric constant. Energy absorption in dielectrics with polar molecules. *Transactions of the Faraday Society*, 30(0):679--684, 1934.

[169] K. Asami. Characterization of heterogeneous systems by dielectric spectroscopy. *Progress in Polymer Science*, 27(8):1617--1659, 2002.

[170] U. Kaatze. Hydrogen network fluctuations and the microwave dielectric properties of liquid water. *Subsurface Sensing Technologies and Applications*, 1(4):377--391, 2000.

[171] K. S. Cole and R. H. Cole. Dispersion and absorption in dielectrics I. Alternating current characteristics. *The Journal of Chemical Physics*, 9(4):341--351, 1941.

[172] U. Kaatze. Reference liquids for the calibration of dielectric sensors and measurement instruments. *Measurement Science and Technology*, 18(4):967--976, 2007.

[173] U. Kaatze. Non-conducting and conducting reference liquids for the calibration of dielectric measurement systems. In *In Proc. 7th Conf. ISEMA on Electromagnetic Wave Interaction with Water and Moist Substances*, pages 15--18, 2007.

[174] T. Ishida, T. Makino, and C. J. Wang. Dielectric-relaxation spectroscopy of kaolinite, montmorillonite, allophane, and imogolite under moist conditions. *Clays and clay minerals*, 48(1):75--84, 2000.

[175] D. A. Robinson. Measurement of the solid dielectric permittivity of clay minerals and granular samples using a time domain reflectometry immersion method. *Vadose Zone Journal*, 3(2):705, 2004.

[176] M. T. Hallikainen, F. T. Ulaby, M. C. Dobson, M. A. El-Rayes, and Wu Lil-Kun. Microwave dielectric behavior of wet soil-part 1: Empirical models and experimental observations. *IEEE Transactions on Geoscience and Remote Sensing*, GE-23(1):25--34, 1985.

[177] G. Olhoeft. *Electrical properties of rocks*, pages 261--278. John Wiley & Sons,, London, 1974.

[178] B. A. Campbell. *Radar remote sensing of planetary surfaces*. Cambridge University Press, 2002.

[179] D. A. Robinson and S. P. Friedman. A method for measuring the solid particle permittivity or electrical conductivity of rocks, sediments, and granular materials. *Journal of Geophysical Research: Solid Earth*, 108(B2):2076, 2003.

[180] P. Bohleber, N. Wagner, and O. Eisen. Permittivity of ice at radio frequencies: Part I. Coaxial transmission line cell. *Cold Regions Science and Technology*, 82:56--67, 2012.

[181] P. Bohleber, N. Wagner, and O. Eisen. Permittivity of ice at radio frequencies: Part II. Artificial and natural polycrystalline ice. *Cold Regions Science and Technology*, 83–84: 13--19, 2012.

[182] C. Dirksen and S. Dasberg. Improved calibration of time domain reflectometry soil water content measurements. *Soil Sci. Soc. Am. J.*, 57(3):660--667, 1993.

[183] W. J. Ellison, K. Lamkaouchi, and J. M. Moreau. Water: A dielectric reference. *Journal of Molecular Liquids*, 68(2–3):171--279, 1996.

[184] U. Kaatze. Complex permittivity of water as a function of frequency and temperature. *Journal of Chemical & Engineering Data*, 34(4):371--374, 1989.

[185] U. Kaatze and C. Huebner. Electromagnetic techniques for moisture content determination of materials. *Measurement Science and Technology*, 21(8):082001, 2010.

[186] S. P. Friedman. A saturation degree-dependent composite spheres model for describing the effective dielectric constant of unsaturated porous media. *Water Resources Research*, 34(11):2949--2961, 1998.

[187] T. J. Heimovaara, W. Bouten, and J. M. Verstraten. Frequency domain analysis of time domain reflectometry waveforms: 2. A four-component complex dielectric mixing model for soils. *Water Resources Research*, 30(2):201--209, 1994.

[188] U. Kaatze. The dielectric properties of water in its different states of interaction. *Journal of Solution Chemistry*, 26(11):1049--1112, 1997.

[189] W. J. Ellison. Permittivity of pure water, at standard atmospheric pressure, over the frequency range 0 - 25 THz and the temperature range 0 - 100°C. *Journal of Physical and Chemical Reference Data*, 36(1):1--18, 2007.

[190] J. Hamelin, J. B. Mehl, and M. R. Moldover. The static dielectric constant of liquid water between 274 and 418 K near the saturated vapor pressure. *International Journal of Thermophysics*, 19(5):1359--1380, 1998.

[191] R. Buchner, J. Barthel, and J. Stauber. The dielectric relaxation of water between 0 °C and 35 °C. *Chemical Physics Letters*, 306(1–2):57--63, 1999.

[192] A. Brandelik and G. Krafft. *Measurements of bound and free water in mixtures*, pages 101--109. IEEE Press, New Jersey, 1996.

[193] D. A. Robinson, J. D. Cooper, and C. M. K. Gardner. Modelling the relative permittivity of soils using soil hygroscopic water content. *Journal of Hydrology*, 255(1–4):39--49, 2002.

[194] C. H. Roth, M. A. Malicki, and R. Plagge. Empirical evaluation of the relationship between soil dielectric constant and volumetric water content as the basis for calibrating soil moisture measurements by TDR. *Journal of Soil Science*, 43(1):1--13, 1992.

[195] O. H. Jacobsen and P. Schjonning. A laboratory calibration of time domain reflectometry for soil water measurement including effects of bulk density and texture. *Journal of Hydrology*, 151(2–4):147--157, 1993.

[196] W. A. Wensink. Dielectric properties of wet soils in the frequency range 1 - 3000 MHz. *Geophysical Prospecting*, 41(6):671--696, 1993.

[197] A. Brovelli and G. Cassiani. Effective permittivity of porous media: a critical analysis of the complex refractive index model. *Geophysical Prospecting*, 56(5):715--727, 2008.

[198] X. Yu and V. P. Drnevich. Soil water content and dry density by time domain reflectometry. *Journal of Geotechnical and Geoenvironmental Engineering*, 130(9):922--934, 2004.

[199] S. Jung, V. Drnevich, and M. Abou Najm. New methodology for density and water content by time domain reflectometry. *Journal of geotechnical and geoenvironmental engineering*, 139(5):659--670, 2013.

[200] T. Zakri, J. P. Laurent, and M. Vauclin. Theoretical evidence for `Lichtenecker's Mixture Formulae' based on the effective medium theory. *Journal of Physics D: Applied Physics*, 31(13):1589, 1998.

[201] J. R. Birchak, C. G. Gardner, J. E. Hipp, and J. M. Victor. High dielectric constant microwave probes for sensing soil moisture. *Proceedings of the IEEE*, 62(1):93--98, 1974.

[202] M. Persson and R. Berndtsson. Measuring nonaqueous phase liquid saturation in soil using time domain reflectometry. *Water Resources Research*, 38(5), 2002.

[203] V. L. Mironov, M. C. Dobson, V. H. Kaupp, S. A. Komarov, and V. N. Kleshchenko. Generalized refractive mixing dielectric model for moist soils. *IEEE Transactions on Geoscience and Remote Sensing*, 42(4):773--785, 2004.

[204] V. L. Mironov, L. G. Kosolapova, and S. V. Fomin. Physically and mineralogically based spectroscopic dielectric model for moist soils. *IEEE Transactions on Geoscience and Remote Sensing*, 47(7):2059--2070, 2009.

[205] D. Or and J. M. Wraith. Temperature effects on soil bulk dielectric permittivity measured by time domain reflectometry: A physical model. *Water Resources Research*, 35(2): 371--383, 1999.

[206] S. I. Siddiqui and V. P. Drnevich. A new method of measuring density and moisture content of soil using the technique of time domain reflectometry. Technical report, Joint Highway Research Project, Indiana Department of Transportation, Purdue University, 1995.

[207] S. Jung, V. Drnevich, and M. Abou Najm. Temperature corrections for time domain reflectometry parameters. *Journal of geotechnical and geoenvironmental engineering*, 139(5):671--683, 2013.

[208] ASTM D6780 / D6780M-12. Standard test method for water content and density of soil in situ by time domain reflectometry (TDR). American Society for Testing and Materials, ASTM International, West Conshohocken, Pa, 2002.

[209] C. Yu, A. W. Warrick, M. H. Conklin, M. H. Young, and M. Zreda. Two- and three-parameter calibrations of time domain reflectometry for soil moisture measurement. *Water Resources Research*, 33(10):2417--2421, 1997.

[210] O. H. Jacobsen and P. Schjonning. Comparison of TDR calibration functions for soil water determination, 1995.

[211] C. M. Regalado. A geometrical model of bound water permittivity based on weighted averages: the allophane analogue. *Journal of Hydrology*, 316(1–4):98--107, 2006.

[212] J. M. Blonquist, S. B. Jones, I. Lebron, and D. A. Robinson. Microstructural and phase configurational effects determining water content: Dielectric relationships of aggregated porous media. *Water Resources Research*, 42(5):W05424, 2006.

[213] S. Logsdon and D. Laird. Cation and water content effects on dipole rotation activation energy of smectites. *Soil Science Society of America Journal*, 68(5):1586--1591, 2004.

[214] O. Teschke, G. Ceotto, and E. F. de Souza. Interfacial water dielectric-permittivity-profile measurements using atomic force microscopy. *Physical review. E, Statistical, nonlinear, and soft matter physics*, 64(1):011605, 2001.

[215] N. Wagner and M. Loewer. A broadband 3-d numerical fem study on the characterization of dielectric relaxation processes in soils. In *10th International Conference on Electromagnetic Wave Interaction with Water and Moist Substances (ISEMA)*, pages 231--241. ISEMA.

[216] U. Kaatze. Techniques for measuring the microwave dielectric properties of materials. *Metrologia*, 47(2):91--113, 2010.

[217] O. V. Tereshchenko, F. J. K. Buesink, and F. B. J. Leferink. An overview of the techniques for measuring the dielectric properties of materials. In *General Assembly and Scientific Symposium, 2011 URSI*, pages 1--4. IEEE.

[218] M. T. Jilani, M. Zaka ur Rehman, M. A. Khan, M. T. Khan, and S. M. Ali. A brief review of measuring techniques for characterization of dielectric materials. *International Journal of Information Technology and Electrical Engineering*, 1(1):1--5, 2012.

[219] J. A. Huisman, S. S. Hubbard, J. D. Redman, and A. P. Annan. Measuring soil water content with ground penetrating radar. *Vadose Zone Journal*, 2(4):476--491, 2003.

[220] C. P. Lin. Frequency domain versus travel time analyses of tdr waveforms for soil moisture measurements. *Soil Science Society of America Journal*, 67(3):720--729, 2003.

[221] D. J. Daniels. Surface-penetrating radar. *Electronics & Communication Engineering Journal*, 8(4):165--182, 1996.

[222] A. Scheuermann, C. Huebner, S. Schlaeger, N. Wagner, R. Becker, and A. Bieberstein. Spatial time domain reflectometry and its application for the measurement of water content distributions along flat ribbon cables in a full-scale levee model. *Water Resources Research*, 45(4):W00D24, 2009.

[223] O. H. Jacobsen and P. Schjonning. Field evaluation of time domain reflectometry for soil water measurements. *Journal of Hydrology*, 151(2–4):159--172, 1993.

[224] S. B. Jones, J. M. Wraith, and D. Or. Time domain reflectometry measurement principles and applications. *Hydrological Processes*, 16(1):141--153, 2002.

[225] Agilent Technologies Inc. Basics of measuring the dielectric properties of materials (application note). *Agilent Technologies Inc.*, 2006.

[226] N. Wagner, B. Mueller, K. Kupfer, M. Schwing, and A. Scheuermann. Broadband electromagnetic characterization of two-port rod based transmission lines for dielectric spectroscopy of soil. In *Proceedings of the First European Conference on Moisture Measurement, Aquametry*, pages 228--237, 2010.

[227] N. Wagner, M. Schwing, and A. Scheuermann. Numerical 3-D FEM and experimental analysis of the open-ended coaxial line technique for microwave dielectric spectroscopy on soil. *IEEE Transactions on Geoscience and Remote Sensing*, 52(2):880--893, 2014.

[228] D. V. Blackham and Roger D. Pollard. An improved technique for permittivity measurements using a coaxial probe. *IEEE Transactions on Instrumentation and Measurement*, 46(5):1093--1099, 1997.

[229] T. W. Athey, M. A. Stuchly, and S. S. Stuchly. Measurement of radio frequency permittivity of biological tissues with an open-ended coaxial line: Part i. *IEEE Transactions on Microwave Theory and Techniques*, 30(1):82--86, 1982.

[230] M. A. Stuchly and S. S Stuchly. Equivalent circuit of an open-ended coaxial line in a lossy dielectric. *IEEE Transactions on Instrumentation and Measurement*, 1001(2): 116--119, 1982.

[231] T. P. Marsland and S. Evans. Dielectric measurements with an open-ended coaxial probe. *IEE Proceedings H Microwaves, Antennas and Propagation*, 134(4):341--349, 1987.

[232] J. Z. Bao, C. C. Davis, and M. L. Swicord. Microwave dielectric measurements of erythrocyte suspensions. *Biophysical Journal*, 66(6):2173--2180, 1994.

[233] J. Z. Bao, M. L. Swicord, and C. C. Davis. Microwave dielectric characterization of binary mixtures of water, methanol, and ethanol. *The Journal of Chemical Physics*, 104(12):4441--4450, 1996.

[234] M. Schwing, Z. Chen, A. Scheuermann, and N. Wagner. Dielectric properties of a clay soil determined in the frequency range from 1 Mhz to 40 Ghz. In *10th International Conference on Electromagnetic Wave Interaction with Water and Moist Substances, ISEMA 2014*, pages 242--250. ISEMA.

[235] K. Lauer, N. Wagner, and P. Felix-Henningsen. A new technique for measuring broadband dielectric spectra of undisturbed soil samples. *European Journal of Soil Science*, 63(2):224--238, 2012.

[236] A. G. Gorriti and E. C. Slob. Comparison of the different reconstruction techniques of permittivity from s-parameters. *IEEE Transactions on Geoscience and Remote Sensing*, 43(9):2051--2057, 2005.

[237] A. M. Nicolson and G. F. Ross. Measurement of the intrinsic properties of materials by time-domain techniques. *IEEE Transactions on Instrumentation and Measurement*, 19(4):377--382, 1970.

[238] W. B. Weir. Automatic measurement of complex dielectric constant and permeability at microwave frequencies. *Proceedings of the IEEE*, 62(1):33--36, 1974.

[239] J. Baker-Jarvis. *Transmission/reflection and short-circuit line permittivity measurements*. National Institute of Standards and Technology, 1990.

[240] J. Baker-Jarvis. *Measuring the permittivity and permeability of lossy materials: Solids, liquids, metals, building materials, and negative-index materials*. Tech. Rep. 1536, US Department of Commerce, Technology Administration, National Institute of Standards and Technology, 2005.

[241] A. G. Gorriti and E. C. Slob. Synthesis of all known analytical permittivity reconstruction techniques of nonmagnetic materials from reflection and transmission measurements. *Geoscience and Remote Sensing Letters, IEEE*, 2(4):433--436, 2005.

[242] A. G. Gorriti and E. C. Slob. A new tool for accurate s-parameters measurements and permittivity reconstruction. *IEEE Transactions on Geoscience and Remote Sensing*, 43(8):1727--1735, 2005.

[243] M. Schwing, Z. Chen, A. Scheuermann, and N. Wagner. Non-destructive coaxial transmission line measurements for dielectric soil characterization. In *Sensors Applications Symposium (SAS), 2014 IEEE*, pages 248--252, 2014.

[244] K. Zhang and D. Li. *Electromagnetic theory for microwaves and optoelectronics*. Springer, New York; Berlin, 1998.

[245] K. Levenberg. A method for the solution of certain problems in least squares. *Quarterly of applied mathematics*, 2:164--168, 1944.

[246] D. W. Marquardt. An algorithm for least-squares estimation of nonlinear parameters. *Journal of the Society for Industrial & Applied Mathematics*, 11(2):431--441, 1963.

[247] Ansoft HFSS. User's Guide - High Frequency Structure Simulator. 2005. page 801. Ansoft HFSS, 225 West Station Square Drive, Suite 200, Pittsburgh, PA 15219, USA, 2005.

[248] A. Casagrande. Research on the atterberg limits of soils. *United States Bureau of Public Roads*, 13(8):121--130, 1932.

[249] A. Casagrande. Classification and identification of soils. *Transactions, American Society of Civil Engineers*, 113:901--991, 1948.

[250] ASTM D4318-10. Standard test method for liquid limit, plastic limit, and plasticity index of soils. American Society for Testing and Materials, ASTM International, West Conshohocken, Pa, 2010.

[251] ASTM D2487-11. Standard practice for classification of soils for engineering purposes (unified soil classification system). American Society for Testing and Materials, ASTM International, West Conshohocken, Pa, 2011.

[252] ASTM D5550-06. Standard test method for specific gravity of soil solids by gas pycnometer. American Society for Testing and Materials, ASTM International, West Conshohocken, Pa, 2006.

[253] R. Haul and G. Dümbgen. Vereinfachte methode zur messung von oberflächengrössen durch gasadsorption. *Chemie Ingenieur Technik*, 32(5):349--354, 1960.

[254] R. Haul and G. Dümbgen. Vereinfachte methode zur messung von oberflächengrössen durch gasadsorption, 2. mitteilung. *Chemie Ingenieur Technik*, 35(8):586--589, 1963.

[255] ASTM D5604-96. Standard test methods for precipitated silica - surface area by single point BET nitrogen adsorption. American Society for Testing and Materials, ASTM International, West Conshohocken, Pa, 2012.

[256] G. E. Rayment and D. J. Lyons. *Soil chemical methods: Australasia*, volume 3. CSIRO, Collingwood, Vic, 2011.

[257] L. P. Meier and G. Kahr. Determination of the cation exchange capacity (cec) of clay minerals using the complexes of copper (ii) ion with triethylenetetramine and tetraethylenepentamine. *Clays and clay minerals*, 47(3):386--388, 1999.

[258] H. Kaden. *Frequency dependent complex dielectric permittivity and characterization of dielectric properties of clay-water mixtures containing swellable and non-swellable clay minerals at low water contents*. Ph.d. thesis, 2012.

[259] ASTM D422-63. Standard test methods for particle-size analysis of soils. American Society for Testing and Materials, ASTM International, West Conshohocken, Pa, 2007.

[260] H. M. Kingston and P. J. Walter. Microwave assisted acid digestion of siliceous and organically based matrices. *EPA Test Method Collections, United States Environmental Protection Agency (USEPA)*, Draft Method 3052, 1995.

[261] A. Sridharan and P. V. Sivapullaiah. Mini compaction test apparatus for fine grained soils. *Geotechnical Testing Journal*, 28(3):240--246, 2005.

[262] B. V. V. Reddy and K. S. Jagadish. The static compaction of soils. *Géotechnique*, 43 (2):337--341, 1993.

[263] N. S. Pandian, T. S. Nagaraj, and M. Manoj. Re-examination of compaction characteristics of fine-grained soils. *Géotechnique*, 47(2):363--366, 1997.

[264] S. Tombolato, A. Tarantino, and L. Mongiovi. *Suction induced by static compaction*, volume 93 of *Springer Proceedings in Physics*, chapter 8, pages 101--110. Springer Berlin Heidelberg, 2005.

[265] A. Tarantino and S. Tombolato. Coupling of hydraulic and mechanical behaviour in unsaturated compacted clay. *Géotechnique*, 55(4):307--317, 2005.

[266] A. Tarantino and E De Col. Compaction behaviour of clay. *Géotechnique*, 58(3):199--213, 2008.

[267] A. Sawangsuriya, T. B. Edil, and P. J. Bosscher. Modulus−suction−moisture relationship for compacted soils. *Canadian Geotechnical Journal*, 45(7):973--983, 2008.

[268] P. Delage, M. Audiguier, Y. J. Cui, and M. D. Howat. Microstructure of a compacted silt. *Canadian Geotechnical Journal*, 33(1):150--158, 1996.

[269] K. Iyer, S. Jayanth, S. Gurnani, and D. Singh. Influence of initial water content and specimen thickness on the swcc of fine-grained soils. *International Journal of Geomechanics*, 13(6):894--899, 2013.

[270] R. Thom, R. Sivakumar, V. Sivakumar, E. J. Murray, and P. Mackinnon. Pore size distribution of unsaturated compacted kaolin: The initial states and final states following saturation. *Géotechnique*, 57(5):469--474, 2007.

[271] V. Sivakumar and S. J. Wheeler. Influence of compaction procedure on the mechanical behaviour of an unsaturated compacted clay part 1: Wetting and isotropic compression. *Géotechnique*, 50(4):359--368, 2000.

[272] V. Sivakumar, W. C. Tan, E. J. Murray, and J. D. McKinley. Wetting, drying and compression characteristics of compacted clay. *Géotechnique*, 56(1):57--62, 2006.

[273] E. Romero, A. Gens, and A. Lloret. Water permeability, water retention and microstructure of unsaturated compacted boom clay. *Engineering Geology*, 54(1–2):117--127, 1999.

[274] E. Romero and P. H. Simms. Microstructure investigation in unsaturated soils: A review with special attention to contribution of mercury intrusion porosimetry and environmental scanning electron microscopy. *Geotechnical and Geological Engineering*, 26(6):705--727, 2008.

[275] E. Romero, G. Della Vecchia, and C. Jommi. An insight into the water retention properties of compacted clayey soils. *Géotechnique*, 61:313--328, 2011.

[276] S. Diamond. Microstructure and pore structure of impact-compacted clays. *Clays and clay minerals*, 19(4):239--249, 1971.

[277] S. Dhawan, A. Mishra, and S. Rao. *Experimental study on shrinkage behaviour and prediction of shrinkage magnitudes of residual soils experimental unsaturated soil mechanics*, volume 112 of *Springer Proceedings in Physics*, pages 277--284. Springer Berlin Heidelberg, 2007.

[278] K. Osinubi and C. Nwaiwu. Desiccation-induced shrinkage in compacted lateritic soils. *Geotechnical and Geological Engineering*, 26(5):603--611, 2008.

[279] D. E. Daniel and Y. K. Wu. Compacted clay liners and covers for arid sites. *Journal of Geotechnical Engineering*, 119(2):223--237, 1993.

[280] L. Barden and G. R. Sides. Engineering behavior and structure of compacted clay. *Journal of Soil Mechanics & Foundations Div (ASCE)*, 96:1171--1200, 1970.

[281] D. A. Sun, D. C. Sheng, H. B. Cui, and J. Li. Effect of density on the soil-water-retention behaviour of compacted soil. In *Proceedings of the fourth international conference on unsaturated soils*, pages 1338--1347, 2004.

[282] J. M. Tinjum, C. H. Benson, and L. R. Blotz. Soil-water characteristic curves for compacted clays. *Journal of geotechnical and geoenvironmental engineering*, 123(11): 1060--1069, 1997.

[283] A. M. Thomas, D. N. Chapman, C. D. F. Rogers, and N. Metje. Electromagnetic properties of the ground: Part i – fine-grained soils at the liquid limit. *Tunnelling and Underground Space Technology*, 25(6):714--722, 2010.

[284] A. M. Thomas, D. N. Chapman, C. D. F. Rogers, and N. Metje. Broadband apparent permittivity measurement in dispersive soils using quarter-wavelength analysis. *Soil Science Society of America Journal*, 72(5):1401--1409, 2008.

[285] T. Miyamoto, T. Annaka, and J. Chikushi. Extended dual composite sphere model for determining dielectric permittivity of andisols. *Soil Science Society of America Journal*, 69(1):23--29, 2005.

[286] R. M. Neal. *MCMC using Hamiltonian dynamics*, pages 113--162. Chapman & Hall CRC Press, 2011.

[287] O. Stramer and R. L. Tweedie. Langevin-type models II: self-targeting candidates for MCMC algorithms. *Methodology And Computing In Applied Probability*, 1(3):307--328, 1999.

[288] N. Metropolis, A. W. Rosenbluth, M. N. Rosenbluth, A. H. Teller, and E. Teller. Equation of state calculations by fast computing machines. *The Journal of Chemical Physics*, 21(6):1087--1092, 1953.

[289] W. K. Hastings. Monte carlo sampling methods using markov chains and their applications. *Biometrika*, 57(1):97--109, 1970.

[290] L. Tierney. Markov chains for exploring posterior distributions. *The Annals of Statistics*, 22(4):1701--1728, 1994.

[291] P. Neal and G. Robert. Optimal scaling for partially updating MCMC algorithms. *The Annals of Applied Probability*, 16(2):475--515, 2006.

[292] N. Liu. *Soil and site characterization using electromagnetic waves*. Ph.d. thesis, 2007.

[293] A. P. Gregory and R. N. Clarke. Dielectric metrology with coaxial sensors. *Measurement Science and Technology*, 18(5):1372--1386, 2007.

Appendix

Appendix A

Compaction test

A.1 Optimum water content and optimum density

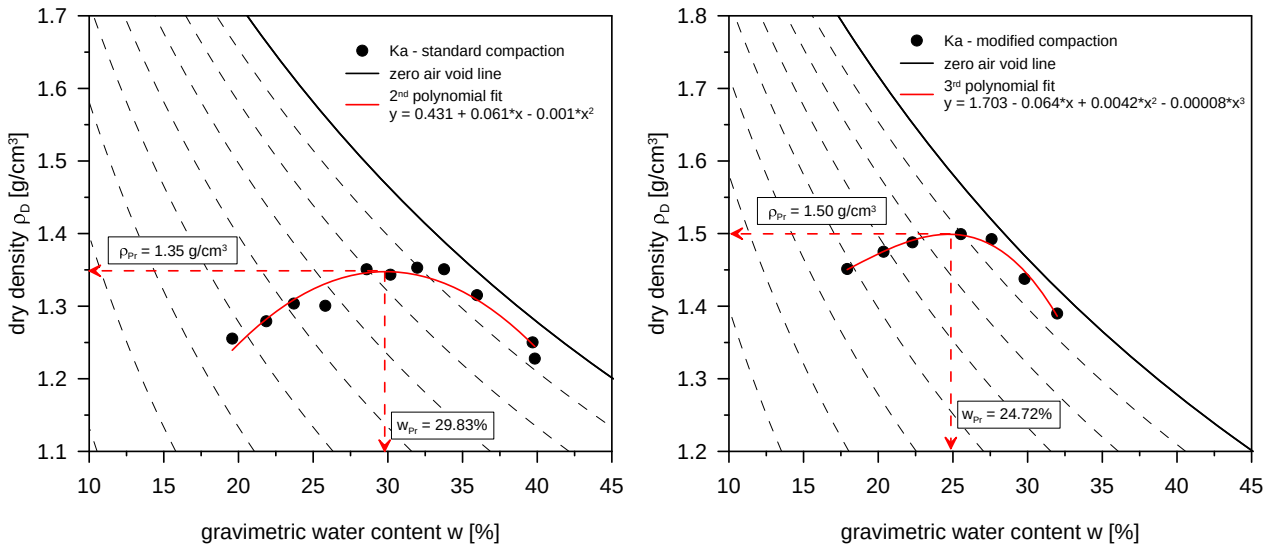

Figure A.1: (A) Standard compaction test on KA indicating the optimum water content and optimum density and (B) modified compaction test on KA indicating the optimum water content and optimum density.

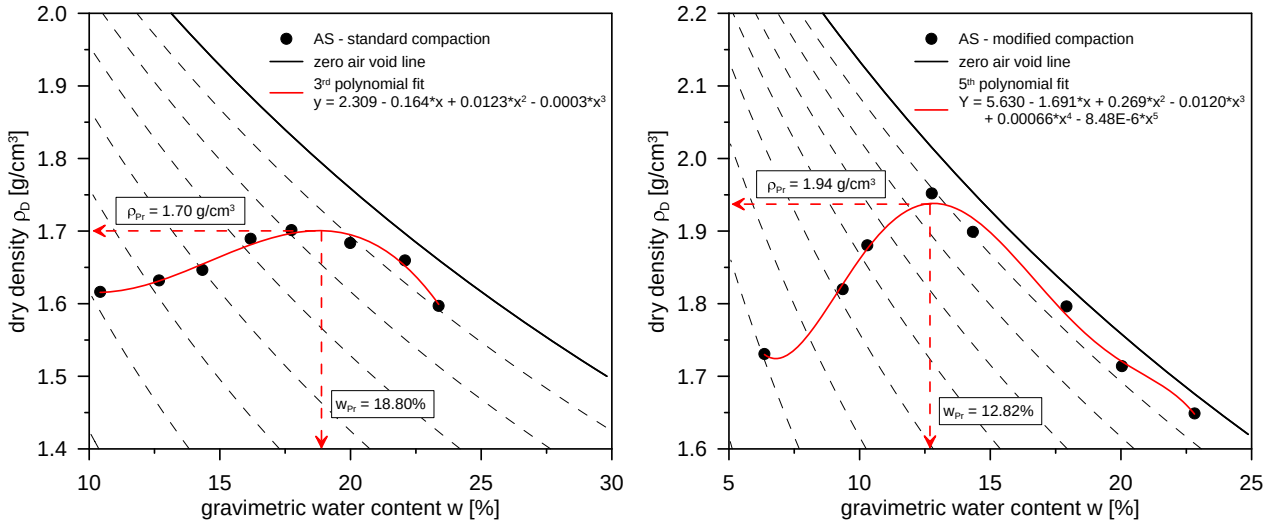

Figure A.2: (A) Standard compaction test on AS indicating the optimum water content and optimum density and (B) modified compaction test on AS indicating the optimum water content and optimum density.

A.2 SWCC of standard and modified compaction tests

Table A.1: Tabular overview of fitting parameter obtained for the dry path of the SWCCs of standard and modified compaction tests on KA and AS using a bimodal van Genuchten model.

Soil	Test	No.	θ_S	θ_R	Mode 1				Mode 2			
					W	a_{vG}	n_{vG}	m_{vG}	W	a_{vG}	n_{vG}	m_{vG}
AS	standard	C1	16.70	0	0.80	0.028	2.511	0.602	0.20	0.053	41.447	0.976
		C2	20.29	0	0.66	0.028	2.511	0.602	0.34	0.086	3.032	0.670
		C3	23.96	0	0.56	0.028	2.511	0.602	0.44	0.135	2.808	0.644
		C4	27.82	0	0.48	0.028	2.511	0.602	0.52	0.192	2.193	0.544
		C5	30.42	0	0.44	0.028	2.511	0.602	0.56	0.437	1.764	0.433
		C6	33.82	0	0.40	0.028	2.511	0.602	0.60	0.256	1.961	0.490
		C7	36.85	0	0.36	0.028	2.511	0.602	0.64	0.519	1.740	0.425
		C8	37.60	0	0.36	0.028	2.511	0.602	0.64	0.590	1.771	0.435
AS	modified	C1	11.32	0	1	0.021	2.563	0.610	0	-	-	-
		C2	16.81	0	0.67	0.021	2.563	0.610	0.33	0.038	20.144	0.950
		C3	19.66	0	0.58	0.021	2.563	0.610	0.42	0.050	3.991	0.749
		C4	24.63	0	0.46	0.021	2.563	0.610	0.54	0.080	2.205	0.546
		C5	26.64	0	0.42	0.021	2.563	0.610	0.58	0.081	3.607	0.723
		C6	31.33	0	0.36	0.021	2.563	0.610	0.64	0.219	2.158	0.537
		C7	34.02	0	0.33	0.021	2.563	0.610	0.67	0.285	2.021	0.505
		C8	38.44	0	0.29	0.021	2.563	0.610	0.71	0.494	1.785	0.440
KA	modified	C1	26.01	0	0.65	0.154	1.947	0.486	0.35	0.205	28.638	0.965
		C2	30.30	0	0.56	0.154	1.947	0.486	0.44	0.182	7.016	0.857
		C3	33.44	0	0.51	0.154	1.947	0.486	0.49	0.231	6.882	0.855
		C4	38.27	0	0.44	0.154	1.947	0.486	0.56	0.228	3.873	0.742
		C5	41.18	0	0.41	0.154	1.947	0.486	0.59	0.280	3.698	0.729
		C6	42.56	0	0.40	0.154	1.947	0.486	0.60	0.274	4.336	0.769
		C7	43.97	0	0.39	0.154	1.947	0.486	0.61	0.296	2.906	0.656

A.3 3-D illustration of dielectric measurements taken from compaction tests

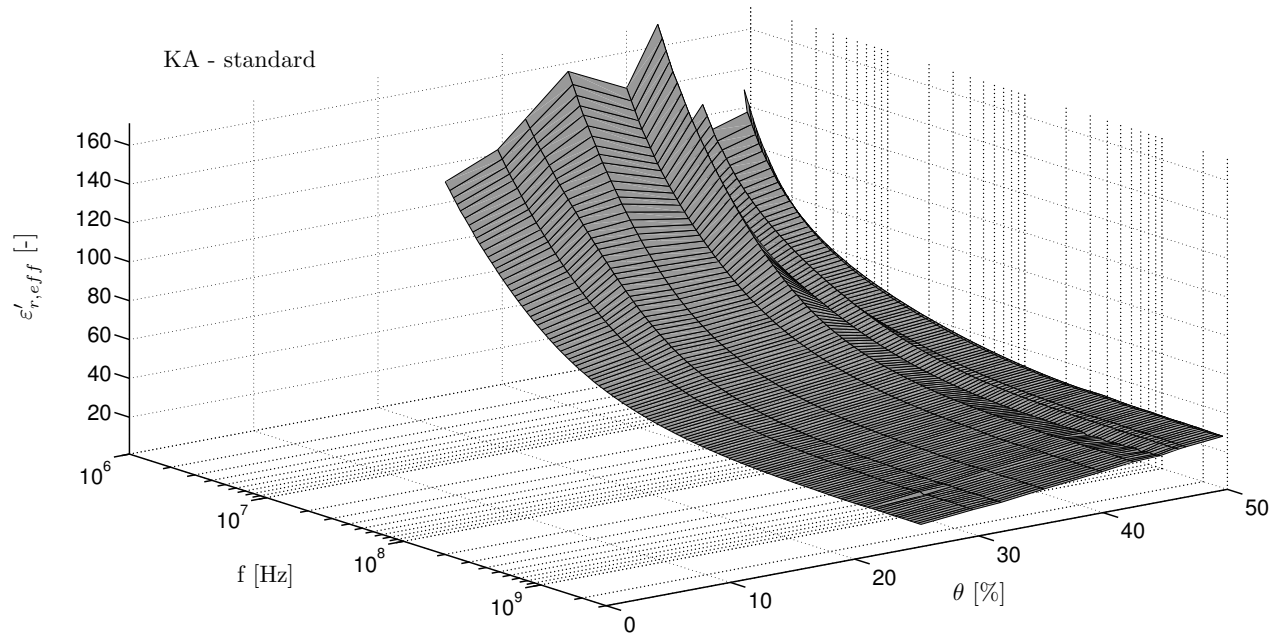

(a)

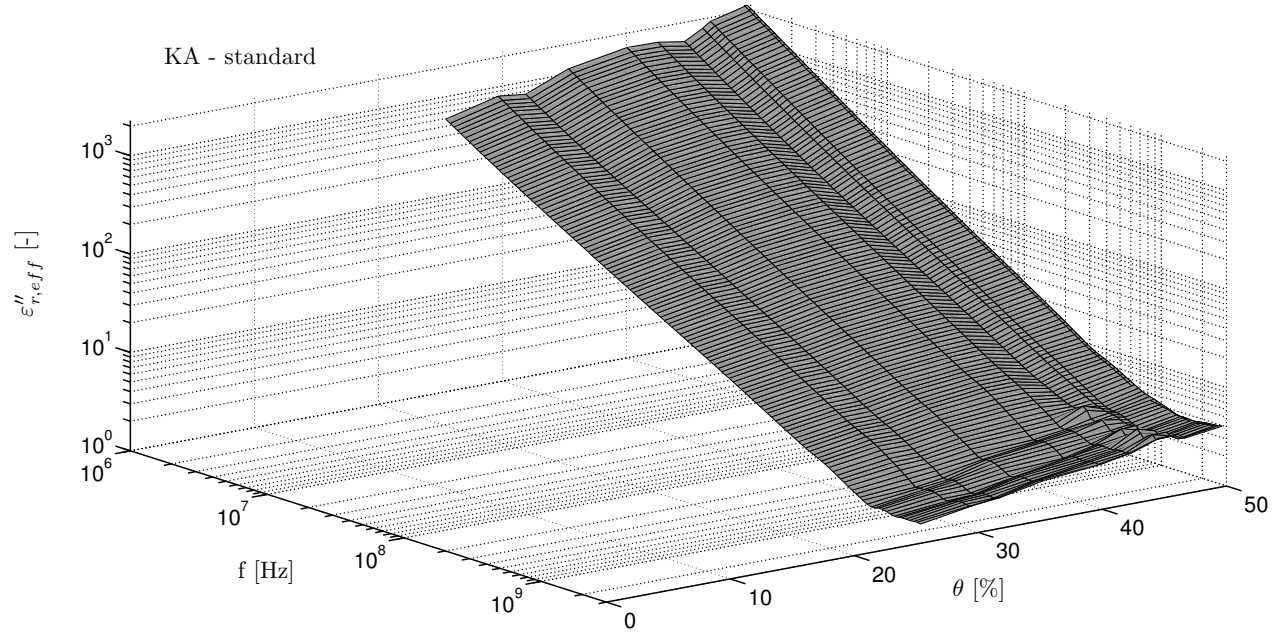

(b)

Figure A.3: 3-D illustration of complex permittivity, $\varepsilon^{\star}_{r,\text{eff}}$, of standard compacted KA dependent on the frequency, f, and volumetric water content, θ: (A) real part, $\varepsilon'_{r,\text{eff}}$, of complex permittivity, and (B) imaginary part, $\varepsilon''_{r,\text{eff}}$, of complex permittivity.

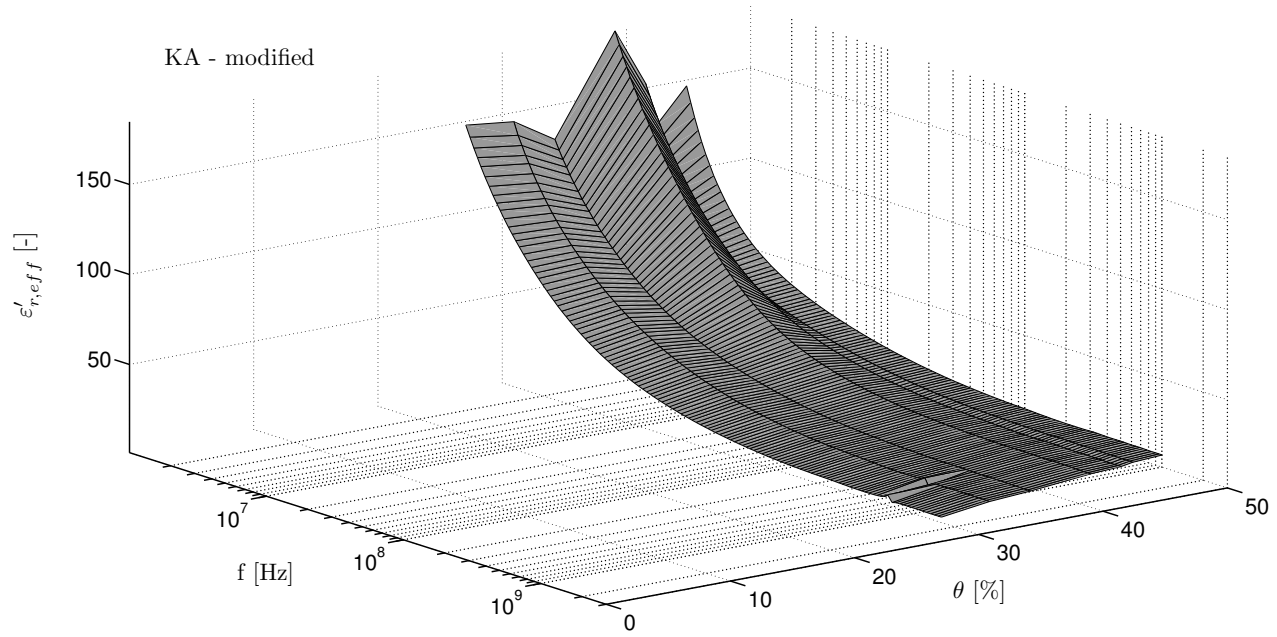

(a)

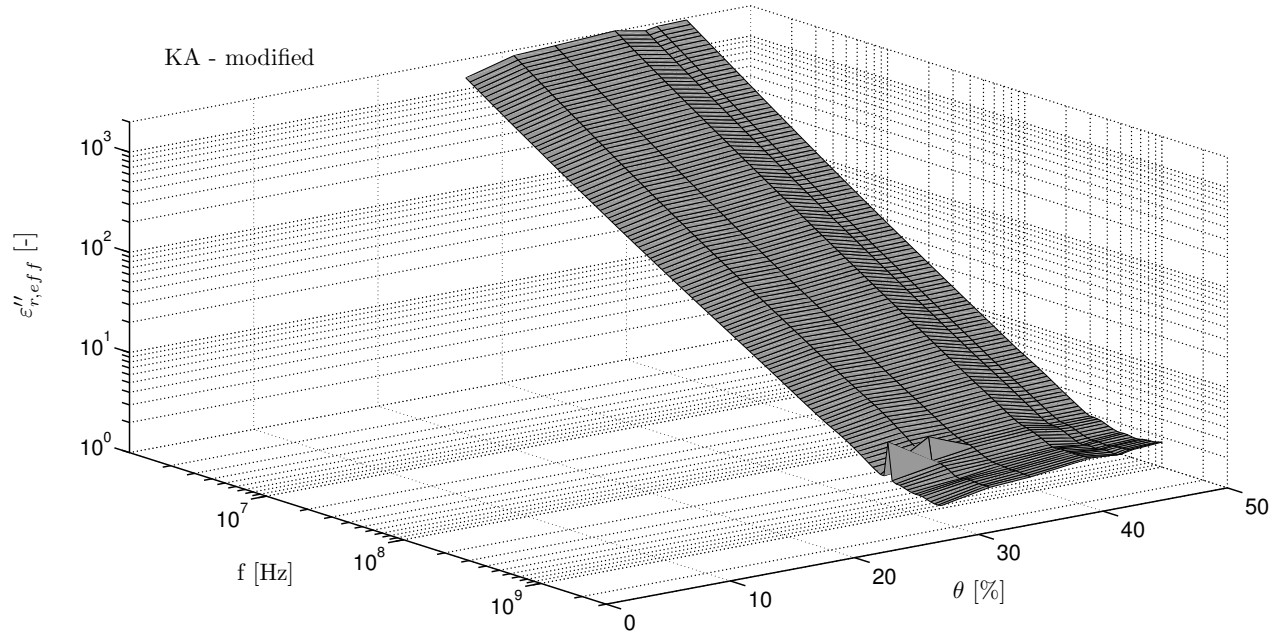

(b)

Figure A.4: 3-D illustration of complex permittivity, $\varepsilon^{\star}_{r,\text{eff}}$, of modified compacted KA dependent on the frequency, f, and volumetric water content, θ: (A) real part, $\varepsilon'_{r,\text{eff}}$, of complex permittivity, and (B) imaginary part, $\varepsilon''_{r,\text{eff}}$, of complex permittivity.

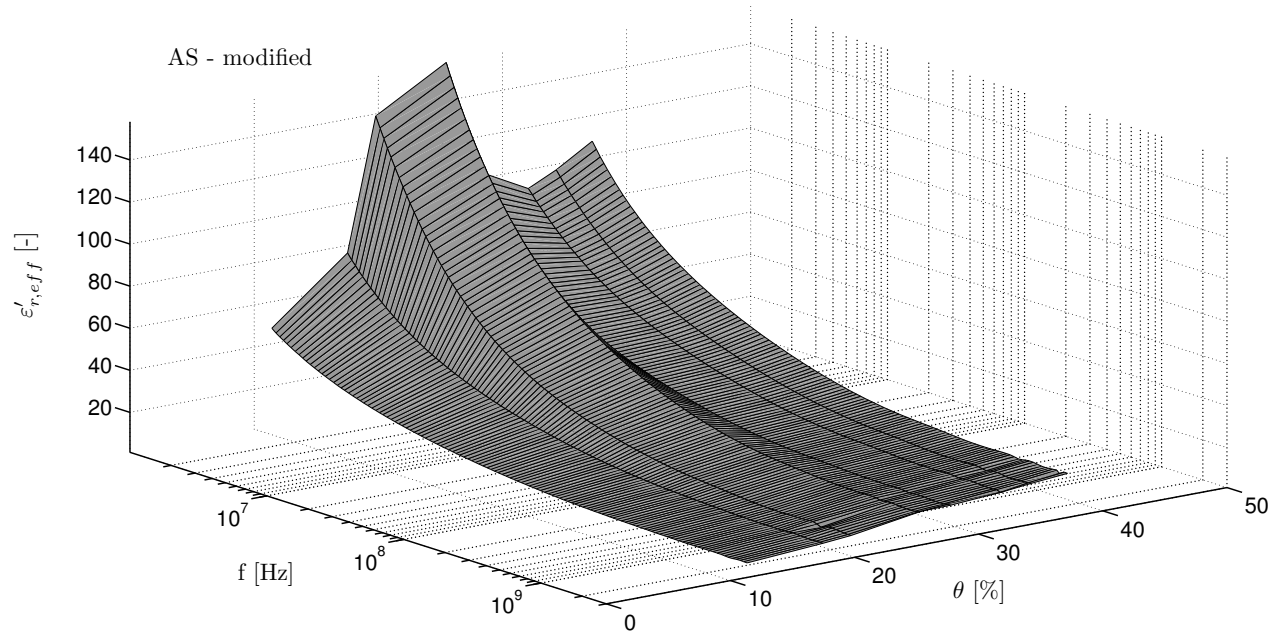

(a)

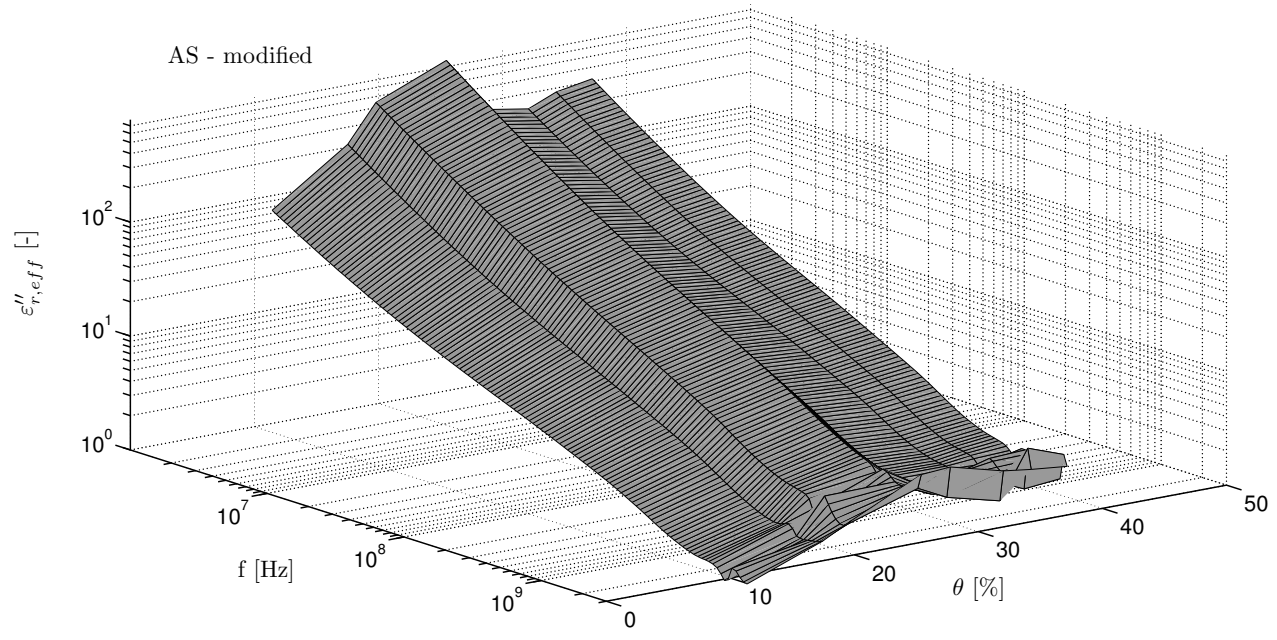

(b)

Figure A.5: 3-D illustration of complex permittivity, $\varepsilon^{\star}_{r,\text{eff}}$, of modified compacted AS dependent on the frequency, f, and volumetric water content, θ: (A) real part, $\varepsilon'_{r,\text{eff}}$, of complex permittivity, and (B) imaginary part, $\varepsilon''_{r,\text{eff}}$, of complex permittivity.

Appendix B

Shrinkage test

B.1 Model parameter of the shrinkage curves of soils

Table B.1: Tabular overview of parameters modelling the shrinkage curve based on Chertkov [3].

Soil	Run No.	a_{ch}	F_Z	ν_Z	ν_S	ν_N	ζ_N	ζ_Z
AS	1	1.065	0.415	0.537	0.386	0.624	0.390	0.102
	2	2.252	0.709	0.526	0.380	0.567	0.305	0.167
	3	4.494	0.855	0.527	0.379	0.547	0.273	0.204
	4	1.784	0.626	0.523	0.379	0.579	0.320	0.146
	5	2.692	0.750	0.520	0.375	0.555	0.290	0.174
	6	2.138	0.702	0.534	0.386	0.579	0.313	0.169
KA	1	2.070	0.760	0.539	0.273	0.596	0.454	0.278
	2	1.218	0.588	0.537	0.275	0.641	0.510	0.212
	3	2.492	0.803	0.541	0.271	0.584	0.444	0.298
	4	2.899	0.823	0.530	0.270	0.565	0.418	0.292
	5	2.120	0.762	0.533	0.268	0.580	0.449	0.276
	6	3.052	0.843	0.548	0.271	0.580	0.439	0.320

B.2 Model parameter of the SWCC using van Genuchten equations

Table B.2: Tabular overview of parameters modelling the SWCC of AS and KA based on a multimodal van Genuchten equation

Mode	Parameter	AS	KA
RMSE		0.634	0.970
	θ_S	61.8	70.6
	θ_R	0.0	0.0
1	W	0.050	0.049
	a_{vG}	0.036	1.8E-05
	n_{vG}	1.949	2.193
	m_{vG}	0.487	0.544
2	W	0.435	0.591
	a_{vG}	8.7E-05	3.5E-04
	n_{vG}	1.941	3.314
	m_{vG}	0.485	0.698
3	W	0.165	0.140
	a_{vG}	0.005	2.3E-03
	n_{vG}	2.480	5.905
	m_{vG}	0.597	0.831
4	W	0.350	0.220
	a_{vG}	0.274	0.056
	n_{vG}	1.347	1.976
	m_{vG}	0.257	0.494

Table B.3: Tabular overview of parameters modelling the SWCC of AS and KA based on an unimodal Genuchten equation, with two and three unknown fitting parameter

Parameter	AS	KA
θ_S	61.8	70.6
θ_R	0.0	0.0
two unknown parameter		
RMSE	3.942	5.184
a_{vG}	0.042	0.003
n_{vG}	1.199	1.688
three unknown parameter		
RMSE	2.498	2.958
a_{vG}	1.4E-07	1.0E-07
n_{vG}	0.296	0.607
m_{vG}	8.879	1.3E+02

B.3 Standard deviation of SWCC fits using van Genuchten model

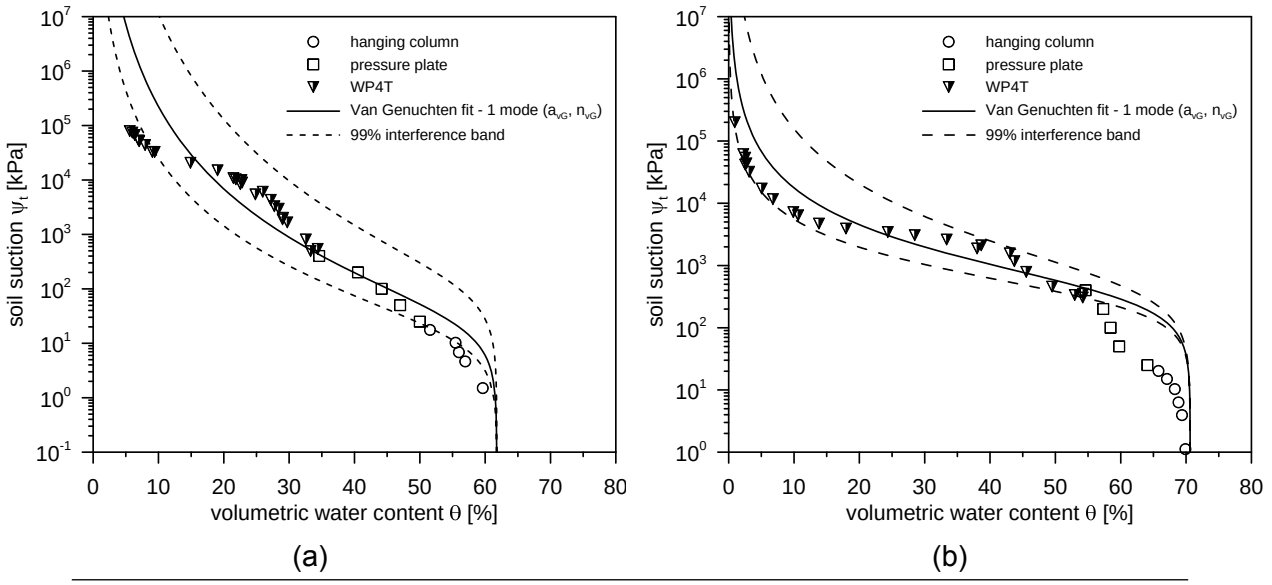

Figure B.1: Standard deviation of the SWCC fits on (A) AS and (B) KA using unimodal van Genuchten model with two unknown parameters, a_{vG} and n_{vG}.

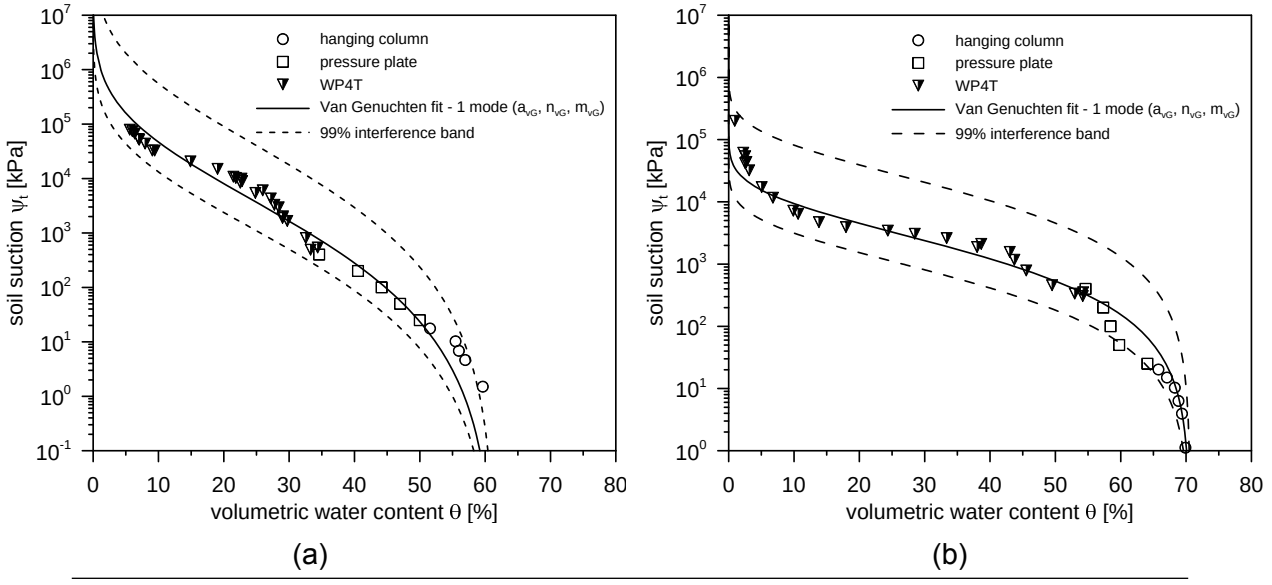

Figure B.2: Standard deviation of the SWCC fits on (A) AS and (B) KA using unimodal van Genuchten model with three unknown parameters, a_{vG}, n_{vG} and m_{vG}.

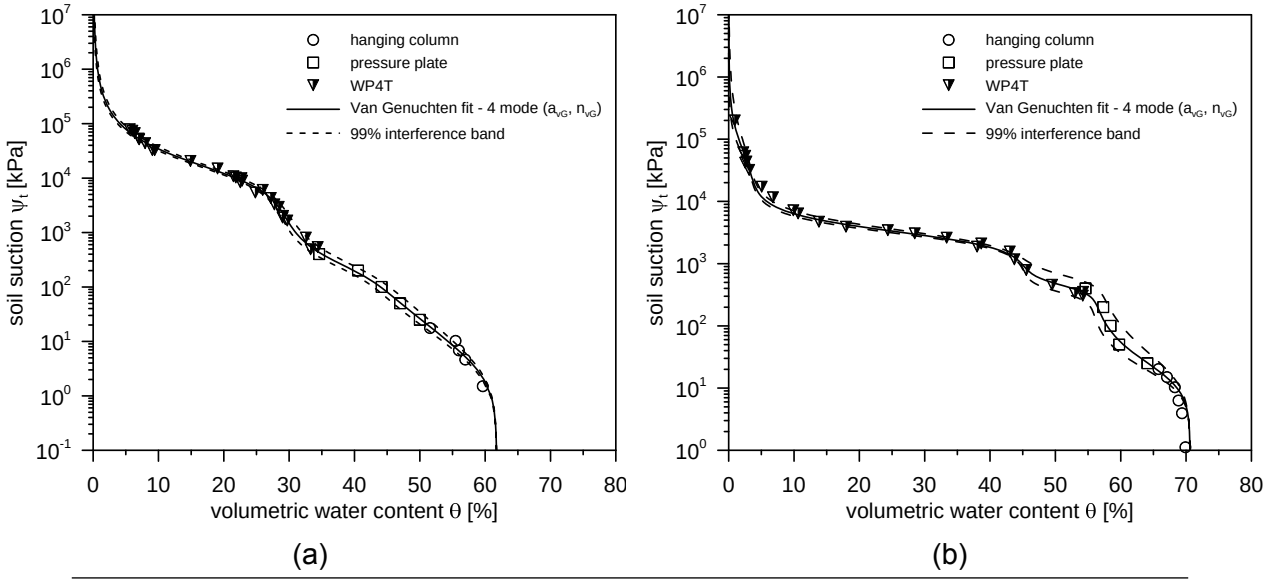

Figure B.3: Standard deviation of the SWCC fits on (A) AS and (B) KA using multimodal van Genuchten model, with two unknown parameters, a_{vG} and n_{vG}, for each mode.

B.4 Numerical simulations on the effect of an air gap between OE probe and a soil sample under shrinkage

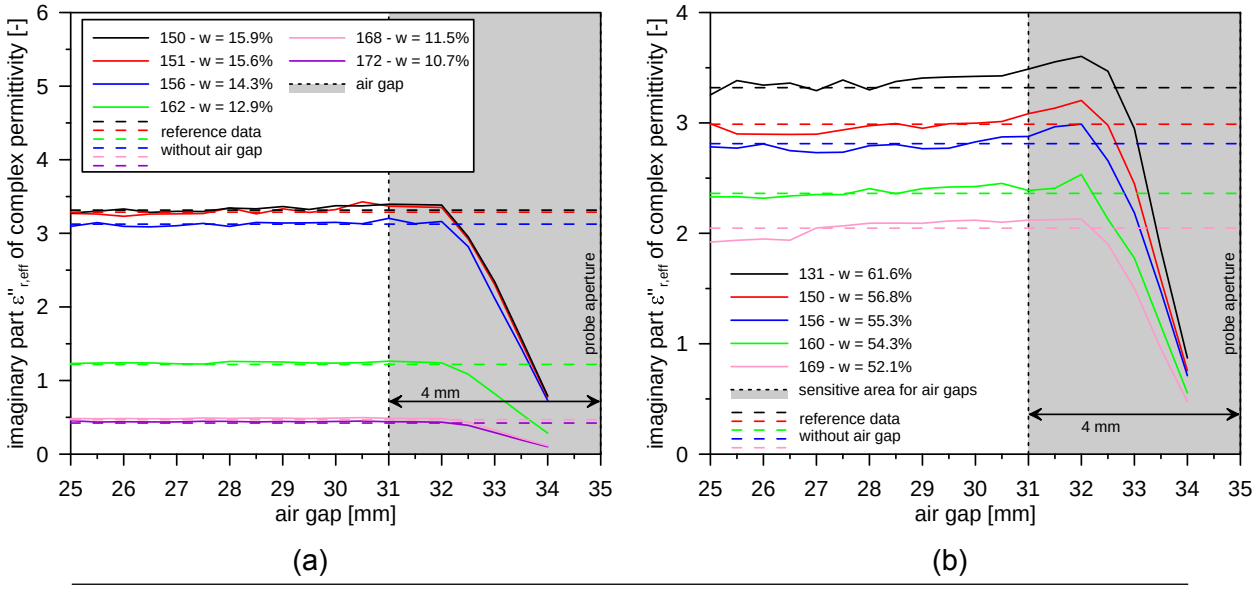

Figure B.4: Results of numerical simulations on the air gap between the soil sample and OE probe aperture. Air gap effect on (A) six measurement on AS and (B) five measurement on KA, at selected gravimetric water contents. Shown is $\varepsilon''_{r,\mathrm{eff}}$ at 1 GHz as a function of air gap length, r_{Gap}, with a fixed height of $h_{\mathrm{Gap}} = 1.0\,\mathrm{mm}$. The propagation of the air gap length, r_{Gap}, starts from sample outside to OE probe aperture (at 35 mm, see Figure 7.30).

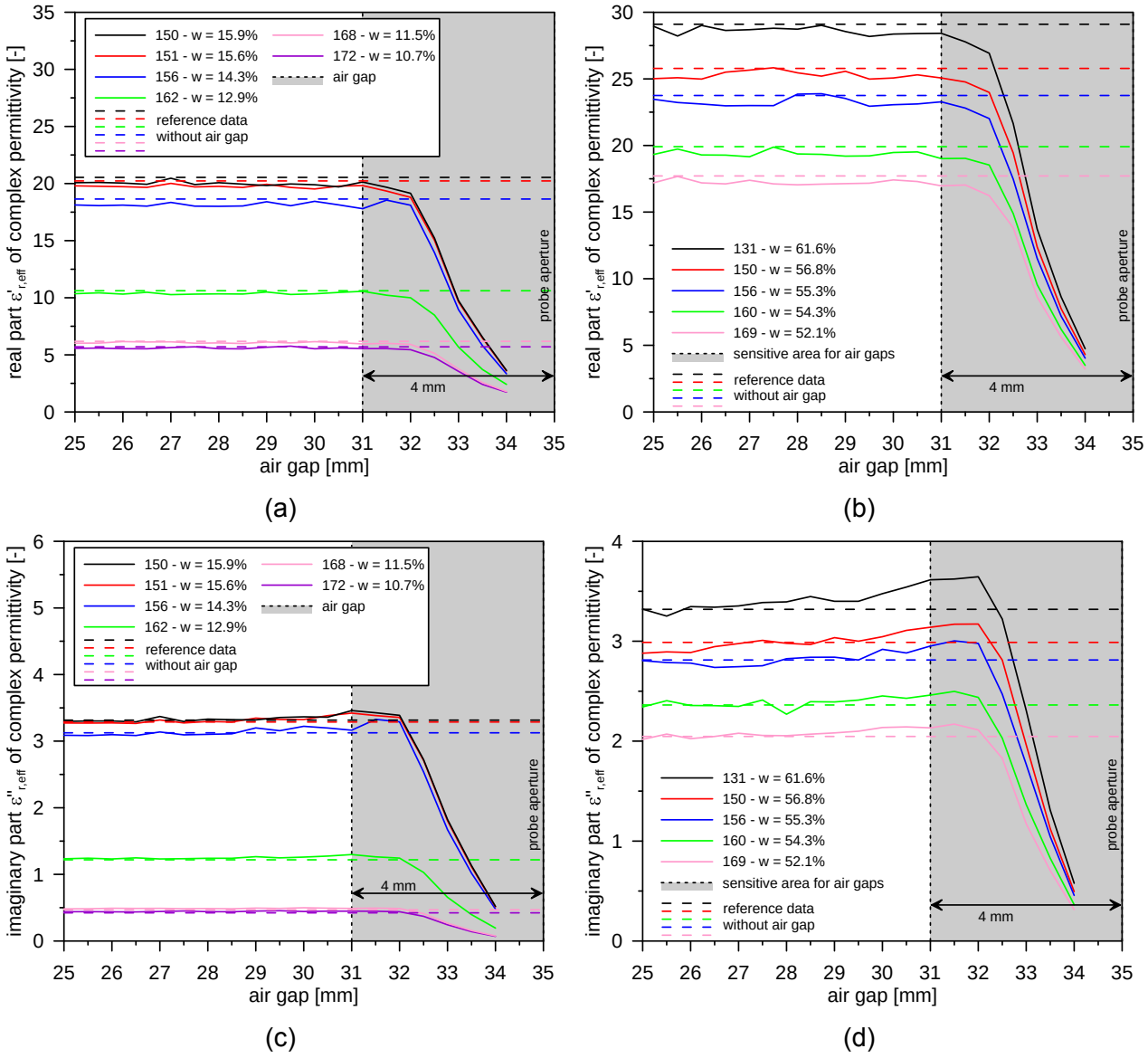

Figure B.5: Results of numerical simulations on the air gap between the soil sample and OE probe aperture. Air gap effect on $\varepsilon'_{r,\mathrm{eff}}$ at 1 GHz as a function of air gap length, r_{Gap}, for (A) AS and (B) KA, with a fixed height of $h_{\mathrm{Gap}} = 2.0\,\mathrm{mm}$. Air gap effect on $\varepsilon''_{r,\mathrm{eff}}$ at 1 GHz as a function of air gap length, r_{Gap}, for (C) AS and (D) KA, with a fixed height of $h_{\mathrm{Gap}} = 2.0\,\mathrm{mm}$. The propagation of the air gap length, r_{Gap}, starts from sample outside to OE probe aperture (at 35 mm, see Figure 7.30).